Propagation et émergence de motifs en biologie

Maxime Estavoyer

Université Claude Bernard Lyon 1

THESE de DOCTORAT DE
L'UNIVERSITE CLAUDE BERNARD LYON 1

Ecole Doctorale N° 512
École doctorale InfoMaths (ED 512)

Discipline : Mathématiques

Soutenue publiquement le 18/11/2024, par :
Maxime ESTAVOYER

Propagation et émergence de motifs en biologie

Devant le jury composé de :

Florence Hubert	Université Aix Marseille	Présidente
Matthieu Alfaro	Université de Rouen	Rapporteur
Laurent Desvillettes	Université Paris Cité	Rapporteur
Jimmy Garnier	CNRS	Examinateur
Marie Manceau	CNRS	Examinatrice
Marielle Simon	Université Claude Bernard Lyon 1	Examinatrice
Thomas Lepoutre	INRIA	Directeur de thèse

Institut Camille Jordan

Laboratoire de recherche en mathématiques Lyon/Saint-Étienne

Propagation et émergence de motifs en biologie

Maxime Estavoyer

Thèse de doctorat

Université Claude Bernard Lyon 1

Université Claude Bernard Lyon 1
École doctorale **InfoMath**, ED 512
Spécialité : **Mathématiques**

Propagation et émergence de motifs en biologie

Thèse de doctorat

Soutenue publiquement le 18 novembre 2024 par Maxime Estavoyer

Maxime Estavoyer

devant le Jury composé de :

M. Matthieu Alfaro	Université de Rouen	Rapporteur
M. Laurent Desvillettes	Université Paris Cité	Rapporteur
M. Jimmy Garnier	CNRS	
Mme Florence Hubert	Université Aix Marseille	
M. Thomas Lepoutre	INRIA	Directeur de thèse
Mme Marie Manceau	CNRS	
Mme Marielle Simon	Université Claude Bernard Lyon 1	

Remerciements

Je tiens à exprimer ma gratitude à toutes les personnes qui ont contribué de près ou de loin à la réalisation de cette thèse.

Mes remerciements vont bien évidemment en premier lieu à mon directeur de thèse, Thomas Lepoutre, dont l'extrême bienveillance a accompagné chaque étape de ce parcours. Ta disponibilité constante et ton écoute attentive m'ont offert un soutien inestimable, aussi bien pour affiner mes compétences mathématiques que pour envisager le futur de ma carrière. Tu m'as laissé une grande liberté dans mon travail tout en restant toujours présent et en me témoignant une confiance profonde. Par ailleurs, ta vaste connaissance de la littérature, couvrant des domaines très variés en mathématiques, combinée à ton impressionnante rapidité de raisonnement, a été pour moi source d'admiration et d'inspiration. Grâce à l'atmosphère stimulante et chaleureuse que tu as su créer, j'ai pu mener cette thèse dans les meilleures conditions possibles, en y trouvant à la fois épanouissement et plaisir. Pour tout cela, je te témoigne mes plus sincères et profonds remerciements.

Je tiens à remercier chaleureusement Marie Manceau, pour m'avoir ouvert les portes de son laboratoire et m'avoir fait découvrir le monde fascinant de l'embryogenèse. Collaborer avec elle a été un immense plaisir et une grande source de motivation dans le but de contribuer à ce domaine passionnant. J'en profite également pour remercier Coline Hermine, sa doctorante, pour nos échanges enrichissants et son précieux partage de connaissances, essentiels à l'avancée de notre projet commun.

Je tiens à exprimer ma profonde gratitude aux rapporteurs de cette thèse, Matthieu Alfaro et Laurent Desvillettes, pour le temps et l'attention qu'ils ont consacrés à évaluer mon travail. Un grand merci également à Jimmy Garnier, Florence Hubert, Marie Manceau et Marielle Simon d'avoir accepté d'être membres de mon jury de thèse

Je tiens à remercier Laurent Pujo-Menjouet, avec qui travailler a été un grand plaisir. Son talent pour expliquer avec clarté des phénomènes complexes et son aisance à collaborer avec des biologistes, toujours soucieux de l'application concrète de ses travaux, ont été pour moi une véritable source d'inspiration.

Je remercie Ignacio Madrid Canales et Adil El Abdouni avec qui j'ai pris beaucoup de plaisir à travailler et à échanger lors de l'école d'été au CIRM en 2022. Je tiens également à exprimer ma gratitude envers nos encadrants, Vincent Calvez, Florence Hubert, Julien Olivier et Magali Tournus pour l'élaboration de ce projet ainsi que pour leurs précieux conseils et leur encadrement inspirant. Merci en particulier à Vincent, qui a joué un rôle essentiel en me permettant de poursuivre avec lui sur ce sujet si passionnant. Sa capacité impressionnante à saisir rapidement des concepts complexes et

à trouver des idées si pertinentes a été pour moi un modèle inspirant et a profondément enrichi mon travail. Grâce à lui, j'ai eu l'opportunité de rencontrer et d'échanger à de nombreuses reprises avec le biologiste Tâm Mignot et son équipe, ainsi qu'avec le physicien Antoine Le Gall, des rencontres qui ont grandement enrichi mes connaissances en biologie des bactéries.

Je remercie chaleureusement Grégory Faye, qui a été bien plus qu'un simple membre de mon comité de suivi, notamment pour ses nombreux conseils et son invitation à Toulouse, qui m'ont été d'une grande aide.

Un grand merci aux chercheurs avec qui j'ai eu l'honneur de pouvoir travailler durant ces dernières années. Tout d'abord, je remercie Olivier François pour la supervision de mon stage, qui a été pour moi un véritable plaisir ; sa vision des mathématiques appliquées m'a initié avec enthousiasme à la recherche. Un grand merci à Olivier Gandrillon pour sa capacité à rendre accessibles les subtilités de la biologie et pour nos discussions enrichissantes au sujet des mathématiques appliquées. Je remercie également les chercheurs de l'équipe de Véronique Maguer-Satta pour les données précieuses qu'ils nous ont fournies. Mes sincères remerciements à Vitaly Volpert et Malay Banerjee, dont l'expertise en mathématiques ainsi que leurs conseils m'ont été d'une grande aide. Je remercie Nicolas Foray, pour nos nombreuses discussions enrichissantes et plaisantes, ainsi que pour ses idées toujours innovantes.

Je remercie les chercheurs qui ont pu m'apporter leur aide lors de cette thèse, notamment Léo Girardin pour ses conseils sur les ondes progressives, Michèle Romanos pour nos discussions ainsi que les autres membres de l'équipe DRACULA : Mostafa Adimy, Samuel Bernard, Clément Erignoux, Thibault Espinasse, Léon Matar Tine ainsi que Claire Sauer.

Pour finir, je souhaite exprimer mes remerciements les plus sincères à l'ensemble des enseignants de mon cursus à l'Université de Lyon 1, pour leur engagement et leur disponibilité. Je remercie plus particulièrement Cécile Mercadier, pour son investissement et ses précieux conseils, et sans qui je ne serais peut-être pas en thèse aujourd'hui.

Je remercie grandement Charlotte et Arsène, mes deux co-bureaux, qui ont su, dès le départ, braver mon absence totale d'efforts de sociabilisation pour finalement me donner envie de venir au bureau chaque jour (ou presque). Un grand merci au joueur de foot pro Nathan, mon colocataire du CEMRACS, qui m'a appris les subtilités d'une machine à laver.

Avant de poursuivre, je préviens que les prochaines lignes ne seront compréhensibles que pour une poignée d'initiés...

Tout d'abord, comment pourrais-je oublier Benoît et nos projets de vacances en camping-car, traversant à toute allure les routes vers les quatre coins les plus paumés de France ? Sans oublier également Sébastien et nos futurs week-ends entre Netflix, Disneyland et les virées chez Netto.

Je remercie Clara, ses roulades et ses cookies (P.S. faudrait me rendre les clefs ça urge...). Je remercie mon coéquipier de dualtage Fares, encore désolé pour ton lino carbonisé ainsi que cette pelle trouée que je garde comme une relique. Un grand merci également au beau gosse Steven et à son incontournable Coca-Cola partagé sur les remparts de Saint-Malo. Mes chaleureux remerciements à Joffrey, ce joueur de kem's hors pair, et pour ces milliers d'heures passées à glander ensemble dans le square.

Je tiens également à remercier l'entièreté de la brochette. En particulier, un grand merci à Mathis pour toutes ces bouffes mémorables devant des documentaires aussi passionnants qu'éclectiques,

explorant tour à tour les mystères des animaux, les secrets avoués de Winnie l'ourson, l'histoire des citrons, les aventures électriques de Pikachu, les vertus des orties, et même les relations profondes des galets.

Je remercie chaleureusement Mathieu pour m'avoir offert cette jolie prothèse en plastique et pour avoir décoré la voiture de tous tes trips, sans oublier ton cousin, qui nous a sauvés d'une rencontre pour le moins hasardeuse.

Je tiens à remercier chaleureusement Lucas pour toutes ces escapades inoubliables, qu'il s'agisse de nos road trips déments alliant l'odeur du gaz de ton corbillard et le rythme endiablé de Macumba ; ou encore de ces sorties plus calmes au bord de la rivière en compagnie de ta petite fille Chaïma, où nous savourions tes délicieux cordons-bleus.

Je remercie Nathan, son industrie pharmacologique ainsi que mes mollets semi-pro, pour nous avoir fait gagner tant de matchs de padel et de volley. Plus qu'un simple coéquipier, tu as su diriger avec plus ou moins de fermeté dans ton fief, ce Petit Charran Gang, lors de ces 28 dernières années.

Je remercie Alexandre, pour ces centaines de balades en ville, accompagnées de ces nombreux débats passionnants sur les films taïwanais des années 80, la philosophie des courbes mathématiques, la cuisson des ravioles, ou encore le fameux goût des pâtes. Je te dois énormément, et tu m'en dois pas mal aussi après cette malencontreuse histoire de bâton. J'en profite également pour saluer, comme tu sais si bien le faire Alex, ton frère de tatouage, Mamé — bon stream à toi, mon vieux !

À toi, Poulet (pour préserver l'anonymat), gardien des arcanes ésotériques et des symboles hermétiques les plus obscurs, merci pour tous ces échanges où j'ai découvert que le compas et l'équerre ne servent pas qu'aux cours de géométrie, mais ouvrent des portes vers les plus profonds mystères de la gnose, les secrets alchimiques de la transmutation intérieure, et les rites discrets des loges invisibles.

Plus sérieusement, ces amitiés si rares qui, pour la plupart, durent depuis plus de vingt ans et dureront encore, ont été et continueront d'être une source inestimable de soutien et de bonheur. Pour cela, je vous en suis profondément reconnaissant.

Je tiens à exprimer toute ma gratitude envers ma famille, qui me soutient sans faille et partage mes joies et mes défis. Vous savez déjà combien je vous en suis reconnaissant

Un immense merci à mes parents, pour m'avoir toujours soutenu dans mes choix. Vous m'avez transmis des valeurs de persévérance, de courage et d'entraide qui m'accompagnent au quotidien, et votre présence est pour moi une source de force et de soutien inestimable.

Un grand merci à mon frère Jérémy, qui a toujours été protecteur et à mes côtés. Merci pour ta présence rassurante, ta bonne humeur constante et pour être là, à chaque étape de ma vie. Ton soutien et ta compréhension me sont infiniment précieux. Une pensée amicale aussi à Maëliss qui t'accompagne.

Je remercie également mon grand-père, qui est pour moi un véritable modèle et une source d'admiration. Passionné et passionnant, il est à la fois homme de science et de lettres, profondément spirituel et solidement ancré dans la terre. Il m'a transmis le goût de la recherche, et ses conseils, son savoir, ainsi que sa sagesse m'inspirent chaque jour.

Table des matières

Table des figures

Résumé

Résumé (FR)

Cette thèse explore la modélisation de phénomènes de propagation et d'émergence de motifs dans l'espace :

• Une partie importante de ma thèse se concentre sur l'émergence des plumes d'oiseaux lors de l'ovogenèse. Au cours de celle-ci, les follicules plumeux émergent généralement rangée par rangée, suivant une vague médio-latérale, à travers un processus de développement en deux étapes : d'abord, une densification du derme le rendant compétent, suivie de l'émergence d'agrégats de cellules menant à la formation des futures plumes. En utilisant un modèle de réaction-diffusion-taxis nous proposons, à l'aide d'une analyse linéaire et faiblement non linéaire, des formules explicites des vitesses associées à ces deux étapes. Grâce à une étude numérique de l'interaction entre ces deux étapes, nous proposons une formule de la vitesse d'émergence des plumes lors de la morphogenèse aviaire.

• Cette thèse se focalise également sur l'invasion de la bactérie prédatrice *Myxococcus xanthus*. Les bactéries *M. xanthus* sont capables de former des agrégats ayant des propriétés différentes des bactéries isolées. Notamment, elles possèdent deux systèmes de motilité complètement différents : la motilité aventureuse (A) pour les bactéries isolées et la motilité sociale (S) pour les bactéries dans les agrégats. Cette différence entraîne des variations significatives de la vitesse individuelle et le type de mouvement effectué. Pour modéliser l'invasion collective de cette bactérie, nous proposons et étudions plusieurs modèles : par exemple un modèle proie-prédateur, un modèle de réaction-diffusion et un modèle cinétique non linéaire avec une structure en taille. L'étude numérique et théorique des solutions d'onde progressive permet de déterminer les facteurs influençant la vitesse de prédation. Notamment, notre dernier modèle suggère que l'interaction entre les motilités A et S est synergique.

• Un autre projet développé lors de cette thèse porte sur la modélisation des expériences de relaxation cellulaire. Ces expériences consistent à sélectionner une sous-fraction d'une population cellulaire et à observer la vitesse à laquelle cette sous-population revient à son état de repos ou d'équilibre. Pour modéliser ce phénomène, nous proposons un modèle mécaniste à deux états prenant en compte la prolifération. Afin de confronter notre modèle aux données expérimentales, nous avons mené une expérience de relaxation de l'antigène CD34 à la surface des cellules TF1-BA. Que ce soit en isolant les populations avec les niveaux d'expression de CD34 les plus élevés ou les plus bas, nous observons dans les deux cas qu'après environ 25 jours, la distribution de CD34 dans la population revient à

son état stationnaire initial. Des simulations numériques de notre modèle, basées sur des valeurs de paramètres estimées à partir de nos données expérimentales, ont montré que les solutions du modèle s'alignent étroitement aux résultats de nos expériences.

• Enfin, nous étudions les motifs spatiaux d'un système de réaction-diffusion modélisant la formation des plaques amyloïdes dans le cerveau en lien avec la maladie d'Alzheimer. Une analyse linéaire et de nombreuses simulations numériques révèlent plusieurs types de solutions spatialement hétérogènes. L'analyse approfondie de la stabilité et des bifurcations des motifs stables nous permet de formuler des conjectures sur l'influence de l'inflammation et des cellules microgliales dans la formation des plaques amyloïdes.

Summary (ENG)

This thesis explores the modeling of propagation phenomena and the emergence of periodic patterns in space :

• This thesis also focuses on the emergence of bird feathers during ovogenesis. During this process, feather follicles generally emerge row by row, following a medio-lateral wave, through a two-step development process : first, a condensation of the dermis making it competent, followed by the emergence of cell aggregates leading to the formation of future feathers. Using a reaction-diffusion-taxis model, we propose, through linear and weakly nonlinear analysis, explicit formulas for the speeds associated with these two steps. Through a numerical study of the interaction between these two steps, we propose a formula for the emergence speed of feathers during avian morphogenesis.

• Another project developed during this thesis involves the invasion of the predatory bacterium *Myxococcus xanthus*. These bacteria can form clusters with properties distinct from those of isolated cells. Notably, they possess two different motility systems : adventurous (A) motility for isolated bacteria and social (S) motility for bacteria in clusters. This difference leads to significant variations in individual speed and movement type. To model the collective invasion of this bacterium, we propose and study several models, such as a prey-predator model, a reaction-diffusion model, and a nonlinear kinetic model with size structure. The numerical and theoretical study of traveling wave solutions allows us to identify the factors influencing the predation speed. Notably, our latest model suggests that the interaction between A and S motilities is synergistic.

• A significant part of my thesis focuses on the modeling of cell relaxation experiments. These experiments involve selecting a sub-fraction of a cell population and observing the speed at which this sub-population returns to its equilibrium state. To model this phenomenon, we propose a two-state mechanistic model that takes proliferation into account. To compare our model with experimental data, we conducted a relaxation experiment of the CD34 antigen on the surface of TF1-BA cells. Whether isolating populations with the highest or lowest levels of CD34 expression, we observe in both cases that after approximately 25 days, the CD34 distribution in the population returns to its initial steady state. Numerical simulations of our model, based on parameter values estimated from our experimental data, showed that the model solutions closely align with our experimental results.

• Finally, we study the spatial patterns of a reaction-diffusion system modeling the formation of amyloid plaques in the brain related to Alzheimer's disease. Linear analysis and numerous numeri-

cal simulations reveal several types of spatially heterogeneous solutions. An in-depth analysis of the stability and bifurcations of stable patterns allows us to formulate conjectures on the influence of inflammation and microglial cells in the formation of amyloid plaques.

Première partie

Introduction générale

Emergence des motifs de Turing

Introduction

Les motifs peuvent être observés dans une multitude de systèmes naturels, depuis des motifs de réaction-diffusion en chimie aux motifs de couleurs du pelage des animaux illustrés dans la figure I.1. Comprendre comment ces motifs se forment et évoluent est essentiel pour dévoiler les mécanismes sous-jacents à de nombreux phénomènes naturels. En 1952, le mathématicien et logicien britannique Alan Turing a introduit la théorie des *motifs de Turing* dans son célèbre article intitulé « *The Chemical Basis of Morphogenesis* ». La question posée est la suivante : quels mécanismes permettent de faire émerger de l'instabilité à partir d'un état initialement homogène ?

Pour y répondre, Alan Turing propose d'étudier deux espèces chimiques qui se diffusent, appelées communément « morphogènes », et qui interagissent entre elles. Sous certaines conditions, il démontre qu'un état homogène peut être stable en l'absence de diffusion, mais devenir instable face à des perturbations spatialement hétérogènes lorsque la diffusion est prise en compte. Dans cette situation, nous utiliserons le terme de point Turing-instable pour décrire la stabilité de l'état homogène. Cette idée révolutionnaire est particulièrement contre-intuitive, car la diffusion a tendance à homogénéiser, comme dans l'équation de la chaleur. Dans la section suivante de cette introduction, nous détaillerons comment des motifs de Turing peuvent apparaître dans un système de deux équations de réaction-diffusion.

Ces motifs de Turing ont une multitude d'applications, principalement en biologie, en chimie, en écologie et même dans les sciences sociales. Nous développons certaines de ces applications dans cette thèse. Pour les lecteurs intéressés par cette vaste littérature, voici quelques articles de revue récents, notamment sur les motifs cutanés [1], la couleur de la peau des vertébrés [2], la formation des motifs chez les poissons zèbres [3], et concernant les motifs de Turing dans les systèmes chimiques [4]. Pour un tour d'horizon des avancées mathématiques développées depuis l'article fondateur d'Alan Turing, on pourrait également se référer à l'article de revue récent et complet de Krause, Gaffney, Maini et Klika [5].

FIGURE I.1 – **Exemples de motifs au niveau du pelage des mammifères : léopard, zèbre et girafe.**

Système à deux équations de réaction-diffusion

Considérons un système de deux équations de réaction-diffusion,

$$\begin{cases} \partial_t u_1(t,x) = D_1 \partial_{xx} u_1 + f_1(u_1,u_2), & x \in [0,L], \\ \partial_t u_2(t,x) = D_2 \partial_{xx} u_2 + f_2(u_1,u_2), & x \in [0,L], \end{cases} \tag{I.1}$$

avec L la taille du domaine unidimensionnel, D_1 et D_2 les coefficients de diffusion, f_1 et f_2 les termes de réaction (par exemple, production, dégradation, activation, etc.). Nous choisissons des conditions aux bords de Neumann, c'est-à-dire sans flux aux bords de l'espace, $\partial_{\mathbf{n}} u_1(x,t) = \partial_{\mathbf{n}} u_2(t,x) = 0$ pour tout $x \in \partial\Omega$, où $\mathbf{n}$ est la normale extérieure du bord du domaine. Pour simplifier les calculs, nous réécrivons le système (I.1) sous la forme matricielle suivante,

$$\partial_t \mathbf{u} = \mathbf{D}\partial_{xx}\mathbf{u} + \mathbf{F}(\mathbf{u}),$$

où $\mathbf{D} = \mathrm{diag}(D_1, D_2)$ est la matrice de diffusion et $\mathbf{F}(u_1,u_2) := (f_1(u_1,u_2), f_2(u_1,u_2))$ correspond à la fonction de réaction.

Supposons maintenant l'existence d'un équilibre stationnaire homogène en espace, c'est-à-dire l'existence d'un vecteur $\mathbf{u}^\star$ satisfaisant $\mathbf{F}(\mathbf{u}^\star) = 0$. Nous nous intéressons à la dynamique des perturbations autour de ce point d'équilibre $\mathbf{u}^\star$, que nous définissons par $\mathbf{p} := \mathbf{u} - \mathbf{u}^\star$. En linéarisant autour de ce point d'équilibre, nous obtenons l'équation suivante régissant l'évolution de la perturbation,

$$\partial_t \mathbf{p} = \mathbf{D}\partial_{xx}\mathbf{p} + \mathbf{J}.\mathbf{p}, \tag{I.2}$$

avec $\mathbf{J}$ la jacobienne de $\mathbf{F}$ en $\mathbf{u}^\star$, définie par les dérivées partielles que l'on note $f_{ij} = \partial_{u_j} f_i|_{\mathbf{u}=\mathbf{u}^\star}$ avec $i,j = 1,2$.

Pour obtenir un motif *spatialement hétérogène*, il est nécessaire que la déstabilisation de l'équilibre provienne de la partie diffusion, les termes de réaction étant homogènes dans l'espace. Nous supposons que le point d'équilibre $\mathbf{u}^\star$ est stable en l'absence de diffusion. Par conséquent, les deux valeurs propres de la jacobienne doivent avoir des parties réelles négatives, ce qui est le cas à condition que :

$$\text{Condition } ❶ : \qquad \mathrm{Tr}\,\mathbf{J} < 0, \quad \text{et} \quad \det \mathbf{J} > 0. \tag{I.3}$$

En revanche, nous souhaitons que l'ajout des opérateurs de diffusion déstabilise d'une certaine manière l'état d'équilibre. L'idée principale est de décomposer la perturbation sur les différents modes spatiaux correspondant aux vecteurs propres du laplacien, afin de les étudier individuellement et de déterminer lesquels seront atténués ou, si possible, amplifiés. Nous cherchons donc des solutions sous la forme : $\mathbf{p}_n(x,t) = \mathbf{q}_n \cos(k_n x)\, e^{\lambda_n t}$ où $k_n := n\pi/L$ est le nombre d'onde. La substitution de cet ansatz dans l'équation (I.2) nous donne

$$\left(\mathbf{J} - k_n^2 \mathbf{D} - \lambda_n \mathbf{I}_2\right) \mathbf{q}_n = 0,$$

conduisant à la relation de dispersion,

$$\det\left(\mathbf{J} - k_n^2 \mathbf{D} - \lambda_n \mathbf{I}_2\right) = 0 \quad \Longleftrightarrow \quad \lambda_n^2 - \mathrm{Tr}(\mathbf{M}_{k_n})\lambda_n + \det(\mathbf{M}_{k_n}) = 0, \tag{I.4}$$

avec $\mathbf{M}_{k_n}$ la matrice définie par $\mathbf{M}_{k_n} := J - k_n^2 D$. Pour déstabiliser l'état homogène $\mathbf{u}^\star$, nous souhaitons qu'au moins une des racines λ_n ait une partie réelle positive, tout en respectant les conditions données dans (I.3). Cela se produit lorsque $\det(\mathbf{M}_{k_n}) < 0$, ce qui conduit à la condition suivante,

$$\text{Condition ❷ :} \qquad D_2 f_{11} + D_1 f_{22} > 2\sqrt{D_1 D_2 (f_{11} f_{22} - f_{12} f_{21})} > 0. \tag{I.5}$$

Une dernière condition nécessaire concerne la taille du domaine. En effet, il peut exister un certain $k^\star \in \mathbb{R}$ tel que $\det(\mathbf{M}_{k^\star}) < 0$, mais que pour tout $n \in \mathbb{N}$, nous avons toujours $\det(\mathbf{M}_{k_n}) > 0$. Nous notons $k^\pm$ les deux racines de la fonction $k \longmapsto \det(\mathbf{M}_k)$ avec $k^- < k^+$. La dernière condition est donnée par l'inégalité suivante :

$$\text{Condition ❸ :} \qquad \text{Il existe un } n^\star \in \mathbb{N} \text{ tel que : } k_- < k_{n^\star} < k_+. \tag{I.6}$$

La combinaison des conditions ❶, ❷ et ❸ est une condition nécessaire et suffisante à l'émergence de motif de Turing.

Dans la figure I.2, nous présentons un exemple de relation de dispersion. La courbe noire représente la valeur de $\lambda(k)$ pour différentes valeurs de k. Pour $k = 0$, la valeur de λ est bien négative, assurant ainsi la stabilité du point d'équilibre $\mathbf{u}^\star$ en l'absence de diffusion. Comme nous pouvons le voir, pour $k \in [k^-, k^+]$, la valeur propre devient positive. Par conséquent, les modes $n = 3, 4, 5, 6, 7, 8$ sont déstabilisés par l'ajout des opérateurs de diffusion.

Scénarios possibles pour l'émergence de motifs de Turing. Pour satisfaire la condition sur la trace, $\mathrm{Tr}\,\mathbf{J} < 0$, il est nécessaire qu'au moins l'un des termes f_{11} ou f_{22} soit négatif. Quitte à inverser les variables u et v, supposons que f_{22} soit négatif. Selon la condition ❷, nous devons vérifier que $D_2 f_{11} + D_1 f_{22} > 0$. Etant donnée la négativité de f_{22}, le terme f_{11} doit être nécessairement positif. Finalement, puisque les termes de la diagonale de la jacobienne ont des signes opposés ($f_{11} f_{22} < 0$) et que le déterminant doit être positif selon la condition ❶, nous savons que les termes de l'antidiagonale doivent également avoir des signes opposés ($f_{12} f_{21} < 0$). Nous avons ainsi deux scénarios possibles concernant les signes des termes dans la jacobienne,

$$\text{Scénario 1 : } \begin{pmatrix} + & - \\ + & - \end{pmatrix}, \quad \text{ou,} \quad \text{Scénario 2 : } \begin{pmatrix} + & + \\ - & - \end{pmatrix}, \tag{I.7}$$

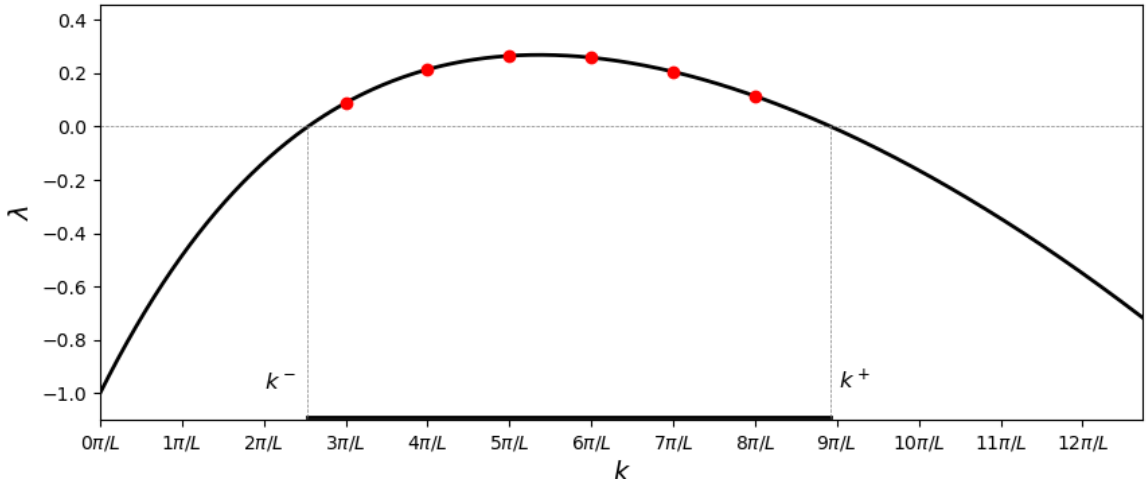

FIGURE I.2 – **Illustration de la relation de dispersion pour $D_2 > D_2^c$.** La courbe noire représente le tracé de $\Re(\lambda(k))$ en fonction de k. Les modes $n = 3, 4, 5, 6, 7, 8$ sont instables tandis que les autres sont stables.

que l'on nomme *règle des signes de Turing*, popularisée par Murray [6].

La condition ❷ fournit également des informations sur les coefficients de diffusion. Tout d'abord, lorsque les deux coefficients sont égaux, $D_1 = D_2$, il est clair que la condition ❶ entre en conflit avec la condition ❷, puisque $D_2 f_{11} + D_1 f_{22} = D_1 \mathrm{Tr}\,\mathbf{J} < 0$. Toujours dans le cas où le second composant s'inhibe lui même, $f_{22} < 0$, nous pouvons remarquer que cette condition implique que D_2 doit être strictement supérieur à D_1. De plus, pour D_2 suffisamment grand par rapport à D_1, la condition ❷ sera satisfaite. Ainsi, lorsque le système satisfait les conditions appropriées, nous savons qu'il existe une valeur critique D_c telle que pour $D_2 < D_c D_1$, le point d'équilibre $\mathbf{u}^\star$ est stable, tandis que pour $D_2 > D_c D_1$, il devient Turing-instable. L'espace des valeurs de paramètres pour lesquelles le point est Turing-instable se nomme l'espace de Turing. En conclusion, il est nécessaire d'avoir une espèce (auto-)activatrice qui se diffuse à courte portée et une espèce (auto-)inhibitrice qui se diffuse à longue portée [7].

Pour obtenir des motifs de Turing pour un système de deux équations de réaction-diffusion, il existe ainsi deux scénarios illustrés dans la figure I.3 :

Scénario 1 : « *Short-range activation* – *Long-range inhibition* » : Dans ce premier scénario, v agit comme un inhibiteur, inhibant à la fois u et lui même. En revanche, u, qui se diffuse moins rapidement que v, active la production de v ainsi que sa propre production, ce qui en fait un activateur. En calculant les vecteurs propres, il est possible de montrer que dans cette situation, les motifs sont spatialement corrélés : les maxima de u correspondent aux maxima de v (voir la figure I.3). Ce scénario est prédominant dans la littérature.

Scénario 2 : « *Substrate-depletion*» ou « *Cross kinetics* » : Dans ce second cas, v est un substrat à diffusion rapide qui favorise localement la production du composant u. En retour, u, épuise localement v, inhibant ainsi des concentrations élevées de u à proximité. Les vecteurs

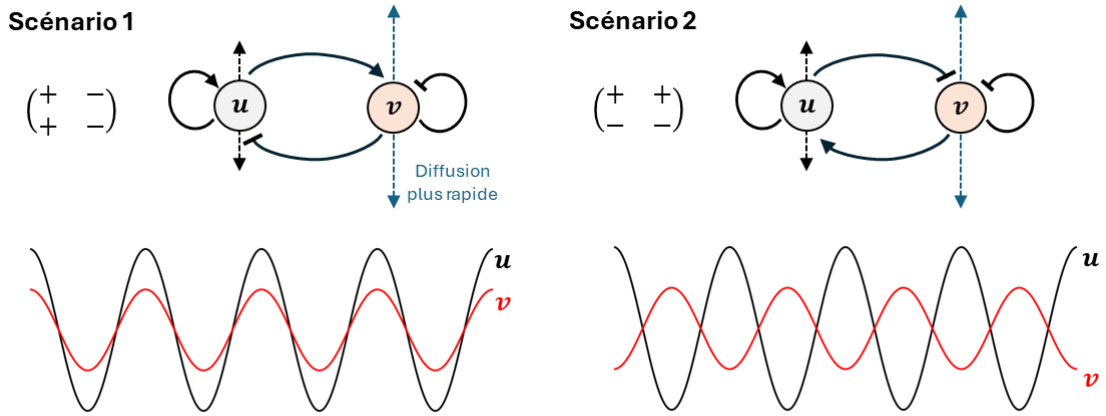

FIGURE I.3 – **Illustration des deux scénarios menant à l'émergence de motifs de Turing.**

propres montrent que dans ce cas, les motifs sont anti-corrélés : les maxima de u correspondent aux minima de v.

Que sait-on sur ces motifs de Turing ? Tout d'abord, l'analyse linéaire effectuée ici permet de prédire l'espace de Turing dans lequel nous nous attendons à avoir des motifs de Turing ($D_2 > D_c D_1$, où D_c dépend des termes de réaction). Il est important de rappeler que cette analyse ne nous fournit qu'une prédiction qui peut s'avérer fausse (pour des exemples voir Krause et al. [8]). Concernant la forme des motifs, à la bifurcation de Turing, une nouvelle branche de motif émerge, associée à la fréquence critique notée k_c, c'est-à-dire la première fréquence qui devient admissible lorsque D_2 croît. Cependant, la branche créée n'est pas forcément stable, c'est par exemple le cas lorsque la bifurcation est sous-critique. En revanche, lorsqu'elle est stable, nous nous attendons à obtenir des motifs stationnaires de la forme $\mathbf{u}^\star + \mathbf{A}_\infty \cos(k_c x)$, où $\mathbf{A}_\infty$ représente un vecteur de l'amplitude des motifs des composants. Le signe des composants de $\mathbf{A}_\infty$ peut être déduit du calcul des vecteurs propres, mais leur expression ou leur approximation ne peut pas être prédite par une simple analyse linéaire.

Compléments sur les motifs de Turing

Quels sont les autres outils à notre disposition ?

Analyse faiblement non linéaire. Comme son nom l'indique, l'analyse faiblement non linéaire permet d'approfondir l'analyse linéaire en y incluant certains termes non linéaires [9, 10]. Cette approche permet notamment de déterminer si la bifurcation est super-critique ou sous-critique (voir la figure I.4). Pour une bifurcation super-critique, cette méthode ouvre de nouvelles possibilités, telles que la prédiction de l'amplitude des motifs, l'étude de la compétition entre deux modes admissibles, et l'identification des types de motifs en 2D (points, rayures, etc.) [11, 12, 13]. Nous détaillons cette méthode dans le chapitre suivant.

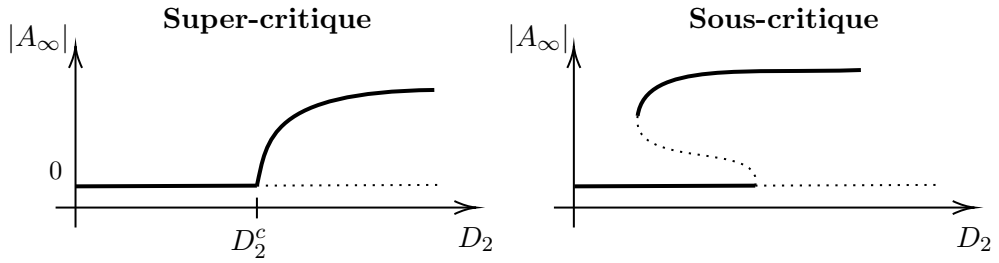

FIGURE I.4 – **Illustration de bifurcation de Turing super-critique et sous-critique.** Les lignes pleines sont stables tandis que les lignes pointillées sont instables.

Analyse de bifurcation et continuation numérique. Les deux méthodes présentées précédemment fournissent des informations sur l'analyse des motifs de manière locale, c'est-à-dire uniquement à proximité de la bifurcation de Turing. Dans le chapitre 6, nous traçons un diagramme de bifurcation à l'aide d'un logiciel de continuation numérique afin d'analyser l'existence et la stabilité des branches de motifs loin de l'équilibre. Pour les domaines spatiaux considérés, nous trouvons l'ensemble des branches stables associées à des motifs obtenus dans des simulations numériques indépendantes. Ce travail sur l'analyse des motifs loin de l'équilibre nous permet d'obtenir des résultats de modélisation pertinents sur l'influence de l'inflammation et des cellules microgliales dans la progression de la maladie d'Alzheimer.

Peut-on aller plus loin qu'un système activateur-inhibiteur ?

Suite à la publication d'Alan Turing, de nombreux modèles connus de systèmes à deux équations de réaction-diffusion ont été développés, tels que ceux de Gierer-Meinhardt [14], de Schnakenberg [15] et de Gray-Scott [16]. Cependant, la famille des systèmes à deux équations de réaction-diffusion ne représente qu'une petite fraction de l'ensemble des systèmes capables de générer de tels motifs.

Premièrement, il est possible d'ajouter un ou plusieurs nouveaux morphogènes couplés. Dans ce cas, les outils d'analyse linéaire ou faiblement non linéaire restent toujours applicables, notamment à l'aide du critère de stabilité de Routh-Hurwitz. Cependant, ces analyses deviennent plus complexes à réaliser en raison des nombreux nouveaux scénarios pouvant survenir. De même, l'espace de Turing devient beaucoup plus difficile à caractériser explicitement (voir par exemple, pour m équations, [17, 18, 19]).

Deuxièmement, le cadre des motifs de Turing peut également s'étendre aux opérateurs de transport au sens large. De nombreuses extensions de la diffusion fickienne peuvent être envisagées, telles que la diffusion non linéaire [20, 21], la diffusion fractionnaire [22, 23, 24], la diffusion anisotrope [25, 26, 27, 28] ou encore la diffusion croisée [29, 30, 31, 32, 33, 34]. Il est également possible d'obtenir des motifs en utilisant des opérateurs spatiaux d'ordre supérieur, comme par exemple dans l'équation de Swift-Hohenberg, ou dans l'équation de Cahn-Hilliard [35, 36].

Dans cette thèse, lorsque nous étudions l'émergence de motifs, nous considérons des modèles de réaction-diffusion avec un terme de chimiotaxie. Dans ce processus, on suppose qu'un morphogène est attiré par les forts gradients d'un autre morphogène agissant comme attractant. Pour modéliser ce

mouvement biaisé, l'idée est d'ajouter un terme de la forme $\nabla \cdot (\alpha u \nabla a)$ dans l'équation de u, où a est le morphogène attractant et α est un coefficient positif correspondant à la sensibilité à l'attraction. Pour ce type de système, l'espace de Turing peut être caractérisé par un seuil de chimiotaxie, $\alpha > \alpha_c$, où α_c représente le seuil critique et est dépendant des autres paramètres du système (voir l'article de revue de Hillen et Painter [37]). A noter que ceci est moins contre intuitif car la chimiotaxie est connue pour générer de l'hétérogénéité spatiale

Front de propagation dans un état instable

La notion de propagation dans un état instable est largement documentée dans la littérature scientifique. Dans cette introduction, nous nous concentrons sur des concepts clés développés initialement dans le domaine de la physique durant les années 1980 (voir par exemple [38, 39, 40, 41, 42, 43, 44]). Ces travaux ont été, plus récemment, approfondis par des mathématiciens comme Avery, Faye, Holzer et Scheel, aboutissant à la démonstration de résultats majeurs que nous présenterons partiellement [45, 46, 47, 48, 49, 50, 51, 52, 53, 54, 55].

Considérons un système physique spatio-temporel initialement dans un état instable, que nous supposons pour simplifier être $\mathbf{u} \equiv \mathbf{0}$. En perturbant ce système localement dans l'espace, la perturbation va progressivement s'amplifier et commencer à se propager, laissant dans son sillage un nouvel état stable, noté $\mathbf{u}_s$. Un exemple pertinent pour illustrer un tel phénomène est l'introduction localisée d'une espèce invasive dans un écosystème, ou encore l'ajout de personnes malades dans l'étude de la propagation d'une épidémie. Cela soulève deux questions fondamentales concernant ce phénomène de propagation : à quelle vitesse l'état stable envahit-il l'état instable ? Et quelle est la forme de l'état stable dans le sillage ?

La première question, est d'une grande complexité et sera le leitmotiv de cette introduction. Quant à la seconde question, elle dépend en grande partie des termes non linéaires de notre système. Pour de nombreux modèles, ils permettent la saturation de la croissance de la perturbation, conduisant ainsi à l'observation d'un de ces deux états stables possibles :

- **Sillage *homogène* en espace :** Dans le premier cas de figure, $\mathbf{u}_s$ est simplement un état stable spatialement homogène (voir Fig. I.5A). En considérant le référentiel en mouvement, ce front de propagation correspond simplement, dans le plan de phase, à une hétérocline reliant le point stable au point instable. Nous nous concentrons sur ce type de front dans la section I.
- **Sillage *hétérogène* en espace :** Dans cette situation, le front est considéré comme un front de formation de motifs au sens le plus large du terme, englobant des motifs stationnaires ou périodiques dans le référentiel mobile, ainsi que des motifs plus « *chaotiques* » (voir la revue de Van Saarloos pour une large gamme d'exemples théoriques et expérimentaux [40]). Dans la section I, nous nous concentrons sur les fronts de formation des motifs spatiaux stationnaires en temps t, illustrés dans la figure I.5B, que nous nommons « *front modulé* ».

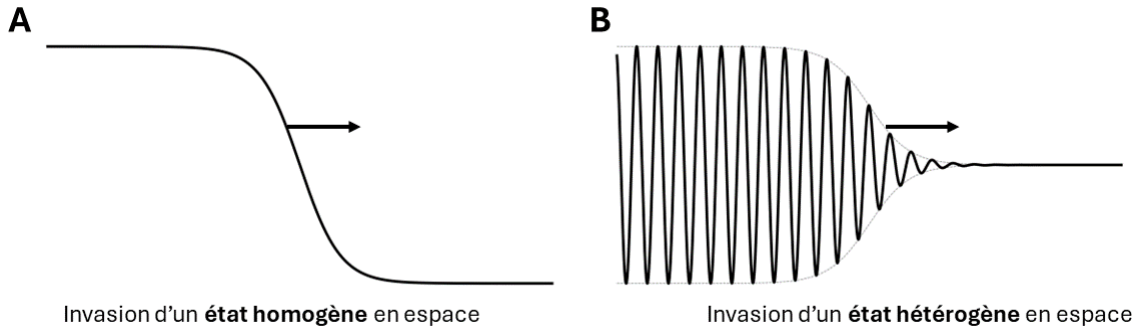

FIGURE I.5 – **Schéma des deux types d'invasion possibles. A.** Front reliant un point d'équilibre instable à un point d'équilibre stable. **B.** Front reliant un point d'équilibre instable à un motif stable hétérogène en espace.

Une méthode appropriée pour analyser cette dynamique de propagation consiste à étudier $\mathbf{u}$ dans le référentiel en mouvement de vitesse c, ce qui nous donne un certain front $\mathbf{q}$ défini par $\mathbf{q}(x - ct; c) := \mathbf{u}(x, t)$. Ce front relie l'état stable en $+\infty$ à l'état instable en $-\infty$. Une étude numérique de la dynamique de $\mathbf{u}$, ou alors une analyse théorique des systèmes les plus simples, révèle que $\mathbf{u}$ converge bien vers un front d'invasion $\mathbf{q}$ associé à une certaine vitesse de propagation. De plus, l'étude de cette vitesse montre que, pour la propagation dans un milieu instable, il existe une large gamme de vitesses admissibles, correspondant aux vitesses c supérieures à une certaine vitesse critique $c^\star$. La question concernant la vitesse de propagation se reformule ainsi : comment caractériser les vitesses admissibles et laquelle est sélectionnée ? La sélection de cette vitesse, parmi celles admissibles, dépend fortement des conditions initiales. Dans cette introduction, nous considérons uniquement le cas des conditions initiales suffisamment raides. Par simplicité, nous prenons la perturbation initiale suivante, $\mathbf{u}(x, t = 0) = H(x)\mathbf{u}_s$, où H est la fonction de Heaviside.

Concept de *stabilité marginale*. S'inspirant des travaux sur la théorie physique de l'instabilité absolue et convective [38, 56, 57, 58], Dee et Langer ont proposé pour l'étude des fronts de propagation la conjecture suivante :

Conjecture 1 (Conjecture de stabilité marginale [39]):
Une onde progressive issue d'une donnée initiale raide converge vers un front marginalement stable *associé à la vitesse critique* $c^\star$.

La notion de stabilité marginale doit être comprise dans le sens où, les solutions du front se déplaçant plus lentement sont instables face aux perturbations (dans le référentiel en mouvement), tandis que celles se déplaçant plus rapidement sont stables. Pour une introduction rigoureuse à la notion de stabilité dans ce cadre, nous renvoyons le lecteur aux travaux de Holzer et Scheel [55] ainsi que ceux de Avery et Scheel [45]. L'intérêt de se concentrer uniquement sur la stabilité spectrale réside dans la possibilité de faire des prédictions quasi universelles concernant la vitesse de propagation, évitant, par exemple, la nécessité de satisfaire à un principe de comparaison.

Concept de *vitesse de propagation linéaire.* Une question demeure en suspens : comment caractériser la vitesse des fronts marginalement stables ? Un premier pas consiste à se concentrer sur la dynamique du bord d'attaque en étudiant le système linéarisé autour du point d'équilibre instable $\mathbf{u} \equiv \mathbf{0}$. Comme nous l'expliquerons ci-dessous, en utilisant le concept de stabilité convective et absolue, nous pourrons définir une certaine vitesse $c^\star_{\text{lin}}$, correspondant à la vitesse de propagation prédite par le système linéarisé. Cette prédiction peut s'avérer extrêmement utile pour caractériser la vitesse d'invasion d'une large gamme de systèmes non linéaires.

Front monostable à translation uniforme

Nous considérons le système de réaction-diffusion général suivant,

$$\partial_t \mathbf{u} = \mathbf{D}\partial_{xx}\mathbf{u} + \mathbf{F}(\mathbf{u}), \qquad x \in \mathbb{R}, \quad \mathbf{u} \in \mathbb{R}^n. \tag{I.8}$$

où $\mathbf{D} \in \mathbb{R}^{n\times n}$ est une matrice de diffusion avec des valeurs propres strictement positives et $\mathbf{F}$ une fonction correspondant au terme de réaction. Nous supposons que ce système admet deux points d'équilibre, $\mathbf{0}$ un point d'équilibre instable et $\mathbf{u}_s$ un état stable homogène en espace, $\mathbf{u}_s \in \mathbb{R}^n$.

Comment déterminer la *vitesse de propagation linéaire* ?

La linéarisation autour de $\mathbf{u} \equiv \mathbf{0}$, dans le référentiel en mouvement de vitesse c, nous donne la relation de dispersion suivante :

$$d_c(\lambda, \nu) = \det(\mathbf{D}\nu^2 + c\nu\mathbf{I} + \mathbf{F}'(\mathbf{0}) - \lambda\mathbf{I}).$$

La vitesse de propagation linéaire est la vitesse critique à laquelle un observateur en mouvement assiste à une transition d'une stabilité exponentielle ponctuelle à une instabilité exponentielle ponctuelle. À toute vitesse supérieure à la vitesse de propagation linéaire, l'observateur dépasse l'instabilité (instabilité convective) tandis qu'à des vitesses plus lentes, l'instabilité dépasse l'observateur (instabilité absolue). Mathématiquement, cette vitesse de propagation linéaire peut être déterminée en identifiant les racines doubles pincées de la relation de dispersion.

Définition (Racine double pincée):

- ***Racine double :*** *On dit que* $(\lambda_\star, v_\star)$ *est une* racine double *de la relation de dispersion* d_c *si*

$$d_c(\lambda_\star, v_\star) = 0, \qquad \partial_\nu d_c(\lambda_\star, v_\star) = 0$$

- ***Condition de pincement :*** *On dit qu'une racine double* $(\lambda_\star, v_\star)$ *est* pincée *s'il existe une courbe continue* $\lambda(\tau)$, $\tau \in \mathbb{R}^+$, *telle que* $\text{Re}\ \lambda(\tau)$ *est strictement croissante,* $\lambda(0) = \lambda_\star$, $\text{Re}\ (\lambda(\tau)) \to \infty$ *quand* $\tau \to \infty$ *ainsi que deux autres courbes de racines de la relation de dispersion, notées* $\nu^\pm(\lambda(\tau))$ *qui satisfont,* $\nu^\pm(\lambda_\star) = \nu_\star$ *ainsi que les limites asymptotiques suivantes :*

$$\lim_{\tau\to\infty} \text{Re}\ \nu^\pm(\lambda(\tau)) = \pm\infty$$

Cette notion nous permet de définir la vitesse de propagation linéaire :

Définition (Vitesse de propagation linéaire):
La vitesse de propagation linéaire *est donnée par la formule,*

$$c^\star_{lin} = \sup\{c : \ d_c \text{ possède une racine double pincée avec } \mathrm{Re}\,\lambda \geq 0\}.$$

Limites de la définition 2. Pour fournir une explication intuitive des raisons pour lesquelles les racines doubles pincées correspondent à la stabilité marginale, il serait nécessaire d'introduire de nouveaux outils qui dépassent le cadre de cette introduction (voir [40, 55] pour plus d'informations). A noter que, pour des exemples génériques, cette définition de la vitesse de propagation linéaire peut s'avérer imparfaite. Dans certains cas de figure, des racines doubles pincées peuvent ne pas avoir d'impact sur la vitesse de propagation linéaire et ne devraient ainsi pas être considérées dans l'étude de la propagation. Une méthode plus rigoureuse, que nous ne détaillerons pas, consiste à étudier les singularités d'une certaine fonction de Green associée à notre problème [55].

Exemple 1 : Equation scalaire de Fisher-KPP. Pour illustrer ces notions, nous considérons l'équation scalaire de Fisher-KPP [59, 60], donnée par la formule :

$$\partial_t v = \partial_{xx} v + v(1-v). \tag{I.9}$$

La relation de dispersion associée à cette équation est donnée par,

$$d_c(\lambda, \nu) = \nu^2 + c\nu + 1 - \lambda,$$

que l'on peut factoriser par,

$$d_c(\lambda, \nu) = (\nu - \nu^+(\lambda))(\nu - \nu^-(\lambda)), \qquad \text{avec } \nu^\pm(\lambda) = \frac{-c \pm \sqrt{c^2 - 4 + 4\lambda}}{2}.$$

La seule racine double est donnée par l'égalité, $\nu^+ = \nu^-$, conduisant à l'égalité suivante, $c^2 - 4 + 4\lambda = 0$. Il est clair que cette racine satisfait la condition de pincement. En recherchant le maximum des vitesses admissibles, nous remarquons que la vitesse de propagation linéaire s'obtient lorsque $\lambda = 0$, correspondant au front marginalement stable. Par conséquent, la vitesse de propagation linéaire est ainsi donnée par $c^\star_{\mathrm{lin}} := 2$.

Exemple 2 : Système de deux équations de Fisher-KPP couplées. L'exemple présenté ci-dessous provient de l'article de Holzer [54], veuillez s'y référer pour davantage d'informations. Considérons deux populations u et v régies toutes deux par une certaine équation de Fisher-KPP

$$\begin{cases} \partial_t u = d\partial_{xx} u + \alpha u(1-u), \\ \partial_t v = \partial_{xx} v + v(1-v). \end{cases}$$

A ce stade, la population u aura pour vitesse de propagation linéaire $2\sqrt{d\alpha}$ tandis que celle de la population v correspondra à la vitesse 2 calculée précédemment.

La force de la méthode de stabilité marginale est de pouvoir facilement calculer l'impact du couplage d'une équation sur une autre lorsque les systèmes ont une structure linéaire triangulaire. Supposons par exemple l'ajout d'un terme de couplage logistique dans la première équation, nous obtenons alors le système suivant,

$$\begin{cases} \partial_t u = d\partial_{xx} u + \alpha u(1-u) + v(1-v), \\ \partial_t v = \partial_{xx} v + v(1-v). \end{cases} \tag{I.10}$$

Que se passe-t-il concernant la vitesse de propagation linéaire de la population u ? Si la vitesse de la population u sans couplage, donnée par $2\sqrt{d\alpha}$ est plus grande que la vitesse de la population v, très rapidement la population v se situe loin derrière le front d'invasion. Par conséquent, dans ce cas de figure, on s'attend à sélectionner la vitesse $2\sqrt{d\alpha}$. A l'inverse, si la population v se propage plus rapidement on peut imaginer que la vitesse de propagation de la population u devienne celle de la population v. Quoiqu'il advienne, naïvement, nous pouvons nous attendre à toujours satisfaire la majoration suivante, $c^\star_{\text{lin}} \leq \max(2, 2\sqrt{d\alpha})$.

Néanmoins cette inégalité s'avère être fausse, en effet le couplage de v peut entraîner une vitesse plus rapide que l'on nomme *vitesse anormale*. Cette notion a été pour la première fois introduite par Lewis, Li et Weinberger dans l'article [61], que l'on peut expliquer à l'aide des notions que nous venons de présenter [54]. En effet, pour ce système, la structure triangulaire nous permet de facilement calculer la relation de dispersion donnée par :

$$d_c(\lambda,\nu) = d_c^u(\lambda,\nu) d_c^v(\lambda,\nu) = \left(\nu - \nu_u^+\right)\left(\nu - \nu_u^-\right)\left(\nu - \nu_v^+\right)\left(\nu - \nu_v^-\right),$$

avec,

$$\nu_u^\pm(\lambda) = \frac{-c \pm \sqrt{c^2 - 4d\alpha + 4d\lambda}}{2d}, \qquad \nu_v^\pm(\lambda) = \frac{-c \pm \sqrt{c^2 - 4 + 4\lambda}}{2}.$$

Les racines doubles pincées se produisent pour les valeurs de c et λ pour lesquelles nous vérifions une des égalités, $\nu_{u,v}^+(c,\lambda) = \nu_{u,v}^-(c,\lambda)$. Notamment, nous retrouvons facilement, les deux vitesses de propagation attendues $2\sqrt{d\alpha}$ et 2, correspondant aux racines en $\nu_u^+(2\sqrt{d(\alpha-\lambda)},\lambda) = \nu_u^-(2\sqrt{d(\alpha-\lambda)},\lambda)$ et $\nu_v^+(2\sqrt{1-\lambda},\lambda) = \nu_v^-(2\sqrt{1-\lambda},\lambda)$, pour $\lambda = 0$. Les deux dernières racines $\nu_u^+(c,\lambda) = \nu_v^-(c,\lambda)$ et $\nu_v^+(c,\lambda) = \nu_u^-(c,\lambda)$ conduisent à une même vitesse anormale donnée par :

$$c_{\text{anom}}(\alpha,d) := \sqrt{\frac{\alpha-1}{1-d}} + \sqrt{\frac{1-d}{\alpha-1}},$$

obtenue pour $\lambda = 0$.

Selon la définition 2, la vitesse de propagation linéaire est simplement déterminée par le maximum des racines doubles pincées existantes. Nous illustrons la sélection de cette vitesse dans l'espace des paramètres (d,α) dans la figure I.6A, ainsi que dans l'espace $(d, \alpha = 1/2)$ dans le panneau B. Dans le panneau inférieur, nous représentons les quatre racines $\nu_{u,v}^\pm(\lambda = 0)$ pour les valeurs des paramètres $(d = 1, \alpha = 1/2)$ et $(d = 2, \alpha = 1/2)$. Pour $d = 1$, nous observons deux racines doubles pincées associées aux vitesses *normales*, la vitesse de propagation linéaire correspond ainsi à la plus grande des deux, ici $c^\star_{\text{lin}} = 2$. En revanche, pour $d = 2$, nous identifions une nouvelle racine double pincée en $\nu_u^+(0) = \nu_v^-(0)$, située à droite des deux autres. Par conséquent, la vitesse linéaire devient anormale

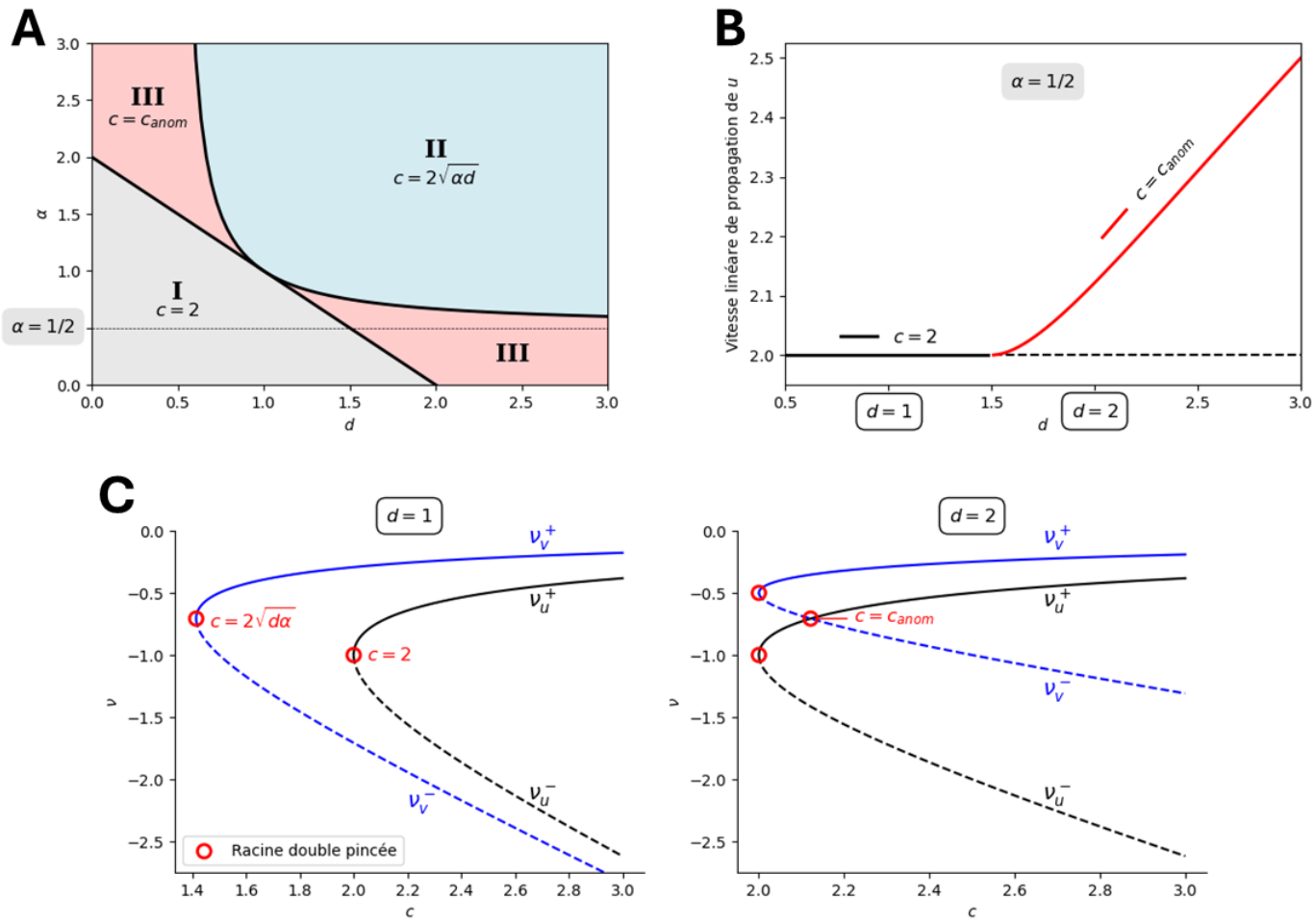

FIGURE I.6 – **Vitesse de propagation linéaire de u pour le système** (I.10)**. A.** Vitesse de propagation linéaire de u pour différentes valeurs des paramètres α et d. **B.** Vitesse de propagation linéaire de u pour $\alpha = 1/2$ et différentes valeurs du paramètre d. **C.** Représentation des quatre racines $\nu_{u,v}^{\pm}(\lambda = 0)$ pour $d = 1$ (*gauche*) et $d = 2$ (*droite*) avec $\alpha = 1/2$. Pour $d = 1$, nous observons deux racines doubles pincées, une en $c = 2$ et une en $c = 2\sqrt{d\alpha}$. Pour $d = 2$, l'intersection des courbes ν_u^+ et ν_v^- donne une nouvelle racine double pincée, associée à une vitesse anormale plus élevée que les deux précédentes.

pour ces valeurs de paramètres. Dans cet exemple, le couplage s'effectue via un terme linéaire. Des termes de couplage d'ordre supérieur ont également été étudiés dans les travaux suivants [50, 52].

Dans la partie II de cette thèse, nous utiliserons ce concept de racines doubles pincées pour calculer des vitesses anormales de propagation linéaire pour un système d'équations de réaction-diffusion étudié théoriquement dans le chapitre 3. De plus nous remarquons que cette notion peut être étendue à un modèle cinétique non linéaire que nous introduisons dans le chapitre 4.

Régime non linéaire

Dans la précédente section nous avons défini la vitesse de propagation linéaire. Cette vitesse persiste-elle pour le système non linéaire ?

Parfois oui, notamment pour des équations avec des non linéarités « suffisamment faibles », comme par exemple l'équation de Fisher-KPP (I.9). Dans ce cas, la dynamique de propagation est régie par la queue du bord d'attaque, de sorte que les fronts sont dits **tirés**, signifiant que seule la sous-population en amont du front va contribuer à l'avancée de l'ensemble de la population [62]. Pour le régime de fronts tirés, la conjecture de stabilité marginale a récemment été démontrée dans un cadre d'équations paraboliques scalaires d'ordre supérieur dans l'article d'Avery et Scheel [45], puis pour les systèmes de réaction-diffusion par Avery [46]. En d'autres termes, pour des conditions initiales raides, la vitesse asymptotique du front, solution du système universel de réaction-diffusion monostable (I.8), correspond à la vitesse de propagation linéaire, $c^\star_{\text{lin}}$.

Parfois non, en effet, l'ajout de non-linéarités peut altérer les prédictions du système linéarisé. Dans ce cas, on utilise la notion de front **poussé**, symbolisant l'action de la population dans la zone non linéaire en aval, qui pousse la propagation par le biais du terme de réaction non linéaire. Contrairement au cas précédent, la vitesse critique des fronts ne correspond pas à la vitesse de propagation linéaire. Plus précisément, pour des équations scalaires, la vitesse de propagation du front non linéaire est toujours supérieure à la prédiction linéaire, $c^\star > c^\star_{\text{lin}}$. Pour des systèmes, ce résultat ne se généralise pas ; il est en effet possible de fournir des contre-exemples où les fronts poussés sont plus lents [53].

L'exemple le plus connu de front poussé est donné par l'équation de Nagumo,

$$\partial_t u = \partial_{xx} u + u(1-u)(1+au).$$

Pour ce problème, la vitesse critique, $c^\star$, est d'abord linéairement déterminée, c'est-à-dire que $c^\star = c^\star_{\text{lin}} := 2$ lorsque $a \in [0, 2]$. Cependant, lorsque le terme non linéaire devient « suffisamment important » ($a > 2$), la vitesse critique est donnée par $c^\star = \sqrt{2/a} + \sqrt{a/2} > c^\star_{\text{lin}}$ [63, 64]. Un autre exemple de front poussé est fourni par le système étudié précédemment, donné par les équations (I.10). Dans le régime non linéaire, Holzer a démontré que la vitesse anormale induite par la racine double $\nu_u^- = \nu_v^+$ (Zone III avec $d < 1$ dans la figure I.6A) persiste, contrairement à celle provenant de la racine $\nu_v^- = \nu_u^+$ (Zone III avec $d > 1$).

Comme l'illustrent ces deux exemples, une onde peut, selon les valeurs des paramètres, passer d'un régime de front tiré à un régime de front poussé, et inversement. Dans le chapitre 3 de cette

thèse, nous démontrons l'existence d'une telle transition pour un modèle relatif à l'invasion d'une bactérie prédatrice. Ce résultat théorique nous permet également de mieux comprendre, en termes de modélisation, la dynamique et l'importance des différents acteurs impliqués dans la prédation de cette bactérie.

Front modulé

Introduction

Les concepts présentés dans la section précédente, tels que la définition de la vitesse de propagation linéaire ainsi que la distinction entre les fronts tirés et les fronts poussés, s'étendent également aux fronts de formation de motifs (Voir par exemple [39, 40, 55, 64, 65, 66, 67]). Dans cette introduction, nous nous intéressons uniquement au front qui laisse dans son sillage un motif spatialement hétérogène qui est stationnaire en temps, et que l'on nomme « *front modulé* ». Par exemple, supposons l'existence d'un état homogène, $\mathbf{u}^\star \in \mathbb{R}^n$, qui est Turing-instable. Mathématiquement, les fronts modulés correspondent aux solutions de la forme :

$$\mathbf{u}(t,x) = \mathbf{q}(x - ct, x), \quad \text{avec } \mathbf{q}(-\infty, x) = \mathbf{P}(x), \quad \mathbf{q}(+\infty, x) = \mathbf{u}^\star,$$

où $\mathbf{P}$ le motif dans le sillage, correspondant à une solution stationnaire du problème spatial. Les premiers résultats connus sur l'existence d'ondes progressives modulées proviennent des travaux d'Eckmann, Collet et Wayne [44, 68, 43]. Ils ont initialement démontré l'existence de fronts modulés pour l'équation de Swift-Hohenberg avec une non-linéarité cubique. Par la suite, de nombreux autres résultats ont enrichi cette théorie en traitant divers modèles. Par exemple, Faye et Holzer ont prouvé l'existence de fronts modulés pour une équation de Fisher-KPP non-locale [51]. Néanmoins, la démonstration de ce type de résultat pour des systèmes de réaction-diffusion complexes reste d'une grande difficulté.

Un moyen simple d'établir un lien entre les fronts de formation de motifs et les fronts monostables à translation uniforme est de considérer l'enveloppe des motifs dans le sillage, que nous représentons en pointillés dans la figure I.5B. La partie inférieure et la partie supérieure de cette enveloppe correspondent toutes deux à des solutions d'ondes progressives se propageant à une certaine vitesse inconnue.

Dans le cas d'une bifurcation super-critique, Avery a récemment démontré que, près de celle-ci, le front est tiré [69]. Dans cette situation, l'application du critère de stabilité marginale permet d'obtenir une approximation explicite précise de la vitesse d'invasion des motifs [70]. Cependant, contrairement à la méthode que nous allons introduire ci-dessous, la méthode de stabilité marginale ne fournit aucune information sur l'amplitude des motifs ou le profil transitoire de l'onde.

Pour obtenir des informations plus détaillées que celles fournies par la méthode précédente, il est nécessaire de prendre en compte des termes non linéaires. Toutefois, il est généralement très complexe d'obtenir des résultats pour le modèle incluant toutes les non-linéarités. C'est pourquoi nous privilégions une méthode dite d'*analyse faiblement non linéaire* pour approcher l'évolution spatio-temporelle de l'enveloppe des motifs. À noter que, dans l'article de Klika, Gaffney et Maini [70], les

auteurs ont montré que, pour un système de deux équations de réaction-diffusion, la méthode d'analyse faiblement non linéaire fournit, près de la bifurcation, la même estimation de vitesse que la méthode de la stabilité marginale. Nous nous concentrons donc sur la méthode d'analyse faiblement non linéaire, que nous présentons dans la section suivante.

Méthode d'analyse faiblement non linéaire pour déterminer la dynamique de l'enveloppe

Le principe central de l'analyse faiblement non linéaire est que, près de la valeur de bifurcation, le motif évolue sur une échelle de temps lente. Cela permet, grâce à la méthode des échelles multiples, de déterminer une équation d'évolution pour l'enveloppe du motif créé. L'application de cette méthode est très répandue dans la littérature, notamment pour les systèmes d'équations de réaction-diffusion et de réaction-diffusion-taxis (voici quelques exemples de références [9, 10, 70, 71, 72, 73]).

Méthode de l'analyse faiblement non linéaire. Pour présenter cette méthode, considérons à nouveau un système de deux équations de réaction-diffusion similaire à (I.1), où nous supposons que la première composante correspond à un activateur tandis que la seconde à un inhibiteur. Supposons également que les termes de réactions soient choisis de manière à ce que le système admette un point d'équilibre, $\mathbf{u}^\star := (u_1^\star, u_2^\star)$, qui soit Turing-instable. Autrement dit, il existe une certaine constante positive $D_c > 0$ telle que pour $D_2/D_1 < D_c$, l'état $\mathbf{u}^\star$ est stable, tandis que pour $D_2/D_1 > D_c$, les termes de diffusion rendent cet état homogène instable. Comme précédemment, nous nous intéressons à l'évolution de la perturbation autour du point d'équilibre $\mathbf{u}^\star$, notée $\mathbf{p}$. Afin d'identifier l'équation d'enveloppe approximative de la perturbation, nous développons l'équation de la perturbation comme suit,

$$\partial_t \mathbf{p} = \mathcal{L}_1 \mathbf{p} + \mathcal{N}_2 \mathbf{pp} + \mathcal{N}_3 \mathbf{ppp}, \tag{I.11}$$

où l'opérateur linéaire, $\mathcal{L}_1$, est donné par $\mathcal{L}_1 := \mathbf{D}^{D_2}\partial_{xx} + \mathbf{J}$ avec $\mathbf{D}^{D_2}$ la matrice de diffusion et $\mathbf{J}$ la jacobienne de $\mathbf{F}$ évaluée en $\mathbf{u}^\star$. Les termes $\mathcal{N}_2$ et $\mathcal{N}_3$, eux, correspondent respectivement à l'approximation quadratique et cubique.

Pour décrire la dynamique spatiale des motifs, nous introduisons une nouvelle échelle temporelle lente, comme suit

$$t = \mathcal{T}(T_1, T_2, T_3, \ldots), \quad T_i = \epsilon^i t, \quad i = 1, 2, \ldots ,$$

et également une nouvelle échelle spatiale en définissant l'échelle de longueur caractéristique de la modulation spatiale, $X := \epsilon x$ [74], où $\epsilon \ll 1$ représente la distance entre D_2 et sa valeur de bifurcation en $D_2^c := D_c D_1$. Compte tenu de ces changements d'échelle, la dérivée seconde en espace, ∂_{xx}, correspond à l'ensemble des dérivées $\partial_{xx} + 2\epsilon\partial_{xX} + \epsilon^2\partial_{XX}$; tandis que la dérivée temporelle, ∂_t, est maintenant donnée par le développement, $\epsilon\partial_{T_1} + \epsilon^2\partial_{T_2} + \epsilon^3\partial_{T_3} + \cdots$. Finalement nous développons, en puissance de ϵ, notre paramètre de bifurcation, D_2, ainsi que la variable de la perturbation autour du point d'équilibre,

$$D_2 = D_2^c + \epsilon D_2^{(1)} + \epsilon^2 D_2^{(2)} + \ldots, \quad \text{et,} \quad \mathbf{p} = \epsilon\mathbf{p}^{(1)} + \epsilon^2\mathbf{p}^{(2)} + \epsilon^3\mathbf{p}^{(3)} + \ldots .$$

En utilisant ces précédentes relations, nous développons maintenant l'opérateur linéaire $\mathcal{L}^1$, en termes de puissances de ϵ,

$$\mathcal{L}_1 = \mathcal{L}_1^{(0)} + \epsilon\mathcal{L}_1^{(1)} + \epsilon^2\mathcal{L}_1^{(2)} + \epsilon^3\mathcal{L}_1^{(3)} + \dots,$$

avec $\mathcal{L}_1^{(0)} := D^{D_2^c}\partial_{xx} + \mathbf{J}$ et $\mathcal{L}_1^{(i)} := D_2^{(i)}\begin{pmatrix}0 & 0\\ 0 & 1\end{pmatrix}$, pour $i \in \mathbb{N}^\star$. En développant tous les termes de l'équation (I.11) et en identifiant les contributions pour chaque puissance de ϵ, nous obtenons

$$\begin{array}{rcc|c|c|c}
\partial_t\mathbf{p} = & 0 & +\epsilon.0 & +\epsilon^2\partial_{T_1}\mathbf{p}^{(1)} & +\epsilon^3\left(\partial_{T_1}\mathbf{p}^{(2)} + \partial_{T_2}\mathbf{p}^{(1)}\right) & +O(\epsilon^3),\\
\mathcal{L}_1\mathbf{p} = & 0 & +\epsilon\mathcal{L}_1^{(0)}\mathbf{p}^{(1)} & +\epsilon^2\left(\mathcal{L}_1^{(0)}\mathbf{p}^{(2)} + \mathcal{L}_1^{(1)}\mathbf{p}^{(1)}\right) & +\epsilon^3\left(\mathcal{L}_1^{(0)}\mathbf{p}^{(3)} + \mathcal{L}_1^{(1)}\mathbf{p}^{(2)} + \mathcal{L}_1^{(2)}\mathbf{p}^{(1)}\right) & +O(\epsilon^3),\\
\mathcal{N}_2\mathbf{pp} = & 0 & +\epsilon.0 & +\epsilon^2\mathcal{N}_2\mathbf{p}^{(1)}\mathbf{p}^{(1)} & +\epsilon^3 2\mathcal{N}_2\mathbf{p}^{(1)}\mathbf{p}^{(2)} & +O(\epsilon^3),\\
\mathcal{N}_3\mathbf{ppp} = & 0 & +\epsilon.0 & +\epsilon^2.0 & +\epsilon^3\mathcal{N}_3\mathbf{p}^{(1)}\mathbf{p}^{(1)}\mathbf{p}^{(1)} & +O(\epsilon^3).
\end{array}$$

Par conséquent, pour assurer une correspondance jusqu'à l'ordre 3, il faut résoudre pour $\mathbf{p}^{(1,2,3)}$ le système suivant

$$0 = \mathcal{L}^{(0)}\mathbf{p}^{(1)} + 0 + 0, \quad \text{(I.12)}$$

$$\partial_{T_1}\mathbf{p}^{(1)} = \mathcal{L}_1^{(0)}\mathbf{p}^{(2)} + \mathcal{L}_1^{(1)}\mathbf{p}^{(1)} + \mathcal{N}_2\mathbf{p}^{(1)}\mathbf{p}^{(1)} + 0, \quad \text{(I.13)}$$

$$\partial_{T_1}\mathbf{p}^{(2)} + \partial_{T_2}\mathbf{p}^{(1)} = \mathcal{L}_1^{(0)}\mathbf{p}^{(3)} + \mathcal{L}_1^{(1)}\mathbf{p}^{(2)} + \mathcal{L}_1^{(2)}\mathbf{p}^{(1)} + 2\mathcal{N}_2\mathbf{p}^{(1)}\mathbf{p}^{(2)} + \mathcal{N}_3\mathbf{p}^{(1)}\mathbf{p}^{(1)}\mathbf{p}^{(1)}. \quad \text{(I.14)}$$

• $O(\epsilon)$ **:** Pour la première équation (I.12), nous obtenons le problème linéaire $\mathcal{L}^0\mathbf{p}^{(1)} = 0$, dont la solution prend la forme suivante,

$$\mathbf{p}^{(1)} = A(T_1, T_2, \dots; X)\mathbf{q}\cos(k_c x), \quad \text{(I.15)}$$

où k_c est le premier et unique mode instable et $\mathbf{q}$ est un vecteur explicite dont les détails ne seront pas fournis ici. Le terme $A(T_1, T_2, \dots; X)$ représente l'amplitude spatiale du motif, et notre objectif est de déterminer l'équation régissant cette amplitude.

• $O(\epsilon^2)$ **:** En combinant la formule de $\mathbf{p}^{(1)}$ et l'alternative de Fredholm il s'ensuit les égalités suivantes, $T_1 = 0$, et $D_2^{(1)} = 0$. Par conséquent, en utilisant l'équation (I.13), nous pouvons en déduire que le terme de précision supérieure, $\mathbf{p}^{(2)}$ est donné par l'égalité,

$$\mathbf{p}^{(2)} = A^2\mathbf{q}_{20} + A^2\mathbf{q}_{22}\cos(2k_c x) + \frac{\partial A}{\partial X}\mathbf{q}_{21}\sin(k_c x), \quad \text{(I.16)}$$

avec $\mathbf{q}_{2i}$, $i = 0, 1, 2$, des vecteurs explicites non détaillés.

• $O(\epsilon^3)$ **:** Finalement en remplaçant les formules (I.15) et (I.16) dans l'équation (I.14) et en utilisant la condition de solvabilité, nous obtenons que, A, l'enveloppe du motif, doit être solution d'une équation de Ginzburg-Laudau réelle, donnée par :

$$\partial_{T_2}A = \nu\partial_{XX}A + \sigma A - LA^3, \quad \text{(I.17)}$$

où les coefficients ν, σ et L sont calculables explicitement et dépendent des paramètres du système. Le taux de croissance, σ, est toujours positif, tandis que le signe du coefficient L dépend du type de bifurcation : L est positif pour une bifurcation super-critique et négatif pour une bifurcation sous-critique.

Dans le cas d'une bifurcation sous-critique, nous ne nous attendons pas à une bonne approximation de l'enveloppe pour plusieurs raisons. Tout d'abord, dans ce régime, la propagation est fortement influencée par les termes non linéaires. De plus, l'étude de l'équation (I.17) montre que l'amplitude réelle prédite est d'ordre $O(1)$ [70, 73]. Ce manque de précision, lorsque l'on a $L < 0$, a été observé dans de nombreux articles [12, 13, 73]. Nous nous concentrons donc sur le cas des bifurcations super-critiques, où $L > 0$.

Conclusion. L'équation (I.17) possède deux points d'équilibre non négatifs, à savoir le point d'équilibre nul instable $A_0 := 0$ et le point stable, $A_\infty := \sqrt{\sigma/L}$, qui représente l'amplitude asymptotique prédite des motifs, $\lim_{T_2 \to +\infty} A(T_2, X) = A_\infty$. De plus, cette équation admet des solutions d'ondes progressives reliant A_0 à A_∞, dont la vitesse critique associée est donnée par $2\epsilon\sqrt{\nu\sigma}$ dans le référentiel du laboratoire [63]. En utilisant la méthode d'analyse faiblement non linéaire, nous avons prédit que le comportement de $\mathbf{u}$, proche d'une bifurcation super-critique, est donné par l'égalité

$$\mathbf{u} = \mathbf{u}^\star + \epsilon A(\epsilon x, \epsilon^2 t)\mathbf{q}\cos(k_c x) + O(\epsilon^2),$$

où A, représentant l'amplitude du motif, est une solution de l'équation de Ginzburg-Landau (I.17).

Dans le premier chapitre de la seconde partie de cette thèse, nous appliquons cette méthode à un système de réaction-diffusion-taxis modélisant l'émergence des follicules de plumes. Cette étude couplée à des simulations numériques, nous permet de déterminer une bonne approximation explicite de la vitesse de formation des plumes, et ainsi d'évaluer l'influence des différents facteurs en jeu.

Deuxième partie

Modélisation de l'émergence des follicules plumeux

Introduction

Introduction biologique concernant les follicules plumeux

Comment les plumes se forment-elles ? Chez les oiseaux, les plumes se développent à partir de follicules plumeux répartis dans des zones ptilogènes ou ptéryles, séparées par des régions glabres appelées aptéries. Ces zones varient en nombre, taille et étendue entre les espèces, mais restent cohérentes au sein d'une même espèce. Dans ce travail, nous nous intéresserons particulièrement à la ptéryle dorsale, correspondant à la plus grande de ces zones et s'étendant de la région cervicale jusqu'au croupion. La peau des oiseaux est composée de l'épiderme et du derme. Les cellules épidermiques sont fixées entre elles, tandis que les cellules du derme sont libres de se déplacer. La formation des plumes commence au stade embryonnaire avec l'apparition de placodes dermiques, correspondant à des épaississements de l'épiderme. Pour les espèces aviaires auxquelles nous nous intéressons, la formation des follicules plumeux est fortement symétrique (Voir Fig. II.1) par rapport à l'axe antéro-postérieur. Pour simplifier nous considérerons uniquement l'un des deux demi-espaces.

Apparition temporelle des follicules. La formation des follicules plumeux se déroule en deux phases distinctes :

❶ *Vague de compétence :* Au début du développement de l'embryon, le derme des zones ptilogènes se densifie au cours du temps, en suivant une vague médio-latérale. Cette étape, illustrée par l'icône ❶ dans la figure II.2, est cruciale dans la structuration des différentes zones [76].

❷ *Émergence de follicules plumeux dans la zone compétente :* Une fois que le derme est compétent, un dialogue, entre le derme et l'épiderme, par le biais de différents signaux, permet la formation de placodes épidermiques. Ces placodes vont, peu à peu, envoyer des signaux au derme, entraînant une forte condensation cellulaire. Ce processus aboutit à la formation d'un bourgeon qui donnera, par la suite, naissance à une plume. Nous illustrons la formation de placodes par l'icône ❷ dans la figure II.2.

Répartition spatio-temporelle des follicules plumeux. Chez la plupart des espèces d'oiseaux, l'apparition initiale des primordia des plumes se fait le long d'une ou deux rangées suivant l'axe antéro-postérieur. Ensuite, une vague médio-latérale entraîne l'émergence progressive de nouvelles rangées de follicules de chaque côté de la rangée initiale, jusqu'à atteindre les limites de la zone ptilogène.

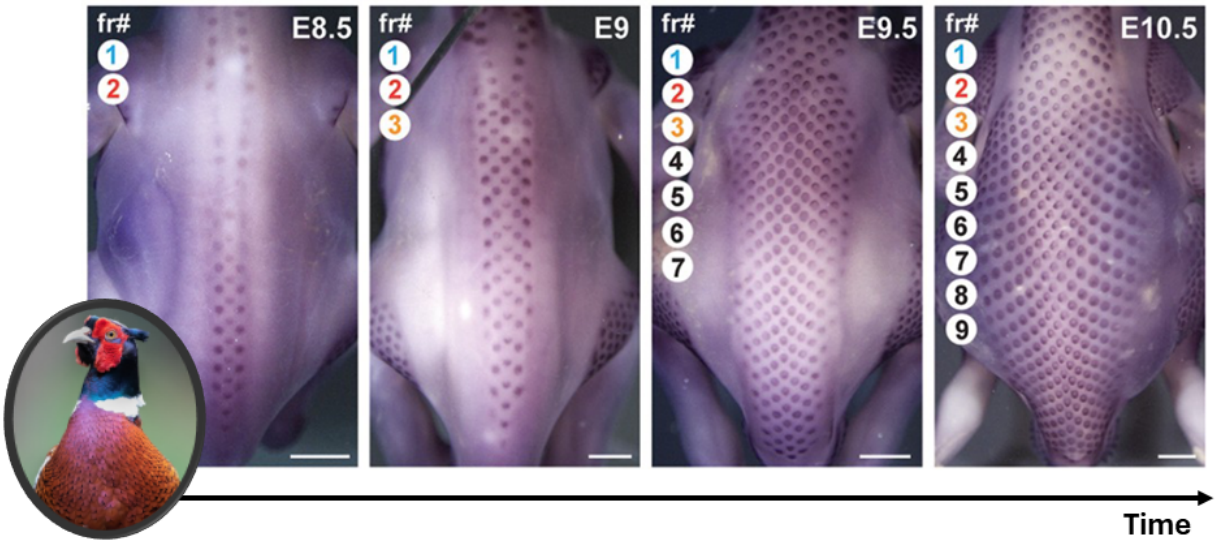

FIGURE II.1 – **Évolution temporelle de la région dorsale d'un embryon de Faisan de Colchide.** L'évolution temporelle des embryons est illustrée de la gauche vers la droite. Les termes E8.5, E9, etc., indiquent les stades de développement de l'embryon, correspondant respectivement aux jours 8.5, 9, etc., après la ponte de l'œuf. Les rangées de bourgeons plumeux apparaissent progressivement selon une vague médio-latérale. Les rangées de bourgeons présents à chaque stade de développement sont illustrées par les numéros en haut à gauche de chaque image. La figure encadrée est une photo de Faisan de Colchide adulte. Cette figure provient de l'article [75], est reproduite et modifiée avec la permission des auteurs.

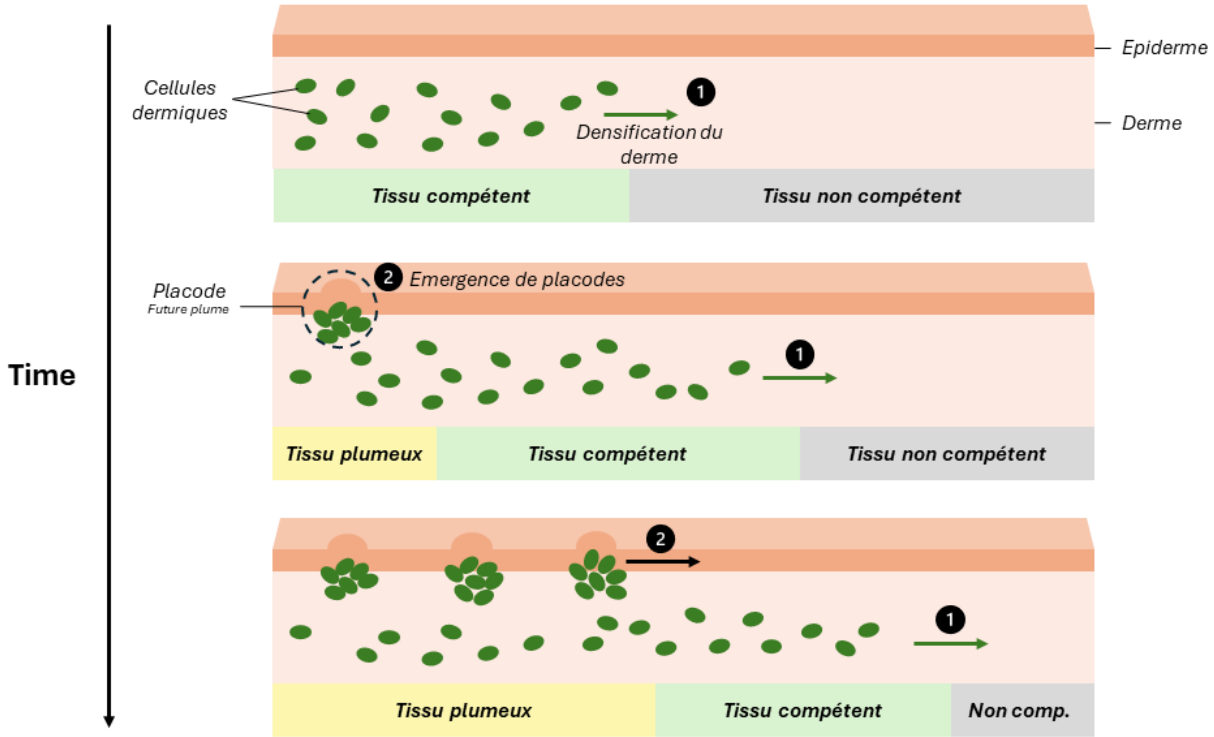

FIGURE II.2 – **Illustration de la formation des follicules plumeux.** L'émergence a lieu en deux étapes. La première étape, illustrée par l'icône ❶, correspond à une prolifération des cellules du derme suivant une certaine vague médio-latérale. Suite à cette densification du derme le tissu autrefois naïf devient compétent. Ensuite, au sein d'un tissu compétent, nous remarquons l'émergence progressive de placodes, induisant par la suite la formation de condensats de cellules dermiques (Voir l'icône ❷). Ces placodes correspondent aux futurs lieux de développement des plumes.

La figure II.1, correspondant à l'évolution temporelle de la région dorsale d'un embryon de Faisan de Colchide, illustre parfaitement cette émergence progressive des follicules plumeux. La répartition spatiale finale des follicules plumeux varie également d'une espèce à l'autre. Néanmoins, les espèces pour lesquelles nous retrouvons un tel phénomène de propagation, présentent généralement des motifs réguliers hexagonaux où chaque follicule plumeux est entouré de six voisins.

Etat de l'art

Dans la littérature, il existe de nombreux travaux sur la modélisation spatiale de l'émergence des follicules plumeux, dont une grande part se base sur des modèles de réaction-diffusion voire de réaction-diffusion-chimiotaxie qui reproduisent des motifs à pois proches des motifs que l'on retrouve chez les embryons [75, 77, 78, 79, 80, 81]. Chacun de ces articles se concentre sur certaines particularités de l'émergence des follicules. Par exemple, dans l'article [77], Diez et ses collaborateurs font le choix d'un modèle prenant en compte les caractéristiques d'un domaine avec deux couches (épiderme et derme). Dans un autre travail, Tseng et al., eux, ont fait le choix de se concentrer sur la formation des bourgeons plumeux ectopiques en étudiant des morphogènes se déplaçant à l'aide de jonctions lacunaires [78].

Dans l'article [75] les auteurs Bailleul et al. ont, eux, modélisé non seulement l'émergence d'un motif hexagonal des follicules, mais également les aspects directionnels et séquentiels de la formation des plumes, et cela pour de nombreuses espèces d'oiseaux. Pour ce faire, les auteurs introduisent un nouveau modèle mathématique en combinant le système activateur-inhibiteur introduit dans l'article de Michon et al. [79], connu pour former les motifs hexagonaux souhaités, couplé à une équation classique de réaction-diffusion régissant la dynamique spatio-temporelle des cellules du derme. Plus précisément, le modèle comprend trois équations, une pour la densité cellulaire, représentée par la variable n, donnée par,

$$\partial_t n = D_n \Delta n - \nabla\cdot(\kappa n \nabla u) + \alpha_n n(1-n), \tag{II.1}$$

à laquelle nous ajoutons deux équations de réaction-diffusion pour les espèces morphogènes activatrice u et inhibitrice v,

$$\partial_t u = D_u \Delta u + \frac{\alpha_u n(1+\omega u^2)}{(\beta_u^2+u^2)(1+v)} - \delta_u u, \tag{II.2}$$

$$\partial_t v = D_v \Delta v + \alpha_v n u^2 - \delta_v v. \tag{II.3}$$

Selon des travaux récents, deux candidats se démarquent concernant les morphogènes u et v : le facteur de croissance des fibroblastes (FGF) pour l'activateur, et la BMP (Bone Morphogenetic Protein) pour l'inhibiteur [82]. Dans ce modèle, les trois morphogènes diffusent avec un certain coefficient de diffusion propre à chacune d'entre elles. Il est également supposé que les cellules du derme sont attirées par les forts gradients de la protéine FGF [82]. De plus, les auteurs ont supposé une croissance logistique des cellules, qui s'avère être déterminante pour la densification du derme. A l'aide de simulations numériques, les auteurs ont montré que leur modèle mathématique reproduit fidèlement la dynamique spatio-temporelle d'émergence des motifs que nous avons décrite précédemment (Voir également Fig. II.1 et II.2), ainsi que les variations entre les différentes espèces.

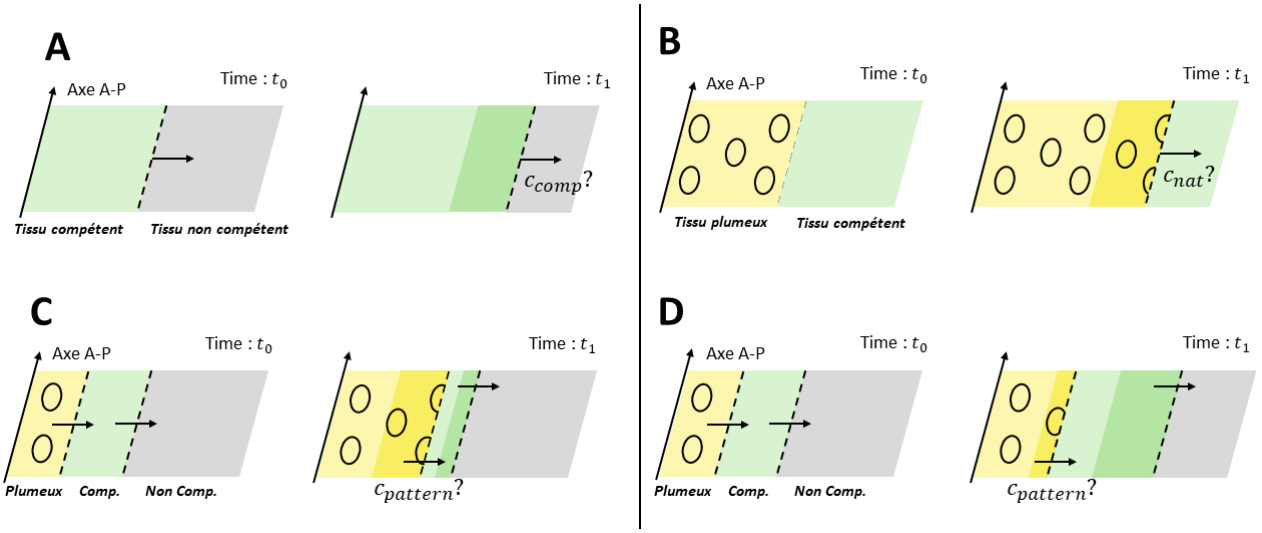

FIGURE II.3 – **Illustration des différentes problématiques.**

Problématiques

Notre but dans ce travail est d'étudier mathématiquement les acteurs ainsi que les vitesses des différents processus agissant dans la formation des follicules de plumes. Notamment nous nous concentrons sur les questions suivantes :

A. Quelle est la vitesse de propagation de la vague de compétence ?

B. Quelle est la vitesse d'émergence de follicules dans une zone compétente ?

C. Que se passe-t-il quand la vague de compétence est plus lente que la vitesse d'émergence des follicules dans la zone compétente ?

D. Que se passe-t-il quand la vague de compétence est plus rapide que la vitesse d'émergence des follicules dans la zone compétente ?

Ces différentes problématiques sont illustrées dans la figure II.3.

Résultats

• **Chapitre 1 : Mathematical modeling of dermal competence and cellular aggregation effects on feather follicle emergence speed.**

Ce travail est en collaboration avec Marie Manceau et Thomas Lepoutre.

Méthodes. Vu que l'onde de compétence est unidirectionnelle (médio-latérale), nous commençons par simplifier notre problème en supposant un espace unidimensionnel $\Omega = [0, \ell]$. De plus, les termes de réaction n'ont pas nécessairement d'interprétation biologique ; par conséquent nous les simplifions

en appliquant la troncature suivante aux morphogènes :

$$\begin{cases} \partial_t u = D_u \Delta u + n\chi_M(\gamma_u u - \gamma_v v + c_u) - \delta_u u, \\ \partial_t v = D_v \Delta v + n\chi_M(\eta_u u + c_v) - \delta_v v, \end{cases}$$

avec $\chi_M(x) = x\mathbf{1}_{0\leq x\leq M}(x) + M\mathbf{1}_{x>M}(x)$, illustrée ci-dessous, où M est une constante positive arbitraire.

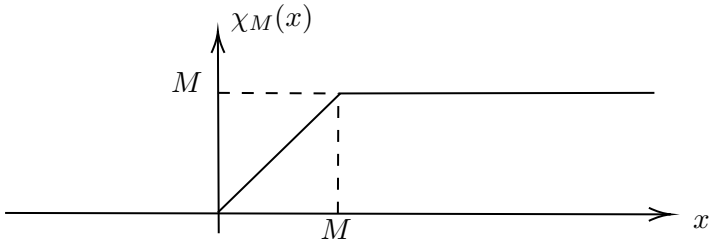

Cette idée de troncature est inspirée de la troncature introduite dans l'article [83] et est couramment utilisée dans le domaine de la morphogénèse (par exemple dans les articles [84, 85, 86]). Les objectifs principaux sont d'éviter les interactions biologiquement irréalistes et d'obtenir un modèle plus général. Pour des amplitudes proches de l'état stationnaire instable, si la constante M est supposée assez grande, la fonction de coupure n'aura aucun impact sur la solution du système. Dans la mesure où l'analyse est valide pour des perturbations de faible amplitude, nos calculs se ramènent à l'étude du modèle suivant sans fonction de coupure,

$$\begin{cases} \partial_t n = D_n \Delta n - \nabla\cdot(\kappa n \nabla u) + \alpha_n n\,(1-n)\,, \\ \partial_t u = D_u \Delta u + n(\gamma_u u - \gamma_v v + c_u) - \delta_u u, \\ \partial_t v = D_v \Delta v + n(\eta_u u + c_v) - \delta_v v. \end{cases} \tag{II.4}$$

Notre modèle étant maintenant introduit, nous nous intéressons à l'émergence des follicules plumeux. Celle-ci a lieu en deux étapes, qui correspondent mathématiquement, aux phénomènes suivants

❶ *Vague de compétence :* Tout d'abord, il existe une onde progressive reliant le point d'équilibre $(0,0,0)$ (Tissu *naïf*) à l'unique point d'équilibre positif $(1,u_s,v_s)$ (Tissu *compétent*).

❷ *Émergence des follicules plumeux dans la zone compétente :* Puis, dans un second temps, l'instabilité linéaire du point $(1,u_s,v_s)$ conduit à l'émergence de motifs spatiaux. L'apparition de ces motifs se fait de manière progressive dans l'espace, plus précisément ils apparaissent pic par pic au cours du temps. En d'autres termes nous avons une onde reliant un certain motif périodique en espace et stationnaire en temps, dénoté $P^\star$, au point d'équilibre Turing-instable $(1,u_s,v_s)$. Pour caractériser la vitesse d'émergence des follicules, nous étudions l'enveloppe de ces motifs, illustrée en bleu dans la figure ci-dessous, dont la dynamique s'approche fortement d'une solution d'onde progressive reliant la valeur maximale du motif au point d'équilibre positif.

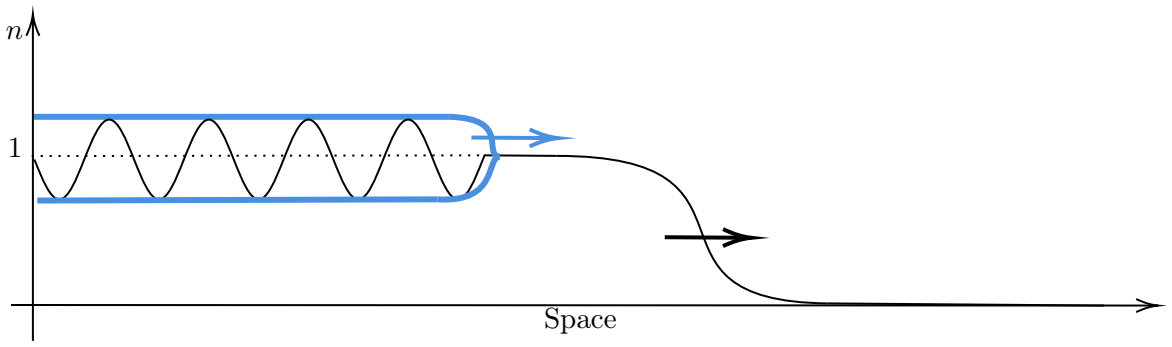

Nous allions des investigations théoriques (analyse linéaire et faiblement non linéaire) avec des investigations numériques pour déterminer les vitesses associées à ces deux étapes.

Résultats principaux. Nous répondons aux différentes problématiques :

A. Selon notre étude, l'onde de compétence se rapproche étroitement de la prédiction linéaire correspondant à la solution de l'équation scalaire de Fisher-KPP, $\partial_t n = D_n \Delta n + \alpha_n n(1-n)$, dont la vitesse critique est donnée par, $c_{\text{comp}} = 2\sqrt{D_n \alpha_n}$, qui dépend uniquement des paramètres liés aux cellules dermiques [59, 60].

B. Grâce à l'analyse faiblement non linéaire (voir par exemple [12, 13, 70, 87]) de notre modèle, nous pouvons approcher l'équation de l'évolution spatio-temporelle de l'enveloppe du motif. Cela nous permet notamment, sous certaines conditions, de déterminer une approximation explicite précise de la vitesse d'émergence des follicules dans un tissu dermique compétent, donnée par la formule, $c_{\text{nat}} = 2\epsilon\sqrt{\nu\sigma}$, dans laquelle la constante positive ϵ représente la distance des paramètres par rapport au point de bifurcation et les constantes positives ν et σ seront présentées ultérieurement. Nous appelons cette vitesse la *vitesse naturelle des motifs*.

Finalement, nous nous intéressons à la façon dont la vague de compétence peut influencer la formation de motifs et, inversement, comment la formation des motifs peut accélérer ou ralentir la vitesse de l'onde de compétence.

C. Premièrement, lorsque la vitesse naturelle des motifs (c_{nat}) est supérieure à la vitesse de la vague de compétence (c_{comp}), l'émergence des motifs va rattraper l'onde de compétence et se « verrouiller » à celle-ci sans l'impacter. Autrement dit, au bout d'un certain temps, la vitesse d'apparition des motifs est égale à la vitesse de l'onde de compétence, les motifs étant forcés d'attendre la montée en compétence.

D. Dans le cas contraire, l'onde de compétence ne semble pas avoir d'impact sur la vitesse de propagation des motifs et, par conséquent, la vitesse d'émergence des follicules plumeux s'aligne sur la vitesse naturelle des motifs.

La combinaison de ces deux cas nous donne une approximation très précise de la vitesse de l'apparition des motifs, donnée par la formule suivante

$$c_{\text{pattern}} \approx \min(2\sqrt{\alpha_n D_n}, 2\epsilon\sqrt{\sigma\nu}) = \begin{cases} c_{\text{comp}} = 2\sqrt{\alpha_n D_n}, & \text{si } c_{\text{nat}} > c_{\text{comp}}, \text{ (Cas } \mathbf{C}\text{)}, \\ c_{\text{nat}} = 2\epsilon\sqrt{\sigma\nu}, & \text{sinon, (Cas } \mathbf{D}\text{)}. \end{cases}$$

1 Mathematical modeling of dermal competence and cellular aggregation effects on feather follicle emergence speed

1.1 Introduction

Cutaneous appendages, such as hairs, feathers, and scales, exhibit a multitude of possibilities in terms of arrangement patterns, color variations, shape differences, and timing of appearance among different species. Modeling plays a crucial role in elucidating the underlying mechanisms governing their development and evolution. One influential theoretical framework applied in the field of modeling appendage formation is the reaction-diffusion model, also known as the activator-inhibitor model, developed by Alan Turing [88] (See e.g. [1, 85, 89, 90, 91, 82]). For many species, appendages do not form simultaneously across the entire skin surface, but follow a pattern of sequential development, unfolding in coordinated stages in time and space. This is notably the case for the formation of shark skin denticles [92], the formation of zebrafish scales [93], the formation of bat teeth [85, 94], the formation of feather follicles [82, 75], the formation of corn snake scales [95]. The formation of skin appendages is often correlated with the spatial expansion of the competent tissue region in which the structures can develop. This spatial extension of the competent domain can result from various factors, either dependent on or independent from the morphogens associated with appendage formation. For example, the growth of the dental lamina in bats is directly associated with the formation of molars and premolars [94]. Additionally, the competent zone can also form in the wake of signaling waves, such as Eda waves [82, 95] or NF-κB [93]. Moreover, mechanical phenomena, such as dermal densification, can also render the tissue competent in avian species [75]. In this paper, we focus on the emergence speed of these appendages and choose to concentrate on modeling the spatio-temporal formation of feather follicles.

In birds, feathers are implanted in feather follicles, which are spatially distributed in so-called tracts, or pterylae, separated by glabrous regions. The number, size and extent of tracts vary across the avian phylogeny, but are reproducible within individual species or given families. However, the arrangement of these tracts remains consistent within individual species. Tract variation has been best described in the dorsal region : the dorsal tract may form a thin longitudinal band extending from the neck to the tail (e.g., passerine birds), a thick segment (e.g., ground-dwelling poultry birds), or

cover the entire dorsal surface (e.g. ostriches). Strikingly, the local distribution of feather follicles also varies between species, from regular hexagonal patterns where each feather follicle is surrounded by six neighbours to squared meshes or irregular arrangement.

The formation of feather follicles occurs in two distinct phases :

1. *Competent wave :* Early in embryo development, the cells of the dermis begin to organize themselves in different ways depending on their location, which creates structuring spaces. Specifically, the dermis of future appendage areas tends to densify over time, following a medio-lateral wave, playing a crucial role in determining where feathers will emerge [76].
2. *Emergence of feather follicles in the competent area :* Once the dermis is competent, it instructs the overlying epidermis, through local signals, to thicken the epithelial sheet, thereby producing epidermal placodes. These placodes, in turn, send feedback to the dermis, leading to cellular condensation. This process results in the formation of a feather bud from which the feather will emerge.

Note that in the article [82], the authors showed that an ectodysplasin A (Eda) signaling wave cooperates with dermal densification to make the tissue competent. This spatio-temporal propagation of Eda lowers the cell density threshold required for follicle development by inducing FGF20, which acts as a chemoattractant leading to the aggregation of dermal cells into placodes. However, this signal is neither absolutely necessary nor sufficient for the process of feather follicle formation. In this work, we focus solely on modeling dermal densification as a wave of competence.

In most bird species, the initial appearance of feather primordia is along one or two longitudinal rows in the spinal region. Then, following a medio-lateral wave, new rows of follicles gradually emerge on either side of the initial row, until they reach the boundaries of the appendage fields.

Our aim, through mathematical modeling, is to first compute the respective speeds of these two processes. Then, to investigate the interactions between these stages to determine the speed of emergence of feather follicles during morphogenesis.

In the literature, there are several different reaction-diffusion or reaction-diffusion-chemotaxis models that reproduce regularly spaced dots, closely resembling the feather pattern [75, 77, 78, 79, 80, 81]. Recently, Bailleul et al. explored not only this final hexagonal pattern but also the directional and sequential aspects of feather formation in many bird species [75]. In these articles, the authors defined a mathematical model that intrinsically reproduces this pattern emergence dynamic, as well as the variations between different species. This model combines a system of two reaction-diffusion equations, inspired by the model used in the article by Michon et al. [79], coupled with a classical chemotaxis equation including a logistic proliferation term. More precisely, the model comprises three equations, one for the term n, corresponding to the cell density,

$$\partial_t n = D_n \Delta n - \nabla\cdot(\kappa n \nabla u) + \alpha_n n(1-n), \tag{1.1}$$

to which we add two reaction-diffusion equations for the species u and v,

$$\partial_t u = D_u \Delta u + \frac{\alpha_u n(1+\omega u^2)}{(\beta_u^2+u^2)(1+v)} - \delta_u u, \tag{1.2}$$

$$\partial_t v = D_v \Delta v + \alpha_v n u^2 - \delta_v v. \tag{1.3}$$

We assume that these three species diffuse with a certain diffusion coefficient specific to each one. Concerning the first equation (1.1), the part in κ is a chemotaxis term, corresponding to a biased diffusion where cells are attracted by the strong gradients of the species u. The cell proliferation term is assumed to be logistic with proliferation rate α_n. This term plays a crucial role in the competence wave, which biologically corresponds to the densification of the dermis. The species u and v correspond, respectively, to the activator and to the inhibitor. Biologically, the exact nature of these species remains uncertain. According to recent work, two candidates stand out : fibroblast growth factor (FGF) for the activator, and BMP (Bone Morphogenetic Protein) for the inhibitor [82]. The system (1.1)-(1.3), studied mathematically in the supplementary materials of the article [75], admits, for certain values of parameters, a unique positive equilibrium point denoted as $(1, u_s, v_s)$. This homogeneous state can be Turing unstable, leading to the emergence of patterns representing the arrangement of tracts.

As indicated in the articles [75, 79], this model is mainly chosen for its ability to produce points sequentially. However, the reaction terms of the equations (1.2) and (1.3) do not necessarily have a biological interpretation. Therefore, we propose a simplified, but also more general model, to facilitate the proof of theoretical results. First of all, since the competence wave is unidirectional (medio-lateral), we simplify our problem to a one-dimensional space. Moreover, due to the symmetry around the antero-posterior axis we consider the domain, $\Omega = [0, \ell]$, where ℓ is a positive constant. To simplify the reaction terms of the equations (1.2) and (1.3) we employ the following truncation

$$\begin{cases} \partial_t u = D_u \Delta u + n\chi_M(\gamma_u u - \gamma_v v + c_u) - \delta_u u, \\ \partial_t v = D_v \Delta v + n\chi_M(\eta_u u + c_v) - \delta_v v, \end{cases}$$

with $\chi_M(x) = x\mathbf{1}_{0\leq x\leq M}(x) + M\mathbf{1}_{x>M}(x)$, where M is an arbitrary positive constant. To ensure that the truncated model preserves certain essential properties of the original system (1.1)-(1.3), we select the constants γ_u, γ_v, and η_u such that the truncated model has the same unique positive equilibrium point $(1, u_s, v_s)$ and the same Jacobian matrix. Therefore, these constants γ_u, γ_v and η_u, are defined as follows,

$$\gamma_u = \frac{2\alpha_u u_s(\omega\beta_u - 1)}{(\beta_u + u_s^2)^2(1 + v_s)}, \quad \gamma_v = \frac{\alpha_u(1 + \omega u_s^2)}{(\beta_u + u_s^2)(1 + v_s)^2}, \qquad \eta_u = 2\alpha_v u_s, \tag{1.4}$$

concerning the constants c_u and c_v, they are defined by $c_u = -\gamma_u u_s + \gamma_v v_s + \delta_u u_s$ and $c_v = -\eta_u u_s + \delta_v v_s$. This idea of truncation is inspired by the truncation introduced in article [83] ; the aim is to avoid biologically unrealistic interactions. The use of truncation is widely used in the field of pattern emergence modeling, such as for modeling the colors of lizard skin scales [84, 96], the formation of mouse molars [85], the formation of shark skin denticles [92], the color of zebrafish [83], or even the rugae in the mammalian oral palate [86].

Our choice of cut-off function preserves, the positivity of the species u and v and also prevents the explosion by means of the positive constant M for the one and two-dimensional case [97]. If the constant M is assumed to be sufficiently large compared to the amplitudes of the final stationary pattern, the cutoff function will have no impact on the solution of the system. Since the theoretical

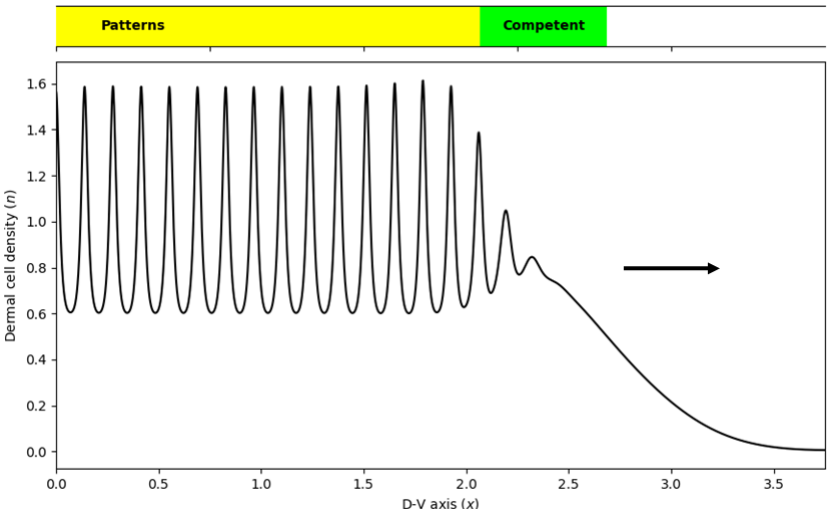

FIGURE 1.1 – **Emergence of feather follicles.** Snapshot of the density of dermal cells, n, solution of system (1.5). In the left zone, represented by the yellow color, we observe spatially distributed peaks representing aggregations of dermal cells that are the origin of feather buds. Then, we notice a transition zone, represented by the green color, corresponding to an area where the tissue is competent and where the pattern begins to emerge. Finally, on its right, the naive tissue starts to densify to become competent.

analysis we perform in this work is only valid for small amplitude perturbations, our calculations reduce to the study of the following model without a cutoff function,

$$\begin{cases} \partial_t n = D_n \Delta n - \nabla\cdot(\kappa n \nabla u) + \alpha_n n\,(1-n)\,, \\ \partial_t u = D_u \Delta u + n(\gamma_u u - \gamma_v v + c_u) - \delta_u u, \\ \partial_t v = D_v \Delta v + n(\eta_u u + c_v) - \delta_v v. \end{cases} \tag{1.5}$$

In this article, we are interested in the emergence of patterns, which biologically corresponds to the successive appearance of tracts during morphogenesis. Mathematically, for our model (1.5), this emergence occurs in two different steps.

1. *Competent wave :* First of all, there is a traveling wave connecting the point $(0,0,0)$ (*naive*) to the unique positive equilibrium point $(1,u_s,v_s)$ (*competent*) which corresponds to a densification of the dermis. This step corresponds to the transition between the white area and the green area in Figure 1.1.
2. *Emergence of feather follicles in the competent area :* Then, in a second step, the linear instability of the point $(1,u_s,v_s)$ leads to the emergence of spatial patterns corresponding to the formation of feather buds. This step corresponds to the transition between the green area and the yellow area in Figure 1.1.

For the model (1.5), the competence wave is intrinsic to our model. Note that, in many other works, this primary wave is modeled by a wave of competence completely external to the system [80, 98]. More specifically, according to our numerical simulations, this wave of competence closely

approximates the solution of the Fisher-KPP scalar equation

$$\partial_t n = D_n \Delta n + \alpha_n n(1-n), \tag{1.6}$$

corresponding to equation (1.1) in the case $u = 0$.

This famous equation has been extensively studied [59, 60], and it has been shown that the critical speed is given by $c_{\text{comp}} = 2\sqrt{D_n \alpha_n}$. So, according to our numerical simulations, this competence wave depends solely on dermal densification and the speed is independent of the morphogens u and v.

To study pattern formation in a competent area, we conduct a linear analysis, as well as a weakly nonlinear analysis (WNL) (see for example [13, 12, 87, 70]) to approximate the spatiotemporal evolution of the pattern envelope in a competent area. More precisely, this approximation of the envelope is characterized by the real following Ginzburg-Laudau equation,

$$\partial_T A(X,T) = \nu \partial_{XX} A(X,T) + \sigma A(X,T) - L A^3(X,T). \tag{1.7}$$

Defined on another scale of time and space $X = \epsilon x$ and $T = \epsilon^2 t$ where the constant $\epsilon > 0$ represents the distance to the Turing bifurcation. When $L > 0$, this weakly nonlinear analysis method proves to be highly relevant close to the bifurcation ($\epsilon \approx 0$) and loses precision as one moves away from this critical bifurcation. The parameters ν, σ, and L depend on the parameters of the system (1.5) and are given respectively by the formulas (B.33), (B.34), and (B.35). The study of equation (1.7) allows us to determine the emergence speed of follicles in a competent dermal tissue, which is given by the formula $c_{\text{nat}} = 2\epsilon\sqrt{\nu\sigma}$, and we will refer to this speed as the *natural speed of patterns*. Unlike the competence wave, the species u and v play an important role in the emergence speed of patterns in a competent area.

Finally, we are interested in the interaction between these two distinct processes, particularly how the competence wave can influence pattern formation and conversely, whether pattern formation can accelerate or slow down the speed of the competence wave. First, when the natural speed of patterns (c_{nat}) is greater than the speed of the competence wave (c_{comp}), pattern emergence will catch up with the competence wave front and "lock" to it without impacting it. In other words, after a certain time, in this case, the speed of the appearance of the patterns is equal to the speed of the primary wave. In the opposite case, the competence wave does not seem to impact the speed of pattern propagation, and consequently, the emergence speed of feather follicles aligns with the the natural speed of patterns. Therefore, the actual speed of feather follicle emergence may either be solely dictated by dermal condensation ($c_{\text{pattern}} = c_{\text{comp}}$) or depend on the complex interactions between dermal cells and the proteins FGF and BMP ($c_{\text{pattern}} \approx c_{\text{nat}}$). The combination of these two cases gives us a very accurate approximation of the speed of appearance of the patterns, given by the following formula

$$c_{\text{pattern}} \approx \min(2\sqrt{\alpha_n D_n}, 2\epsilon\sqrt{\sigma\nu}) = \begin{cases} c_{\text{comp}} = 2\sqrt{\alpha_n D_n}, & \text{if } c_{\text{nat}} > c_{\text{comp}}, \\ c_{\text{nat}} = 2\epsilon\sqrt{\sigma\nu}, & \text{otherwise.} \end{cases} \tag{1.8}$$

This article is structured as follows. In Section 2, we conduct both linear stability analysis and weakly nonlinear analysis to investigate pattern formation within a competent zone. Additionally, we compare theoretical predictions obtained with numerical simulations. Section 3 is dedicated to the

numerical study of the competence wave and its interaction with pattern emergence speed. We perform numerous numerical simulations to propose an approximation of the feather follicle emergence speed in an initially naive tissue.

1.2 Emergence of feathers in a competent area

1.2.1 Linear analysis

The linear analysis of the equilibrium $(0, 0, 0)$ can be found in [75], this point is always unstable. In this work, we perform a linear analysis of the positive equilibrium point $(1, u_s, v_s)$. This analysis is presented in Appendix A. More precisely, we are interested in the occurrence of a Turing bifurcation. Specifically, we describe a method to determine the critical value κ_c, such that for all $\kappa > \kappa_c$, the equilibrium point $(1, u_s, v_s)$, which is stable without chemotaxis and diffusion, becomes unstable.

However, the chemotaxis term, κ, is not necessarily required for pattern formation. Indeed, under the assumption $\kappa = 0$, we can find parameter values for which we can observe a Turing instability driven solely by the diffusion coefficients. Nevertheless, chemotaxis greatly facilitates the emergence of patterns. Specifically, an increase in the chemotaxis value, leads to a significant increase in the zone of parameter values where the positive equilibrium point $(1, u_s, v_s)$ exhibits a Turing-type instability [99].

Chemotaxis also plays an important role in the spatial regularity of the stationary pattern. In the article [99], the authors showed that increasing chemotaxis tends to greatly reduce the regularity of the stationary pattern. This loss of regularity can take various forms, such as irregularities in the periodicity of buds, fusion of plumage buds, the appearance of ectopic buds, etc. The regularity of the arrangement of feather follicles in birds varies greatly between species, ranging from low regularity (common ostrich, emu) to nearly perfect regularity (zebra finch, penguin) [100]. However, in bird species with a sequential wave of follicle emergence (e.g. zebra finch, japanese quail, domestic chicken), the arrangement of pterylae is consistently regular. Therefore, in this article, we opt for chemotaxis coefficients close to the critical parameter, that is, $\kappa \gtrsim \kappa_c$, in order to obtain regular stationary patterns.

1.2.2 Weakly nonlinear analysis (WNL)

The study of linear stability is a useful first step in understanding pattern formation, but it provides only a rough indication of the expected results. Through linear analysis, we determine the conditions on the system parameters required to obtain patterns, and also their frequencies. However, these solutions that grow exponentially according to linear theory do not have physical significance. To predict the amplitude and shape of the pattern near the bifurcation threshold, nonlinear terms must be included in the analysis.

Since this approach allows us to derive explicit quantitative information linking system parameters and pattern amplitude, it can be extremely useful in comparing theoretical system expectations with biological experiments. The key idea of the weakly nonlinear analysis is that, near the bifurcation value, the pattern evolves on a slow time scale so that, using the multiple scales method, one can

derive an evolutionary equation for the pattern amplitude. In one-dimensional space domains, a real Ginzburg-Landau type amplitude equation is obtained, which theoretically admits travelling wave type solutions for which the critical speed and the steepness of the wave can be theoretically calculated. Similar work has been conducted for various models related to the system (1.5), such as nonlinear reaction-diffusion systems [12, 70], with cross-diffusion terms [13, 33, 20, 73, 101], and for volume-filling chemotaxis model [87, 102, 103].

The application of the weakly nonlinear analysis method is detailed in Appendix B. In this section, we summarize the idea of this method. We begin by translating the uniform steady state to the origin, by setting

$$(\tilde{n}, \tilde{u}, \tilde{v}) = (n-1, u-u_s, v-v_s)\,.$$

To simplify reading, we will omit the tildes and refer to this vector as

$$\mathbf{w} := (\tilde{n}, \tilde{u}, \tilde{v})^T = (n, u, v)^T.$$

Therefore the system (1.5) can be rewritten as the combination of a linear term and a nonlinear term

$$\partial_t \mathbf{w} = \mathcal{L}\mathbf{w} + \mathcal{B}(\mathbf{w}, \mathbf{w}), \tag{1.9}$$

where, the linear part $\mathcal{L}$ is defined by

$$\mathcal{L} = J + D^\kappa \partial_{xx}, \quad \text{with} \quad J := \begin{pmatrix} -\alpha_n & 0 & 0 \\ \delta_u u_s & \gamma_u - \delta_u & -\gamma_v \\ \delta_v v_s & \eta_u & -\delta_v \end{pmatrix}, \quad D^\kappa := \begin{pmatrix} D_n & -\kappa & 0 \\ 0 & D_u & 0 \\ 0 & 0 & D_v \end{pmatrix},$$

and the nonlinear part is given by

$$\mathcal{B}(\mathbf{w}, \mathbf{w}') := \frac{1}{2} \begin{pmatrix} -\kappa \partial_x (n' \partial_x u + n \partial_x u') - 2\alpha_n n' n \\ \gamma_u (n'u + nu') - \gamma_v (n'v + nv') \\ \eta_u (n'u + un') \end{pmatrix}.$$

To describe the spatial dynamics of the pattern we introduce a new time slow scale as follows

$$t = \mathcal{T}(T_1, T_2, T_3, \ldots), \quad T_i = \epsilon^i t, \quad i = 1, 2, \ldots\,,$$

and a new space scale by defining the characteristic length scale of spatial modulation ($X = \epsilon x$), where $\epsilon \ll 1$ represents the distance from the Turing bifurcation point and will be detailed mathematically in the Appendix B. Considering these changes in scale, we have

$$\begin{cases} \partial_x \to \partial_x + \epsilon \partial_X, \\ \partial_{xx} \to \partial_{xx} + 2\epsilon \partial_{xX} + \epsilon^2 \partial_{XX}, \\ \partial_t \to \epsilon \partial_{T_1} + \epsilon^2 \partial_{T_2} + \epsilon^3 \partial_{T_3} + \cdots\,. \end{cases} \tag{1.10}$$

Moreover, we expand κ and $\mathbf{w}$ in the small parameter as

$$\begin{cases} \kappa = \kappa_c + \epsilon \kappa_1 + \epsilon^2 \kappa_2 + \epsilon^3 \kappa_3 + \ldots\,, \\ \mathbf{w} = \epsilon \mathbf{w}_1 + \epsilon^2 \mathbf{w}_2 + \epsilon^3 \mathbf{w}_3 + \ldots\,. \end{cases} \tag{1.11}$$

where $\mathbf{w}_i = (n_i, u_i, v_i)^T$. Using the relations (1.10) and (1.11), we expand the linear part and the nonlinear part in terms of powers of ϵ, which yields for fixed f

$$\mathcal{L}(f) = \mathcal{L}^0(f) + \epsilon\mathcal{L}^1(f) + \epsilon^2\mathcal{L}^2(f) + \epsilon^3\mathcal{L}^3(f) + \cdots , \tag{1.12}$$

and,

$$\mathcal{B}(f,g) = \mathcal{B}^0(f,g) + \epsilon\mathcal{B}^1(f,g) + \epsilon^2\mathcal{B}^2(f,g) + \cdots . \tag{1.13}$$

where $(\mathcal{L}^i)_i$ and $(\mathcal{B}^i)_i$ are operators specified in Appendix B. We expand each term of equation (1.9) to identify the terms of each power of ϵ, it gives,

$$\begin{array}{rcccccc}
\partial_t\mathbf{w} = & 0 & +\epsilon.0 & +\epsilon^2\partial_{T_1}\mathbf{w}_1 & +\epsilon^3(\partial_{T_1}\mathbf{w}_2 + \partial_{T_2}\mathbf{w}_1) & +O(\epsilon^3), \\
\mathcal{L}(\mathbf{w}) = & 0 & +\epsilon\mathcal{L}^0(\mathbf{w}_1) & +\epsilon^2\left(\mathcal{L}^0(\mathbf{w}_2) + \mathcal{L}^1(\mathbf{w}_1)\right) & +\epsilon^3\left(\mathcal{L}^0(\mathbf{w}_3) + \mathcal{L}^1(\mathbf{w}_2) + \mathcal{L}^2(\mathbf{w}_1)\right) & +O(\epsilon^3), \\
\mathcal{B}(\mathbf{w},\mathbf{w}) = & 0 & +\epsilon.0 & +\epsilon^2\mathcal{B}^0(\mathbf{w}_1,\mathbf{w}_1) & +\epsilon^3\left(2\mathcal{B}^0(\mathbf{w}_1,\mathbf{w}_2) + \mathcal{B}^1(\mathbf{w}_1,\mathbf{w}_1)\right) & +O(\epsilon^3).
\end{array}$$

Therefore, to ensure a matching up to order 3, one needs to solve for $\mathbf{w}_{1,2,3}$ the system

$$0 = \mathcal{L}^0(\mathbf{w}_1) + 0, \tag{1.14}$$

$$\partial_{T_1}\mathbf{w}_1 = \left(\mathcal{L}^0(\mathbf{w}_2) + \mathcal{L}^1(\mathbf{w}_1)\right) + \mathcal{B}^0(\mathbf{w}_1,\mathbf{w}_1), \tag{1.15}$$

$$(\partial_{T_1}\mathbf{w}_2 + \partial_{T_2}\mathbf{w}_1) = \left(\mathcal{L}^0(\mathbf{w}_3) + \mathcal{L}^1(\mathbf{w}_2) + \mathcal{L}^2(\mathbf{w}_1)\right) + \left(2\mathcal{B}^0(\mathbf{w}_1,\mathbf{w}_2) + \mathcal{B}^1(\mathbf{w}_1,\mathbf{w}_1)\right). \tag{1.16}$$

At $O(\epsilon)$ we recover the linear problem $\mathcal{L}^0(\mathbf{w}_1) = 0$, whose solution satisfying the Neumann boundary conditions is

$$\mathbf{w}_1 = A(T_1, T_2, \ldots; X)\rho\cos(k_c x), \tag{1.17}$$

where k_c corresponds to the first and unique unstable mode and $A(T_1, T_2, \ldots; X)$ is the spatial amplitude of the pattern. The vector ρ is derived in the appendix B and given by the relation (B.25).

At $O(\epsilon^2)$, we combine formula (1.17) and the Fredholm alternative to determine the following equalities.

$$T_1 = 0, \qquad \kappa_1 = 0,$$

as well as the definition of the vector $\mathbf{w}_2$, defined as follows

$$\mathbf{w}_2 = A^2\mathbf{w}_{20} + A^2\mathbf{w}_{22}\cos(2k_c x) + \frac{\partial A}{\partial X}\mathbf{w}_{21}\sin(k_c x), \tag{1.18}$$

where $\mathbf{w}_{2i}$, $i = 0, 1, 2$, are the solutions of the system (B.32).

Finally, at $O(\epsilon^3)$, using the solvability condition and equality (1.18), one finds the following real Ginzburg-Landau equation for the amplitude A,

$$\partial_{T_2}A = \nu\partial_{XX}A + \sigma A - LA^3.$$

where the parameters ν, σ and L are given by the equations (B.33), (B.34) and (B.35) respectively. Since the growth rate coefficient σ is always positive, the dynamics of the real Ginzburg-Landau

equation (1.7) can be divided into two different cases depending on the sign of the constant L : the supercritical case, when L is positive, and the subcritical case, when L is negative.

When $L < 0$ the real Ginzburg-Landau equation (1.7) is not able to capture the amplitude of the pattern. Therefore, it's necessary to push the weakly nonlinear expansion up to order five. However, in this case, the actual expected amplitude, ϵA, is of order $O(1)$ [73]. Therefore, the approximation proposed by the weakly nonlinear analysis generally does not match the asymptotic solutions. This lack of precision has been observed in many articles (e.g., [13, 103, 73]). Moreover when we add the slow modulation in space, the equation obtained at order 5 is very complex [102] and, to our knowledge, there is no work concerning the theoretical existence of a positive traveling wave for this kind of equation. Therefore, in the following we will only be interested in the case where L is positive.

Conclusion of the weakly nonlinear analysis To sum up, the asymptotic expression for the spatial pattern of (1.5), when $L > 0$, is given by

$$\begin{pmatrix} n \\ u \\ v \end{pmatrix} = \begin{pmatrix} 1 \\ u_s \\ v_s \end{pmatrix} + \epsilon A(\epsilon x, \epsilon^2 t)\rho \cos(k_c x) + O(\epsilon^2), \tag{1.19}$$

where the amplitude A is the solution of the Eq. (1.7).

Expected stationary patterns. The Eq. (1.7) admits two nonnegatives points equilibrium, the unstable point $A = 0$ and the stable positive point $A_\infty := \sqrt{\sigma/L}$. This equilibrium point is globally asymptotically stable and we thus have $\lim_{T_2 \to +\infty} A(X, T_2) = A_\infty$ for all X. Therefore the weakly nonlinear analysis, at order 3, gives us the following approximation for the final stationary pattern

$$\begin{pmatrix} n(x) \\ u(x) \\ v(x) \end{pmatrix} = \begin{pmatrix} 1 \\ u_s \\ v_s \end{pmatrix} + \epsilon A_\infty \rho \cos(k_c x) + \epsilon^2 A_\infty^2 \left(\mathbf{w}_{20} + \mathbf{w}_{22} \cos(2k_c x)\right) + O(\epsilon^3). \tag{1.20}$$

Expected speed of pattern spread. It is well known from the literature that, for L positive, the equation (1.7) admits traveling wave type solutions connecting 0 to A_∞. The associated critical speed, denoted $c^\star_{\mathrm{WNL}}$, is given by $c^\star_{\mathrm{WNL}} := 2\sqrt{\nu\sigma}$ [63]. For an initial condition with finite initial support, the selected speed corresponds to the critical speed [60]. For $c = c^\star_{\mathrm{WNL}}$ the steepness of the front, denoted $\mu^\star$, is given by, $\mu^\star = \sqrt{\sigma/\nu}$.

Note that the speed $c^\star_{\mathrm{WNL}}$ correspond to the pattern emergence speed in the slow scale. To obtain the emergence speed of follicles in the correct scale, we must multiply it by ϵ, resulting in,

$$c_{\mathrm{nat}} = \epsilon c^\star_{\mathrm{WNL}} = 2\epsilon\sqrt{\nu\sigma}.$$

1.2.3 Expected stationary patterns

When ϵ is small enough, we can see in the figure 1.2A that the approximation (1.20) predicted by the weakly nonlinear analysis is very accurate. The dashed red line corresponding to the approximation (1.20), while the black line corresponds to a solution of the equation (1.5), obtained using a numerical

simulation. Similarly, for $\epsilon = 0.3$, we notice that the analysis remains quite close to the numerical solution (Fig. 1.2B below). We have also computed the bifurcation diagram of model (1.5), shown in Figure 1.2C, using the `Matlab` package `pde2path` [104, 105]. The code is adapted from the codes presented in the tutorial [106]. In Figure 1.2C we also plot, in red, the prediction given by weakly nonlinear analysis (1.20). The bifurcation diagram validates both the numerical simulations in Figure 1.2A-B and the accuracy of the weakly nonlinear analysis.

1.2.4 Expected speed of pattern spread in a competent area

In Figure 1.3 we compare over time the result of the weakly nonlinear analysis (dashed red line) with the numerical solution of the system (1.5) (black line) for a small ϵ ($\epsilon = 0.05$). The initial amplitude chosen is given by $A_0(X) = A_\infty.\mathbf{1}_{|X|\leq K}$ with K some positive constant. For this initial data, it is known that the speed of the wave corresponds to the critical speed $c^\star_{\text{WNL}}$ [60]. The approximation obtained by the weakly nonlinear analysis closely matches the numerical results.

In Figure 1.14, we again compare the numerical solution of the system (1.5) (black line) with the prediction of the weakly nonlinear analysis (blue dashed line), but this time for $\epsilon = 0.2$. As expected, the analysis loses precision, however the approximation of the speed of pattern emergence is still very precise. More particularly we notice an overshoot phenomenon, when the inhomogeneity appears it tends to increase very quickly up to a certain maximum then will decrease towards a stationary amplitude quite close to the amplitude predicted by the weakly nonlinear analysis, ϵA_∞. In other words, far enough from the Turing bifurcation, the amplitude wavefront becomes non-monotonic.

1.2.5 Influence of parameter values on pattern formation

In this section we are interested in the impact of the different parameters on the values of interest of our problem which are : the final stationary amplitude of the pattern A_∞, the critical speed of the emergence of the patterns $c^\star_{\text{WNL}}$ as well as the steepness of the front $\mu^\star$. The variation of a parameter affects these values in two ways, firstly it directly influences the variables σ, L and ν defined explicitly in terms of the system parameters (1.5) ; moreover, the variation of a parameter, also impacts critical value κ_c and the eigenvalues. We only focus in the impact of the system parameters (1.5) on the variables σ, L and ν. Therefore for each variation of parameter values, we recalculate κ_c again.

Influence of parameters on critical speed, $c^\star_{\text{WNL}}$, and on the steepness of the amplitude front, $\mu^\star$. The critical speed $c^\star_{\text{WNL}} := 2\sqrt{\sigma\nu}$, of the traveling wave type solutions for the equation (1.7), obtained following the analysis weakly nonlinear, is dependent on the parameters σ and ν, themselves dependent on the parameters of the system (1.5). In the figure 1.11, we are interested in the influence of the different parameters of the system (1.5) on the critical speed $c^\star_{\text{WNL}}$. The increase of the diffusion coefficient D_n leads to a faster critical speed, this growth is initially exponential and then goes almost to zero. The influence of the coefficients D_u and D_v is ambivalent. Indeed, the critical speed increases when the diffusion coefficient D_u also increases. Conversely, the speed decreases as the coefficient D_v increases. The impact of the α_n parameter on the critical speed $c^\star_{\text{WNL}}$ is very small compared to the strong variations of the parameter. The influence of the parameters γ_u, γ_v and η_u

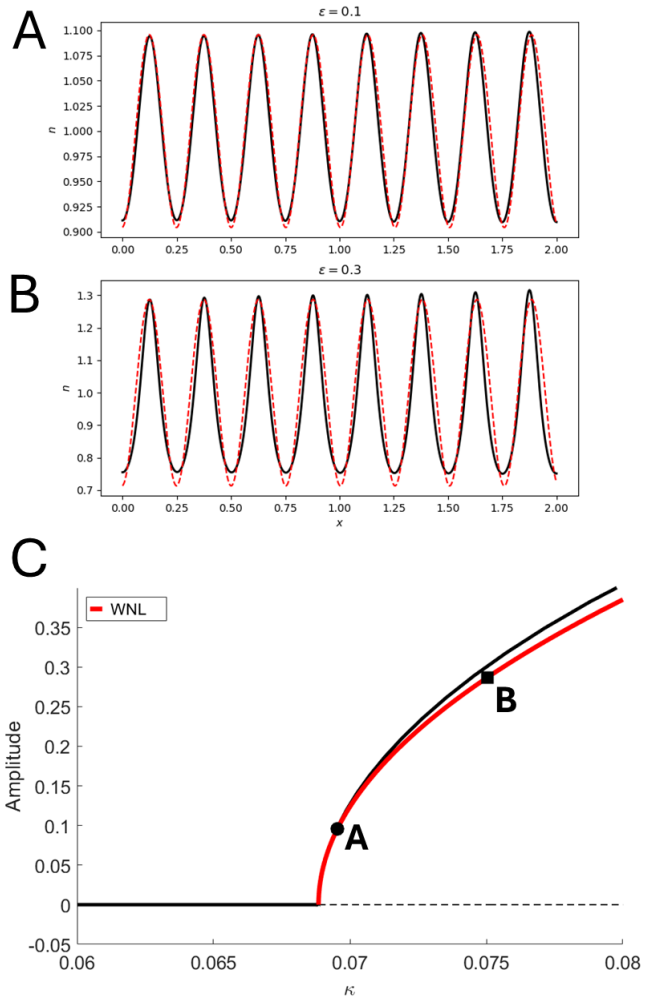

FIGURE 1.2 – **Expected stationary patterns.** *A-B.* Comparison between the weakly nonlinear approximation (1.20) (red dashed line) and the numerical solution of (1.5) (black solid line). *A.* $\epsilon = 0.1$. *B.* $\epsilon = 0.3$. *C.* Comparison of the bifurcation diagram obtained with `pde2path` (black curve) and the prediction obtained using the weakly nonlinear analysis (1.20) (red curve). The dotted line corresponds to the equilibrium point becoming unstable following a super-critical Turing bifurcation. The black circle corresponds to $\epsilon = 0.1$ (A.) and the black square to $\epsilon = 0.3$ (B.). Parameter values are : $D_n = 0.1$, $D_u = 6\text{e} - 3$, $Dv = 0.13$, $\gamma_u = 15.539$, $\gamma_v = 0.01$, $\eta_u = 3931$, $c_u = 2.9672$, $c_v = -1104$ and $\alpha_n = 0.5$.

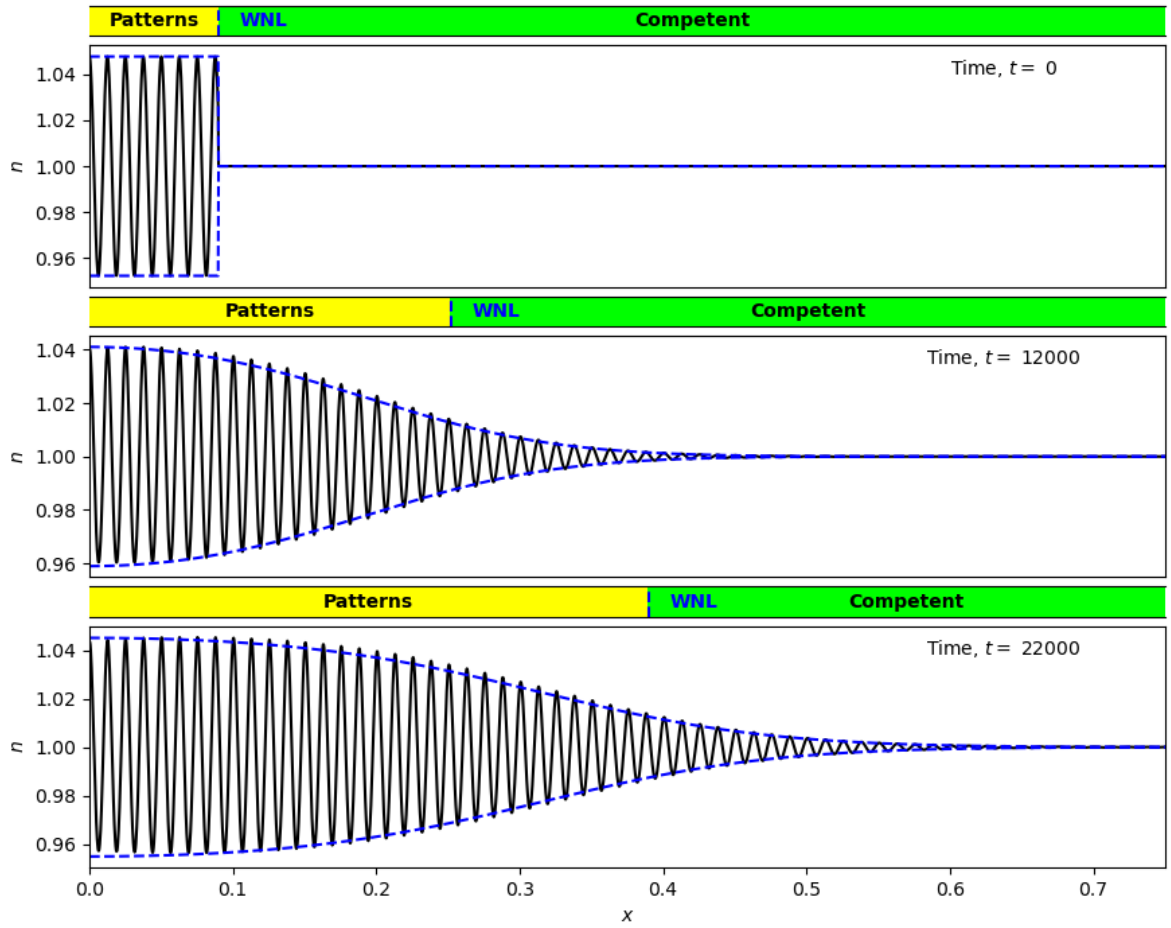

FIGURE 1.3 – **Comparison between the solution of the equation** (1.7) **(blue dashed line) and the numerical solution of** (1.5) **(black solid line) at different times.** The panels above the figures respectively represent the competent zone (green), the zone where patterns are present (yellow), and the prediction of the weakly nonlinear analysis (blue dashed line). Parameter values are given by : $D_n = 7\mathrm{e}-5$, $D_u = 6\mathrm{e}-3$, $Dv = 0.13$, $\gamma_u = 14.5389$, $\gamma_v = 0.099932$, $\eta_u = 3931$, $c_u = 2.9672$, $c_v = -1104$, $\alpha_n = 0.001$ and $\epsilon = 0.05$.

is quite similar : the speed of emergence of the patterns increases as the parameter value increases. Concerning the parameter δ_v, the speed $c^\star_{\mathrm{WNL}}$ decreases linearly. Finally, for the parameter γ_u, it has the opposite effect of its counterpart, γ_v.

A similar work for the steepness of the propagation front is illustrated in Figure 1.12. For the parameters D_v, δ_u, δ_v, γ_u, γ_v and η_u, their influence on the steepness is similar to their influence on the speed of the wave, $c^\star_{\mathrm{WNL}}$. Conversely, the variation of the parameter D_n has the opposite effect than its impact on the critical speed. For the proliferation parameter α_n, we notice that the front steepness is proportional to it. Concerning the parameter D_v, it is more difficult to draw conclusions, when D_v increases the steepness is initially increased then it decreases.

Influence of parameters on stationary amplitude, A_∞. In the same way, we study the influence of the parameters on the final amplitude of the spatial patterns. In the case $L > 0$, the final amplitude is given by $A_\infty = \sqrt{\sigma/L}$, with σ and L defined respectively by (B.34) and (B.35). We illustrate in figure 1.13, the impact of each parameter of the system (1.5) on the value of A_∞.

For this work, we have chosen to study the parameters γ_u, γ_v and η_u directly. By definition (1) we can also deduce the impact of the parameters used in the system (1.1)-(1.3) defined in the article [75]. For example, a variation of the α_u parameter would impact both the γ_u term and the γ_v term and thus have a particular influence on the critical speed or on the steepness. However, as stated before, the system (1.1)-(1.3) is not based on a biological interpretation, so we only focus on our simplified model (1.5), which is, in a certain sense, more general.

1.3 Competence wave followed by the emergence of feather follicles

In the previous section, we showed that weakly nonlinear analysis, sufficiently close enough to the bifurcation, accurately predicts the behavior of solutions of system (1.5) when initialized near the unstable equilibrium point $(1, u_s, v_s)$, that is, when the tissue is assumed to be already competent. In this section, we focus on the impact of having an initially mostly naive tissue, with low or even null quantity of cells and proteins. In other words, mathematically, we study the impact of taking initial data with finite support on the speed of pattern emergence. More precisely, we are interested in a two-step process, first a wave connecting $(0, 0, 0)$ to $(1, u_s, v_s)$, corresponding to a *wave of competence*, and then, in the wake of this primary wave, the emergence of patterns around this unstable point, corresponding to *the emergence of feather follicles.*

1.3.1 Competence wave

First of all, we are interested in the competence wave. Numerically, we notice that the system (1.5) numerically admits traveling wave solutions connecting the null point to the equilibrium point $(1, u_s, v_s)$. First we derive the linear spreading speed of the system (1.5). In our case, the linearization decouples the system and the linearized system shares the same linear part as the Fisher-KPP scalar

equation,

$$\partial_t n = D_n \Delta n + \alpha_n n(1-n).$$

For this equation, it is known that traveling wave type solutions have the critical speed $c_{\text{comp}} := 2\sqrt{D_n \alpha_n}$, which therefore corresponds to the linear spreading speed of the system (1.5). Even if the linear speed is often a good prediction of the nonlinear speed, theoretically it can be different [107]. Numerically, for the different parameter values tested, the nonlinear speed seems always equal to the linear spreading speed, and this, for the different cases described just below. However, due to the large number of parameters and the difficulty of accurately approximating speed of a traveling wave, it is possible that the nonlinear speed may differ from the linear speed for some untested parameter areas. When nonlinear speed corresponds to linear speed, the traveling wave is caused by the spread of cells and more particularly by the diffusion term and by the proliferation term in the first equation of the system (1.5). Conversely, chemotaxis has not impact on the speed of competence wave.

The equilibrium point $(1, u_s, v_s)$ can be linearly stable or unstable. In the case where this equilibrium point does not admit Turing instability, we notice that this system numerically admits a traveling wave type solution with a speed and a front very close to the solution of the Fisher-KPP equation (1.6). This result is represented in the figure 1.4 in which the black lines correspond to the numerical solution n of the system (1.5) at differents times and the red line represents the numerical solution of the associated Fisher-KPP equation (1.6). For both simulations we take the same initial condition which is represented in the top panel. For this type of initial data, the selected speed of the traveling wave solution of the associated Fisher-KPP equation (1.6), corresponds the critical Fisher-KPP speed [60].

1.3.2 Competence wave and the natural speed of patterns

When the point $(1, u_s, v_s)$ is unstable, the solutions become more complex as a heterogenous pattern now forms in the wake of the competence wave. In this case, the space is structured into three distinct zones. The first zone corresponds to an area where feather buds are well established, mathematically it corresponds to a zone where patterns are present and well-defined. The second zone is an intermediate area, corresponding both to tissue that has just become competent and to tissue where aggregates are beginning to form. As we shall see, this zone may be small in size or even non-existent. The third zone corresponds to naive tissue, in which dermal cells are sparse, this zone is mathematically defined by $\{x : \ n(t,x) < 1/2, \ x \in \Omega\}$. Assuming that these two processes occur independently, we know that the speed of the first stage, the competence wave (transition between naive and competent tissue), is given by c_{comp}. The second stage, corresponding to the natural emergence of patterns in a competent zone (transition between the "Patterns" zone and the "Competent" zone), occurs at a speed c_{nat}, predicted by weakly nonlinear analysis. In this case, there are two possible scenarios : either the speed c_{comp} is greater than the speed c_{nat}, or the opposite. We discuss these two possibilities below.

Competence wave slower than the natural speed of patterns. When the speed predicted by the weakly nonlinear analysis, denoted c_{nat}, is, greater than the speed c_{comp}, the spread of the patterns will "lock" with the primary competence wave. Indeed, as we can see in the figure 1.6, the speed of

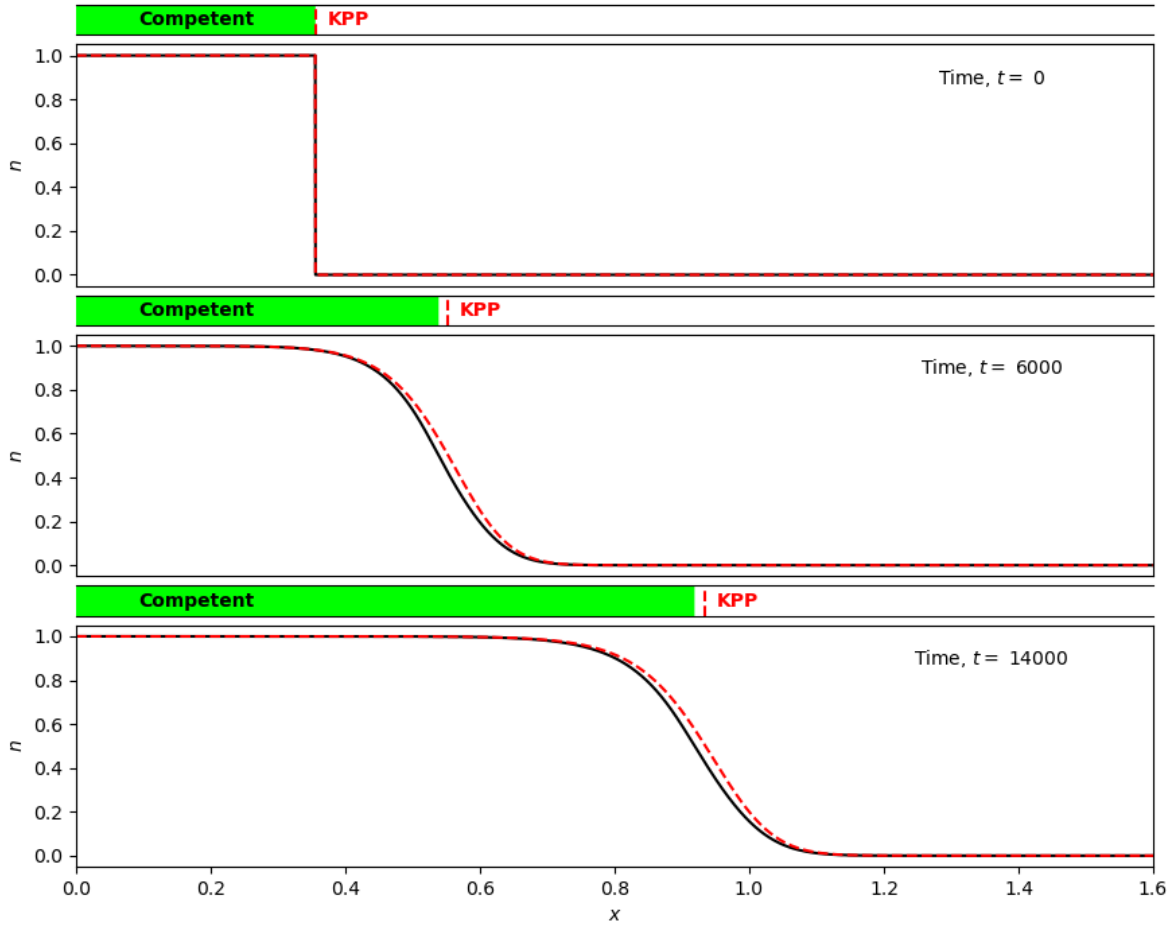

FIGURE 1.4 – **Competence wave.** Numerical simulation of the system (1.5) (black line) and of the associated Fisher-KPP equation (1.6) (red dashed line) when the equilibrium point $(1, u_s, v_s)$ is stable. The panels above the figures represent the competent zone (in green) and the propagation of the solution to the Fisher-KPP equation (red dashed line). Parameter values are given by : $D_n = 7\text{e}{-5}$, $D_u = 6\text{e}{-3}$, $Dv = 0.13$, $\gamma_u = 14.5389$, $\gamma_v = 0.099932$, $\eta_u = 3931$, $c_u = 2.9672$, $c_v = -1104$, $\alpha_n = 0.001$ and $\kappa = 4.84\text{e} - 5 < \kappa_c$.

pattern emergence of the numerical solution of the system (1.5) (curve in black), will correspond to the speed of the primary wave connecting $n = 0$ to $n = 1$, itself very close to the speed of the solution of the associated Fisher-KPP equation (1.6) represented in red dashed line in the figure 1.6. Consequently, the fact that the natural speed is greater will not affect the speed of the competence wave. In this case, the competence zone will remain constant and small in size throughout the simulation. This phenomenon is also illustrated in the top kymograph of Figure 1.7. The gray color intensity represents the density of cells, n. The dashed red line corresponds to the theoretical speed of the Fisher-KPP equation. In this figure, we notice that the pattern emergence perfectly aligns with this speed. Numerically, we can conclude that, in this case, $c_{\text{pattern}} \approx c_{\text{comp}} < c_{\text{nat}}$. We tried for several sets of parameter values and the behavior was always similar.

We have also studied a system similar to the system (1.5), where dermal cell proliferation is now given by the growth term $\alpha_n n(1-n)(1+an)$, with $a \in [-1, +\infty[$. The equation associated with this system sharing the same travelling wave of competence is given by the following scalar equation

$$\partial_t n = D_n \Delta n + \alpha_n n(1-n)(1+an). \tag{1.21}$$

This equation has also been extensively studied and the critical speed has been derived explicitly. For this slightly modified system, we notice again the "locking" phenomenon for the different sets of parameters tested. Note that we have tested for different values a, notably for large a for which the associated Fisher-KPP equation, called also Nagumo equation, admits pushed fronts [63].

Competence wave faster than the natural speed of patterns. Concerning the opposite case, i.e. when the primary wave is faster than the speed of emergence of the patterns, the result is quite different. Indeed, as we can see in the figure 1.6, the speed of appearance of the patterns will be almost similar to that predicted by the weakly nonlinear analysis. The black curve corresponds to the numerical simulation of the system (1.5), for three different times. The curves in blue correspond to the theoretical envelope calculated using the equation (1.7) given by the weakly nonlinear analysis. In this simulation, the choice of the initial condition can create a certain delay between the amplitude predicted by the weakly nonlinear analysis and the actual amplitude of the patterns. Therefore, we illustrate the solution with a certain delay, similar for the 3 sub-figures, $A(t_i + T)$, with $T = 9000$. The red curve corresponds to the numerical solution of the Fisher-KPP equation associated with our problem. Again we notice that the first wave connecting $(0, 0, 0)$ to $(1, u_s, v_s)$ is very close to the wave of the Fisher-KPP equation associated with our system, and we also notice that the weakly nonlinear analysis describes very precisely the installation of patterns in the wake of this primary wave. In this scenario, since the competence speed is faster, the competent zone will continue to grow, mathematically corresponding to the formation of a "terrace". Furthermore, this competence wave has absolutely no impact on the pattern installation speed. These conclusions are also confirmed in the lower kymograph of Figure 1.7.

Influence of parameter values α_n and D_n on the speed of feather follicle emergence. The parameters α_n and D_n are crucial as they influence both critical speeds c_{comp} and c_{nat}. In Figure 1.8, we plot the influence of parameters value D_n and α_n on the two theoretical critical speeds. The

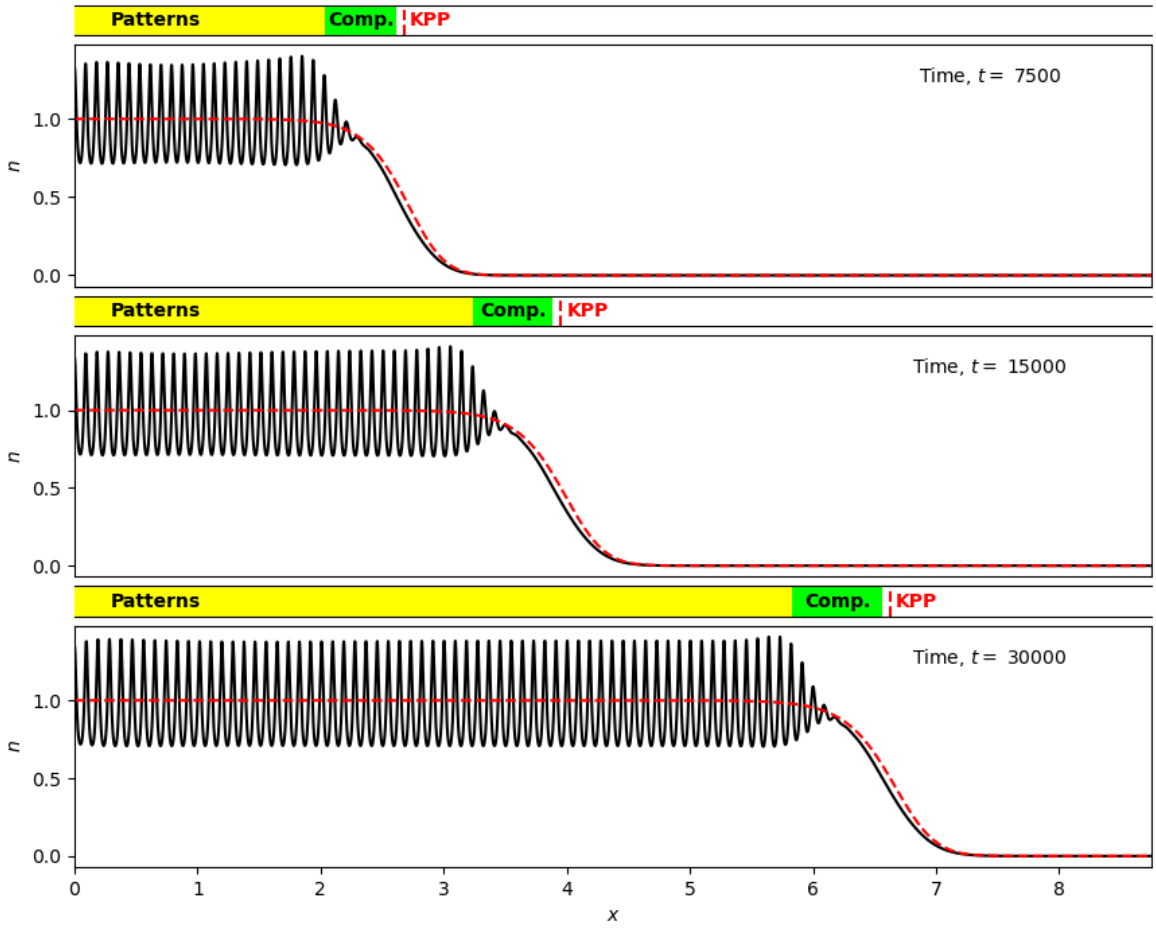

FIGURE 1.5 – **Competence wave slower than the natural speed of patterns.** Numerical simulation of the system (1.5) (black line) and of the associated model (1.6) (red dashed line) when the point $(1, u_s, v_s)$ is unstable and when $c_{\text{comp}} < c_{\text{nat}}$. The panels above the figures show the patterns/competence areas (green/yellow) and the propagation of the solution to the Fisher-KPP equation (red dotted line). Parameter values are given by : $\epsilon = 0.3$, $D_n = 7\text{e}-5$, $D_u = 6\text{e}-3$, $D_v = 0.13$, $\gamma_u = 14.5389$, $\gamma_v = 0.099932$, $\eta_u = 3931$, $c_u = 2.9672$, $c_v = -1104$, $\alpha_n = 0.001$.

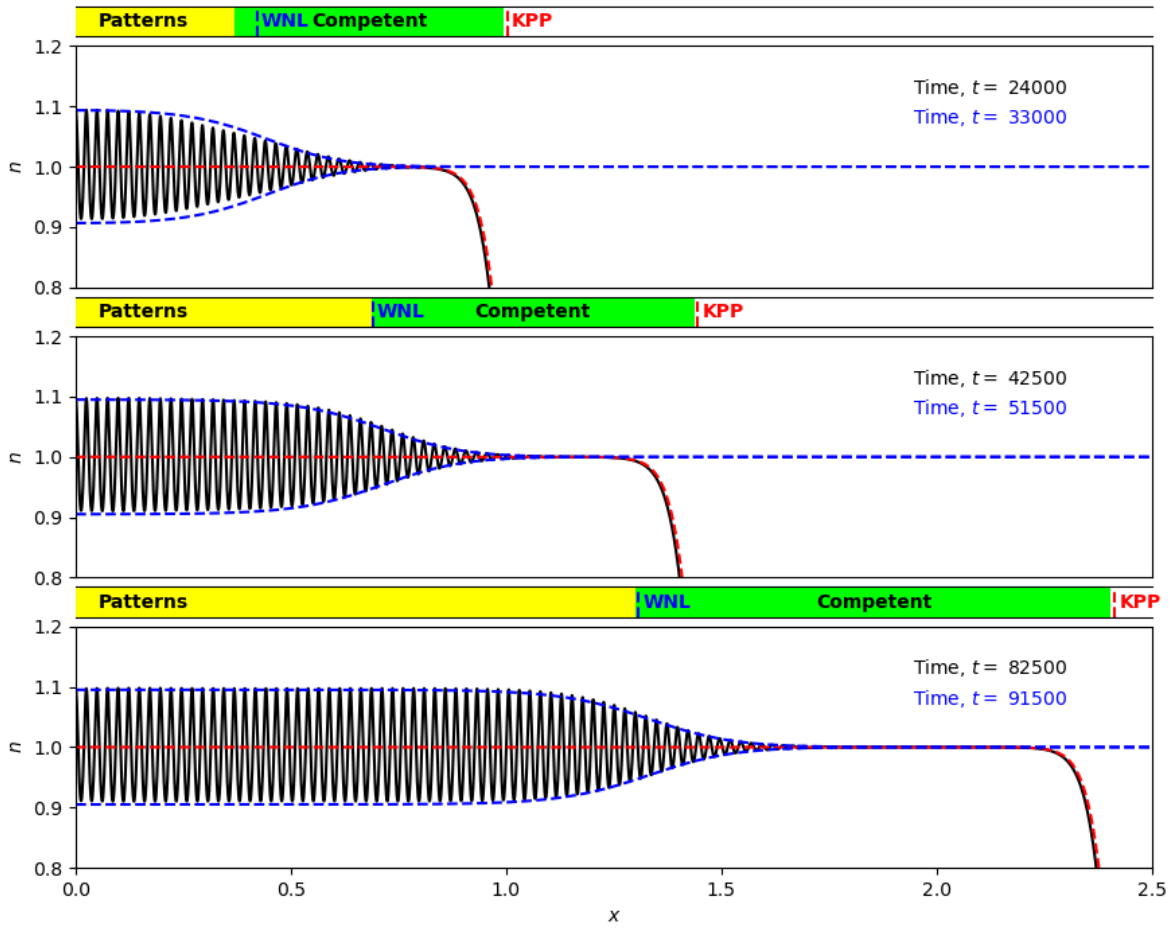

FIGURE 1.6 – **Competence wave faster than the natural speed of patterns.** Numerical simulation of the system (1.5) (black line) and of the associated model (1.6) (red dashed line) when the point $(1, u_s, v_s)$ is unstable and when $c_{\text{comp}} \geq c_{\text{nat}}$. The blue curve corresponds to the approximation (1.19) obtained using the weakly nonlinear analysis, with a similar time delay for the 3 figures. The panels above the figures show the patterns/competence areas (green/yellow), the propagation of the solution to the Fisher-KPP equation (red dotted line) and the propagation of the approximate envelope (blue dotted line). Parameter values are given by : $D_n = 7\text{e}-5$, $D_u = 6\text{e}-3$, $D_v = 0.13$, $\gamma_u = 14.5389$, $\gamma_v = 0.099932$, $\eta_u = 3931$, $c_u = 2.9672$, $c_v = -1104$, $\alpha_n = 0.001$ and $\kappa = 4.9\text{e}-5$.

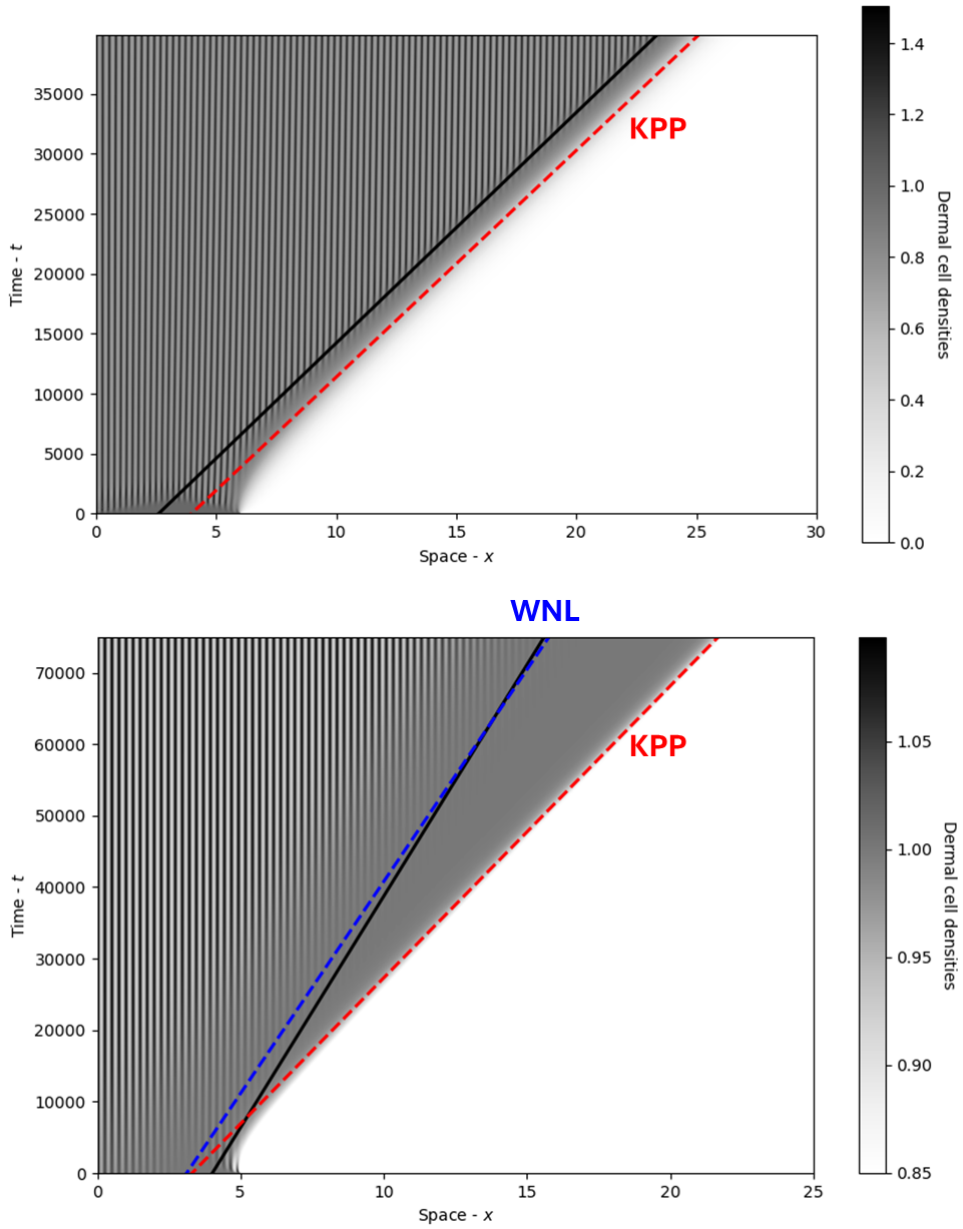

FIGURE 1.7 – **Density plot of n of the numerical solution to the system** (1.5) **when $c_{\mathbf{nat}} > c_{\mathbf{comp}}$ (*Top*) and when $c_{\mathbf{nat}} < c_{\mathbf{comp}}$ (*Bottom*).** The dashed red and blue lines correspond respectively to the theoretical speed c_{comp} and c_{nat}. The parameter values are similar to those in Figure 1.5 and 1.6 respectively.

blue curve corresponds to the natural speed, c_{nat}, and the red curve corresponds to the competence wave speed, c_{comp}. The black crosses correspond to the actual speed of pattern installation from the numerical solution of system (1.5). To determine the pattern installation speed, we first identify local maxima associated with the patterns, then interpolate them to obtain an approximate envelope of the patterns. Once this envelope is obtained, we use a scout & spot algorithm to determine its speed over time. Instead of directly comparing these approximate values to theoretical speeds, we also illustrate, with colored points, the approximate numerical speeds using a similar algorithm, of travelling wave solutions of the Fisher-KPP equation (1.6) (Red points) and of the envelope equation (1.7) (Blue points). We take care to use the same discretization and simulation time to ensure comparable results. In Figure 1.8, we observe the two previously mentioned possibilities. When the natural speed is faster, the competence wave governs the speed of follicle installation (Bold red curve). Conversely, when the competence wave speed is faster, the speed of follicle installation corresponds to the natural emergence speed of the pattern (Bold blue curve).

1.4 Conclusion

In conclusion, based on our theoretical and numerical work on a general model inspired by the article [75], we propose an approximation of the speed of emergence of feather follicles. Specifically, two possibilities arise. If the competence wave is slow compared to the natural emergence speed of feather buds, these buds will invade the competent zone and synchronize with the competence wave. Consequently, in this scenario, the speed is solely determined by the dermal densification, which mathematically corresponds to the speed $c_{\text{comp}} = 2\sqrt{D_n \alpha_n}$, with D_n being the diffusion coefficient and α_n the dermal cell proliferation rate. Conversely, when the competence wave is faster than the natural speed, it no longer directly impacts the speed of pattern emergence. This is akin to studying pattern emergence within a competent zone. To accomplish this, we opt for a weakly non-linear analysis, which allows us to obtain, under certain conditions, a precise approximation of the envelope. Specifically, it is necessary for the parameter L to be positive (supercritical case) and to be sufficiently close to the critical bifurcation. The envelope equation (1.7) admits travelling wave solutions that have a critical speed $c_{\text{nat}} = 2\sqrt{\epsilon\nu\sigma}$, denoted as the natural emergence speed of patterns, where ν and σ are defined by the equalities (B.33) and (B.34) while ϵ represents the proximity with respect to the Turing bifurcation. By combining these two possibilities, we derive the speed of feather follicle emergence as given by the following relation $c_{\text{pattern}} \approx \min(2\sqrt{\alpha_n D_n}, 2\epsilon\sqrt{\sigma\nu})$. Although this work is based on modeling feather follicle formation, the theory studied in this article can be adapted to modeling various periodic patterns within other species during embryo development (see, for example, the review [108])

In this article, to determine the speed of follicle formation in the competent zone, we opted for a method based on weakly nonlinear analysis. However, another well-known usable method is based on the marginal stability criterion [39, 40, 55, 64, 65, 66]. Klika, Gaffney, and Maini demonstrated in [70] that, for a system of two reaction-diffusion equations, the application of this method, close to a supercritical bifurcation, predicts the same propagation speed as the weakly nonlinear analysis. However, this marginal stability method does not provide any information about the pattern amplitude

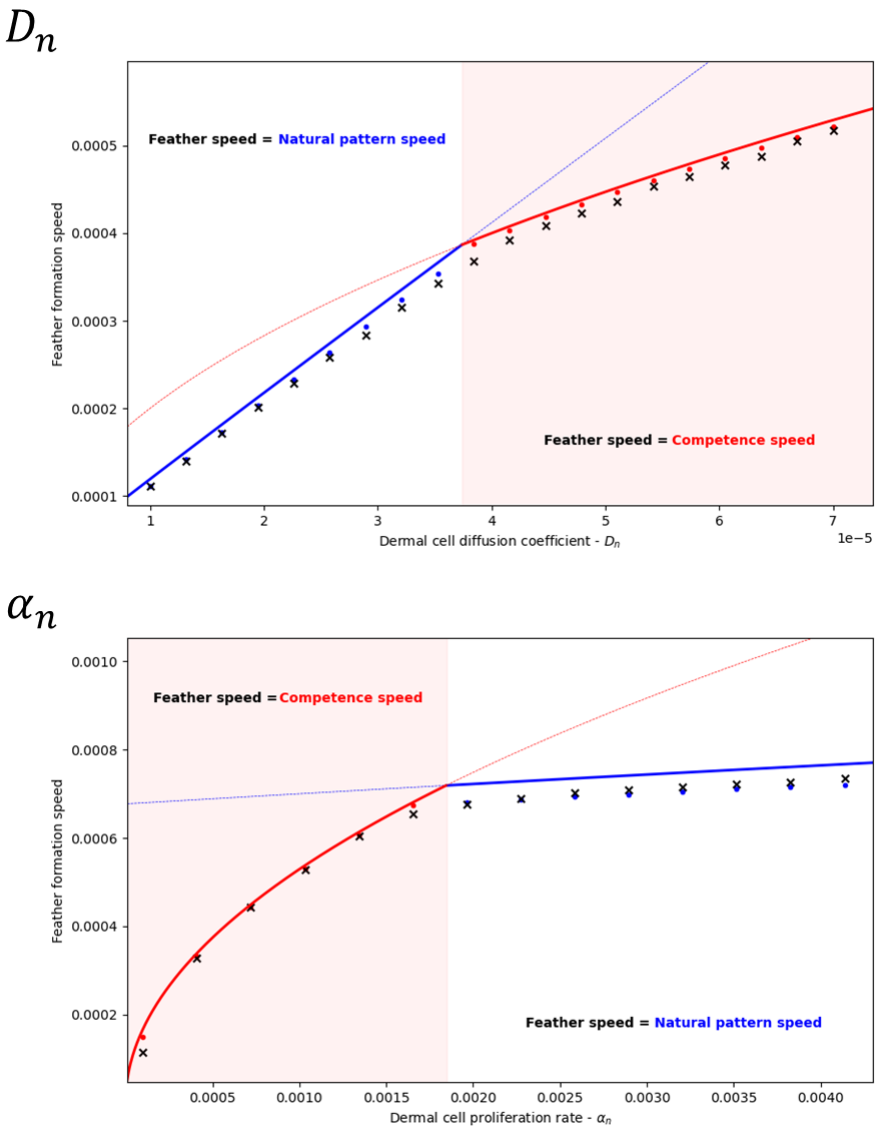

FIGURE 1.8 – **Speed of emergence of patterns (feather follicles) as a function of D_n and α_n.** The lines represent the influence of the diffusion coefficient D_n (*Top*) and the cell proliferation parameter α_n (*Bottom*) on the natural speed c_{nat} (blue) as well as on the competence speed c_{comp} (red). The black crosses correspond to the estimated emergence speed of patterns from numerical simulations of the system (1.5). The colored dots represent the values of speeds calculated numerically, with simulation parameter values similar to the black crosses (same time and space discretization), of travelling waves solutions of the Fisher-KPP equation (1.6) (red) and of the envelope equation (1.7) (blue). The bold solid lines emphasize the selection principle presented in the equality (1.8), $c_{\text{pattern}} = \min(c_{\text{comp}}, c_{\text{nat}})$. The values of other parameters are the same as in Figure 1.2.

or the transient profile of the wave.

Other aspects of the problem can be considered in subsequent works. A first direction we are going to would involve extending the present analysis to the two dimensional setting. When the domain is two dimensional new phenomena appear, such as rhombi, hexagons or mixed-mode patterns ; which can also be predicted by the weakly nonlinear analysis [12, 71, 109, 31, 72].

Another direction of improvement would be to consider the notion of modulated front. A modulated front solution is a front connecting an unstable homogeneous stationary state to a spatially periodic pattern. The first known results of the existence of modulated traveling waves come from the articles of Eckmann, Collet and Wayne [44, 68, 43]. Initially they showed the existence of modulated fronts for the Swift-Hohenberg equation with cubic nonlinearity. Subsequently, many results improved this theory and several models were treated, such as the existence of modulated front for a non-local Fisher equation KPP in the article [51]. Similarly, the theory of a "triggered/quenched front" combining a pattern-forming front with a wave of external competence developed notably by Ryan Goh & Arnd Scheel, could be a useful tool [110, 111, 112, 113, 114].

A Additional information on linear analysis

In this section we shall investigate, for the system (1.5), the possibility of pattern emergence with a linear stability analysis. We will show that the point equilibirum $(1, u_s, v_s)$ can be stable for the kinetic part of the system (1.5), but unstable for the full reaction-diffusion system.

The linearized system in the neighborhood of $(1, u_s, v_s)$ is :

$$\mathbf{w}_t = J\mathbf{w} + D^\kappa \nabla^2 \mathbf{w}, \quad \text{with } \mathbf{w} \equiv \begin{pmatrix} n-1 \\ u-u_s \\ v-v_s \end{pmatrix}, \tag{A.22}$$

where J and D^κ are given by

$$J := \begin{pmatrix} -\alpha_n & 0 & 0 \\ \delta_u u_s & \gamma_u - \delta_u & -\gamma_v \\ \delta_v v_s & \eta_u & -\delta_v \end{pmatrix}, \quad D^\kappa := \begin{pmatrix} D_n & -\kappa & 0 \\ 0 & D_u & 0 \\ 0 & 0 & D_v \end{pmatrix}.$$

The solution of (A.22) with the form $\mathbf{w} = \overline{\mathbf{w}} e^{ikx+\lambda t}$ leads to the following dispersion relation, which characterizes the relation between eigenvalue λ and the wavenumber k

$$0 = \lambda^3 + a_2(k^2)\lambda^2 + a_1(k^2)\lambda + a_0(k^2), \tag{A.23}$$

where

$a_2(k^2) = \delta_u - \gamma_u + k^2 D_u + \delta_v + k^2 D_v + \alpha_n + k^2 D_n,$
$a_1(k^2) = (\alpha_n + k^2 D_n)\left[\delta_u - \gamma_u + k^2 D_u + \delta_v + k^2 D_v\right] + \left[\gamma_v \eta_u + (\gamma_u - \delta_u - k^2 D_u)(-\delta_v - k^2 D_v)\right] - k^2 \kappa \delta_u u_s,$

and $a_0(k^2) = -\det(A(k^2))$, where $A(k^2) := J - k^2 D$. The Routh-Hurwitz criterion provides three conditions for ensuring that the equilibrium is stable (i.e. eigenvalues have strictly negative real part). In detail, all eigenvalues have strictly negative real part if and only if these conditions hold

$$a_0(k^2) > 0,\ a_2(k^2) > 0 \quad \text{and} \quad a_2(k^2)a_1(k^2) - a_0(k^2) > 0. \tag{A.24}$$

Turing instability emerges when the real parts of two eigenvalues remain negative and the remaining one eigenvalue passes through zero. Without any loss of generality, we assume that λ_1, λ_2 and λ_3 represent the roots of the characteristic equation, and accordingly, we obtain

$$\lambda_1+\lambda_2+\lambda_3=-a_2(k^2),\quad \lambda_1\lambda_2+\lambda_2\lambda_3+\lambda_3\lambda_1=a_1(k^2),\quad \lambda_1\lambda_2\lambda_3=-a_0(k^2),$$

$$\text{and,}\quad -(\lambda_1+\lambda_2)(\lambda_2+\lambda_3)(\lambda_3+\lambda_1)=a_2(k)a_1(k^2)-a_0(k^2).$$

We assume that there is a Turing instability and k_c denotes the critical wavenumber. Thus, at this critical wavenumber $k=k_c$, we can assumme without any loss of generality

$$\lambda_1|_{k^2=k_c^2}=0,\quad \text{Re }(\lambda_2)|_{k^2=k_c^2}<0,\text{ and Re }(\lambda_3)|_{k^2=k_c^2}<0.$$

Hence, we have $a_0(k^2)=0$ at the critical wavenumber $k=k_c$.

Moreover, the conditions for Turing instability leads to $a_2(k_c^2)>0$, $a_1(k_c^2)=\lambda_2\lambda_3>0$ and $a_2(k_c^2)a_1(k_c^2)-a_0(k_c^2)=a_1(k_c^2)a_2(k_c^2)>0$. Thus, the point equilibrium $(1,u_s,v_s)$ becomes Turing unstable when $\det(A(k^2))>0$ holds for at least one $k>0$ and it remains stable when $\det(A(k^2))<0$ holds for all $k\geq 0$.

The determinant of the matrix $A(k^2)$ has the following form

$$\det(A(k^2))=k^6A_6+k^4A_4(\kappa)+k^2A_2(\kappa)+A_0,$$

with

$$\begin{aligned}
A_6&=-D_nD_uD_v<0,\\
A_4(\kappa)&=-\alpha_nD_uD_v-D_nD_u\delta_v+D_nD_v(\gamma_u-\delta_u)+\kappa\delta_u u_sD_v,\\
A_2(\kappa)&=\alpha_n\left(D_v(\gamma_u-\delta_u)-D_u\delta_v\right)-D_n\left(\gamma_v\eta_u-\delta_v(\gamma_u-\delta_u)\right)-\kappa\left[\gamma_v\delta_v v_s-\delta_u u_s\delta_v\right],\\
A_0&=-\alpha_n\left[\gamma_v\eta_u-\delta_v(\gamma_u-\delta_u)\right].
\end{aligned}$$

The condition for the marginal stability at some $k=k_c$ is

$$\max\left[\det\left(A(k_c^2)\right)\right]=0.$$

The minimum of a_0 is attained when

$$k^2_{\max}(\kappa)=\frac{A_4(\kappa)+\sqrt{A_4(\kappa)^2+3A_2(\kappa)|A_6|}}{3|A_6|},$$

which requires $A_4(\kappa)^2+3A_2(\kappa)|A_0|>0$ and $A_4(\kappa)+\sqrt{A_4(\kappa)^2+3A_2(\kappa)|A_6|}>0$. As shown in Fig. 1.9, the graph of $a_0(k)$ depends on κ, which plays the role of the bifurcation parameter. Bifurcation can occur at the critical value, κ_c defined by the root of the function,

$$\kappa\longmapsto k^6_{\max}(\kappa)A_6+k^4_{\max}(\kappa)A_4(\kappa)+k^2_{\max}(\kappa)A_2(\kappa)+A_0,$$

and k_c is given by $k_c^2:=k^2_{\max}(\kappa_c)$. This function does not necessarily admit a unique root, when it does, the root is approximated numerically. In the case $\kappa<\kappa_c$, the equilibrium point $(1,u_s,v_s)$ is stable for all k (See Fig. 1.9) While, for $\kappa>\kappa_c$ the system admits a pattern-forming stationary instability. The unstable wavenumbers stay in between the roots of $a_0(k)$, denoted by k_1 and k_2 (See Fig. 1.9).

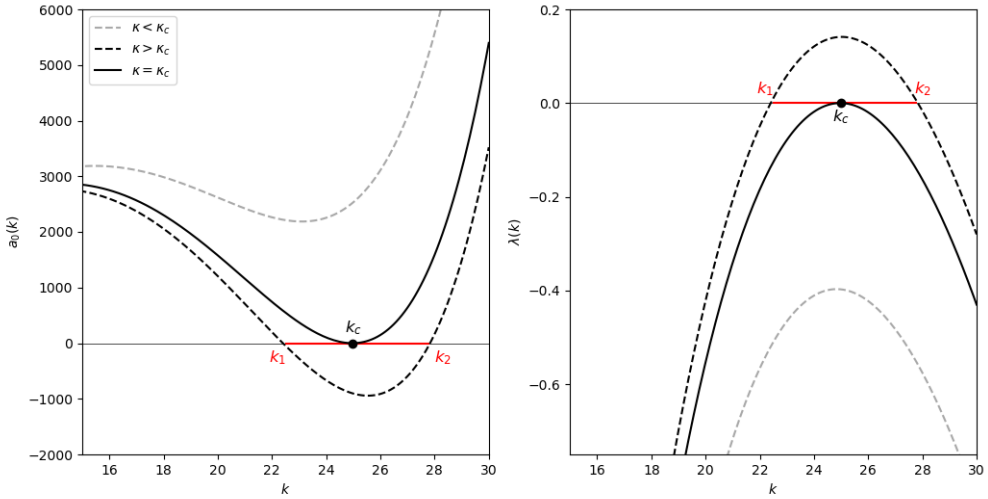

FIGURE 1.9 – *Left* : Plot of $a_0(k)$. *Right* : Growth rate of the kth mode, with a band of growing modes.

B Additional information on weakly nonlinear analysis

In this section, we detail the application of weakly nonlinear analysis to the model (1.5). We begin by explicitly providing the definitions of the operators $(\mathcal{L}^i)$ and $(\mathcal{B}^i)$ for $i = 0, 1, 2$, introduced in the equations (1.12) and (1.13),

$$\mathcal{L}^0(\mathbf{w}) := (J + D^{\kappa_c}\partial_{xx})\mathbf{w}, \qquad \mathcal{L}^1(\mathbf{w}) := 2D^{\kappa_c}\partial_{xX}\mathbf{w} - M_{\kappa_1}\partial_{xx}\mathbf{w},$$

$$\mathcal{L}^2(\mathbf{w}) := D^{\kappa_c}\partial_{XX}\mathbf{w} - M_{\kappa_2}\partial_{xx}\mathbf{w} - 2M_{\kappa_1}\partial_{xX}\mathbf{w}, \qquad \text{with } M_{\kappa_i} := \begin{pmatrix} 0 & \kappa_i & 0 \\ 0 & 0 & 0 \\ 0 & 0 & 0 \end{pmatrix},$$

$$\mathcal{B}^0(\mathbf{w}, \mathbf{w}') := \frac{1}{2}\begin{pmatrix} -2\alpha_n n' n \\ \gamma_u(n'u + nu') - \gamma_v(n'v + nv') \\ \eta_u(n'u + un') \end{pmatrix} - \frac{\kappa_c}{2}\begin{pmatrix} \partial_x(n'\partial_x u + n\partial_x u') \\ 0 \\ 0 \end{pmatrix},$$

and

$$\mathcal{B}^i(\mathbf{w}, \mathbf{w}') := -\frac{\kappa_i}{2}\begin{pmatrix} \partial_x(n'\partial_x u + n\partial_x u') \\ 0 \\ 0 \end{pmatrix}, \qquad \text{for } i = 1, 2.$$

The vector ρ, introduced in the equality (1.17), is defined up to a constant and can be normalized in the following way

$$\rho = \begin{pmatrix} 1 \\ M_y \\ M_z \end{pmatrix} \in \ker(K - k_c^2 D^{\kappa_c}), \tag{B.25}$$

with

$$M_y = \frac{\alpha_n + k_c^2 D_n}{k_c^2 \kappa_c}, \qquad M_z = \frac{\delta_u u_s + M_y[\gamma_u - \delta_u - k_c^2 D_u]}{\gamma_v}.$$

The equations (1.15), and (1.16) can be rewritten in the following form

$O(\epsilon^2)$:

$$\mathcal{L}^0(\mathbf{w}_2) = \mathbf{F}, \tag{B.26}$$

$O(\epsilon^3)$:

$$\mathcal{L}^0(\mathbf{w}_3) = \mathbf{G}, \tag{B.27}$$

with

$$\mathbf{F} =: \partial_{T_1}\mathbf{w}_1 - \mathcal{L}^1(\mathbf{w}_1) - \mathcal{B}^0(\mathbf{w}_1, \mathbf{w}_1), \tag{B.28}$$

and

$$\mathbf{G} =: \partial_{T_2}\mathbf{w}_1 + \partial_{T_1}\mathbf{w}_2 - \mathcal{L}^1(\mathbf{w}_2) - \mathcal{L}^2(\mathbf{w}_1) - \mathcal{B}^1(\mathbf{w}_1, \mathbf{w}_1) - 2\mathcal{B}^0(\mathbf{w}_1, \mathbf{w}_2). \tag{B.29}$$

Substituting (1.17) into (B.28) leads to

$$\mathbf{F} = \cos(k_c x)\rho\left[\frac{\partial A}{\partial T_1} - k_c^2 A M_{\kappa_1}\right] + 2k_c D^{\kappa_c}\rho\frac{\partial A}{\partial X}\sin(k_c x) - \frac{A^2\cos(2k_c x)}{2}\begin{pmatrix} 2\kappa_c k_c^2 M_y - \alpha_n \\ \gamma_u M_y - \gamma_v M_z \\ \eta_u M_y \end{pmatrix} - \frac{A^2}{2}\begin{pmatrix} -\alpha_n \\ \gamma_u M_y - \gamma_v M_z \\ \eta_u M_y \end{pmatrix}.$$

By the Fredholm alternative, Eq. (B.26) admits solution if and only if

$$\langle \mathbf{F}, \mathbf{W}^\star \rangle = 0, \tag{B.30}$$

where $\mathbf{W}^\star = \psi\cos(k_c x) \in \ker(L^\star)$ with $L^\star$ the adjoint operator of $\mathcal{L}^0$ and $\langle\cdot,\cdot\rangle$ is the scalar product in $L^2(0, 2\pi/k_c)$. Due to the Neumann boundary condition, for (1.5) we can construct a solution in the whole domain using reflection and periodic extension. The vector ψ is defined up to a constant,

$$\psi := \begin{pmatrix} 1 \\ M_y^\star \\ M_z^\star \end{pmatrix}, \text{ with } M_y^\star = -M_z^\star\frac{\delta_v + k_c^2 D_v}{\gamma_v},\ M_z^\star = \frac{\gamma_v k_c^2 \kappa_c}{(\delta_v + k_c^2 D_v)(\gamma_u - \delta_u - k_c^2 D_u) - \eta_u\gamma_v}.$$

The condition (B.30) gives us

$$\partial_{T_1} A = \gamma A, \quad \gamma = \frac{k_c^2 \kappa_1 M_y}{1 + M_y M_y^\star + M_z M_z^\star}. \tag{B.31}$$

Obviously, the above equation cannot correctly predict the evolution of amplitude. Thus, we take $T_1 = 0$ and $\kappa_1 = 0$ such that the solvability condition (B.30) holds. Therefore the solution of (B.26) with the boundary condition has the following form

$$\mathbf{w}_2 = A^2\mathbf{w}_{20} + A^2\mathbf{w}_{22}\cos(2k_c x) + \frac{\partial A}{\partial X}\mathbf{w}_{21}\sin(k_c x),$$

where vectors $\mathbf{w}_{2i}$, $i = 0, 1, 2$, are the solutions of the following linear systems :

$$\begin{cases} J\mathbf{w}_{20} = \dfrac{1}{2}\begin{pmatrix} -\alpha_n \\ \gamma_u M_y - \gamma_v M_z \\ \eta_u M_y \end{pmatrix}, \\ (J - k_c^2 D^{\kappa_c})\mathbf{w}_{21} = 2k_c D^{\chi_c}\rho, \\ (J - 4k_c^2 D^{\kappa_c})\mathbf{w}_{22} = -\dfrac{1}{2}\begin{pmatrix} 2\kappa_c k_c^2 M_y - \alpha_n \\ \gamma_u M_y - \gamma_v M_z \\ \eta_u M_y \end{pmatrix}. \end{cases} \tag{B.32}$$

To understand the evolution of the amplitude A we must consider the third order coefficient equation (B.27). The solvability condition $\langle \mathbf{G}, \mathbf{W}^\star \rangle = 0$ leads to this following equation for the amplitude A,

$$\partial_{T_2} A = \nu \partial_{XX} A + \sigma A - L A^3,$$

where the parameters ν, σ and L are given by

$$\nu := \frac{\langle 2k_c D^{\kappa_c}\mathbf{w}_{21} + D^{\kappa_c}\rho, \psi \rangle}{\langle \rho, \psi \rangle}, \tag{B.33}$$

$$\sigma := \frac{\langle \mathbf{G}_{11}, \psi \rangle}{\langle \rho, \psi \rangle}, \tag{B.34}$$

$$L := \frac{\langle \mathbf{G}_{13}, \psi \rangle}{\langle \rho, \psi \rangle}, \tag{B.35}$$

with

$$\mathbf{G}_{11} = -k_c^2 M_{\kappa_2}\rho, \quad \text{and} \quad \mathbf{G}_{13} := -\kappa_c k_c^2 \begin{pmatrix} M_y W_{20}^{(1)} + W_{22}^{(2)} - \dfrac{M_y}{2} W_{22}^{(1)} \\ 0 \\ 0 \end{pmatrix} - \mathbf{V}_{20} - \mathbf{V}_{22},$$

where $W_{2j}^{(i)}$ corresponds to the i-th component of $\mathbf{w}_{2j}$. The two vectors $\mathbf{V}_{20}$ and $\mathbf{V}_{22}$ are defined by

$$\mathbf{V}_{20} := \begin{pmatrix} -2\alpha_n W_{20}^{(1)} \\ \gamma_u \left[W_{20}^{(2)} + M_y W_{20}^{(1)} \right] - \gamma_v \left[W_{20}^{(1)} M_z + W_{20}^{(3)} \right] \\ \eta_u \left[W_{20}^{(2)} + M_y W_{20}^{(1)} \right] \end{pmatrix},$$

$$\mathbf{V}_{22} := \frac{1}{2}\begin{pmatrix} -2\alpha_n W_{22}^{(1)} \\ \gamma_u \left[W_{22}^{(2)} + M_y W_{22}^{(1)} \right] - \gamma_v \left[W_{22}^{(1)} M_z + W_{22}^{(3)} \right] \\ \eta_u \left[W_{22}^{(2)} + M_y W_{22}^{(1)} \right] \end{pmatrix}.$$

C Supplementary Figures

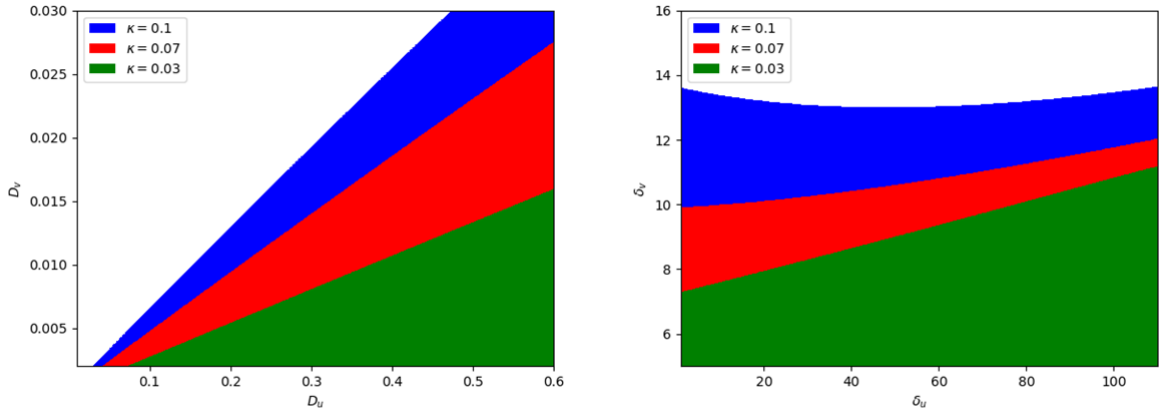

FIGURE 1.10 – The colored areas correspond to parameter values for which the point $(1, u_s, v_s)$ admits a Turing-type instability. The different colors correspond to different chemotaxis parameters 0.1, 0.07 and 0.03. In the left figure, the parameters studied are the pair of diffusion coefficients (D_u, D_v) and on the right figure, the parameters studied are the pair of degradation coefficients (δ_u, δ_v).

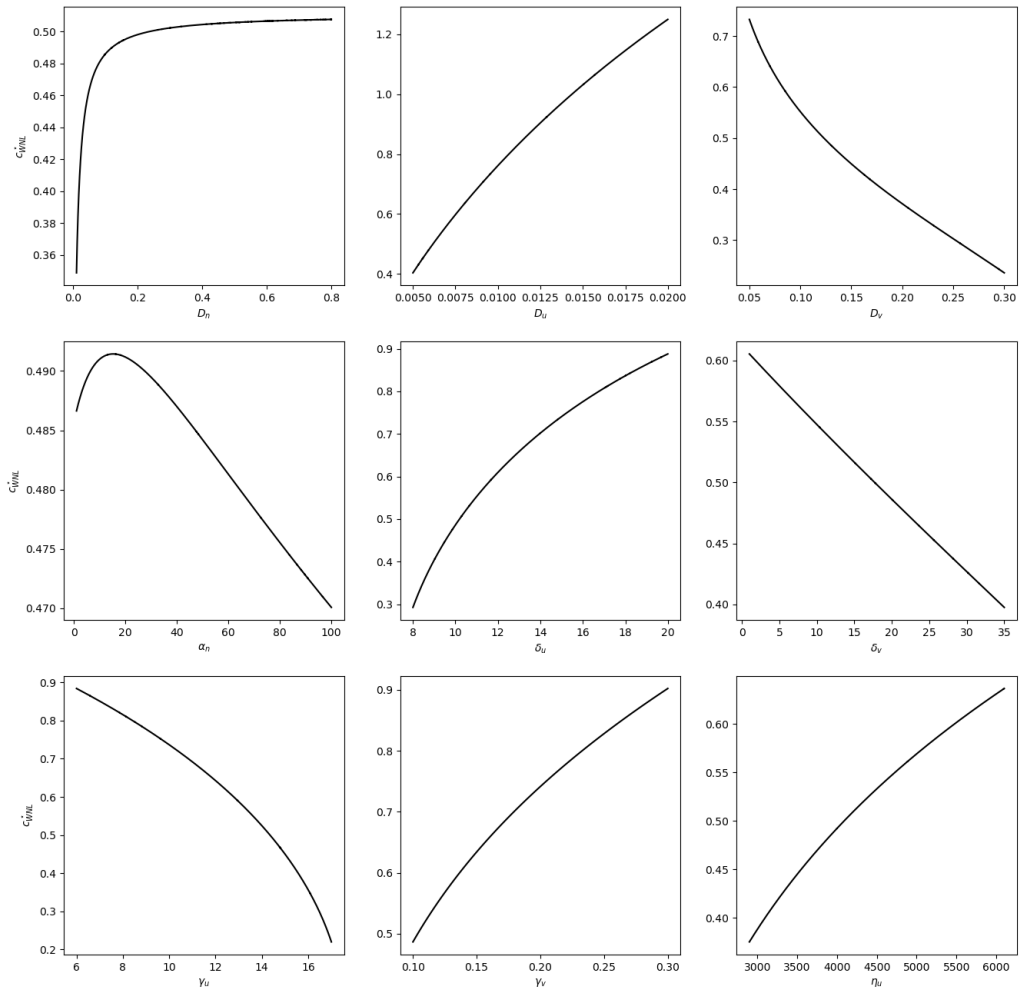

FIGURE 1.11 – **Influence of the parameter values on the critical speed $c^\star_{\mathbf{WNL}}$ of the equation** (1.7)**.** For each sub figure we change only one parameter, the values of the other parameters are the same as in Figure 1.2. For each parameter value we calculate again the critical bifurcation value.

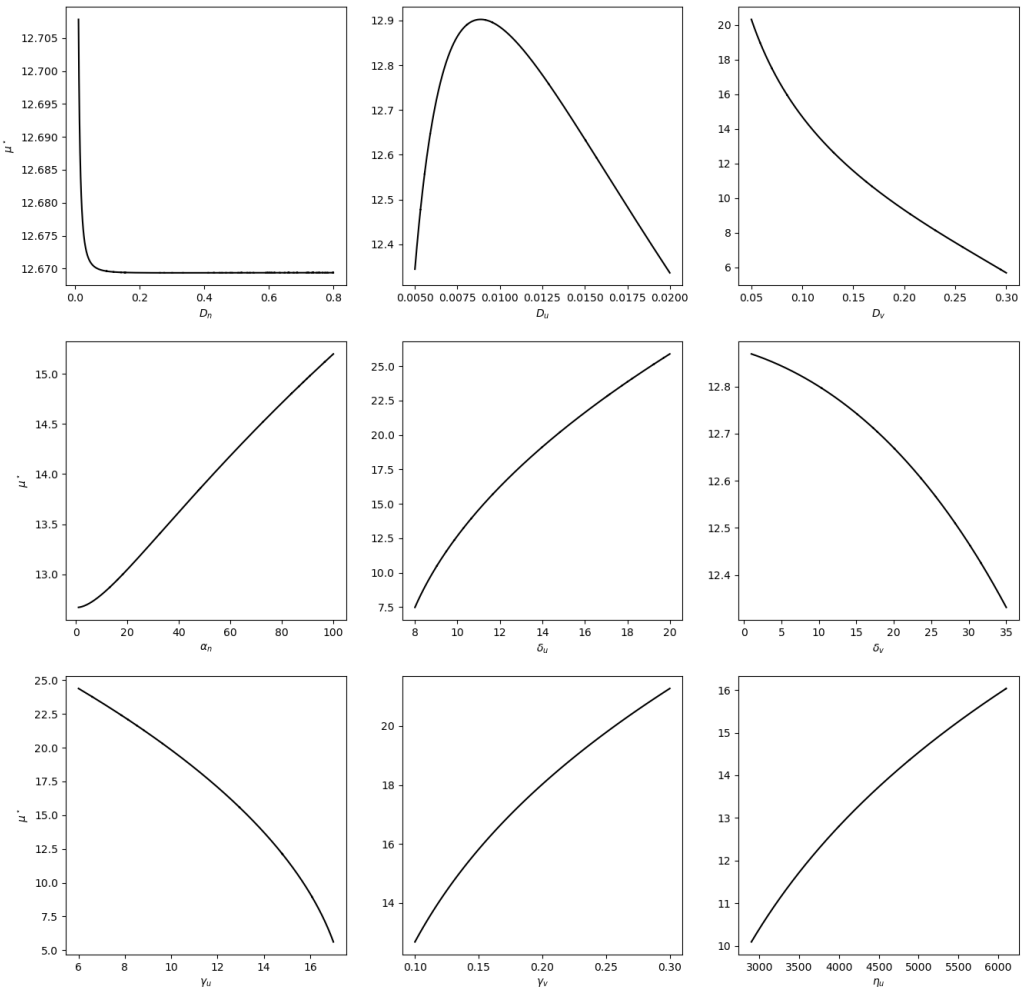

FIGURE 1.12 – **Influence of the parameter values on the steepness $\mu^\star$ of the equation** (1.7) **at the critical speed.** For each sub figure we change only one parameter, the values of the other parameters are the same as in Figure 1.2. For each parameter value we calculate again the critical bifurcation value.

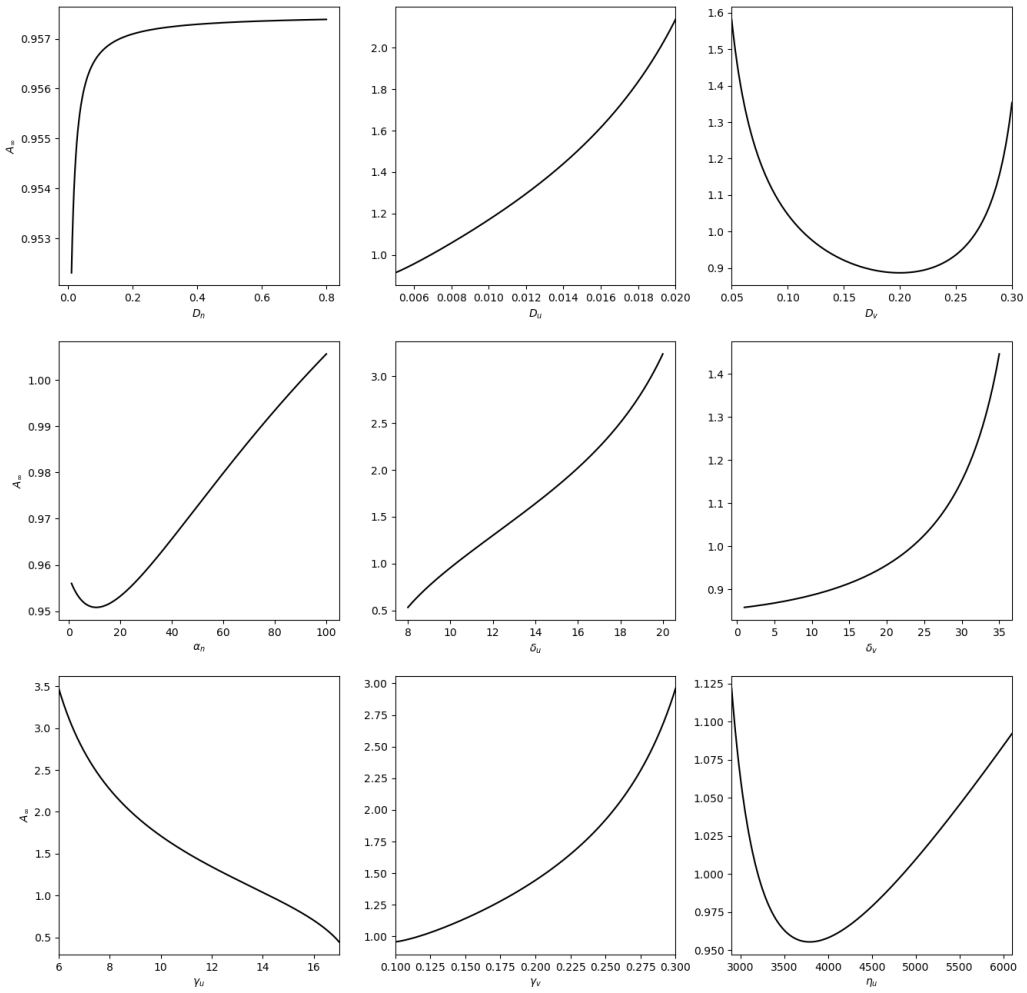

FIGURE 1.13 – **Influence of the parameter values on the final amplitude of the patterns, A_∞, of the equation** (1.7)**.** For each sub figure we change only one parameter, the values of the other parameters are the same as in Figure 1.2. For each parameter value we calculate again the critical bifurcation value.

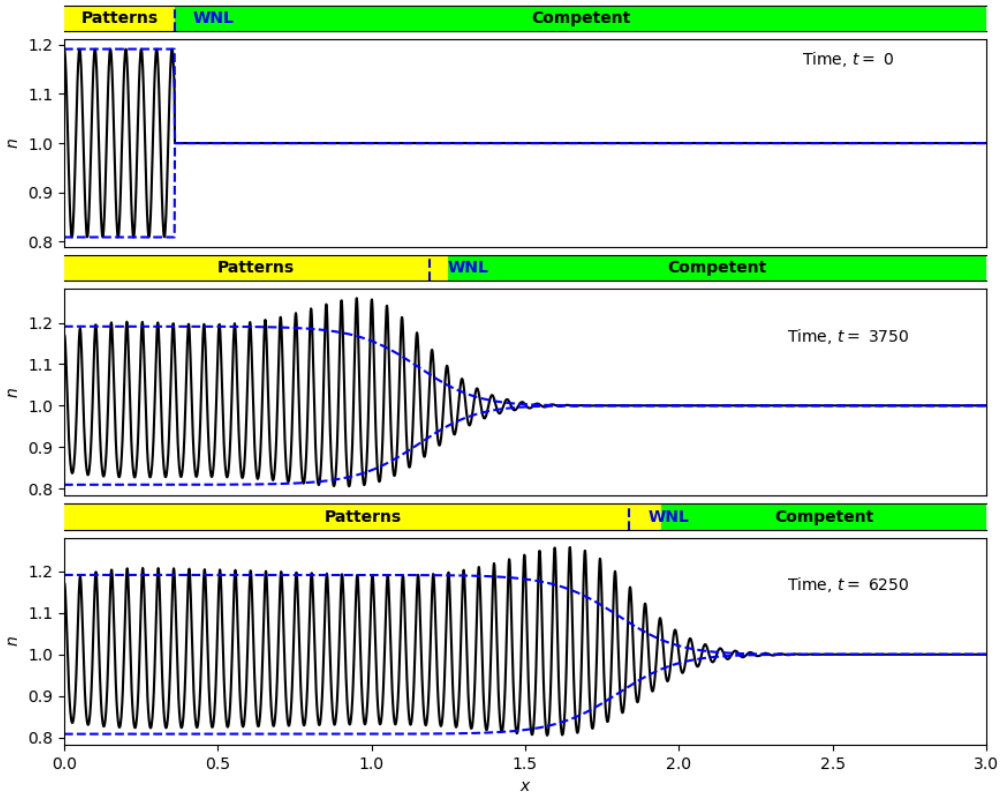

FIGURE 1.14 – **Comparison between the solution of the equation** (1.7) **(blue dashed line) and the numerical solution of** (1.5) **(black solid line) at different times.** The panels above the figures respectively represent the competent zone (green), the zone where patterns are present (yellow), and the prediction of the weakly nonlinear analysis (blue dashed line). Parameter values are the same as in the previous figure 1.3 except for $\epsilon = 0.2$.

Troisième partie

Modélisation de l'invasion de la bactérie prédatrice Myxococcus Xanthus

Introduction

Propriétés de la bactérie Myxococcus xanthus

Myxococcus xanthus, une bactérie du sol du groupe des myxobactéries, appelée aussi par la suite *M. xanthus*, est notamment connue pour sa capacité à former des structures complexes, pour ses mécanismes de motilité, sa coopération cellulaire ainsi que pour de nombreuses autres propriétés propres importantes. Par exemple, cette bactérie est dite « sociale » dans le sens qu'elle peut se déplacer en groupe de manière coordonnée, semblable aux comportements collectifs que l'on retrouve chez les animaux. Nous verrons de plus que ces groupes de bactéries jouent un rôle crucial dans le comportement de *M. xanthus*. Dans cette introduction, nous nous focalisons sur le comportement en lien avec le caractère prédateur de la bactérie *M. xanthus* et en particulier sur son activité au niveau du front d'invasion. Nous omettrons volontairement d'autres caractéristiques bien étudiées de *M. xanthus* telles que la formation de structures de survie appelées corps fructifères, survenant lorsque la bactérie est confrontée à la famine [115], ainsi que le phénomène de mouvements ondulatoires connus sous le nom de « *rippling* » [116, 117, 118, 119]. Ces comportements, bien que cruciaux pour comprendre la biologie globale de cette bactérie, sortent du cadre de notre étude actuelle sur les mécanismes d'invasion et de prédation.

Motilité. Les bactéries *Myxococcus xanthus* utilisent deux modes de motilité distincts : la motilité sociale (S) et la motilité aventureuse (A). La motilité sociale est associée à la présence de « *pili* », qui agissent comme des grappins présents au niveau du pôle bactérien, favorisant un mouvement coordonné au sein des groupes de bactéries [120]. La motilité aventureuse, quant à elle, implique des moteurs latéraux qui permettent aux bactéries individuelles, principalement à la périphérie de la colonie, de se déplacer [121]. Ces deux systèmes de motilité, qui dépendent de l'expression de deux ensembles de gènes distincts [122], présentent des caractéristiques complètement différentes. Notamment, les bactéries regroupées en agrégats ont tendance à être individuellement plus rapides que les bactéries isolées [123]. Inversement, au niveau du front de prédation, les bactéries isolées auraient tendance à être plus persistantes le long d'une trajectoire que les bactéries dans les agrégats. Ces deux systèmes de motilité sont illustrés dans la figure III.1A.

Ces bactéries en forme de bâtonnets peuvent se déplacer le long de leur axe principal grâce à l'un des deux systèmes de motilité à disposition. À certains moments, ces bactéries inversent leur direction en changeant de polarité (Voir Fig. III.1B.). En d'autres termes, le pôle cellulaire de tête

devient le pôle de queue, et inversement [124]. Pour désigner un tel phénomène on utilise la notion de « réversion ». A noter que, contrairement à d'autres espèces de bactéries, plusieurs études ont montré que *M. xanthus* n'est pas chimiotactique envers sa proie [125], et la question de savoir si la bactérie présente des comportements chimiotactiques en général reste controversée [126, 127].

Prédation. *M. xanthus* est une bactérie prédatrice, connue pour s'attaquer à une grande variété de proies [128, 129] comme par exemple la bactérie *E. coli*. La biomasse libérée par les micro-organismes proies est riche en acides aminés et en lipides, qui constituent leurs principales sources de carbone et d'énergie. *Myxococcus xanthus* utilise deux stratégies d'attaque, choisies en fonction du type de proie [130]. La première stratégie implique une attaque frontale, illustrée dans la figure III.2, où les bactéries prédatrices pénètrent progressivement dans la colonie de la proie et lysent peu à peu les cellules de la proie [116, 131]. Dans l'autre stratégie, appelée « meute de loups », les cellules de *M. xanthus* entourent la colonie proie et ondulent avant de la tuer [116, 132]. Cette capacité prédatrice fait de Myxococcus xanthus un candidat potentiel pour des applications en biotechnologie médicale, notamment dans la production de nouveaux antibiotiques [128, 130, 133, 134].

Comment la bactérie *M. xanthus* tue sa proie ? Le principal mécanisme de destruction des proies est la destruction par contact des bactéries. Selon plusieurs études récentes, les chercheurs ont observé que les bactéries isolées de *Myxococcus xanthus* s'approchent tout d'abord des cellules proies grâce à leur motilité aventureuse. Ensuite, au contact direct de celles-ci, elles cessent leur mouvement et provoquent la mort de la cellule proie [135, 136, 137]. La coopération entre les cellules de *M. xanthus*, observée par Rosenberg et al. favorise la croissance végétative et la prédation [138]. Cette collaboration permet une sécrétion commune d'enzymes hydrolytiques, améliorant l'efficacité de la dégradation de la biomasse des proies au sein d'un groupe, ce qui suggère une prédation plus efficace des agrégats de bactéries par rapport aux cellules individuelles [138]. De plus, Zhang et al. ont remarqué que les bactéries isolées de *M. xanthus* quittent fréquemment les proies *Escherichia coli* tuées sans dégrader la biomasse, probablement en raison d'une production insuffisante d'enzymes de dégradation [132, 136]. A nouveau, le rapport vis-à-vis des proies et de leur ressource sécrétée est complètement différent entre les bactéries isolées et les agrégats de bactéries.

Répartition spatiale hétérogène des différentes tailles d'agrégats de bactéries. Les récents progrès des techniques de microscopie à haut débit et des techniques de segmentation cellulaire ont considérablement fait progresser notre connaissance de la bactérie *M. xanthus* [139]. Notamment, la distribution de la taille des agrégats de bactéries est très hétérogène en fonction de leur position dans le front de prédation. En amont du front, on trouve principalement des bactéries isolées ou des groupes de petite taille. Plus on recule à l'arrière du front d'invasion, plus on trouve de grands amas de bactéries dont la taille est proportionnelle à la distance par rapport au front [140].

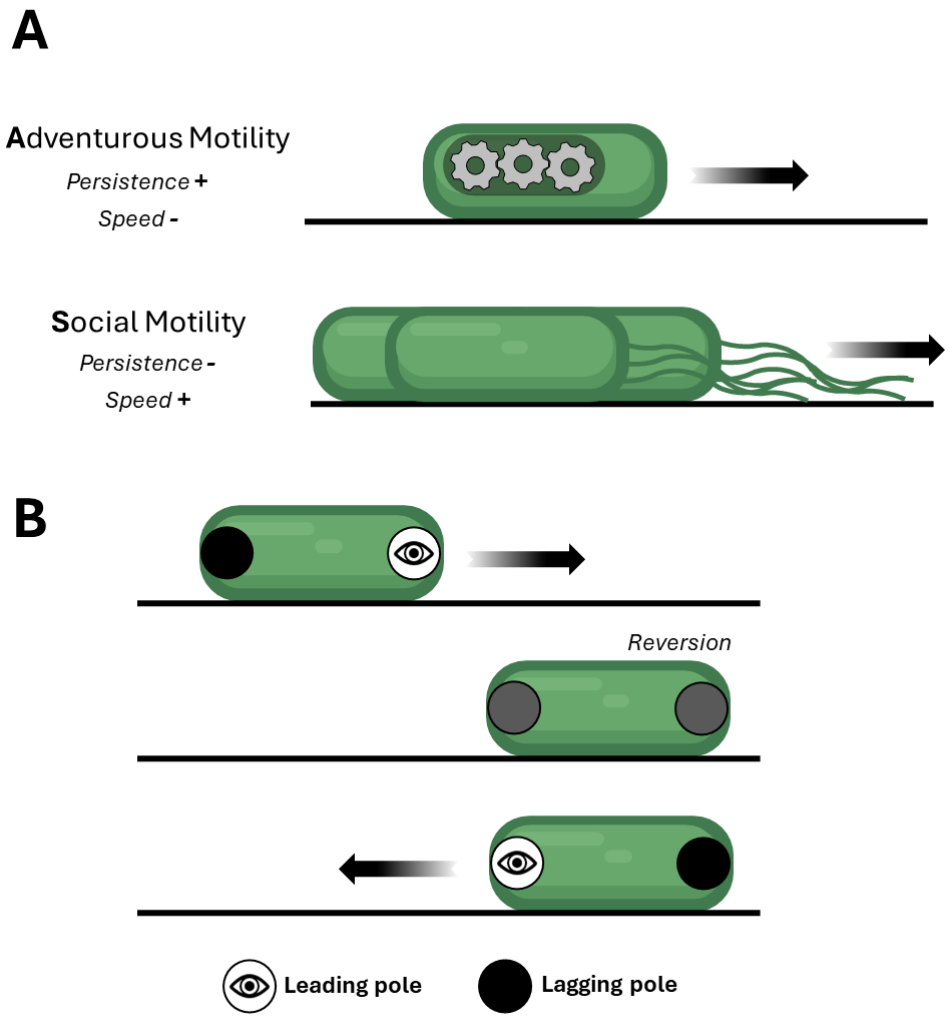

FIGURE III.1 – **Schéma de la motilité de la bactérie *Myxococcus xanthus*. A.** La bactérie *M. xanthus* possède deux systèmes de motilité bien distincts, la motilité aventureuse (A) et la motilité sociale (S). La motilité aventureuse se caractérise par l'activation de moteurs cellulaires latéraux, permettant à des bactéries isolées, généralement situées en périphérie de la colonie, de se déplacer de manière autonome [121]. En revanche, la motilité sociale de *Myxococcus xanthus* repose sur l'utilisation de pili situés aux pôles des cellules, fonctionnant comme des grappins pour favoriser un déplacement coordonné parmi les groupes de bactéries [120]. Ces deux motilités ont des propriétés de déplacement différentes concernant les caractéristiques de vitesse ou de temps de persistance le long d'une trajectoire. **B.** Illustration du phénomène de « *réversion* ». La bactérie possède deux pôles, l'un correspondant à la tête (Leading pole) et l'autre à la queue (Lagging pole). Ces deux pôles peuvent s'inverser, la tête devenant queue et inversement.

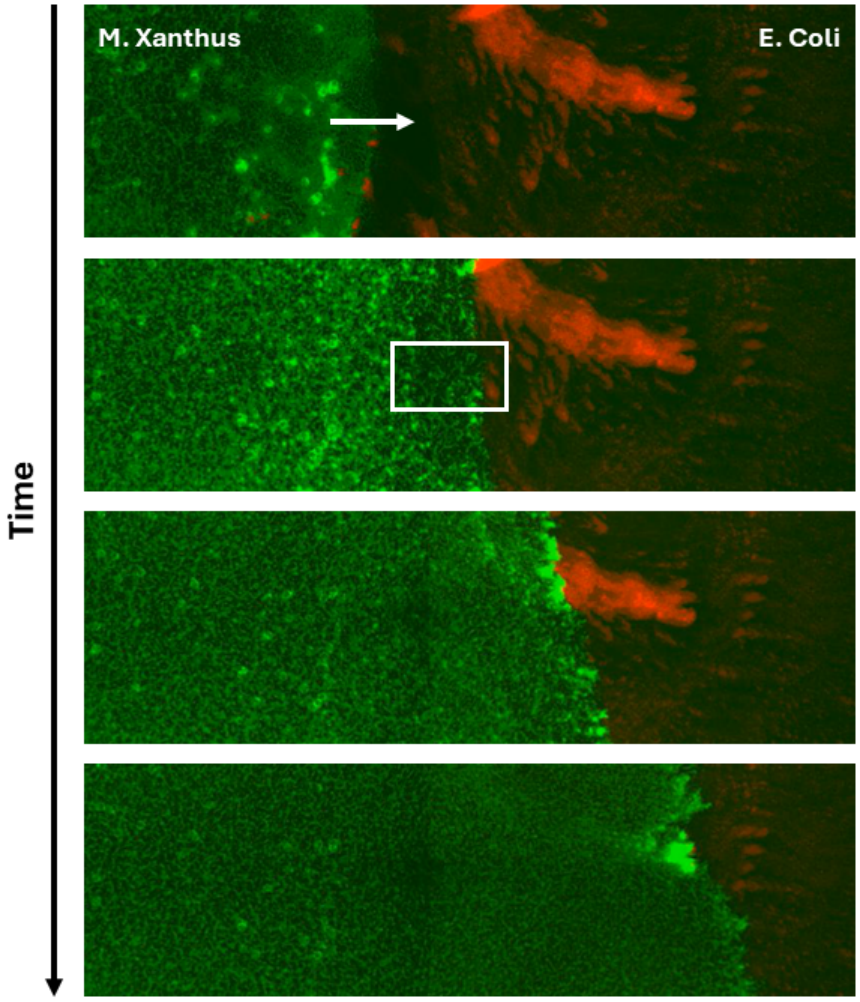

FIGURE III.2 – **Invasion de la bactérie prédatrice *Myxococcus xanthus*.** La bactérie à gauche, en vert, correspond à la bactérie prédatrice *Myxococcus xanthus* et la bactérie à droite, en rouge, à la bactérie proie *Escherichia coli*. Au cours du temps (de haut en bas), la bactérie prédatrice *Myxococcus xanthus* envahit peu à peu sa proie. Le rectangle blanc correspond au domaine du schéma présenté dans la Figure III.3. Cette figure a été fournie par le laboratoire Mignot Lab et provient d'une expérience réalisée par Jean-Baptiste Saulnier.

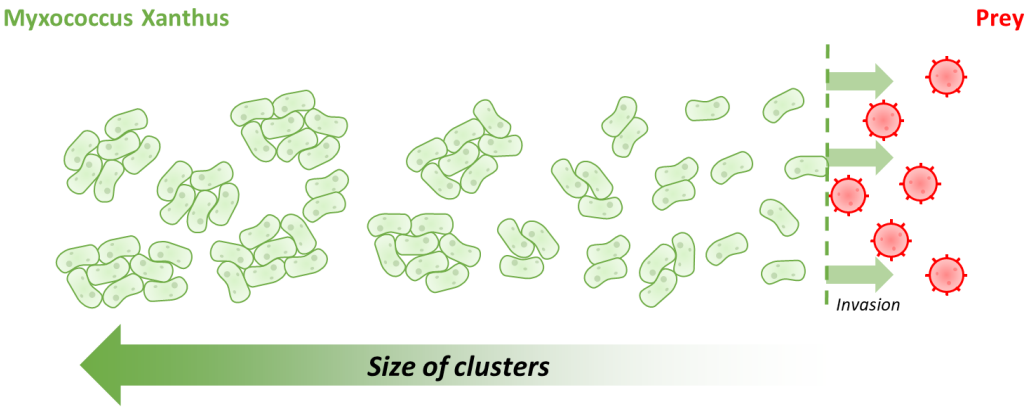

FIGURE III.3 – **Schéma de la répartition des différentes tailles d'agrégats de *Myxococcus xanthus* au niveau du front d'invasion.** Dans l'article [140], les auteurs ont montré, à l'aide d'expériences biologiques que la répartition des agrégats de bactéries au niveau du front d'invasion est hétérogène en espace. A l'avant du front, proche des proies, on retrouve principalement des bactéries isolées. Ensuite, plus on recule dans la colonie de *M. xanthus*, plus on remarque la présence d'agrégats de nombre de bactéries de plus en plus grand.

Etat de l'art

D'autres modèles plus anciens ont été introduits pour modéliser la propagation de *M. xanthus* [141, 142]. Dans l'article Patra et al. [142], les auteurs se concentrent sur la modélisation de la motilité sociale et, plus spécifiquement, sur l'impact de l'EPS (Extracellular Polysaccharide Substance) sur cette motilité. L'EPS, sécrétée par les bactéries elles-mêmes, est reconnue pour faciliter le mouvement des agrégats bactériens. Les auteurs ont introduit un modèle de réaction-diffusion et s'intéressent notamment à la vitesse d'expansion de la colonie des cellules S-motiles.

Dans l'article [141], Gallegos et al. proposent un autre modèle de réaction-diffusion, qui prend en compte l'interaction entre la bactérie *M. xanthus* et des nutriments initialement ajoutés dans la boîte de Pétri. A notre connaissance, il n'existe pas de modèle mathématique s'intéressant au caractère prédateur de la bactérie, ni même de modèle prenant en compte les deux systèmes de motilité A et S.

Notons également qu'il existe une importante littérature sur la modélisation mathématique des mouvements ondulatoires appelés « rippling », dont nous donnons quelques références bibliographiques [143, 144, 145, 146, 147].

Problématiques

Notre but dans cette partie est de proposer des modèles mathématiques cohérents du caractère prédateur de la bactérie *M. xanthus*, qui prennent notamment en compte les propriétés fondamentales de la bactérie et qui retranscrivent le mieux possible les phénomènes observés. Ces modèles auront pour but de proposer des réponses à de nombreuses questions biologiques ouvertes, comme par exemple :

- Pourquoi les agrégats, bien que plus rapides, restent à l'arrière du front d'invasion ?

- La plus grande rapidité des agrégats permet-elle d'accélérer l'invasion de la bactérie *M. xanthus* ?
- Quels sont les paramètres prédominant sur le comportement de la vitesse de propagation ?
- Pourquoi existe-t-il une coexistence de deux systèmes de motilité, A et S, si distincts ?

Résultats

• Chapitre 2 : Regime switching on the propagation speed of travelling waves of some size-structured Myxobacteria population models.

Ce travail a été effectué lors du CEMRACS 2022 avec Adil El Abdouni et Ignacio Madrid, et a été supervisé par Vincent Calvez, Florence Hubert, Julien Olivier et Magali Tournus. Ce projet a mené à la publication d'un proceedings dans le journal *ESAIM : Proceedings and Surveys* [148].

Méthodes. Dans ce projet, nous introduisons différents modèles de réaction-diffusion pour modéliser le caractère prédateur de la bactérie *Myxococcus Xanthus* que nous étudions à l'aide de nombreuses simulations numériques. Tout d'abord, nous proposons un modèle minimal de réaction-diffusion d'une population de bactéries simplifiée, où nous ne prenons en compte que les bactéries isolées, correspondant à la densité p_1 et également la densité des agrégats de deux bactéries, associée à la densité p_2. Les deux équations de réaction-diffusion sont données par

$$\partial_t p_1 = \theta_1 \Delta p_1 - \tau_1 p_1^2 + 2\tau_2 p_2 + \alpha p_1(1 - p/K), \tag{III.1}$$

et,

$$\partial_t p_2 = \theta_2 \Delta p_2 + \frac{\tau_1}{2} p_1^2 - \tau_2 p_2, \tag{III.2}$$

avec p, la densité du nombre total de bactéries, donnée mathématiquement par la relation, $p := p_1 + 2p_2$. Pour simplifier, nous avons supposé que le mouvement des bactéries est modélisé par un opérateur de diffusion et que les deux coefficients de diffusion sont donnés par θ_1 pour les bactéries isolées et θ_2 pour les agrégats de deux bactéries. Pour prendre en compte l'avantage de rapidité des agrégats nous supposons que $\theta_2 > \theta_1$. Dans ces deux équations, nous modélisons également la possibilité des bactéries isolées de former un agrégat et, inversement, la possibilité qu'un agrégat de deux bactéries puisse se fragmenter. Finalement, nous supposons que les bactéries isolées ont la capacité de se diviser, entraînant ainsi une prolifération. Mathématiquement, nous faisons le choix d'une prolifération logistique avec une capacité de charge qui dépend du nombre total de bactéries, p. Par la suite, nous complexifions ce modèle initial de deux manières. Premièrement, nous considérons un modèle généralisé avec une structure de taille continue concernant la taille des agrégats de bactéries. Dans un second temps, nous étendons également le modèle initial pour inclure des interactions avec une population de proies *E. Coli*.

Résultats principaux. Dans ce travail nous avons effectué de nombreuses expériences numériques. L'étude numérique du système (III.1)-(III.2) montre que ce modèle présente des solutions d'ondes

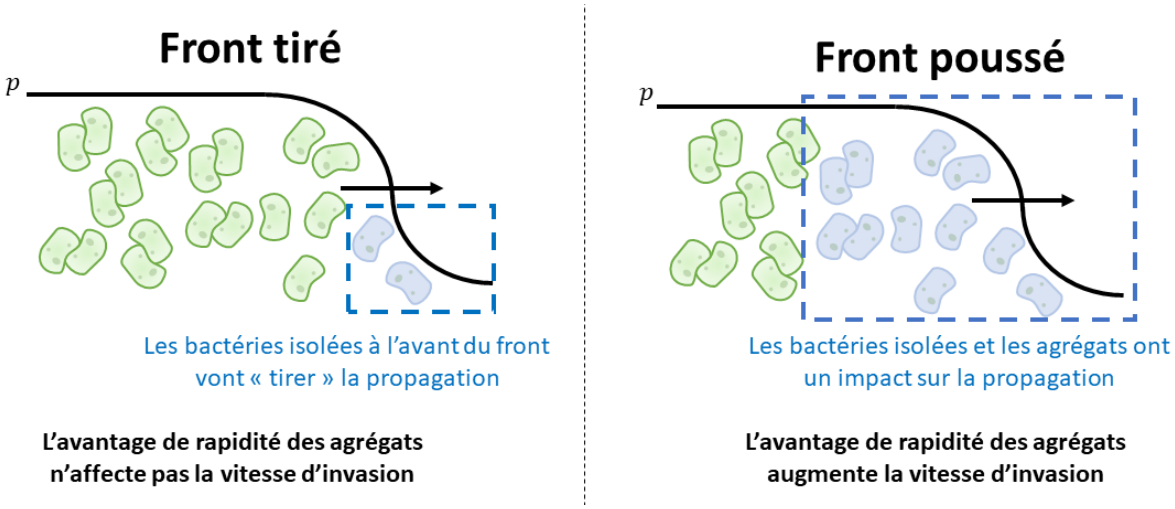

FIGURE III.4 – **Illustration du régime de front tiré et de front poussé pour l'invasion de *M. xanthus*.** Quand le front est tiré, seules les bactéries isolées en amont du front vont contribuer à la propagation de la bactérie prédatrice [62]. Ainsi l'avantage de vitesse que possèdent les agrégats n'aura aucun effet sur la vitesse d'invasion. A l'inverse, dans le régime de front poussé, les agrégats ont cette fois-ci également un rôle, ils « poussent » le front. Dans ce cas de figure, l'avantage de vitesse des agrégats permet une invasion plus rapide.

progressives. De plus, l'étude numérique de la vitesse dévoile l'existence d'un niveau de seuil critique $\theta^\star$ sur le rapport entre la motilité des agrégats et la motilité des bactéries isolées, θ_2/θ_1. Ce seuil sépare deux régimes distincts de front que l'on nomme **front tiré** et **front poussé**. Selon nos résultats, si la différence de motilité entre les bactéries isolées et les agrégats n'est pas suffisamment significative, $\theta_2/\theta_1 < \theta^\star$, nous sommes dans un régime de front tiré et l'avantage de vitesse des agrégats n'affecte pas la vitesse d'invasion globale de la bactérie *Myxococcus xanthus*. Dans ce cas, le front d'invasion se propage grâce aux bactéries isolées en amont du front. D'autre part, si cette différence de coefficient de diffusion devient suffisamment grande, $\theta_2/\theta_1 > \theta^\star$, la vitesse de propagation augmentera proportionnellement à cette différence et nous serons dans ce cas dans le régime de front poussé. En d'autres termes, la présence des agrégats facilitera la prédation de la bactérie *M. xanthus*. Ces résultats sont résumés dans la Figure III.4.

Les simulations numériques du modèle généralisé avec une taille continue d'agrégats présentent des résultats similaires au modèle simplifié (III.1)-(III.2). En effet nous retrouvons cette dichotomie front tiré et front poussé ainsi que les résultats de modélisation associés. Finalement les solutions numériques du modèle proie-prédateur se rapprochent visuellement fortement des expériences biologiques présentées dans la Figure III.2.

• **Chapitre 3 : Travelling waves for a fast reaction limit of a discrete coagulation-fragmentation model with diffusion and proliferation.**

Ce travail est en collaboration avec Thomas Lepoutre, et fait l'objet d'une publication dans le journal *Journal of Mathematical Biology* [149].

Méthodes. Dans ce second chapitre, nous nous concentrons sur les preuves des résultats théoriques en lien avec les investigations numériques effectuées dans le chapitre précédent. Sur ce travail, nous nous focalisons sur le modèle simplifié donné par les équations (III.1)-(III.2), que nous adimensionnons en introduisant le paramètre, $\theta := \theta_2/\theta_1$, correspondant à l'avantage de diffusion qu'ont les agrégats par rapport aux bactéries isolées. De plus les données biologiques présentées dans l'article [140] montrent une symétrie entre la coagulation et la fragmentation. Nous nommerons le taux associé à la coagulation et la fragmentation par k. Dans le but d'étudier le caractère tiré ou poussé du front nous rappelons la valeur de la vitesse critique linéaire pour notre modèle. Notamment, le terme de couplage, donné par la fragmentation des agrégats conduit à une vitesse dite « anormale ». Cette notion a été introduite pour la première fois par Weinberger, Lewis et Li [61] et par la suite théoriquement étudiée (Voir par exemple [54, 55, 50]).

Malgré la connaissance explicite de la vitesse linéaire, l'étude de la transition entre front tiré et front poussé reste complexe pour notre modèle. En effet la complexité de ce modèle ne nous permet pas d'effectuer une méthode classique d'analyse plan de phase, que nous pouvons retrouver dans d'autres travaux, comme par exemple dans l'article [150]. Pour simplifier le problème, nous nous plaçons dans un régime de coagulation et de fragmentation rapide, ce qui mathématiquement se retranscrit par la supposition $k = +\infty$. Sous cette hypothèse nous arrivons à grandement simplifier le modèle (III.1)-(III.2) en une équation scalaire sur p de la forme suivante,

$$\partial_t p = \partial_{xx}(\Phi_\theta(p)) + F(p),$$

avec Φ_θ et F deux fonctions que nous détaillerons par la suite. Pour cette équation scalaire, nous obtenons des résultats théoriques sur la transition entre front tiré et front poussé, ainsi que sur la vitesse de propagation.

Résultats principaux. Sous le régime de coagulation-fragmentation rapide, $k = +\infty$, la vitesse linéaire critique est donnée par $c^\star_{\text{lin}} = 2$. Nous prouvons l'existence d'une unique transition entre front tiré et front poussé ayant lieu en $\theta^\star$, avec $\theta^* \in [2, 6.5]$, tel que :

- Lorsque $\theta \in [1, \theta^\star]$, la vitesse d'invasion est égale à 2, et le front est **tiré**.
- Lorsque $\theta > \theta^\star$, la vitesse d'invasion est strictement supérieure à 2, et le front est **poussé**.

Grâce aux avancées numériques récentes d'Avery, Holzer et Scheel, présentées dans l'article [48], nous approchons avec une grande précision le seuil théorique de transition entre ces deux régimes, donnant l'approximation suivante, $\theta^\star \approx 3.149$. De plus, nous pouvons également trouver un équivalent à la vitesse critique non-linéaire, donné par la formule, $c^\star \underset{\theta\to+\infty}{\sim} \sqrt{K\theta}$, avec K une constante positive que nous détaillerons dans ce chapitre.

• **Chapitre 4 : A reaction telegraph model reveals synergy between motility strategies in *Myxococcus xanthus* predation**

Ce travail a été soumis en prépublication.

Méthodes. Dans ce dernier projet, notre objectif est d'enrichir le modèle précédent afin de mieux refléter les réalités biologiques. Nous nous concentrons sur trois axes principaux d'amélioration :

❶ **La motilité des bactéries.** Dans le précédent travail, nous supposions, pour simplifier, que le mouvement de la bactérie peut être modélisé par un opérateur de diffusion. Néanmoins, même si cette hypothèse est couramment admise, elle reste assez forte dans notre cas. Notamment, par définition de l'opérateur, il nous est impossible de retranscrire la persistance le long d'une trajectoire avant ou après un phénomène de reversion. Pour palier ce problème, nous considérons maintenant un processus nommé *Run and Tumble*, qui en dimension un, modélise parfaitement le mouvement de la bactérie avec ses nombreuses inversions de pôles. Celui-ci nous permet notamment de prendre en compte les différences, induites par la présence des deux modes de motilité A et S, de la vitesse instantanée et également du temps de persistance le long des trajectoires entre les bactéries isolées et les agrégats.

❷ **La consommation des nutriments libérés par la proie.** Dans le précédent travail, nous ne prenions pas en compte, la différence de comportement, entre les bactéries isolées et les agrégats, en lien avec la proie de *M. xanthus*. Pour ce nouveau modèle, nous allons supposer que les bactéries isolées tuent les proies, libérant dans l'environnement des nutriments. Ces nutriments sont par la suite consommés par les agrégats de bactéries, permettant aux bactéries dans ces agrégats de pouvoir également se diviser et contribuer à la prolifération. Lorsqu'une bactérie dans un agrégat se divise nous supposons que les deux bactéries filles restent dans ce même agrégat.

❸ **La prise en compte des agrégats de taille supérieure à 2 bactéries.** Dans le précédent modèle, dans le but de simplifier le problème, nous avions uniquement des bactéries isolées et des agrégats de deux bactéries. Dans ce projet, nous étendons ce modèle aux agrégats de différentes tailles en rajoutant une structure discrète de taille. Cette hypothèse, complexifie grandement le modèle, notamment concernant les opérateurs de coagulation et de fragmentation.

Résutats principaux. Pour le nouveau modèle plus complexe, en supposant la conjecture de stabilité marginale, nous déterminons une formule explicite de la vitesse linéaire critique. Comme pour

le modèle parabolique précédent nous retrouvons deux scénarios possibles : un régime *normal* et un régime *anormal*. A l'aide de simulations numériques, nous étudions également la vitesse non-linéaire critique. Ces simulations révèlent l'existence à la fois d'un régime de front tiré et d'un régime de front poussé.

Finalement, l'étude numérique de ce modèle nous permet d'obtenir deux résultats de modélisation :

- *Nos solutions numériques sont en accord avec les expériences biologiques effectuées avec les souches de* Myxococcus xanthus. La bactérie *M. xanthus* possède deux souches $A+S-$ et $A-S+$ correspondant respectivement à une population de bactéries *M. xanthus* composée uniquement de bactéries aventureuses et à une autre population composée uniquement de bactéries sociales. Selon les résultats des expériences biologiques présentées dans l'article [137], la souche *Wild-type* (ou $A+S+$) et la souche $A+S-$ envahissent la proie *E. coli* beaucoup plus rapidement que la souche $A-S+$. Sur la base de notre modèle, nous proposons deux systèmes mathématiques correspondant respectivement aux souches $A+S-$ et $A-S+$. Nos simulations numériques donnent des résultats cohérents avec les expériences biologiques, montrant la difficulté de la souche $A-S+$ d'envahir la proie.
- *La coexistence de la motilité A et S serait un avantage pour la prédation des proies.* Comme nous l'avons spécifié dans l'introduction, les motilités A et S engendrent une grande différence entre les bactéries isolées et les agrégats de bactéries concernant les propriétés liées au mouvement comme la vitesse instantanée et le temps de persistance avant un changement de direction. Notamment, au niveau du front d'invasion, les agrégats seraient plus rapides mais en contrepartie changeraient de direction plus régulièrement. Pour savoir si ces propriétés induites par la coexistence des deux systèmes de motilité sont optimales nous avons introduit trois stratégies différentes. Dans la *stratégie 1*, il n'y aucune différence concernant la vitesse ou la persistance entre les bactéries isolées et les agrégats. La *stratégie 2* correspond à celle présente dans la nature (Agrégats plus rapides mais moins persistants). Finalement dans la *stratégie 3*, nous faisons la supposition inverse de la seconde (Agrégats moins rapides mais plus persistants). En ajoutant une contrainte, nous pouvons comparer ces trois stratégies pour déterminer la plus rapide en termes d'invasion. Il s'avère que dans le régime tiré, ces stratégies auront un résultat similaire. Par contre, dans le régime de front poussé, toutes nos simulations numériques montrent que la stratégie optimale correspond bien à la seconde, celle qui est biologiquement raisonnable. Ainsi la coexistence de motilité, selon notre modèle, entraîne une augmentation de la vitesse de prédation, ce qui pourrait, d'un point de vue évolutif, expliquer pourquoi il existe deux systèmes de motilité si différents.

2 Regime switching on the propagation speed of travelling waves of some size-structured Myxobacteria population models

This chapter corresponds to a proceedings published in the journal *ESAIM : Proceedings and Surveys*, in collaboration with Vincent Calvez, Adil El Abdouni, Ignacio Madrid, Julien Olivier and Magali Tournus [148].

2.1 Introduction

Recent developments in high-throughput cell segmentation techniques have allowed microbiologists to closely follow complexly structured bacterial populations [139]. Interactions between individuals, both cooperative and competitive, and the emergence of subpopulations with distinct behaviours, have revealed the effects that this underlying structure might have across the different scales of the population dynamics [151, 152]. One important aspect that might be affected is the way they explore their surroundings.

One interesting example of this is the behaviour of *Myxococcus xanthus*, a species of motile predatory bacteria found in soil which forms multicellular biofilms to prey on other microorganisms [153]. Thanks to high-throughput microscopy techniques, it has been shown that this biofilm has not a homogeneous structure, but is in fact composed of bacteria clusters of various sizes, from isolated individuals, to large swarms of closely packed bacteria. In particular, recent works have shown that these clusters can exhibit distinct motility behaviours, which depend on their size and composition. This affects the macroscopic motility of the biofilm during the predatory incursions [140].

In particular, the cluster structure of *M. xanthus* populations has been shown to be determined by the phenotypic heterogeneity among individual cells [140]. Indeed, *M. xanthus* cells are capable to switch between two different motility regimes, namely : the adventurous A-motility, and the social S-motility, which result from the expression of two distinct sets of genes [122]. A-motile cells can glide over the surface, using a complex protein machinery that anchors and pushes the cell forward. S-type motion, on the other hand, is contact-dependent. S-motile cells move thanks to the projection of pili, hair-like structures that grow from the cell and can attach to other cells or the surrounding extracellular matrix, to then retract and drag the cell. This movement depends on the presence of a

key component of the extracellular matrix : the exopolysaccharides (EPS). EPS is secreted and left as a chemical trail by *M. xanthus* as it moves, which allows the adhesion and cohesion of cells, thus favouring the emergence of swarms of bacteria which move collectively.

Importantly, the proportion of A-motile and S-motile cells, and therefore, the distribution of the cluster sizes, has been shown to impact the fitness of *M. xanthus* populations. On the one hand, predation is initiated by pioneer A-motile cells that explore the area around the colony first. On the other hand, the collective motion of S-motile cells can increase the efficiency of predation, since killing is contact-dependent [137]. Therefore, both motility systems play synergistic roles [140].

In this work, we aim to study the impact of cellular cohesion on the global motility of the population. In particular, we will focus on population dynamics in which individuals have an advantage when coagulating (social synergy), which is expressed as a higher motility. To that extent, we will consider some structured population models, with a spatial position variable and a structuring variable which corresponds to the cluster size. Clusters of different sizes may grow, divide, and coagulate, and based on previous observations, larger clusters will diffuse at higher rates [123].

The paper is organised as follows. In Section 2 we present the various models that we will study. First, we present a "discrete" model in which we only consider two cluster sizes : singletons of isolated A-motile bacteria, and clusters of two S-motile bacteria. Next, we present a continuous cluster-size model that generalises this model, accounting for the possibility to produce, through fragmentation and coagulation, clusters of any size. Finally we consider a derived predator-prey model, where the bi-type clustered population introduced in the first model will interact with a prey population of *E. coli*. In Section 3, we study theoretically and numerically the discrete model. In Section 4 and Section 5, we do the same for respectively the continuous model and the predator-prey model.

2.2 Proposed models and main results

2.2.1 Discrete size model

Let us consider first a minimal model in which we have isolated bacteria (i.e. clusters of size one) and paired bacteria (clusters of size two) that move in the real line. We suppose that both species are well mixed and call $p_1(x,t)$ the density of isolated bacteria, and $p_2(x,t)$ the density of clusters of size two, at a given location in space $x \in \mathbb{R}$ and at a given time $t \geq 0$. We suppose that p_1 and p_2 solve the following system of two reaction–diffusion partial differential equations :

$$\partial_t p_1 = \theta_1 \Delta p_1 - \tau_1 p_1^2 + 2\tau_2 p_2 + \alpha p_1 \left(1 - \frac{p}{K}\right), \tag{2.1}$$

$$\partial_t p_2 = \theta_2 \Delta p_2 + \frac{\tau_1}{2} p_1^2 - \tau_2 p_2, \tag{2.2}$$

with p the total number of bacteria, $p = p_1 + 2p_2$.

The first terms in the right-hand side of Equations (2.1) and (2.2) are diffusion terms, and describes respectively the spatial random movement of isolated bacteria and clusters of bacteria. We assume that $\theta_2 > \theta_1$, *i.e.* clusters spread faster than isolated bacteria. The second term $\tau_1 p_1^2$ represents the coagulation of isolated bacteria, which happens at rate $\tau_1 > 0$ and changes two isolated bacteria into one cluster of size two. The term $\tau_2 p_2$ corresponds to the fragmentation of clusters of size two, which

happens at rate $\tau_2 > 0$ and produces two isolated bacteria. Moreover, we assume that only isolated bacteria can divide. This growth term is assumed to be logistic, with growth rate $\alpha > 0$ and carrying capacity of the environment K. The model (2.1)-(2.2) is an extension of the Fisher-KPP model [59, 60], which reduces to the Fisher-KPP equation when $\tau_1 = \tau_2 = 0$ and $p_2(t = 0, \cdot) = 0$. In that case, the propagation minimal speed is well known to be given by $c^* = 2\sqrt{\alpha\theta_1}$.

Numerical simulations of this system, presented in Section 2.3, suggest the existence of travelling waves solutions for all positive parameters. Moreover, we observe two distinct regimes separated by a constant threshold level θ^* for the ratio θ_2/θ_1. When $\theta_2/\theta_1 < \theta^*$, the critical speed of the travelling wave of p is equal to the critical speed $c^* = 2\sqrt{\alpha\theta_1}$ of the equation (2.1) without coagulation and fragmentation. When $\theta_2/\theta_1 > \theta^*$, the critical speed of the travelling wave becomes strictly larger than this value. There are two possible explanations for this phenomenon : the existence of an anomalous speed [61] and the nonlinear interaction of the coagulation term. For the first phenomenon, the increase in speed is caused by the linear terms of the system, and mainly by the coupling induced by the fragmentation term. In the second case, the increase is explained by the presence of the nonlinear coagulation term, in which case the propagation front being referred to as *pushed* waves. Conversely, when the front is determined linearly, the front is called a *pulled* front. A formal definition of pulled and pushed waves in the context of the *inside dynamics* of the population can be consulted in [62]. In the next chapter [149], we show that, for $\theta_2/\theta_1 > \theta^\star$, the numerical speed of the traveling wave does not correspond to the anomalous linear speed. Therefore, in this chapter we numerically study the transition between pulled and pushed fronts. In biological terms, we conclude that when the motility of clusters is significant enough with respect to the motility of isolated bacteria, the collective behaviour of *M. xanthus* allows the whole population to propagate faster than in the asocial case. We also study the system theoretically and numerically under the assumptions $\tau_1, \tau_2 \to +\infty$. In this case, the system reduces to a scalar equation.

2.2.2 Continuous cluster-size model

Empirically, the cluster structure of *M. xanthus* swarms can vary from lonely scout cells to thousands of densely packed social bacteria. We can extend the model (2.1)-(2.2) to a general Diffusion-Growth-Fragmentation-Coagulation model, described by (2.3)-(2.6), where we define $\rho(t, x, z)$ as the density at position $x \in \mathbb{R}$ and time $t \geq 0$ of clusters of size $z \in [0, z_{max}]$ (or more precisely, the total mass or volume of the cluster, which is a continuous variable), with $z_{\max} \in \mathbb{R}_\star^+ \cup \{+\infty\}$ the maximum admissible size. The model is defined by the following integro-differential equation :

$$\partial_t \rho(t, x, z) = \partial_{xx} \left[\theta(z)\rho(t, x, z)\right] - \partial_z \left[v(z, m(t, x))\rho(t, x, z)\right] + \mathcal{F}[\rho](t, x, z) + \mathcal{G}[\rho](t, x, z), \tag{2.3}$$

with

$$\mathcal{F}[\rho](t,x,z) = 2\int_z^{z_{\max}} \beta(z')k(z',z)\rho(t,x,z')\ dz' - \beta(z)\rho(t,x,z), \tag{2.4}$$

$$\mathcal{G}[\rho](t,x,z) = \frac{1}{2}\int_0^z \gamma(z-z',z')\rho(t,x,z-z')\rho(t,x,z')\ dz' - \rho(t,x,z)\int_0^{z_{\max}-z} \gamma(z',z)\rho(t,x,z')dz', \tag{2.5}$$

and

$$m(t,x) = \int_0^{z_{\max}} z'\rho(t,x,z')\ dz'. \tag{2.6}$$

As before, the first term in (2.3) corresponds to the spatial diffusion of the clusters. The diffusion coefficient of a cluster is a function of its size. The second term in (2.3) is a transport term representing the growth of cluster size through cell division within each cluster. The function $v(z,m) \geq 0$ is the instantaneous growth speed of a cluster of size z when the total mass at its spatial position is m, as defined by (2.6). In $z = 0$, we assume this speed to be zero, hence no condition is required at this boundary. Notice that the division mechanism conveyed by this term is different than the one considered in (2.1)-(2.2), conveyed by a proliferation term. Indeed, we made the simplifying assumption that a dividing bacterium will necessarily increase the size of its cluster. We assume that this speed is zero for clusters of maximal size, $z_{\max}$. The third term in (2.3), defined in (2.4), corresponds to the fragmentation of clusters, which occurs at a fragmentation rate $\beta(z) \geq 0$, which is a function of the cluster size. When a cluster of size z' fragments, it produces two clusters of respective sizes z and $z'-z$ with probability $k(z',z)dz = k(z',z'-z)dz$. The first term in (2.4) corresponds to the creation of clusters of size z by the fragmentation of a cluster of larger size, while the second term corresponds to the loss of clusters of size z due to fragmentation into clusters of smaller sizes. Finally, the last term in (2.3) corresponds to the coagulation of clusters, as defined by the operator in (2.5). Two clusters of respective sizes z and z' coagulate at a rate $\gamma(z,z')$, which we call the coagulation rate. We assume that the coagulation rate is symmetrical, $\gamma(z,z') = \gamma(z',z)$. The first term in (2.5) corresponds to the creation of clusters of size z through the coagulation of clusters of sizes z' and $z-z'$, with $z' < z$. The second term corresponds to the loss of clusters of size z through coagulation with clusters of any other size.

The existence of travelling waves in spatial models with continuous structure has been studied by various authors in many particular cases (for example [154, 155, 156, 157]). However, to our knowledge, the existence of travelling waves in structured populations involving a coagulation operator is being studied numerically for the first time in this work. For the presented numerical simulations, we select specific functions for the fragmentation, division, and coagulation rates. For these specific choices, we exhibit numerically the existence of travelling waves connecting the null function to the stationary solution of the problem without spatial diffusion. As for the discrete model, we notice the existence of a diffusion coefficient value corresponding to a threshold. That is, for a smaller diffusion coefficient, the wave speed is constant with respect to this parameter and for a larger value, the wave speed increases.

2.2.3 Predator-resource model

M. xanthus are predator bacteria. This predation is initiated by isolated cells known as *scouts*, which explore the surroundings of the colony to identify potential nutrient sources [158]. Their attack strategy depends on several parameters, but it depends crucially on the prey density [159]. This way, as prey become scarce, *M. xanthus* increase their scouting capabilities. Once the prey has been found, they can switch behaviours to start killing the prey and consuming the nutriments released by the prey. Although the exact mechanism used by *M. xanthus* to kill its prey is not fully understood, it is known that cell killing can only occur in close proximity to *M. xanthus* (contact-dependent) [160, 133]. Moreover, cluster size structure also play an important role in predation. While the forefront of the assault is mainly constituted by singletons or small groups of scouts, the rear of the front consists of rather large clusters exhibiting distinct macroscopic behaviours, called *swarms* [140].

To model this phenomenon, we propose a new model in which we assume the existence of two additional bacterial types : diffusive individuals, which move around alone or in clusters, and eating individuals, consisting of isolated bacteria and clusters capable to kill and consume the prey, but remaining immobile. This supplementary structure gives a total of four subtypes. For this model, we consider a two-dimensional space. We denote by $\rho_1^D(x,y,t)$ the density of isolated bacteria in the diffusing state, and $\rho_1^E(x,y,t)$ the density of isolated bacteria in the eating state, which are solutions to the following equations

$$\partial_t\, \rho_1^D = \theta_1 \Delta \rho_1^D + \alpha_D \rho_1^D (1-\rho) - \tau_1^{DE}(e)\rho_1^D + \tau_1^{ED}(e)\rho_1^E - \tau_1(\rho_1^D)^2 + 2\tau_2\rho_2^D, \tag{2.7}$$

$$\partial_t\, \rho_1^E = \alpha_E(\rho_1^E + 2\rho_2^E)(1-\rho) + \tau_1^{DE}(e)\rho_1^D - \tau_1^{ED}(e)\rho_1^E - \tau_1(\rho_1^E)^2 + 2\tau_2\rho_2^E. \tag{2.8}$$

On the other hand, the density of clusters of two bacteria in diffusing state, $\rho_2^D(x,y,t)$, and those which eat, $\rho_2^E(x,y,t)$, are given by

$$\partial_t\, \rho_2^D = \theta_2 \Delta \rho_2^D + \frac{\tau_1}{2}(\rho_1^D)^2 - \tau_2\rho_2^D - \tau_2^{DE}(e)\rho_2^D + \tau_2^{ED}(e)\rho_2^E, \tag{2.9}$$

$$\partial_t\, \rho_2^E = \tau_2^{DE}(e)\rho_2^D - \tau_2^{ED}(e)\rho_2^E + \frac{\tau_1}{2}(\rho_1^E)^2 - \tau_2\rho_2^E. \tag{2.10}$$

As previously we are interested in the situation in which clusters have got an enhanced motility, so $\theta_2 > \theta_1$. Finally, the density of the prey, which is supposed to be immobile, is given by

$$\partial_t\, e = -\delta_1\rho_1^E - \delta_2\rho_2^E, \tag{2.11}$$

with δ_1 and δ_2 being the consumption rates of the prey by, respectively, isolated predatory bacteria in the "eating" state and clusters of predatory bacteria in the "eating" state. In our model, the prey bacteria corresponds solely to a resource. We do not focus on its own dynamics but on its interaction with the predatory bacteria. We assume that the dispersion of the prey is negligible.

In equations (2.7) and (2.8) we define ρ as the total of predatory bacteria, *i.e.* $\rho = \rho_1^E + \rho_1^D + 2\rho_2^E + 2\rho_2^D$. The model (2.7)-(2.11) is schematized in figure 2.1. We assume that the change between the "diffusion" state and the "eating" state is dependent on the local amount of prey. Diffusing bacteria can

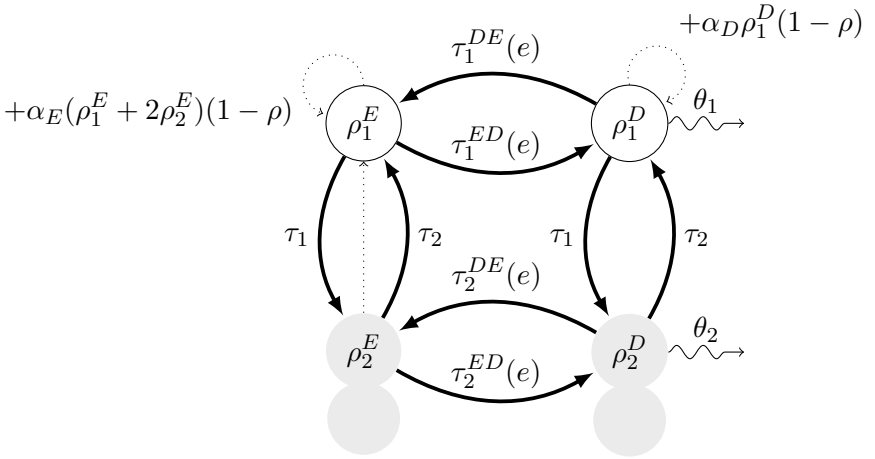

FIGURE 2.1 – Schematic representation of the model (2.7)-(2.11)

change state with a certain rate τ_i^{DE}, and conversely bacteria become diffusing with a rate τ_i^{ED}, with $i = 1$ or $i = 2$ which corresponds to the size of the cluster. For this model, we assume that a bacteria in a cluster of two bacteria consuming the prey can divide to produce an isolated bacteria. We assume that bacteria that consume have a significant division advantage compared to isolated bacteria that disperse ($\alpha_E > \alpha_D$). The transitions between the clusters of two bacteria and the isolated bacteria are the same as in the previous model. The proliferation terms are assumed to be logistic with a carrying capacity dependent on the total number of bacteria, ρ. For the model (2.7)-(2.11), the Laplacian operator only depends on space, *i.e.*, $\Delta u(x, y, t) = \partial_{xx}u(x, y, t) + \partial_{yy}u(x, y, t)$. This term corresponds to the movement of bacteria. For the biological reasons mentioned above, it is assumed that the clusters of two bacteria have a faster diffusion than the isolated bacteria, i.e. $\theta_2 > \theta_1$.

We assume that the rates of transitions between the "diffusion" and the "eating" state are linearly dependent on the density of the prey e, i.e. τ_i^{DE} and τ_i^{ED} are given by

$$\tau_i^{DE}(e) = \tau_i^{DE}e, \quad \text{and} \quad \tau_i^{ED}(e) = \tau_i^{ED}(e_{\max} - e), \tag{2.12}$$

with $e_{\max}$ the maximum in space of $e(x, y, t = 0)$. As the density of the prey e decreases over time, $e_{\max}$ corresponds to the maximum of e in both time and space.

We perform a numerical analysis of this model. Simulations for different parameters show that the model exhibits similarities with the biological experiments of predation by the *Myxococcus xanthus* bacterium. We notice that, as expected, the sociability and the strong diffusion of the clusters play an important role in the speed of predation.

2.3 Discrete size model

2.3.1 Some properties of the mathematical model (2.1),(2.2)

We consider the equivalent nondimensional system given by

$$\partial_\tau \rho_1 = \partial_{\chi\chi}\rho_1 - k_1\rho_1^2 + 2k_2\rho_2 + \rho_1(1-\rho), \tag{2.13}$$

$$\partial_\tau \rho_2 = \theta \partial_{\chi\chi} \rho_2 + \frac{1}{2} k_1 \rho_1^2 - k_2 \rho_2, \tag{2.14}$$

where $\rho_i(\chi, \tau) = p_i(x,t)/\kappa$ for $i \in \{1,2\}$, $\chi = \sqrt{\alpha/\theta_1}x$, $\tau = \alpha t$, $\theta = \theta_2/\theta_1$, $k_1 = K\tau_1/\alpha$ and $k_2 = \tau_2/\alpha$ are the only three free parameters.

This model has a unique spatially homogeneous positive equilibrium point $\rho^\star = (\rho_1^\star, \rho_2^\star)$, given by

$$\rho_1^\star = 1 - 2\rho_2^\star, \quad \text{and} \quad \rho_2^\star = \frac{2k_1 + k_2 - \sqrt{k_2(4k_1 + k_2)}}{4k_1},$$

with $\rho_1^\star + 2\rho_2^\star = 1$.

The point $(0,0)$ is another equilibrium point of the system (2.13)-(2.14). Linearising around these equilibrium points, we obtain the following Jacobian matrices

$$J(0,0) = \begin{pmatrix} 1 & 2k_2 \\ 0 & -k_2 \end{pmatrix}, \quad \text{and,} \quad J(\rho_1^\star, \rho_2^\star) = \begin{pmatrix} -2k_1\rho_1^\star - \rho_1^\star & 2k_2 - 2\rho_1^\star \\ k_1\rho_1^\star & -k_2 \end{pmatrix}.$$

The point $(0,0)$ is unstable while the point $\rho^\star$ is stable, therefore we are in a monostable case.

Asymptotics in fast fragmentation-coagulation regime.

In order to simplify the theoretical study of the system (2.13)-(2.14), we consider the limit where both rates k_1 and k_2 tend towards infinity at the same speed (in the sense that $k_1/k_2 < +\infty$ and $k_2/k_1 < +\infty$). This means that both cluster fragmentation and the coagulation of isolated bacteria occur at the same time scale, which is much faster than the growth and diffusion time scale. Equation (2.14) can be written

$$\partial_t \rho_2 - \theta \Delta \rho_2 = k_1 \left(\frac{1}{2}\rho_1^2 - \frac{k_2}{k_1}\rho_2 \right). \tag{2.15}$$

Since $k_1 \to +\infty$, we must have $\frac{1}{2}\rho_1^2 - \frac{k_2}{k_1}\rho_2 = 0$ in the RHS of Eq. (2.15). Then, recalling that $\rho = \rho_1 + 2\rho_2$ we obtain

$$\rho_1 = f(\rho) := \frac{-1 + \sqrt{1 + 4\frac{k_1}{k_2}\rho}}{2\frac{k_1}{k_2}}.$$

Therefore, since $2\rho_2 = \frac{k_1}{k_2}\rho_1^2 = \frac{k_1}{k_2} f(\rho)^2$, adding equations (2.13) and (2.14) yields

$$\partial_t \rho - \Delta \phi(\rho) = F(\rho), \tag{2.16}$$

with $\phi(\rho) := f(\rho) + \theta \frac{k_1}{k_2} f(\rho)^2$ and $F(\rho) := f(\rho)(1-\rho)$. Note that now $F(p) = 0$ if and only if $p = 0$ or $p = 1$ which are the only spatially homogeneous states. Differentiating twice the functions ϕ and F leads to

$$\phi''(x) = \frac{2k_1(\theta - 1)}{(4k_1x + k_2)\sqrt{1 + 4\frac{k_1}{k_2}x}} \quad \text{and} \quad F''(x) = -2\frac{3k_1x + k_1 + k_2}{(4k_1x + k_2)\sqrt{1 + 4\frac{k_1}{k_2}x}}.$$

Thereby, F is concave, positive and verifies $F(0) = F(1) = 0$. Moreover, we have that ϕ is convex if $\theta > 1$.

For the equation $\partial_t \rho - \theta \Delta \rho = F(\rho)$ with F concave, the minimal speed front is given by $c^* = 2\sqrt{\theta F'(0)}$ (see for instance [60]). On the other hand, the nonlinear diffusion term of Eq. (2.16) does not allow to directly apply this theory. Instead, we approach numerically the minimal speed employing a shooting method [161]. The method is based on the analysis of the phase plane $(\rho, (\phi(\rho))')$. We start by looking for solutions of the form

$$\rho(x,t) = p(x - ct), \quad (t,x) \in \mathbb{R}^2,$$

with c the unknown front speed that we want to determine. We are interested in solutions connecting the equilibrium state $p = 1$ (in $-\infty$) with the equilibrium state $p = 0$ (in $+\infty$). Then, from (2.16), we obtain

$$-cp' - (\phi(p))'' = F(p), \tag{2.17}$$

and if we set $q = (\phi(p))'$ we obtain the following system

$$\begin{cases} p' = \dfrac{1}{\phi'(p)} q, \\ q' = \dfrac{-c}{\phi'(p)} q - F(p), \\ \lim\limits_{\xi \to -\infty} p(\xi) = 1, \quad \lim\limits_{\xi \to +\infty} p(\xi) = 0. \end{cases}$$

So the problem is to find the wave speed $c \in \mathbb{R}$ and the $\mathcal{C}^2$ wave profile $p : \mathbb{R} \longrightarrow [0,1]$ that solves the previous system. For this, we perform a shooting method. We choose a certain value of c, small enough, and simulate the associated heteroclinic orbit solution p. If, at any point, p becomes negative, we reject the value of c and try a larger one, until obtaining an admissible profile. We will compare this speed with the one obtained by numerical simulations of the population dynamics. The method used and the results are given in the next paragraph and Figure 2.2, which is discussed further below.

2.3.2 Numerical simulations

We simulate Eq. (2.13)-(2.14) using a splitting method with a semi-implicit finite difference scheme. That is, we split the diffusion and reaction terms into two separate steps. For the first one, we use an implicit numerical scheme, and for the latter, we use the Runge-Kutta 4 explicit scheme.

Using this method, we numerically approximate solutions of (2.13)-(2.14) for different values of the cluster's relative diffusion coefficient $\theta > 1$ and for equal fragmentation and coagulation rates $k = k_1 = k_2 = k$. We vary both k and θ to study whether the total population density ρ behaves as a wave of the form $\rho(x,t) = u(x - ct)$ with $u(\xi) \sim \exp(-\lambda \xi)$. This exponential decay is observed in the Fisher-KPP equation and is expected from the study of the heterocline in the phase plane. The coefficient λ is the rate of exponential decay towards the stable state 0 and gives the form of the front. When we observe numerically that the density p indeed admits travelling wave solutions, we extract the values of c and λ from the simulated solutions of (2.13)-(2.14). The methods used are explained below.

Firstly, to obtain the wavespeed we compute at each time-step, $n\Delta t$, the estimator $\hat{c}_n$ defined by

$$\hat{c}_n := \sum_{j=1}^{J} \frac{\rho^n(x_j) - \rho^{n-1}(x_j)}{\Delta t} \Delta x, \tag{2.18}$$

where $\{x_j = j\Delta x\}_{j\in\{0,\dots,J\}}$ is the space grid and ρ^n is an approximation of $\rho(j\Delta x, n\Delta t)$. As $\Delta x, \Delta t \to 0$, $\hat{c}_n$ is consistent with the wavespeed. Indeed, if we suppose that we have wave solutions which are of the form $\rho(t,x) = u(x-ct)$, with $u(\xi) \to 1$ as $\xi \to -\infty$, and $u(\xi) \to 0$ as $\xi \to +\infty$, then $\partial_t \rho = -c\partial_x \rho$. Integration of this equation with respect to x gives

$$c = \int_{-\infty}^{+\infty} \partial_t \rho(t,x) dx. \tag{2.19}$$

Equation (2.18) is then a finite difference discretization of the time derivative and the spatial integral in the latter expression.

Secondly, the value λ of the exponential decay constant is computed by fitting an exponential curve to the wavefront, using a least squares estimator.

Fig. 2.2 presents the results of c (panels A and C) and λ (panel B) extracted for $\theta \in [0, 30]$ and $k_1 = k_2 = k \in [0, 15]$. We recall that in the Fisher-KPP case, we have $c = 2$ and $\lambda = 1$. In particular, these values correspond to the regime where the cluster structure does not affect the propagation speed of the population. Fig. 2.2-A and 2.2-C shows the existence of a critical diffusion coefficient θ^* near the value $\theta = 3$ such that for all $\theta < \theta^*$ the wave speed corresponds to the Fisher-KPP speed, and, for all $\theta > \theta^*$, the speed is strictly larger than the Fisher-KPP speed. In the latter case, the speed of propagation is determined by the whole front, including the clusters of bacteria, which therefore contribute to the overall acceleration. To summarise, if the diffusion coefficient of the clusters is sufficiently larger than the diffusion coefficient of isolated bacteria (around 3 times larger), the whole population advances faster than in the Fisher-KPP case. Moreover, the value of this critical θ^* appears to be a constant for all $k > 0$, so this regime switch seems to be independent of the fragmentation-coagulation rate.

The analysis of the exponential decay of the front λ can shed light on the regime switching in speed. Fig. 2.2-B shows that the critical Fisher-KPP value of $\lambda = 1$ is reached in our simulations around two lines : first, around the constant $\theta = 3$, which corresponds to the observed threshold for the speed regimes ; and second, around the line $\theta = 2 + k$. In particular, some heuristic calculations make it possible to explain formally this threshold (see Appendix A). However, it is observed that this line is not associated with a change of regime in the speed.

Finally, in Fig.2.2-C we can see the value of c approximated by the shooting method in the asymptotic $k \to +\infty$. These results, obtained trough a completely different numerical approach, confirm the independence of the threshold θ^* with respect to k and also help validate the results obtained from our numerical scheme.

2.4 Continuous cluster-size model

We make the following assumptions about the functions of the model (2.3)-(2.6)

$$\gamma(z', z) = \gamma z' z . \mathbf{1}_{z+z' \le z_{\max}}, \quad \beta(z) = \beta z, \quad v(z, m) = \alpha z(1 - m/\kappa), \quad k(z', z) = \frac{1}{z'} \mathbf{1}_{z'>z}, \tag{2.20}$$

for $z \in [0, z_{\max}]$, with $\gamma > 0$ a constant coagulation rate by squared unit of size, $\beta > 0$ a constant fragmentation rate by unit of size, $\kappa > 0$ a carrying capacity with respect to the sum of the individual

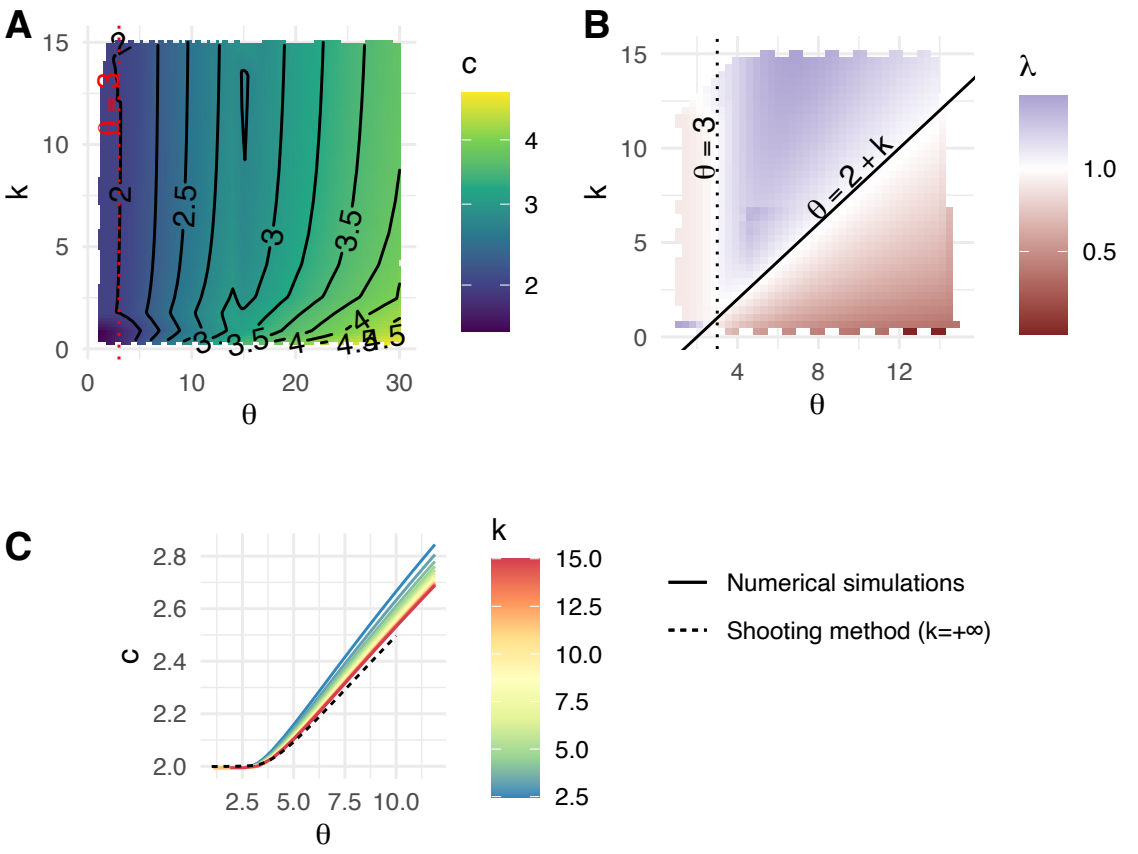

FIGURE 2.2 – Numerical results of the nondimensional system of Eq. (2.13)-(2.14) for different values of the cluster's relative diffusion coefficient $\theta > 1$ and for equal fragmentation and coagulation rates $k = k_1 = k_2$. **A.** Wavefront propagation speed c as a function of θ and k. Contour levels are also indicated along the coloured heatmap. The speed is obtained using (2.18). The critical value of $c = 2$ is reached near the ordinate $\theta = 3$, highlighted in red. **B.** Exponential decay rate λ of the total population wavefront. The line $\theta = 2 + k$ corresponds to the regime change expected by the heuristic (Appendix A). **C.** Value of the wavefront speed c as a function of the clusters' diffusion coefficient θ, for various values of k (solid line). The value predicted by the shooting method described in Section 2.3.1 in the limit $k \to +\infty$ is also presented (dotted line).

sizes of the population, and $\alpha > 0$ some constant growth rate by unit of size, and m is the total mass of the system as defined by Eq. (2.6). We assume that the function v is increasing to model the fact that the larger a cluster is, the higher the probability that one of its bacteria divides. In particular, when $m \approx 0$, the function v becomes linear, and each bacterium in a cluster has the same probability of dividing.

To begin with, we assume that the diffusion coefficient is defined by

$$\theta(z) = \theta_1, \qquad \text{for all } \ z \in [0, z_{\max}] \ . \tag{2.21}$$

Under the assumptions (2.20) and (2.21), we have the following equation for the moment of order 1,

$$\partial_t m = \theta_1 \partial_{xx} m + m\alpha(1 - m/\kappa). \tag{2.22}$$

Note that Eq. (2.22) corresponds to a Fisher-KPP equation, which admits traveling wave type solutions. Searching for a travelling wave solution for the model (2.3)-(2.6), we define the variable $\xi(t, x, z) = x - c(z)t$, where $c(z)$ is a function of z corresponding to the unknown invasion speed. We denote p the wave profile given by

$$\rho(t, x, z) = p(\xi(z), z), \tag{2.23}$$

with the following limits

$$p(-\infty, z) = f(z), \qquad p(+\infty, z) = \tilde{0}(z), \tag{2.24}$$

where $\tilde{0}$ corresponds to the null function and $f(z)$ to a stationary stable solution of the following system

$$\partial_t q(t, z) = -\partial_z \left[\alpha z(1 - M(t)/\kappa)\mathbf{1}_{z<z_{\max}}(z) q(t, z)\right] + \mathcal{F}[q](t, z) + \mathcal{G}[q](t, z), \quad \forall z \in (0, z_{\max}), \tag{2.25}$$

with

$$M(t) = \int_0^{z_{\max}} z' q(t, z') \, \mathrm{d}z'.$$

Moreover, we have $\lim_{t \to +\infty} M(t) \to \kappa$. Under the assumption $M \equiv \kappa$, equation (2.25) simplifies to the following coagulation-fragmentation equation.

$$\partial_t q(t, z) = \mathcal{F}[q](t, z) + \mathcal{G}[q](t, z). \tag{2.26}$$

In the article [162], under the assumption $z_{\max} = +\infty$, the authors derive the existence of the equilibrium profile for different assumptions than those in (2.20) regarding the functions β and γ. Nevertheless, as specified in Remark 5.2 of this article and in the article [163], it is possible to extend this result to our assumptions to obtain the profile of the stationary solution $f(z)$.

According to our numerical simulations, the equilibrium profile in the wake of the invasion front corresponds well to the stationary numerical solution of equation (2.26). For numerical simulations, we extended the method presented in Section 2.3.2.

In figure 2.3-A, we observe an example of a traveling wave type solution for the model (2.3)-(2.6). The initial data was chosen to be $\rho(x, z, 0) = \tilde{f}(z)\mathbf{1}_{x \leq 30}$, where $\tilde{f}(z)$ is the numerical solution of the equation (2.25). Between times $t = 30$ and $t = 50$, the state $\tilde{f}(z)$ spatially invades the null state.

According to our numerical simulations, for these parameter values, the speed of the traveling wave solutions of the equation (2.23) appears to be independent of z and is similar to the speed of the traveling waves of the moment of order 1 given by the equation (2.22). Traveling waves for the term m are illustrated in panel B of Figure 2.3. The colorimetry represents the progression of time, blue for $t = 0$ and red for $t = 80$. For this initial data, it is known that the selected speed of the traveling wave for m corresponds to the critical wave speed, *i.e.* $2\sqrt{\alpha\theta}$. In theory, if the system (2.3)-(2.6) admits solutions of traveling waves, the moments have them too. Moreover, the speed of the traveling waves of the moments is necessarily less than or equal to the speed of the traveling wave of the model (2.3)-(2.6).

Now, for the biological reasons mentioned above, we assume that θ is an increasing function of z. For numerical reasons, we define θ as

$$\theta(z) = \begin{cases} \theta_1 \ , & \text{si } z \leq s, \\ \theta_2 \ , & \text{si } z > s, \end{cases} \tag{2.27}$$

with θ_1, θ_2 two positive constant such that $\theta_2 > \theta_1$ and s a positive constant.

The figure 2.4 corresponds to the evolution of the numerical speed of the traveling wave of the moment of order 1 as a function of θ_2, for the model (2.3)-(2.6) with θ defined by (2.27). Once again, we observe, the existence of a threshold $\tilde{\theta}_2$. Indeed, for $\theta_2 \leq \tilde{\theta}_2$, we notice that the speed of the traveling wave seems to be very close to the speed $c_{\text{KPP}} = 2\sqrt{\theta_1\alpha}$ and becomes strictly larger for $\theta_2 > \tilde{\theta}_2$. For θ_2 sufficiently large (larger than the interval θ in Figure 2.4), we notice that the growth is of order $\sqrt{\theta_2}$, similar to the discrete model (2.1)-(2.2).

2.5 Resource-predator model

Figure 2.5 corresponds to the numerical simulation of the system (2.7)-(2.11) which takes into account two types of bacteria. The first type ρ_i^E is immobile and can consume its prey, while the second ρ_i^D diffuses. The density of the prey, for example *E. coli*, is shown in red. The green color corresponds to the density of diffusing bacteria $\rho_1^D + 2\rho_1^D$, and in blue the bacteria that consume the prey, $\rho_1^E + 2\rho_1^E$. The initial data, represented in the figure 2.5 (top panel) are chosen to be as close as possible to the biological experiments. At first the bacteria are in the "diffusion" state, looking for prey. Some of the diffusing bacteria will, on contact with the prey, change state to become bacteria that consume the prey. This behavior tends to reduce the spread of predation in areas with high prey density. For example, the propagation of predatory bacteria is faster in the middle of *E. coli* than on these edges with a higher initial density (See Figure 2.5 lower left panel). Gradually, the prey will be consumed and will disappear.

To understand the importance of sociability in predator propagation, we define a model similar to the system (2.7)-(2.11) for which isolated bacteria cannot regroup to form a cluster. The model is

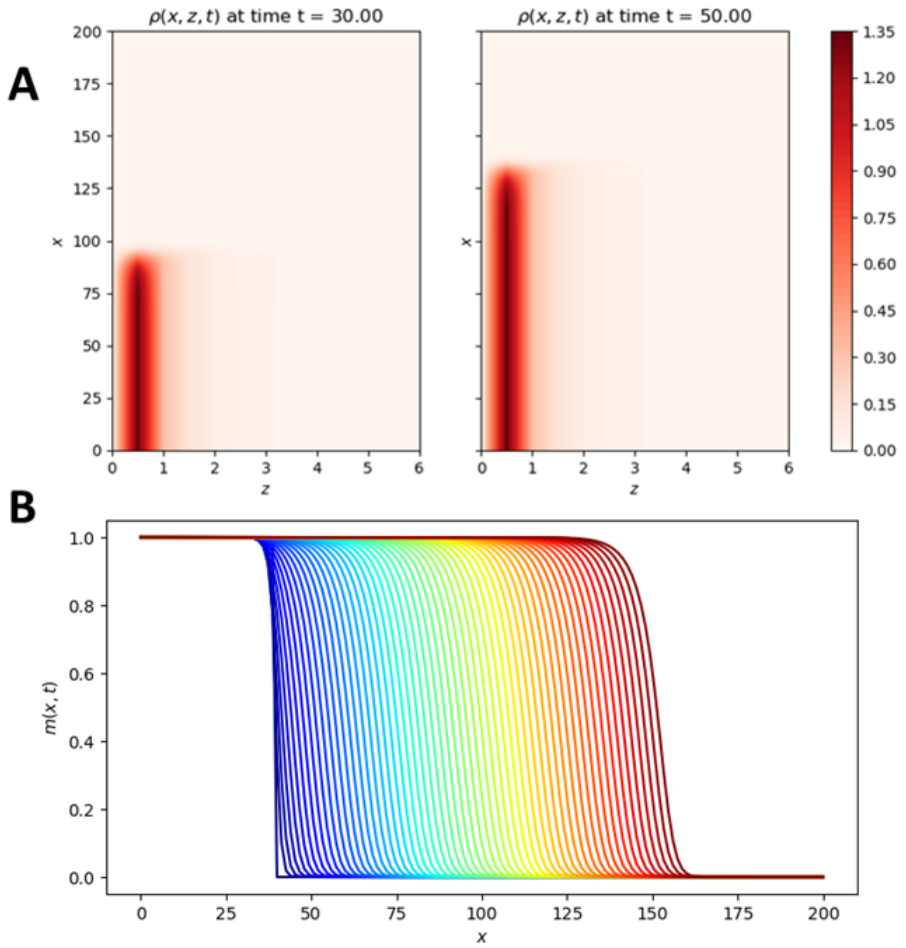

FIGURE 2.3 – **A.** Example of a traveling wave for the model (2.3)-(2.6) under the assumptions (2.20) and (2.21). The state $f(z)$ spatially invades the state $\tilde{0}(z)$ for all z. Concerning the initial data, we assume that, at time $t = 0$, the density is given by $\rho(x, z, 0) = f(z)\mathbf{1}_{x \leq x_0}$ with some positive constant x_0. The parameter values are $\theta_1 = 1$, $\alpha = 1$, $\beta = 1$, $\gamma = 1$, $\kappa = 1$. **B.** Representation over time of the numerical solution $m(x, t)$. The color represents the time, blue $t = 0$ to red $t = T_{\text{end}}$ and the colorimetry is linear. The initial data and parameter values are the same as above.

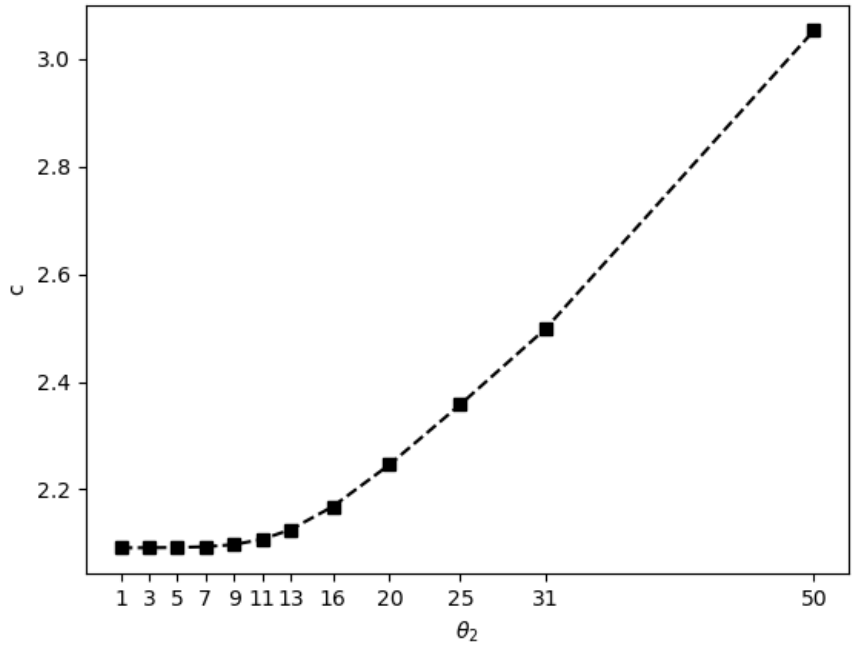

FIGURE 2.4 – Speed of the traveling wave of the equation (2.22), obtained by numerical simulations, for different θ_2, under assumption (2.27). Similarly to the discrete model, there is a threshold $\tilde{\theta}_2$ such that for all $\theta_2 \leq \tilde{\theta}_2$ the speed of the wave is $c_{\text{KPP}} = 2\sqrt{\alpha\theta_1} = 2$, and for $\theta_2 > \tilde{\theta}_2$, the speed becomes strictly higher than the speed c_{KPP}. The parameter values are similar to those in Figure 2.3.

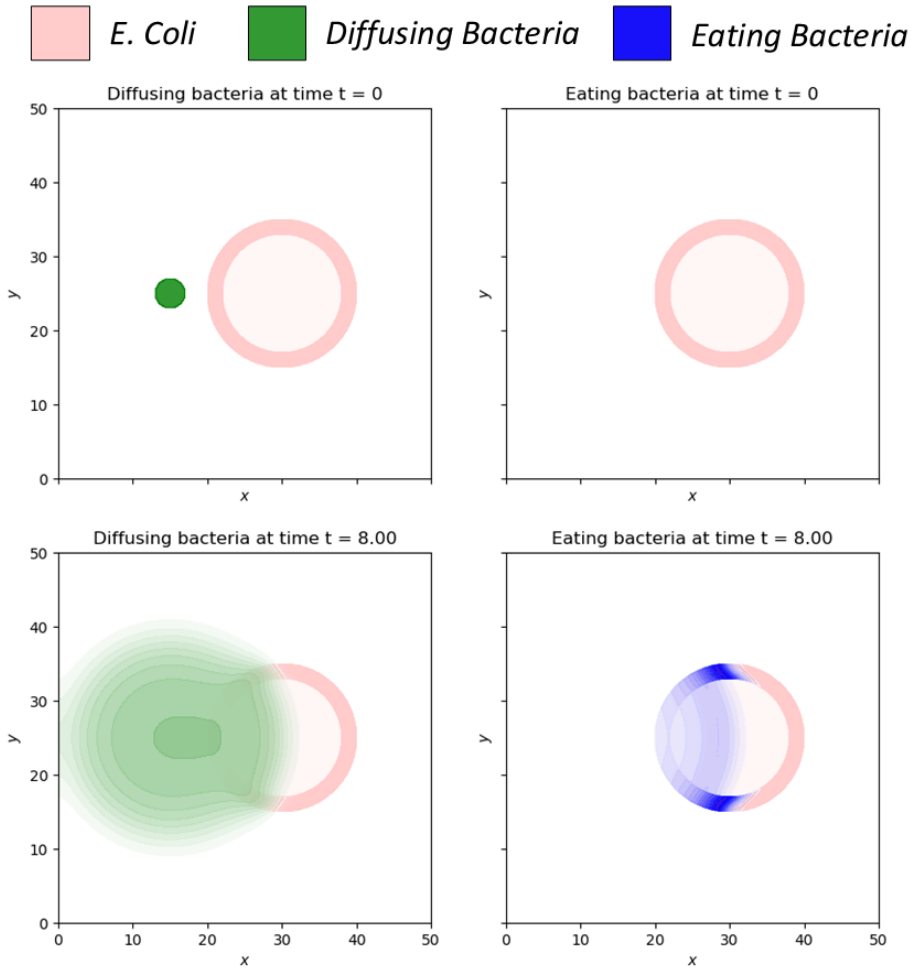

FIGURE 2.5 – Numerical simulations of the model (2.7)-(2.11), under the assumption (2.12). The density of bacteria that diffuse, $\rho_1^D + 2\rho_2^D$, is represented in green and the density of bacteria that consume the prey, $\rho_1^E + 2\rho_2^E$, is represented in blue. The prey density, e, is represented in red. The initial data are shown in the top panel, they are chosen to be as close as possible to the biological experiments. The initial distribution of predatory bacteria is assumed to be homogeneous on a circle, while the initial distribution of prey is assumed to be arranged on a circle with a higher density at the edges. At time $t = 0$, there are no predatory bacteria in the "eating" state. The bottom panel represents the densities at time, $t = 8$, where predatory bacteria have spread and reached the prey, which then began to consume the prey. The parameter values for this numerical simulation are $\theta_1 = 1$, $\theta_2 = 2$, $\alpha_D = 1$, $\alpha_E = 3$, $\tau_1 = 2$, $\tau_2 = 1$, $\tau_1^{DE} = \tau_2^{DE} = 1$, $\tau_1^{ED} = \tau_2^{ED} = 1$, $\delta_1 = \delta_2 = 2$.

defined by

$$\begin{cases} \partial_t \rho_1^D = \theta_1 \Delta \rho_1^D + \alpha_D \rho_1^D (1-\rho) - \tau_1^{DE}(e)\rho_1^D + \tau_1^{ED}(e)\rho_1^E, \\ \partial_t \rho_1^E = \tau_1^{DE}(e)\rho_1^D - \tau_1^{ED}(e)\rho_1^E + \alpha_E \rho_1^E (1-\rho), \\ \partial_t e = -\delta_1 \rho_1^E, \\ \rho = \rho_1^D + \rho_1^E. \end{cases} \tag{2.28}$$

In the figure 2.6 we observe the importance of sociability on the speed of predation. The left part corresponds to the numerical simulation of the model (2.28) at time $t = 0$ and at time $t = 8$ and on the right it corresponds to the numerical simulation of the system (2.7)-(2.11) at the same times. For both simulations we take similar initial data and parameters shared by both models have the same values. Under these assumptions, we observe in Figure 2.6 (bottom panel) that for the (2.7)-(2.11) model, the prey, shown in red, is consumed faster.

The speed of predation is strongly correlated with the value of the parameter θ_2. Contrary to the previous model, the lesser advantage given to clusters has an effect on the predation speed. The figure 2.7 corresponds to two numerical simulations of the system (2.7)-(2.11) at time $t = 8$ for two different coefficients θ_2. The other parameter values and the initial data are similar. The prey density, represented in red, is much lower for a larger θ_2 coefficient. We observe that the speed of predation is an increasing function of $\theta := \theta_2/\theta_1$, for $\theta > 1$.

2.6 Conclusions and perspectives

We studied the effect of social behaviour on the motility of *Myxococcus xanthus* populations. Previous *in vitro* experiments have shown that the capacity to form clusters of bacteria that move collectively begets an enhanced predation efficiency. Our numerical experiments shed some light on this phenomenon. We have first considered a minimal model in which isolated bacteria are able to form clusters of two bacteria that diffuse collectively. The simulations suggest that when the clusters diffuse at least 3 times faster than the isolated individuals, the speed of propagation of the whole population is larger than the critical Fisher-KPP speed. Otherwise, if clusters do not diffuse fast enough, the speed of the population is limited by the propagation speed of isolated individuals. The threshold separating these two regimes seems to be unique and independent of the rates of fragmentation and coagulation. In particular, using a shooting method, the same regime separation was found numerically in the asymptotic case of infinitely fast fragmentation and coagulation.

We also considered two extensions. First, we studied a continuous cluster-size model expressed as an integro-differential equation with fragmentation and coagulation operators. Under biologically relevant parameterizations for these operators, we show that the total sum of cluster sizes (first order moment) of the structured population exhibit travelling waves whose speed is also characterised by a threshold in the diffusion coefficient, below which the speed coincides with Fisher-KPP critical speed. This result seems to extend the regime separation observed in the discrete case to a more general class of population dynamics. In this case, as the population wavefront advances, the cluster structure of the rear of the wave is distributed according to the steady-state distribution of cluster sizes, and the travelling wave connects the steady-state to the null function.

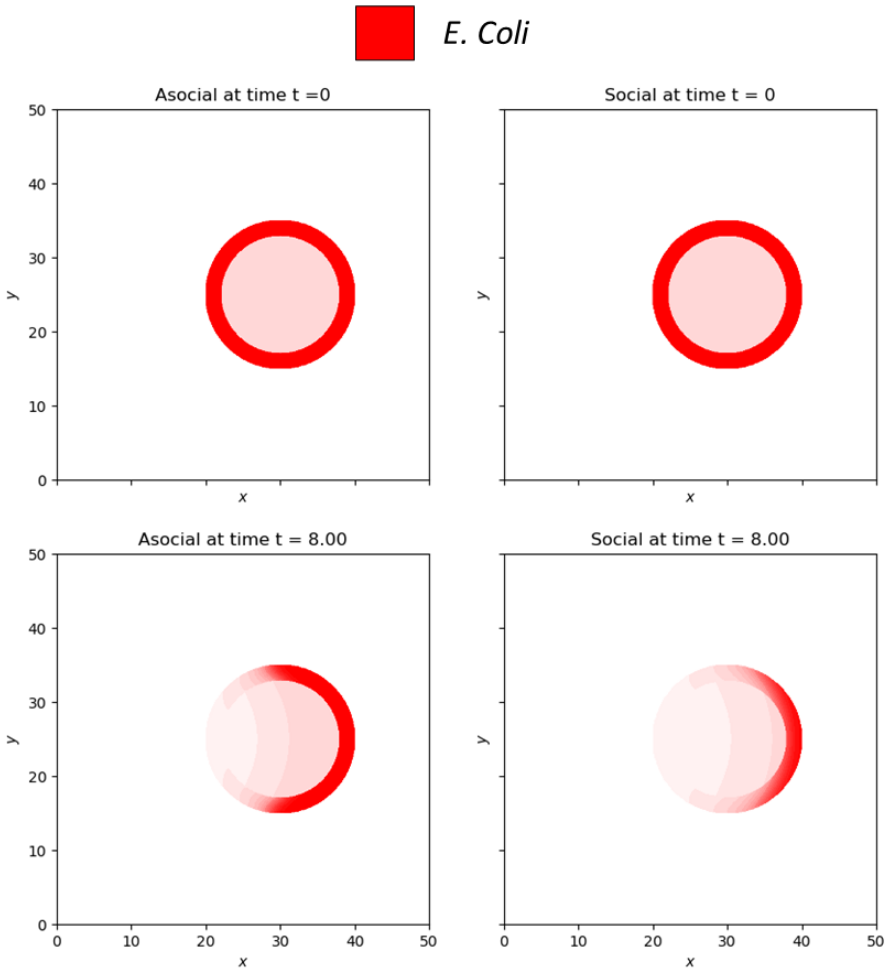

FIGURE 2.6 – The distribution of *E. coli* at time $t = 0$ (top) and $t = 8$ (bottom) is represented in red, for the model (2.28) (left) and for the model (2.7)-(2.11) (right). For both simulations, we assume the linear transition hypothesis (2.12). We assume that there are no advantages/disadvantages other than diffusion, therefore $\delta_2 = \delta_1$, $\tau_2^{ED} = \tau_1^{ED}$ and $\tau_2^{DE} = \tau_1^{DE}$. Under this assumption, predation is faster for the model (2.7)-(2.11) than for the model (2.28). The values of the parameters are the same as in figure 2.5.

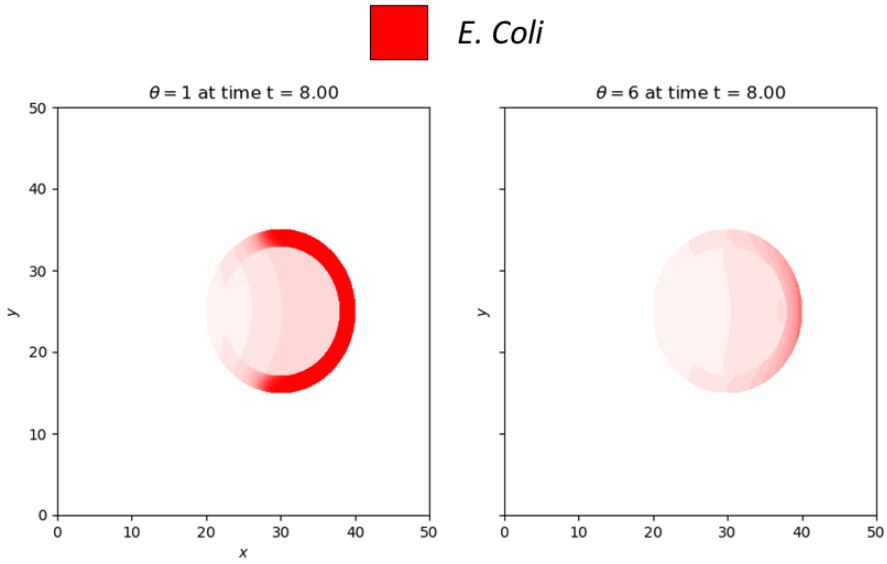

FIGURE 2.7 – Numerical simulations of the model (2.7)-(2.11) with different diffusion coefficients. The distribution of *E. coli* is represented in red at time $t = 8$ with the same initial data. The coefficient θ is defined as the ratio of θ_2 and θ_1, *i.e.* $\theta := \theta_2/\theta_1$ and corresponds to the advantage/disadvantage of cluster diffusion. For the simulation on the left, we assume that $\theta = 1$ and for the simulation on the right we assume that $\theta = 6$. The values of the other parameters are the same for both simulations and are those in figure 2.5.

Finally, we considered an extended model in which both isolated and clustered bacteria have the ability to switch towards an *eating* state when they encounter a positive density of prey. However, they become immobile in this state. With the purpose of observing the effect of clusters in the predatory efficiency, we compared the propagation fronts obtained in presence and absence of clustering. Numerical simulations indicate that the prey is consumed faster when bacteria are allowed to cluster. In this case, the speed of predation is an increasing function of the ratio of the diffusion coefficients of clusters and isolated bacteria.

Regime separation in the discrete case, particularly in the fast fragmentation-coagulation asymptotic, can motivate some theoretical investigations that are not explored here. For example, approaches relying in the variational characterisation of the wave speed can be adapted to obtain bounds on the diffusion threshold θ^*. The numerical simulations can also be extended to include some more realistic cases, taking into account the complex cluster structure of swarms and scouts.

A Heuristics on the $\theta = 2 + k$ threshold line

We give some explanations on the critical threshold $\theta = 2+k$ observed in Fig. 2.2-B at which $\lambda = 1$. To that extent, we assume the existence of a wavefront solution $\rho(t, x) = \rho(x - ct)$ with unknown speed c. Let $\xi = x - ct$. PDE system (2.13)-(2.14) reduces to the following system of second-order ODE on

the variable z :

$$\begin{cases} -c\partial_\xi \rho_1 = \partial_{\xi\xi}\rho_1 - k_1\rho_1^2 + 2k_2\rho_2 + \rho_1\left(1-\rho\right), \\ -c\partial_\xi \rho_2 = \theta\partial_{\xi\xi}\rho_2 + \dfrac{1}{2}k_1\rho_1^2 - k_2\rho_2, \\ \rho = \rho_1 + 2\rho_2. \end{cases}$$

Now, let's suppose that in the forefront of the population the number of isolated individuals and clusters is such that we are under the following hypothesis

$$(H_0): \qquad \rho_1^2 \ll \rho_2 \ll \rho_1.$$

Under (H_0), the first ODE becomes

$$-c\rho_1 = \partial_{\xi\xi}\rho_1 - \rho_1.$$

This is equivalent to the linearisation of Fisher-KPP Equation, for which the critical speed is $c = 2$. Moreover, the solution profile is of the form $\rho_1(z) = C_1\exp(-\lambda\xi)$, with $\lambda = 1$. Now, let's come back to the second ODE and replace ρ_1. We get

$$-c\partial_\xi\rho_2 - \theta\partial_{\xi\xi}\rho_2 + k_2\rho_2 = \frac{k_1}{2}C_1^2 e^{-2\lambda\xi}.$$

We solve this equation finding a solution of the form

$$\rho_2(\xi) = Ae^{-\mu\xi} + Be^{-2\lambda\xi}.$$

In particular, for the particular solution, the constant B is such that

$$\left(2\lambda c - 4\theta\lambda^2 + k_2\right)B = \frac{k_1}{2}C_1^2.$$

Thus, at the critical value $\lambda = 1$ we obtain

$$\left(2c - 4\theta + k_2\right)B = \frac{k_1}{2}C_1^2,$$

which for $2c - 4\theta + k_2 \neq 0$ begets

$$B = \frac{C_1^2 k_1}{2\left(2c - 4\theta + k_2\right)}.$$

On the other hand, for the constant μ, we have :

$$c\mu - \theta\mu^2 + k_2 = 0.$$

Thus, for $\Delta = c^2 + 4\theta k_2 > 0$, we obtain the solutions :

$$\mu_\pm = \frac{-c \pm \sqrt{c^2 + 4\theta k_2}}{-2\theta} = \frac{c \mp \sqrt{c^2 + 4\theta k_2}}{2\theta}.$$

Since $\mu_+ < 0$, we consider only the solution with $\mu = \mu_-$. The critical transition should occur when H_0 is not verified anymore, and thus the nonlinear effects are not negligible. In particular, when we are just at the threshold level, we also have the critical Fisher-KPP values $\mu = 1$ and $c = 2$ which gives

$$\sqrt{1 + \theta k_2} = \theta - 1,$$

from which we derive the relation $\theta = 2 + k_2$. Therefore we should expect that, at fixed k_2, (H_0) is violated for all $\theta > 2 + k_2$.

3 Travelling waves for a fast reaction limit of a discrete coagulation-fragmentation model with diffusion and proliferation

This chapter corresponds to an article published in the journal *Journal of Mathematical Biology*, in collaboration with Thomas Lepoutre [149].

3.1 Introduction

Recent advances in both high-throughput microscopy techniques and cell segmentation techniques have significantly advanced our knowledge of bacterial populations, particularly in the bacterium *Myxococcus xanthus* [139]. Within a bacterial population, individuals have regular interactions with other individuals, which can be cooperative or competitive [151, 152]. In this chapter we are interested in the modeling of the propagation of the motile bacterium *Myxococcus xanthus* and more particularly how the interactions between the different individuals could influence the propagation speed of the bacterium. This family of bacteria forms multicellular biofilms with a complex structure that is highly heterogeneous in time and space [164, 140]. They are composed of a wide variety of bacterial cluster sizes that vary greatly with the amount of local prey. Among the bacteria within these biolfilms, there is also a strong difference in behavior. Indeed, bacteria have two different motility regimes : adventurous motility A and social motility S, which depend on the expression of two distinct sets of genes [122]. The A cells, which move by gliding over the surface in search of prey, tend to be isolated bacteria. On the other hand, S cells tend to form large clusters and move thanks to the projection of pili allowing them to cling to other bacteria. These two motilities have synergistic roles in prey predation.

The size distribution of bacterial clusters is highly heterogeneous depending on their position in the predation front. Upstream of the front, there are mainly isolated bacteria or groups of small sizes. The further away from the invasion front, the more large clusters of bacteria are found in proportion to the distance [140]. The speed of bacteria is also heterogeneous and depends on the size of the clusters. Indeed the average speed of isolated bacteria tends to be slower than the average speed of bacteria in clusters [123, 140]. In this chapter we are mathematically interested in the possible impact of the diffusion advantage that groups of bacteria have on the speed of invasion of the bacterium *Myxococcus*

xanthus. For this, we will theoretically study the model introduced in the previous chapter [148], which models the spread of the social bacterium *Myxococcus xanthus*. We briefly explain this model below.

In this model, clusters of bacteria have two possible sizes : clusters of size 1 that we will also call isolated bacteria and clusters composed of two bacteria. The density of isolated bacteria is denoted by p_1, while the density of pairs of bacteria is denoted by p_2, both depending on space and time. These two densities satisfy the following system of two reaction-diffusion equations

$$\begin{cases} \partial_t p_1 = \theta_1 \Delta p_1 - \tau_1 p_1^2 + 2\tau_2 p_2 + \alpha p_1(1 - p/K), \\ \partial_t p_2 = \theta_2 \Delta p_2 + \dfrac{\tau_1}{2} p_1^2 - \tau_2 p_2, \end{cases} \tag{3.1}$$

where p corresponds to the total number of bacteria, $p := p_1 + 2p_2$. For simplicity, we consider the problem in one-dimensional space $x \in \mathbb{R}$, so the Laplacian operator becomes $\Delta = \partial_{xx}$. The coefficients θ_1 and θ_2 correspond to the diffusion coefficients of isolated and paired bacteria respectively. For the biological reasons described above [123], we assume that $\theta_2 > \theta_1$, i.e. the diffusion coefficient of the groups of bacteria is greater than the diffusion coefficient of the isolated bacteria. The coagulation term is represented by the term $\tau_1 p_1^2$, which models the encounter between two isolated bacteria creating a cluster of two bacteria. The term, $\tau_2 p_2$, corresponds to the fragmentation of a pair of bacteria creating two isolated bacteria. The rates τ_1 and τ_2 correspond to the coagulation rate and the fragmentation rate respectively. Finally, we assume that bacteria must be isolated to divide, this term is modeled by the growth term in the first equation of (3.1). This growth is assumed to be logistic, with growth rate $\alpha > 0$ and carrying capacity K. In the article [140], biological experiments on the bacterium *Myxococcus xanthus* show that the coagulation rate and the fragmentation rate are quite similar. Therefore it is assumed that the rates τ_1 and τ_2 are both equal to the same positive constant denoted by τ.

One equivalent nondimensional system of equations (3.1) is given by

$$\begin{cases} \partial_t p_1 = \partial_{xx} p_1 - k p_1^2 + 2k p_2 + p_1 \left(1 - p\right), \\ \partial_t p_2 = \theta \partial_{xx} p_2 + \dfrac{1}{2} k p_1^2 - k p_2, \end{cases} \tag{3.2}$$

where $k = K\tau/\alpha$, and $\theta = \theta_2/\theta_1$ are the two free parameters of the system. The coefficient $\theta > 1$ corresponds to the diffusion advantage of groups of bacteria compared to isolated bacteria. This system (3.2) admits a unique positive equilibrium point which we note $(p_1^\star, p_2^\star)$, we are thus in the monostable case [148].

In this chapter we are interested in the propagation speed of the system (3.2). It is characterized as the minimal admissible speed for a positive travelling waves solution. We are especially interested in the influence of the parameter value θ on this speed. Travelling waves for spatial fragmentation models with continuous or discrete structure have been already studied theoretically by various authors in many particular cases (See for example [154, 165, 156, 157]). This propagation speed may sometimes correspond to the speed of the linearized problem, in which case the front is referred to as 'pulled'. Conversely, when the linear prediction is incorrect, we designate such fronts as 'pushed' fronts [40]. In Section 2 of the chapter, we briefly recall the derivation of the linear spreading speed of the system

(3.2) already derived in the article [54] and given by the following formula

$$c_{lin}(\theta,k)=\begin{cases}2, & \text{when } \theta\leq 2+k,\\ \sqrt{\dfrac{k+1}{\theta-1}}+\sqrt{\dfrac{\theta-1}{k+1}}, & \text{when } \theta>2+k.\end{cases} \tag{3.3}$$

Using this theoretical formula and the numerical simulations presented in the previous chapter [148], we propose the following conjecture.

Conjecture 2:
There exists a threshold $\theta^\star$ such that the critical nonlinear spreading speed c of the system (3.2) is given by

$$c=\begin{cases}c_{lin}(\theta,k), & \text{when } \theta\leq\theta^\star(k), \quad (\text{Pulled case})\\ \bar{c}(\theta,k)>c_{lin}(\theta,k), & \text{when } \theta>\theta^\star(k), \quad (\text{Pushed case})\end{cases}$$

for $k>0$, where c_{lin} is the linear critical speed defined in (3.3).

Fast reaction limit. In this paper we are mainly interested in the fast fragmentation-coagulation limit, which mathematically corresponds to the limit when k tends to $+\infty$. Biologically this corresponds to the assumption that fragmentation and coagulation occur on a faster time scale than other interactions in the system, such as diffusion or division. In the literature, this kind of fast reaction limit has already been studied and justified for models close to the system (3.1). For example, in the article [166], the authors work on the fast reaction limit for the Aizenman-Bak model of coagulation-breakup with spatial diffusion [167, 168]. Under this assumption, we will see that the system (3.2) simplifies into a simple Fisher-KPP type equation that can be studied theoretically. This regime has already been studied numerically in the previous chapter [148] using a shooting method. Moreover the authors show numerically that the results obtained in the asymptotic case $k=+\infty$ are similar to the numerical experiments for k assumed to be large enough.

The approximation of fast fragmentation-coagulation leads to the study of a scalar nonlinear reaction-diffusion equation, for which we prove our main result :

Main Result *For the fast coagulation-fragmentation limit, $k=+\infty$, the linear speed is given by*

$$c_{lin}(\theta,\infty)=2.$$

Moreover the conjecture 2 is true in this case, more precisely there exists $\theta^*\in[2,6.5]$, such that :

- *When $\theta\in[1,\theta^\star]$, the invasion speed is equal to 2, and the front is pulled. This case corresponds to a predation speed solely governed by isolated bacteria in which the diffusion advantage of the clusters does not affect the invasion of the bacterium Myxococcus xanthus.*
- *When $\theta>\theta^\star$, the invasion speed is strictly greater than 2, and the front is pushed. In this case, the diffusion advantage of the bacterial clusters leads to a faster invasion.*

The plan of the paper is the following : In section 2, we recall the linear spreading speed and the nonlinear speed is compared numerically with the linear speed. In section 3, we study the fast fragmentation-coagulation limit. For this case, we prove the existence and the uniqueness of a transition

between pulled and pushed fronts, as well as an estimate of it. In addition, estimates of the asymptotic critical speed are given.

3.2 General case

Theoretical linear spreading speed

In this section, we briefly recall the results obtained in article [54], which also apply to our system. The method is also explained in more detail in the article [55]. The linearized form of the system (3.2) around the equilibrium state $(0,0)$, and in the moving frame $\xi = x - ct$, is rewritten as follows

$$\begin{cases} \partial_t p_1 = c\partial_\xi p_1 + \partial_{\xi\xi} p_1 + p_1 + 2kp_2, \\ \partial_t p_2 = c\partial_\xi p_2 + \theta\partial_{\xi\xi} p_2 - kp_2. \end{cases} \tag{3.4}$$

Holzer proved in the article [54] that the linear propagation speed can be deduced from the analyticity, or lack of analyticity, of the pointwise Green's function associated with the system (3.4). The dispersion relation for the (3.4) system is given by,

$$D_c(\nu,\lambda) = \left(\nu^2 + c\nu + 1 - \lambda\right)\left[\theta\nu^2 + c\nu - k - \lambda\right], \tag{3.5}$$

which corresponds, by the skew-product nature of the coupling, to the product of the two dispersion relations D_1 and D_2 given by

$$D_1(\nu) := \nu^2 + c\nu + 1 - \lambda = 0,$$
$$D_2(\nu) := \theta\nu^2 + c\nu - k - \lambda = 0.$$

The roots of these dispersion relations are denoted by $\nu_1^\pm$ and $\nu_2^\pm$ respectively. The singularities of Green's function correspond to pairs $(s^\star, \lambda^\star)$ such that the dispersion relation (3.5) admits a pinched double root, i.e. when $(s^\star, \lambda^\star)$ satisfies,

$$D_c(\lambda^\star, \nu^\star) = 0, \qquad \partial_\nu D_c(\lambda^\star, \nu^\star) = 0, \qquad \text{Re } \nu^\pm(\lambda) \to \pm\infty \text{ as Re } (\lambda) \to \infty.$$

This happens when one of these relations is satisfied

$$\nu_1^+(s,\lambda) = \nu_1^-(s,\lambda), \tag{3.6}$$

and

$$\nu_1^\pm(s,\lambda) = \nu_2^\mp(s,\lambda). \tag{3.7}$$

Equality (3.6) gives us the expected speed, denoted by c_1,

$$c_1 = 2.$$

This speed, corresponds to the speed of the problem (3.2) when only isolated bacteria are considered, i.e. when the problem is decoupled ($k = 0$) and without bacteria clusters at initial time (p_2^0 equal to the null function). In this case the system of equations (3.2) simplifies to the following Fisher-KPP scalar equation,

$$\partial_t p_1 = \partial_{xx} p_1 + p_1(1 - p_1), \tag{3.8}$$

This equation has been extensively studied (see [59, 60, 169], among many others), and it has been shown that the critical speed is equal to $c_1 = 2$.

The second equality (3.7) gives us another speed, called anomalous speed, which is given by the following formula

$$c_{anom} = \sqrt{\frac{k+1}{\theta-1}} + \sqrt{\frac{\theta-1}{k+1}}. \tag{3.9}$$

Anomalous propagation refers to a scenario, at first sight unexpected, in which the coupling of two equations results in a critical speed faster than those of two decoupled components. That is, in our case, a spreading speed strictly greater than $c_1 = 2$. This phenomenon was first observed in article [61], and subsequently rigorously studied in [54, 170, 50].

In our case, this anomalous speed exists when the parameter value $\theta > 2 + k$, therefore the linear propagation speed c_{lin} is given by

$$c_{lin} = \begin{cases} 2, & \text{when } \theta \leq 2 + k, \\ c_{anom}, & \text{when } \theta > 2 + k. \end{cases}$$

Linear spreading speed versus Nonlinear spreading speed

In order to estimate the propagation speed, we simulate the system with initial conditions corresponding to Heaviside step functions,

$$p_1(x, t = 0) = p_1^\star \mathbf{1}_{x\leq 0}(x), \qquad p_2(x, t = 0) = p_2^\star \mathbf{1}_{x\leq 0}(x).$$

First, we compare the linear threshold $\theta_{lin} = 2 + k$ with the threshold of the non-linear system. In figure 3.1, we illustrate, the separation between the two possible regimes of the linear problem. The grey area corresponds to the zone of parameter values (k, θ) for which the linear speed is strictly greater than the expected speed $c_1 = 2$.

In the previous chapter [148], the authors illustrate an equivalent figure for the general system (3.2). For the nonlinear system, a large part of this zone is not predicted by the linear analysis. Consequently, for the spreading speed of the system (3.2), the theoretical linear threshold θ_{lin} is not adequate to predict the nonlinear speed behavior. On the other hand, the numerical simulations carried out in the previous chapter [148], show a notable difference concerning the exponential decay rate of the wave of $p = p_1 + 2p_2$ between the two zones separated by θ_{lin} (See Fig. 2 of [148]). Note that the theoretical linear threshold, in the asymptotic case $k \to \infty$, corresponds to $\theta_{lin} \to +\infty$. However, as we will see in the next section, we can theoretically prove that the speed c of the system (3.2) is strictly greater than the speed $c_1 = 2$ for $2 < \theta < 6.6$, which theoretically demonstrates that in our case the linear speed is not a good predictor of the nonlinear speed.

We also compare the anomalous linear spreading speed given by (3.9) with the speed of the system (3.2), determined using numerical simulations. In figure 3.2 we plot the theoretical "normal" (in red) and anomalous (in blue) linear spreading speed given by the formula (3.3) as well as the nonlinear speed of the general system (in black), for different values of θ. For θ large enough, the linear speed

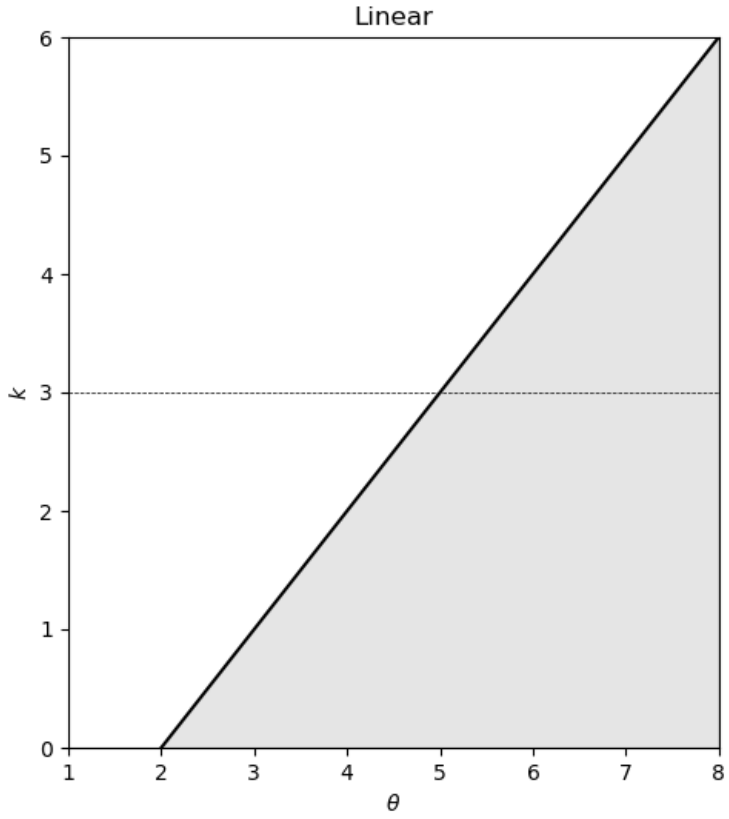

FIGURE 3.1 – The gray zones correspond to the zones for which the spreading speed is strictly greater than $c_1 = 2$. For the linear spreading speed, the threshold corresponds to the line $\theta \mapsto \theta - 2$. The horizontal dotted line, at $k = 3$, represents the choice of parameter value made for figure 3.2.

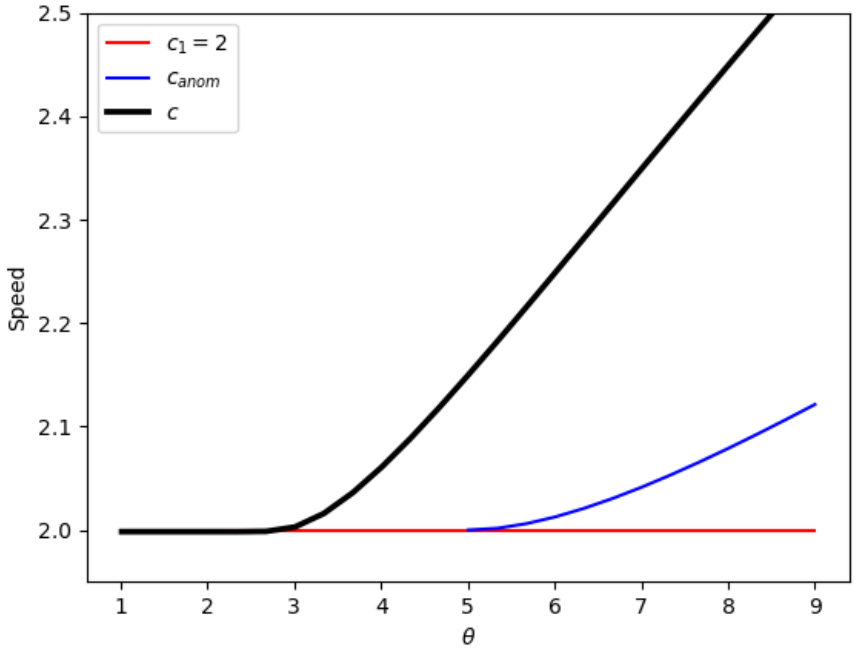

FIGURE 3.2 – Comparison of the linear spreading speed c_{lin} with the experimental speed of the system (3.2) for $k = 3$ and different values of θ. We notice that for θ large enough, the numerically derived spreading speeds, represented in black, are strictly greater than linear spreading speeds.

differs greatly from the nonlinear speed. Moreover, we notice, numerically, that this linear speed is always a lower bound of the nonlinear speed. Contrary to the scalar equations, linear speed is not necessarily a lower bound of the nonlinear speed. This result was shown for a competitive Lotka-Volterra model in the article [53]. We can thus conclude from figure 3.2 that for θ large enough, the problem is not linearly determined.

Note that in the asymptotic case $k \to 0$, the nonlinear speed seems to tend towards the linear speed. In figure 3.3, we represent the speed obtained using numerical experiments for the general system (black $\times$) and we compare it to the theoretical linear speed (red $\cdot$) for a chosen very small k ($k = 1\mathrm{e}-6$) and for different values of θ. We notice that these two speeds are very close to each other. From this figure we propose the following conjecture :

Conjecture 3:

In the asymptotic case $k \to 0^+$, the nonlinear speed is predicted by the linear speed, i.e.

$$\lim_{k \to 0^+} c(k, \theta) = c_{lin}(0, \theta).$$

The numerical simulations in the previous chapter [148] and in this chapter corroborate the conjecture 2. However, they do not allow us to conclude whether or not there really is a pulled front. Indeed, with the help of numerical simulations we can obtain an experimental speed which is close, to a certain accuracy, to the real speed. Thus, using the experimental speed we cannot know for certain when we are in a pulled front regime corresponding to a critical speed equal to the linear speed. Moreover, even

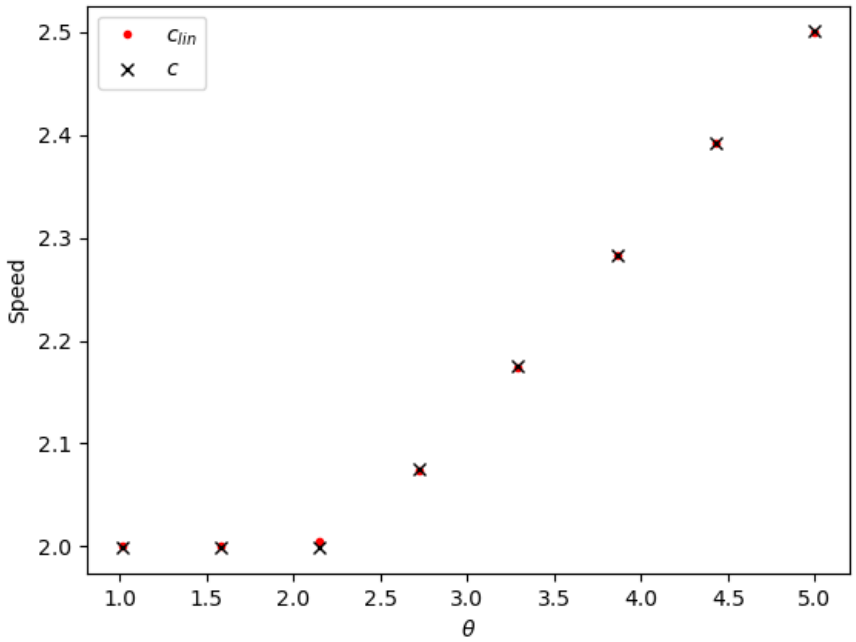

FIGURE 3.3 – Comparison of the linear spreading speed c_{lin} with the experimental speed of the system (3.2) for a very low parameter value k, $k = 1e-6$. The $\times$ in black represent numerically derived spreading speeds of the the system (3.2) and the red $\cdot$ represent the linear spreading speeds given by (3.3). In the asymptotic case $k \to 0^+$, the linear spreading speed seems to be an accurate prediction of the critical speed of the general system.

assuming that there is a pulled front regime for a sufficiently small θ, it is numerically very complex to identify, with certainty, the location of the transition between pulled and pushed fronts. This reason motivates us to study theoretically, the possible transition between pulled and pushed front for the system (3.2).

3.3 Fast fragmentation-coagulation regime

3.3.1 Derivation of an equivalent equation for travelling wave in the limit.

In the limit case $k \to +\infty$, we necessarily have $2p_2 = p_1^2$. Using the definition of p, this gives us the following relation

$$p - p_1 - p_1^2 = 0. \tag{3.10}$$

Therefore there is a function f such that $p_1 = f(p)$, with $f : p \to (\sqrt{1+4p} - 1)/2$. Under the assumption $k = +\infty$, the system (3.2) becomes a single nonlinear equation defined by

$$\partial_t p = \partial_{xx}(\phi_\theta(p)) + F(p), \tag{3.11}$$

with

$$F(p) = f(p)(1-p), \qquad \phi_\theta(p) = f(p) + \theta f(p)^2. \tag{3.12}$$

We express equation (3.11) in the following more conventional equivalent form

$$\partial_t p = \partial_x \left[\psi_\theta(p)\partial_x p\right] + F(p), \tag{3.13}$$

with ψ_θ defined by

$$\psi_\theta(p) := \phi_\theta'(p) = f'(p) + 2\theta f'(p)f(p) = \frac{1}{\sqrt{1+4p}}\left(1 + \theta\left[\sqrt{1+4p} - 1\right]\right).$$

We are interested in the existence of traveling waves for the equation (3.13). To investigate this, we study the equation in the moving reference frame $\xi = x - ct$. The equation (3.13) becomes

$$cp' + (\psi_\theta(p)p')' + F(p) = 0. \tag{3.14}$$

The nonlinear diffusion term complicates the study of the equation (3.14). The existence of traveling waves in the context of nonlinear diffusion has already been extensively studied. There are multiple theories based on different cases depending on the nonlinear diffusion term, ψ_θ, and the reaction term, F. In our case, to simplify the nonlinear diffusion term, we satisfy the assumptions to apply the change of variable initially proposed by Hadeler in the article [171] and independently by Engler in the article [172]. Indeed we have the following conditions satisfied, $\psi_\theta(0) = 1$ and, for all $p \in [0,1]$, the function ψ_θ is positive. The reaction term F satisfies the following properties, $F(0) = F(1) = 0$ and the function F is positive on $]0,1[$ and negative for $p > 1$. The derivative of the function F is given by the following relation

$$F'(p) = f'(p)(1-p) - f(p), \tag{3.15}$$

And applied to $p = 0$, we have $F'(0) = 1 > 0$.

In the phase plane, the equation (3.14) becomes the following system

$$\begin{cases} p' = q, \\ cq + (\psi_\theta(p)q)' + F(p) = 0. \end{cases} \tag{3.16}$$

We perform the change of variables introduced in the article [171]. Rescaling the time by

$$\eta = \int_0^\xi \frac{ds}{\psi_\theta(p(s))}.$$

Setting $\rho(\eta) = p(\xi)$ and $\tilde{q}(\eta) = q(\xi)\psi_\theta(p(\xi))$, we have

$$\begin{cases} \rho' = \tilde{q}, \\ c\tilde{q} + \tilde{q}' + F(\rho)\psi_\theta(\rho) = 0. \end{cases}$$

Thus, we obtain the following equation

$$c\rho' + \rho'' + F(\rho)\psi_\theta(\rho) = 0, \tag{3.17}$$

without nonlinear diffusion, equivalent to the problem (3.14).

For this equation we want to prove the existence of a transition between pulled front and pushed front. This type of theoretical study front has already been studied for many reaction-diffusion equations. For example, the best known result concerns the Nagumo equation [63] or the more recent work on the Fisher-KPP-Burgers equation [173]. Theoretical works on the transition between pulled and pushed fronts have also been carried out for systems of reaction-diffusion equations, notably for a system modeling autocatalytic reactions [150, 174], or for a Lotka-Volterra competition model [175].

3.3.2 Pulled case for $1 \leq \theta \leq 2$

The theoretical study of the equation (3.17) is much simpler than the study of the previous equation (3.13). In particular, it is possible to easily estimate the critical speed, $c^\star$, by the following classical estimate

$$2 \leq c^\star \leq 2\sqrt{\sup_{s\in]0,1[} \frac{\psi_\theta(s)F(s)}{s}}. \tag{3.18}$$

Subsequently, many authors have proposed possible improvements for the estimate of the critical speed $c^\star$ (See for example [176, 177]). For our study, we will use the following inequality, proved in [177],

$$c^\star \leq 2\sqrt{\sup_{u\in(0,1]} \frac{1}{u}\int_0^u \frac{\psi_\theta(s)F(s)}{s} ds}. \tag{3.19}$$

Numerically, in the previous chapter [148], the authors noticed that a transition between pulled and pushed fronts will certainly occur when θ becomes large enough.

The speed of the linearized problem, for the equation (3.17), is $c_{\text{lin}} = 2$. The front is pulled if the critical speed is equal to the linear speed c^{lin} and is pushed if it is greater. First, we will show theoretically that the front is pulled for a θ assumed small enough. We are therefore interested in the upper bound of the estimate (3.18). In particular, one can inject the following bound in (3.18) or (3.19)

● **Lemma 1:**
For $1 \leq \theta \leq 2$ the following inequality holds

$$\psi_\theta(s)F(s) \leq s(\psi_\theta F)'(0) = s. \tag{3.20}$$

Proof: *The function $\psi_\theta F$ is given by the following relation*

$$(\psi_\theta F)(s) = \frac{(1-s)\left(\sqrt{1+4s}-1\right)}{4\sqrt{1+4s}}\left[2+2\theta(\sqrt{1+4s}-1)\right].$$

The derivative of the function $\psi_\theta F$ applied at $s=0$ gives us $(\psi_\theta F)'(0)=1$. By definition of F and ψ_θ, the inequality $(\psi_\theta F)(s) \leq s$ is equivalent to

$$\frac{(1-s)\left(\sqrt{1+4s}-1\right)}{4\sqrt{1+4s}}\left[2+2\theta(\sqrt{1+4s}-1)\right] \leq s.$$

Isolating the term θ, the condition is given by

$$\theta \leq \frac{2s\sqrt{1+4s}}{(1-s)\left(\sqrt{1+4s}-1\right)^2} - \frac{1}{\sqrt{1+4s}-1} := \mathcal{U}(s).$$

Therefore the condition (3.20) holds for all $\theta \leq \min_{s\in[0,1]} \mathcal{U}(s)$. The function $\mathcal{U}$ is an increasing function, whose derivative is given by the following relation

$$\mathcal{U}'(s) = \frac{6s+5\sqrt{4s+1}+9}{4(s-1)^2\sqrt{4s+1}}.$$

This function is positive for $s \in (0,1)$. Therefore, thanks to the growth of $\mathcal{U}$ the minimum of $\mathcal{U}$ is reached at $s=0$. To derive $\lim_{s\to 0}\mathcal{U}(s)$, we perform a Taylor series, this gives us

$$\lim_{s\to 0}\mathcal{U}(s) = \lim_{s\to 0}\frac{8s^2}{4s^2} + o(1) = 2.$$

In conclusion, we have shown that the condition (3.20) holds for $\theta \leq \mathcal{U}(s) = 2$.

□

Thanks to lemma 1 we directly obtain the following result

◆ **Corollary 1 (Pulled case for $\theta \leq 2$):**
For $1 \leq \theta \leq 2$ the critical speed is equal to the linear speed

$$c^\star = 2.$$

This result is illustrated in figure 3.4 (Green and red areas). To prove the existence of a transition between a pulled front and a pushed front, we will use the variational principle of [178, 179], which we will present in the next section.

3.3.3 Pushed case : Application of the variational principle of Benguria and Depassier

To obtain a lower bound of the critical speed we will use the following variational principle.

■ **Theorem 1 (Variational principle of [178, 179]):**
We consider the following one-dimensional problem

$$\partial_t u(x,t) = \partial_{xx} u(x,t) + h(u(x,t)), \quad x \in \mathbb{R},\ t \geq 0.$$

Assume $h \in C^1([0,1],\mathbb{R})$ *and verify* $h(0) = h(1) = 0$. *We assume to be in the monostable case, i.e.* $h(u) > 0$ *for all* $u \in]0,1[$.

Then the critical speed $c^\star$ *is given by*

$$(c^\star)^2 = \sup_{g\in\mathcal{G}} \left(\frac{2\int_0^1 gh\ du}{\int_0^1 (-g^2/g')\ du} \right), \tag{3.21}$$

where

$$\mathcal{G} = \{g \in C^1(]0,1[)|\ g(u) > 0 \text{ and } g'(u) < 0\ \forall u \in]0,1[;\ \int_0^1 u^2 g'(u)du > -\infty\}.$$

We characterize the threshold for transition to pushed front. Let $\theta^\star$ be defined as follows

$$\theta^\star = \inf\{\theta :\ c^\star(\theta) > 2\}. \tag{3.22}$$

We start with

● **Lemma 2:**
Define θ^* *as in* (3.22) *then the following property holds true*

$$2 \leq \theta^* < +\infty.$$

Proof: *To prove lemma 2 , we denote* $\psi_0 = f'$ *and* $\psi_1 = 2f'f$, *so that we can write* $\psi = \psi_0 + \theta\psi_1$. *The functions* ψ_0 *and* ψ_1 *are independent of* θ. *This allows us to separate the part of* ψ *that is independent of* θ *and the part linearly dependent on it. Thereafter, we will denote* $d\mu_g$ *the measure* $Fg/\int(-g^2/g')$. *Under these notations, the equality* (3.21) *of the variational principle of Benguria and Depassier becomes for our case*

$$(c^\star)^2 = 2\sup_{g\in\mathcal{G}} \left(\int_0^1 (\psi_0 + \theta\psi_1)\ d\mu_g \right). \tag{3.23}$$

Therefore, since $\psi_0 \geq 0$, *we have the following estimate*

$$\theta \sup_{g\in\mathcal{G}} \int_0^1 \psi_1 d\mu_g \leq \frac{(c^\star)^2}{2} \leq \sup_{g\in\mathcal{G}} \int_0^1 \psi_0 d\mu_g + \theta \sup_{g\in\mathcal{G}} \int_0^1 \psi_1 d\mu_g. \tag{3.24}$$

We define K *as follows*

$$K = \sup_{g\in\mathcal{G}} \int_0^1 \psi_1 d\mu_g, \tag{3.25}$$

by definition of μ_g and ψ_1, this constant is positive, finite and independent of θ. Therefore we get the following lower bound

$$2K\theta \leq (c^\star)^2. \tag{3.26}$$

A first result, deriving from the estimate (3.26) and from the positivity of K, is that the transition between pulled front and pushed front, $\theta^\star$, exists and we have this following upper bound,

$$\theta^\star \leq \frac{2}{K} < +\infty.$$

which ends the proof of lemma 2 □

The following lemma shows that θ^* corresponds indeed to a transition.

● **Lemma 3:**
The function $\theta \mapsto (c^*)^2(\theta)$ is a continuous, nondecreasing convex function on $[1, +\infty[$. In particular, it is increasing on $[\theta^*, +\infty[$.

Proof: *The fact that $\theta \mapsto (c^\star)^2(\theta)$ is nondecreasing is immediate. The convexity is a direct consequence of the fact that for any admissible g, $\theta \mapsto \int (\psi_0 + \theta\psi_1)$ is linear and thereby convex. As a byproduct, we establish that $\{\theta : (c^\star)^2(\theta) > 4\}$ is an interval, which is necessarily $]\theta^*, +\infty[$. Finally, by convexity, for any $\theta_1 > \theta_2 > \theta^*$, we have $(c^\star)^2(\theta_2) > (c^\star)^2(\theta^*) = 4$*

$$\frac{(c^\star)^2(\theta_1) - (c^\star)^2(\theta_2)}{\theta_1 - \theta_2} \geq \frac{(c^\star)^2(\theta_2) - (c^\star)^2(\theta^*)}{\theta_2 - \theta^*} > 0.$$

□

Using this lemma and previous result, we can summarize the pulled pushed transition in the following

■ **Theorem 2:**
For the equation (3.11), let $0 < K < +\infty$ be defined by (3.25), there exists $\theta^* \in [2, 2/K[$, such that we have the following two results

1. *For $\theta \in [1, \theta^\star]$ the front is pulled and for $\theta > \theta^\star$ the front is pushed.*
2. *The critical speed $c^\star$ of the equation (3.11) satisfies*

$$2K\theta \leq (c^\star)^2 \leq 4 + 2K(\theta - \theta^\star). \tag{3.27}$$

In particular

$$c^\star(\theta) \underset{\theta \to +\infty}{\sim} \sqrt{2K\theta}. \tag{3.28}$$

Proof: *Points 1. and 2. have already been demonstrated. It remains to prove the asymptotics on $\theta^\star$ and K. We can denote that we have established with the proof that $c^* > 2$ for $\theta > 2/K$. Moreover, for*

$\theta \geq \theta^\star$, we can improve the estimate (3.24) into this estimate

$$\theta \sup_{g\in\mathcal{G}} \int \psi_1 d\mu_g \leq \frac{(c^\star)^2}{2} \leq \sup_{g\in\mathcal{G}} \int \psi_0 + \theta^\star \psi_1 d\mu_g + (\theta - \theta^\star) \sup_{g\in\mathcal{G}} \int \psi_1 d\mu_g.$$

Therefore by the definition of K, we have (3.27) and we obtain from this estimate the following limit

$$\lim_{\theta\to+\infty} \frac{(c^\star(\theta))^2}{\theta} = 2K. \tag{3.29}$$

leading to (3.28). □

The theorem 2 is illustrated by the figure 3.4. The blue region represents a lower bound of the theoretical minimal speed, which is obtained by applying the variational principle of Benguria and Depassier to a certain test function.

We end this section with some quantitative estimates on θ^*.

● **Lemma 4:**
The following estimates hold true

$$\theta^* \leq \frac{15\sqrt{5}+21}{(\sqrt{5}-1)(9-\sqrt{5})} \approx 6.5235.$$

Proof: *To show that the front is pushed for $\theta > \theta^\star$, we use the Benguria-Depassier principle recalled below*

$$(c^\star)^2 = \sup_{g\in\mathcal{G}} \left(\frac{2\int_0^1 gF\psi_\theta dp}{\int_0^1 (-g^2/g')dp} \right).$$

We apply the principle of Benguria and Depassier to the following family of test functions $g_\varepsilon(p) = (\sqrt{1+4p}-1)^{\varepsilon-2}$. According to the principle of Benguria and Depassier we obtain the following lower bound for the critical speed

$$(c^\star)^2 \geq \frac{2\int_0^1 g_\varepsilon F\psi_\theta dp}{\int_0^1 (-g_\varepsilon^2/g_\varepsilon')dp} =: \frac{N(\varepsilon)}{D(\varepsilon)}.$$

We compute numerator and denominator separately. Under our assumptions, the denominator becomes

$$\begin{aligned}
D(\varepsilon) &= \int_0^1 (-g_\varepsilon^2/g_\varepsilon')dp, \\
&= \int_0^1 \frac{(\sqrt{1+4p}-1)^{2\varepsilon-4}}{(2-\varepsilon)(\sqrt{1+4p}-1)^{\varepsilon-3}.\frac{2}{\sqrt{1+4p}}}dp, \\
&= \frac{1}{4(2-\varepsilon)}\int_1^{\sqrt{5}} (u-1)^{2\varepsilon-4-\varepsilon+3}u^2 du, \\
&= \frac{1}{4(2-\varepsilon)}\int_0^{\sqrt{5}-1} v^{\varepsilon-1}(v+1)^2 dv, \\
&= \frac{1}{4(2-\varepsilon)}\int_0^{\sqrt{5}-1} \left(v^{\varepsilon+1}+2v^\varepsilon+v^{\varepsilon-1}\right) dv, \\
&= \frac{1}{4(2-\varepsilon)}\left(\frac{(\sqrt{5}-1)^{\varepsilon+2}}{\varepsilon+2}+2\frac{(\sqrt{5}-1)^{\varepsilon+1}}{\varepsilon+1}+\frac{(\sqrt{5}-1)^\varepsilon}{\varepsilon}\right), \\
&= \frac{1}{4(2-\varepsilon)}(\sqrt{5}-1)^\varepsilon \frac{5\varepsilon^2+(2\sqrt{5}+5)\varepsilon+2}{\varepsilon(\varepsilon+1)(\varepsilon+2)},
\end{aligned}$$

leading to

$$D(\varepsilon) = \frac{(\sqrt{5}-1)^\varepsilon}{4\varepsilon(\varepsilon+1)(\varepsilon+2)}\frac{5\varepsilon^2+(2\sqrt{5}+5)\varepsilon+2}{(2-\varepsilon)}. \tag{3.30}$$

Still using the same change of variable $u=\sqrt{1+4p}$, we compute the numerator

$$\begin{aligned}
N(\varepsilon) &= 2\int_0^1 g_\varepsilon F\psi_\theta dp, \\
&= 2\int_1^{\sqrt{5}} (u-1)^{\varepsilon-2}\frac{\frac{(5-u^2)}{4}(u-1)}{4u}\left[2+2\theta(u-1)\right]\frac{u}{2}du, \\
&= \frac{1}{8}\int_1^{\sqrt{5}} (u-1)^{\varepsilon-1}\left(5-u^2\right)(1+\theta(u-1))du, \\
&= \frac{1}{8}\int_0^{\sqrt{5}-1} v^{\varepsilon-1}\left(4-2v-v^2\right)(1+\theta v)dv, \\
&= \frac{1}{8}(I(\varepsilon-1)+\theta I(\varepsilon)),
\end{aligned}$$

where

$$\begin{aligned}
I(\alpha) &= \int_0^{\sqrt{5}-1} v^\alpha\left(4-2v-v^2\right)dv, \\
&= 2\frac{(\sqrt{5}-1)^{\alpha+1}}{(\alpha+1)(\alpha+2)(\alpha+3)}\left((5-\sqrt{5})\alpha+9-\sqrt{5}\right).
\end{aligned}$$

So that

$$N(\varepsilon) = \frac{(\sqrt{5}-1)^\varepsilon}{4\varepsilon(\varepsilon+1)(\varepsilon+2)}\left((5-\sqrt{5})(\varepsilon-1)+9-\sqrt{5}+\frac{\theta\varepsilon(\sqrt{5}-1)}{\varepsilon+3}\left((5-\sqrt{5})\varepsilon+9-\sqrt{5}\right)\right).$$

Finally, we can make the Taylor expansion

$$\frac{N(\varepsilon)}{D(\varepsilon)} = 4 + \varepsilon.\left(-7 - 5\sqrt{5} + \frac{\theta}{3}\left(9 - \sqrt{5}\right)\left(\sqrt{5} - 1\right)\right) + o(\varepsilon),$$

And therefore, for $\theta > \dfrac{21 + 15\sqrt{5}}{\left(9 - \sqrt{5}\right)\left(\sqrt{5} - 1\right)}$, *we have* $(c^*)^2(\theta) \geq \dfrac{N(\varepsilon)}{D(\varepsilon)} > 4$ *for* $\varepsilon > 0$ *small enough which proves the bound* $\theta^* \leq \dfrac{21 + 15\sqrt{5}}{\left(9 - \sqrt{5}\right)\left(\sqrt{5} - 1\right)}$ *of lemma 4.*

□

This lower bound, coupled with the previous corollary 1, provides the following estimate $\theta^\star \in [2, 6.6]$. In article [48], the authors have developed a method to approach numerically, with good precision, the transition between pulled front and pushed front. Applying this method to the equation (3.17) yields the following experimental threshold : $\widetilde{\theta^\star} \approx 3.1489$, which is in agreement with our estimates.

3.4 Conclusion

We exhibit numerically that for $k \geq 0$ the linear speed of model (3.2) is not a good prediction of the nonlinear speed. Moreover, in the asymptotic case, $k = +\infty$, we can, with a change of variables, simplify the system (3.2) into a single reaction-diffusion equation. Thanks to this simplification, we have demonstrated the existence of a transition between pulled and pushed fronts, as well as an estimate of the critical threshold.

Note that if we replace the coagulation term with a linear transfer term, the resulting model is a special case of the general system studied in the article [180]. In this paper, the authors show the existence of zones for which the speed is anomalous, and also exhibit the importance of the critical threshold $\theta^\star = 2$. In their case, however, the linear speed predicts the non-linear speed ; in our case, the addition of the non-linear coagulation term disturbs this prediction when θ is large enough.

In this chapter we have demonstrated the existence of a transition between pulled and pushed fronts only in the asymptotic case $k = +\infty$. For the case $k > 0$, this result is more complex to prove. In the article [150], the authors theoretically prove the existence of a transition between pulled and pushed fronts for a system of reaction-diffusion equations using phase space techniques. However, for the system (3.2), the eigenvectors of the linearization around the positive equilibrium point are explicit but highly complex, making it impossible to use these techniques.

It could be interesting to determine if and how our result for $k = +\infty$ persists for sufficiently large values of k. The resolution of this type of problem is generally carried out using the implicit function theorem. However, the application of this theorem can be complex in the context of traveling wave solutions [181, 182, 183]. There are several possibilities to overcome these problems, for example, refer to the theory presented in the book [181]. Moreover, new methods for the persistence of pulled fronts have been recently introduced in the articles [45, 47, 48, 49]. Regardless of the method used, the nonlinear diffusion in the asymptotic case of $k = +\infty$ considerably complicates the analysis.

It should also be noted that the numerical simulations carried out in the previous chapter [148] can

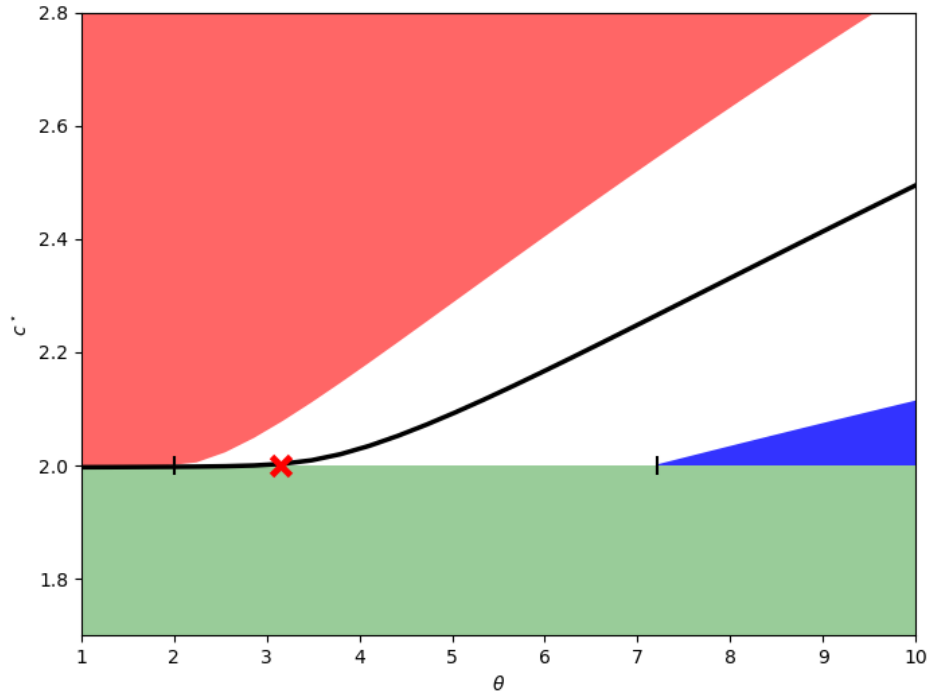

FIGURE 3.4 – The black curve represents the evolution of the critical speed of the numerical solution of the asymptotic problem (3.13) as a function of θ. It is obtained numerically using a shooting method. The green area corresponds to the inequality $c^\star \geq c^{\text{lin}} = 2$. The area in red corresponds to the upper bound of the estimate (3.19) introduced in the article [177]. The blue area is obtained using the variational principle of Benguria and Depassier (3.21) applied to the family of test functions $\tilde{g}_\varepsilon(p) = (\sqrt{1+4p}-1)^{\varepsilon-2}$. For this figure the value of the parameter ε is $\varepsilon = 0.09$. This value of ε is not optimal for estimating the transition between pulled and pushed front. The zone in white corresponds theoretically to the area in which the critical speed is admissible. We observe a transition between pulled and pushed fronts which takes place between the positions, $x = 2$ and $x \approx 7.2$, symbolized by the two markers. The red cross corresponds to the experimental transition threshold between pulled front and pushed front, obtained using the theory and the codes of the article [48].

be improved. In particular, the recent results obtained by [48], based on the far field decomposition, would allow us to obtain an experimental transition between the pulled and the pushed fronts with an extreme accuracy compared to the previous numerical simulations.

There are multiple possible future directions to improve modeling of the spread of the bacterium *Myxococcus xanthus*.

First of all it would be interesting to complexify the size structure of the model (3.2), by including also larger clusters of bacteria. In the previous chapter [148], the authors show numerically, for a similar model structured in continuous size, the existence of numerical results very close to those obtained for the system (3.2). In particular, the authors show, numerically, the existence of a phenomenon equivalent to a transition between pulled and pushed front. Another possibility, concerning the size of the clusters, would be to use the classification recently introduced in biology between 3 types of families : the "scouts" which are small groups of bacteria, the "loners" the medium-sized groups and finally the "swarms" corresponding to the largest clusters [140].

Another interesting axis would be to complexify the reaction terms of the model (3.1) to model as well as possible the behavior of the bacterium *Myxococcus xanthus*. For example, when the bacterium divides, it remains motionless during the time of the division. In this chapter we assume that this time is negligible. Nevertheless it would be interesting to study the effect on the speed of such counterpart on the division. Such an addition would tend to increase the area in which the front regime is pushed. From a mathematical point of view, there already exist in the literature systems modeling division terms close to the desired one. For these models built with a delay term, traveling wave solutions have already been studied (see for example [184, 185] and the references therein).

Finally, it is necessary for the future to take into account the fact that the bacterium *Myxococcus xanthus* is a predatory bacterium attacking prey bacteria such as *E.Coli*. Biologically, the amount of prey and its evolution over time has a major impact on the different motilities of *Myxococcus xanthus* as well as on its speed of propagation. This will be a subject of our future study.

4 A reaction telegraph model reveals synergy between motility strategies in Myxococcus xanthus predation

4.1 Introduction

Biology. *Myxococcus xanthus* is a social bacterium that moves and feeds cooperatively in predatory groups. *Myxococcus xanthus* bacteria employ two distinct modes of motility : social motility (S) and adventurous motility (A). Social motility is associated with the presence of type IV pili, which act as grappling hooks at the bacterial pole, promoting coordinated movement within clusters of bacteria [120]. Adventurous motility, on the other hand, involves gliding mechanisms that enable individual bacteria, mainly at the edge of the colony, to move [121]. These two motility systems, which depend on the expression of two distinct sets of genes [122], exhibit completely different characteristics which we will detail in the remainder of this article.

M. xanthus is a predatory bacterium, known to attack a wide variety of prey [128, 129]. The biomass released by the prey microorganisms is rich in amino acids and lipids, which constitute their main sources of carbon and energy. *Myxococcus xanthus* employs two attack strategies, choosing them based on the prey type [130]. The first strategy involves a frontal attack, where the predatory bacteria gradually penetrate the prey colony and progressively lyse the prey cells [131, 116]. In the other strategy, named *wolf pack*, *M. xanthus* cells surround the prey colony and undulate before killing it [116, 132]. In this article we focus on modeling the frontal attack.

The main mechanism of prey destruction results from contact-dependent killing by the bacteria. According to several recent studies, isolated bacteria of *Myxococcus xanthus* approach prey cells using their adventurous motility. Upon direct contact, they stop their movement and induce the death of the prey cell [135, 136, 137]. Cooperation among *Myxococcus xanthus* cells, as observed by Rosenberg et al., promotes vegetative growth and predation [138]. This cooperation enables a common secretion of hydrolytic enzymes, improving the efficiency of prey biomass degradation within a cluster, suggesting more efficient predation compared to individual cells [138]. In addition, Zhang et al. noted that isolated bacteria of *M. xanthus* frequently leave killed Escherichia coli prey without degrading the biomass, probably due to insufficient production of degrading enzymes [132, 136]. In the mathematical model we introduce, we assume that isolated bacteria lyse prey bacteria and leave the biomass behind. These

nutrients will later be consumed by bacterial clusters.

These rod-shaped bacteria can move along their main axis thanks to their two motility systems. At certain points, these bacteria reverse their direction by changing polarity [124]. Several studies have shown that *M.xanthus* is not chemotactic towards its prey [125], and whether the bacterium exhibits chemotactic behaviors in general remains controversial [126, 127]. Bacteria in bacterial clusters tend to be faster than isolated bacteria [123].

Since the pioneering works of Fisher [59] and Kolmogorov-Petrovskii-Piskunov [186], the dispersion of biological species is commonly modeled using reaction-diffusion equations. A major problem, in our case, with the choice of diffusion is that it does not model the persistence of motion [187]. In one dimension, and only in one dimension, the movement of the bacteria corresponds to a *Run and Tumble* process, also called *telegraph dispersal*, based on a velocity jump process [188, 189]. This choice is increasingly employed to model biological systems (see, for example, [190, 191, 192]), notably for modeling bacterial motility [143, 193, 194, 144].

In one dimension, during the *Run* phase, the particle moves in a straight line to the right or to the left at speed v. Then, after a random time interval, following a Poisson distribution, the particle undergoes a sudden stop and instantly reverses its direction. This movement is modeled by the following two kinetic equations,

$$\begin{cases} \partial_t f^+ + \dfrac{v}{\epsilon}\partial_x f^+ = \dfrac{1}{2\tau\epsilon}(f^- - f^+), \\ \\ \partial_t f^- - \dfrac{v}{\epsilon}\partial_x f^- = \dfrac{1}{2\tau\epsilon}(f^+ - f^-), \end{cases} \tag{4.1}$$

where f^+ (resp. f^-) corresponds to the density of bacteria moving to the right (resp. left). The parameter ϵ is a scaling parameter that represents the ratio between the spatial scale and the mean free path of bacteria. The transport term models the *Run* phase, while the RHS corresponds to the *Tumble* phase/ *Reversal* phase. Making the change of variable $f = f^+ + f^-$ and using the Kac trick [195], the system (4.1) simplifies into a single equation given by

$$\tau\epsilon^2\partial_{tt} + \partial_t f = \tau v^2 \partial_{xx} f. \tag{4.2}$$

When $\epsilon = 0$, equation (4.2) becomes the heat equation, $\partial_t f = D\partial_{xx} f$, where

$$D := \tau v^2. \tag{4.3}$$

This relation linking the diffusion coefficient, to the combination of persistence and instantaneous speed, is crucial in our study. The investigation of the mean square displacement (MSD) also enables the determination of relation (4.3) [189].

Model introduction.

The population of *M. xanthus* is structured into isolated bacteria and different clusters that interact with the nutrients present in the environment. The size of clusters is represented by the variable i, and we assume that the cluster size cannot exceed the size limit n, where n is a positive integer. The density of clusters of size i moving to the right is represented by the variable p_i^+, while the density of

clusters of size i moving to the left is represented by the variable p_i^-. We also denote p_i as the density of bacterial clusters of size i, defined by $p_i := p_i^+ + p_i^-$.

The densities p_1^+ and p_1^- are given by the following system of equations,

$$\begin{cases} \partial_t p_1^+ + \dfrac{1}{\epsilon}\partial_x p_1^+ = \dfrac{1}{2\epsilon^2}(p_1^- - p_1^+) + \mathcal{F}_1^+[p_j^\pm] + \mathcal{C}_1^+[p_j^\pm] + \dfrac{\alpha_1 p_1 (1-p)_+}{2}, \\ \\ \partial_t p_1^- - \dfrac{1}{\epsilon}\partial_x p_1^- = \dfrac{1}{2\epsilon^2}(p_1^+ - p_1^-) + \mathcal{F}_1^-[p_j^\pm] + \mathcal{C}_1^-[p_j^\pm] + \dfrac{\alpha_1 p_1 (1-p)_+}{2}, \end{cases} \tag{4.4}$$

with, p the total number of bacteria given by the following formula, $p := p_1 + 2p_2 + \ldots + np_n$ and $(1-p)_+$ corresponding to the positive part of $1-p$, $(1-p)_+ := \max\{1-p, 0\}$.

By a scaling of the time and space, which we do not detail in this document, the coefficients corresponding to the instantaneous speed and persistence of isolated bacteria are chosen equal to 1. The operator $\mathcal{F}_i^\pm[p_j^\pm]$ represents the fragmentation events associated with bacterial clusters of size i moving to the right (+) or to the left (-) between times t and $t + \mathrm{d}t$. This operator is given in general form by the following equality

$$\mathcal{F}_i^\pm[p_j^\pm] = \frac{1}{2} \times 2 \sum_{j=i+1}^{n} \beta(j)\eta(j,i)p_j - \beta(i)p_i^\pm, \qquad i \in \{1, \ldots, n\},$$

where $\beta(i)$ represents the fragmentation rate of clusters of size i. The first sum represents larger clusters that have fragmented into two distinct parts, with one resulting cluster having size i. We assume that when a cluster of bacteria fragments, the two daughter clusters randomly choose their direction, either to the right or to the left. In this sum, the function η corresponds to the fragmentation kernel ; in other words, $\eta(j,i)$ represents the probability that a cluster of size j fragments into a cluster of size i and a cluster of size $j-i$. The second term of the fragmentation term corresponds to clusters of size i that have fragmented during the time interval $\mathrm{d}t$. In this article, we make the following assumptions

$$\beta(j) = \beta \times j, \qquad \text{and,} \qquad \eta(j,i) = \frac{1}{j-1}, \quad \text{for all } i \in \{1, \ldots, j-1\}.$$

We assume that the larger a cluster is in size, the more likely it is to undergo fragmentation. Regarding possible fragmentation events, we assume them to be uniformly probable.

The operator $\mathcal{C}_i^\pm[p_j^\pm]$ corresponds to the coagulation events during the time interval $\mathrm{d}t$, and it is given by the following formula

$$\mathcal{C}_i^\pm[p_j^\pm] = \frac{1}{2}\sum_{j=1}^{i-1} \gamma(i-j,j)\left[p_j^\pm p_{i-j}^\pm + \frac{1}{2}(p_j^+ p_{i-j}^- + p_j^- p_{i-j}^+)\right] - p_i^\pm \sum_{j=1}^{n-i} \gamma(j,i)p_j, \quad i \in \{1, \ldots, n\}.$$

The first term corresponds to the coagulation event of two clusters of smaller sizes forming a cluster of size i. Here, we assume that if two clusters are moving in the same direction, the resulting cluster from their coagulation will also move in the same direction. When two clusters coagulate but are not moving in the same direction, in this case, the newly formed cluster has an identical probability of moving either to the right or to the left. The function $\gamma(i-j,j)$ represents the probability that a cluster of size j coagulates with a cluster of size $i-j$. We assume that the function γ is given by

$$\gamma(j,j') = \gamma \times j \times j', \qquad \text{for all } j, j' \in \{1, \ldots, n\} \text{ such that } j + j' \leq n.$$

The second term of the coagulation operator represents all clusters of size i that have coagulated with another cluster to form a larger-sized cluster. The fragmentation and coagulation operators preserve the mass, p.

Finally, we model the division of isolated bacteria. When an isolated bacterium divides, we assume that the two daughter bacteria will also be isolated. The parameter α_1 corresponds to the proliferation rate. As the mass p increases, the proliferation term decreases. When the mass exceeds a threshold, we assume that division events are no longer possible.

For clusters of size $i \in \{2, 3, \dots, n\}$, the equations of the couple (p_i^+, p_i^-) are given by

$$\partial_t p_i^\pm \pm \frac{v(i)}{\epsilon}\partial_x p_i^\pm = \pm\frac{1}{2\tau(i)\epsilon^2}(p_i^- - p_i^+) + N\left[d(i-1)p_{i-1}^\pm - d(i)p_i^\pm\right](1-p)_+ + \mathcal{F}_i^\pm[p_j^\pm] + \mathcal{C}_i^\pm[p_j^\pm], \quad (4.5)$$

where N is a spatiotemporal variable corresponding to the nutrient density.

These equations have the same coagulation and fragmentation terms as the equations (4.4). The division term is now given by the term

$$\text{Division term :} \quad N \times \left[d(i-1)p_{i-1}^\pm - d(i)p_i^\pm\right] \times (1-p)_+.$$

The nutrients are created by prey lysis. We assume that N is governed by the following equation,

$$\partial_t N = \delta p_1(1 - N/N_M), \quad (4.6)$$

with δ the rate of nutrient creation and N_M the carrying capacity. We assume that the diffusion of these nutrients is negligible. These nutrients created by the predation of isolated adventurous bacteria will, in proportion to the nutrient presence, enable the division of bacteria within bacterial clusters. In this equation, we assume that the effect of bacteria on prey depends on the size of the clusters. Isolated bacteria kill the prey, creating nutrients, while the clusters consume these nutrients to increase their division rate. Since we focus solely on the invasion phenomenon, we do not model the degradation of these nutrients by bacterial clusters.

We assume, in this division term, that when a bacterium divides within a cluster, the two daughter bacteria remain part of the same cluster. Thus, the evolution of clusters of size i between times t and $t + \mathrm{d}t$ will depend on clusters of size $i-1$ and size i for which a bacterium will divide. We assume that the division rate, d, is given by the following formula

$$d(i) = i \times \alpha_2, \qquad \text{for all } i \in \{2, \dots n-1\}, \quad \text{and} \quad d(1) = d(n) = 0.$$

The linear growth of the function d represents the fact that every bacteria, whether in a cluster or not, has the same chance of dividing. Consequently, the larger a cluster is, the more likely one of its bacteria will divide. To ensure that the maximum size of bacterial clusters is equal to n, we assume that bacteria can no longer divide within clusters of size n. Again, we assume that the division rate decreases with respect to the total mass, p, and is only possible if the mass is below the critical mass of 1.

The function $v : i \in \{2, \dots, n\} \longmapsto v(i)$ represents the instantaneous speed of bacterial clusters of size i relatively to the isolated bacteria and the function $\tau : i \in \{2, \dots, n\} \longmapsto \tau(i)$ represents the average time between a change of direction relatively to the isolated bacteria. For the equations related to the clusters, we assume that the scaling parameter is the same as for the isolated bacteria equations, ϵ.

Mathematical literature. The model (4.4)-(4.5)-(4.6) corresponds to an extension of the model presented in the article by Calvez et al. [148]. In the article [148], the authors introduce a simplified reaction-diffusion model that only considers isolated bacteria and clusters of two bacteria. Their goal was to study the impact of the speed advantage of bacterial clusters. Through numerical simulations, the authors highlight the presence of pulled and pushed fronts. Moreover, in the article [149], the authors have demonstrated that under the assumption of fast coagulation-fragmentation, there is a unique transition between pulled and pushed fronts. In the present article, we enhance this model in several aspects. Firstly, we model bacterial clusters of size greater than 2. Then, for the reasons described above, we favor a telegraph dispersal rather than the previous diffusion operator. We also decide to model the creation of nutrients resulting from the lysis of prey bacteria by isolated predator bacteria, as well as the effect of these nutrients on the proliferation of bacterial clusters. Other, older models have been introduced to model the spread of the *M. xanthus* bacteria [141, 142]. However, these models do not consider the predatory nature of the bacteria and the coexistence of the two motility systems. The study of traveling waves for reaction-telegraph equations has already been studied in numerous articles (See for example [196, 197, 198, 199, 200, 201, 202, 203]) and for more general systems of several hyperbolic equations [204, 205].

Results. In this article, we focus on the linear and nonlinear speeds of the model (4.4)-(4.5)-(4.6). When the nonlinear speed equals the linear speed, the front is said to be pulled. Conversely, when the linear speed differs from the nonlinear speed, the front is pushed [40]. Based on the marginal stability conjecture and under certain assumptions, we propose a formula for the linear speed. Two scenarios are possible : either the linear speed equals the linear speed of the two-equation system (4.4), decoupled from the other equations ; or the linear speed is greater than this speed, in which case the propagation is termed anomalous. To the best of our knowledge, no article reports such a phenomenon for hyperbolic equations. We also perform numerical simulations to determine the nonlinear speed of the model. Our numerical results reveal the existence of both a pulled front regime and a pushed front regime. In our numerical experiments, for the pushed front regime, the nonlinear speed consistently exceeds the linear speed.

$A+S-$ and $A-S+$ corresponding respectively to a population of *Myxococcus xanthus* bacteria composed solely of adventurous bacteria and another composed solely of social bacteria. According to the results of biological experiments presented in the article [137], the *Wildtype* strain (or $A+S+$) and the $A+S-$ strain significantly invade the *E. coli* prey much faster than the $A-S+$ strain. Based on our model, we propose two mathematical systems corresponding respectively to the $A+S-$ and $A-S+$ strains. Our numerical simulations yield results consistent with the biological experiments, showing that the $A-S+$ strain has great difficulty invading the prey.

Finally, we investigate, through numerical simulations, the impact of the existence of both motility systems on the invasion speed. To achieve this, we use the relation (4.3) linking the diffusion coefficient with persistence and instantaneous speed. This allows us to study the invasion speed for various parameter values $(\tau(i), v(i))$ under the constraint $1 = \tau(i)v^2(i)$ for all $i \in \{2, \dots, n\}$. According to our numerical simulations, the characteristics induced by the coexistence of adventurous and social motility systems significantly facilitate the predation of a prey bacteria.

Outline. The document is organized as follows : In Section 4.2 we first study the simplified system, $n = 2$, where only isolated bacteria and pairs of bacteria are considered. We first derive the linear speed of the model. Subsequently, followed by an exploration of the nonlinear speed through numerical simulations. Finally, we conclude this section by describing results related to the biological modeling of this problem. In Section 4.3, we extend this analysis to the more general case where $n > 2$, applying similar methods to investigate the behavior of the extended model.

4.2 Simplified case $n = 2$

In this section, we assume that clusters can only contain two bacteria. According to the biological experimental data presented in the article [140], there is a symmetry between the probability of fragmentation and coagulation. To simplify the calculations presented in this section, we assume that the fragmentation rate equals the coagulation rate, and denote it by k.

Under the assumption $n = 2$, the model (4.4)-(4.5)-(4.6) becomes the following,

$$\begin{cases} \partial_t p_1^+ + \dfrac{1}{\epsilon}\partial_x p_1^+ = \dfrac{1}{2\epsilon^2}(p_1^- - p_1^+) - k(p_1^+)^2 - k p_1^+ p_1^- + k p_2 + \dfrac{\alpha_1}{2} p_1 (1-p)_+, \\ \partial_t p_1^- - \dfrac{1}{\epsilon}\partial_x p_1^- = \dfrac{1}{2\epsilon^2}(p_1^+ - p_1^-) - k(p_1^-)^2 - k p_1^+ p_1^- + k p_2 + \dfrac{\alpha_1}{2} p_1 (1-p)_+, \\ \partial_t p_2^+ + \dfrac{v}{\epsilon}\partial_x p_2^+ = \dfrac{1}{2\tau\epsilon^2}(p_2^- - p_2^+) - k p_2^+ + \dfrac{k}{2}(p_1^+)^2 + \dfrac{k}{2} p_1^+ p_1^-, \\ \partial_t p_2^- - \dfrac{v}{\epsilon}\partial_x p_2^- = \dfrac{1}{2\tau\epsilon^2}(p_2^+ - p_2^-) - k p_2^- + \dfrac{k}{2}(p_1^-)^2 + \dfrac{k}{2} p_1^+ p_1^-, \\ \partial_t N = \delta p_1 (1 - N/N_M). \end{cases} \tag{4.7}$$

The choice of the term modeling bacterial proliferation is specifically motivated for values of n strictly greater than 2. When $n = 2$, this term becomes irrelevant. Indeed, in the system of equations (4.7), clusters of two bacteria gradually disappear, and nutrients do not influence the predation behavior of *M. xanthus*. To overcome this problem, we add a nonlinear, nutrient-dependent logistic

proliferation term into the equations governing the two-bacteria clusters.

$$\begin{cases} \partial_t p_1^+ + \dfrac{1}{\epsilon}\partial_x p_1^+ = \dfrac{1}{2\epsilon^2}(p_1^- - p_1^+) - k(p_1^+)^2 - kp_1^+ p_1^- + kp_2 + \dfrac{\alpha_1}{2}p_1(1-p)_+, \\ \partial_t p_1^- - \dfrac{1}{\epsilon}\partial_x p_1^- = \dfrac{1}{2\epsilon^2}(p_1^+ - p_1^-) - k(p_1^-)^2 - kp_1^+ p_1^- + kp_2 + \dfrac{\alpha_1}{2}p_1(1-p)_+, \\ \partial_t p_2^+ + \dfrac{v}{\epsilon}\partial_x p_2^+ = \dfrac{1}{2\tau\epsilon^2}(p_2^- - p_2^+) - kp_2^+ + \dfrac{k}{2}(p_1^+)^2 + \dfrac{k}{2}p_1^+ p_1^- + \dfrac{\alpha_2}{2}Np_2\,(1-p)_+\,, \\ \partial_t p_2^- - \dfrac{v}{\epsilon}\partial_x p_2^- = \dfrac{1}{2\tau\epsilon^2}(p_2^+ - p_2^-) - kp_2^- + \dfrac{k}{2}(p_1^-)^2 + \dfrac{k}{2}p_1^+ p_1^- + \dfrac{\alpha_2}{2}Np_2\,(1-p)_+\,, \\ \partial_t N = \delta p_1(1 - N/N_M). \end{cases} \tag{4.8}$$

Such a choice would be irrelevant for a larger n. The parameter v (resp. τ) represents the advantage or disadvantage in speed (resp. average time before a change of direction) of clusters of two bacteria.

4.2.1 Linear speeds

In this section, we study the critical linear propagation speed of the model (4.8). Linearizing this model around the zero equilibrium point gives us the following linear model :

$$\begin{cases} \partial_t p_1^+ + \dfrac{1}{\epsilon}\partial_x p_1^+ = \dfrac{1}{2\epsilon^2}(p_1^- - p_1^+) + kp_2 + \dfrac{\alpha_1}{2}p_1, & \text{(4.9a)} \\ \partial_t p_1^- - \dfrac{1}{\epsilon}\partial_x p_1^- = \dfrac{1}{2\epsilon^2}(p_1^+ - p_1^-) + kp_2 + \dfrac{\alpha_1}{2}p_1, & \text{(4.9b)} \\ \partial_t p_2^+ + \dfrac{v}{\epsilon}\partial_x p_2^+ = \dfrac{1}{2\tau\epsilon^2}(p_2^- - p_2^+) - kp_2^+, & \text{(4.9c)} \\ \partial_t p_2^- - \dfrac{v}{\epsilon}\partial_x p_2^- = \dfrac{1}{2\tau\epsilon^2}(p_2^+ - p_2^-) - kp_2^-. & \text{(4.9d)} \end{cases}$$

Note that equations (4.9c)-(4.9d) are independent of the variables p_1^+ and p_1^-. However, the variables $p_2^\pm$, through the coupling term, influence the behavior of the variables $p_1^\pm$. Nevertheless, the variables $p_2^\pm$ decay exponentially to zero at every point for all x as $t \to \infty$. Thus, one might expect that the coupling term in equations (4.9a)-(4.9b) would quickly stop affecting the propagation speed of the traveling wave solutions of p_1. However, we will see that the coupling term can irreversibly increase the wave speed. This type of phenomenon, called *anomalous propagation*, was first introduced in the article [61] and has since been theoretically studied by numerous authors [55, 170, 54, 50].

There are therefore two possibilities concerning the linear propagation speed of (4.9a)-(4.9d). In the first case, the coupling term has no effect, and the critical asymptotic speed is determined solely by the decoupled system of equations (4.9a)-(4.9b), i.e., with $k = 0$. In this case, we will use the term *normal speed*. Conversely, when the pairs of bacteria, through the coupling term, influence the speed of the isolated bacteria, we will refer to it as *anomalous speed*.

We define the linear propagation speed as follows :

Definition (Linear propagation speed):
The linear propagation speed of a linear system (S) is given by

$$s^\star_{lin} = \sup\{s :\ D_s(\nu,\lambda) \text{ has a pinched double root with } \mathrm{Re}\ \lambda \geq 0\},$$

where $D_s(\nu,\lambda)$ is the dispersion relation associated with the problem (S), and the notion of a pinched double root is introduced in the appendix A.

This definition is based on the distinction between convective instability and absolute instability [55]. In certain specific cases, this definition may prove to be imperfect. It then becomes necessary to consider the singularities of the pointwise Green's function associated with the problem. The connection between pinched double roots and these singularities has been studied theoretically for a broad class of parabolic systems, by Holzer and Scheel in the article [55]. However, to simplify the calculations in Appendix A, we will nonetheless use this definition.

In Appendix A, we show that the linear propagation speed, $s^\star_{\text{lin}}$, can take one of four possible values :

- The two *normal speeds* : parabolic and hyperbolic

$$s_{\text{para}} := \frac{2\sqrt{\alpha_1}}{1+\alpha_1\epsilon^2}, \qquad s_{\text{hyp}} := \frac{1}{\epsilon}.$$

- The two *positive anomalous speeds* given by :

$$(s^\pm_{\text{anom}})^2 = s^\pm(0) = \frac{-a_2(0) \pm \sqrt{a_2^2(0) - 4a_0(0)a_4}}{2a_4},$$

  provided these two speeds are well defined. The functions a_0, a_2, and the coefficient a_4 are defined by equations (A.18), (A.19), and (A.20), respectively, in Appendix A.

By definition 1, the selection principle among these possible linear speeds corresponds to the maximum of those that are indeed associated with pinched double roots. Based on this postulate, it is possible to explicitly calculate certain critical transition values, which will not be detailed in this article due to their significant complexity. We illustrate transitions between different possible linear speeds in Figure 4.9.

When isolated bacteria are faster than clusters, we obtain the following result :

- If $\epsilon < 1/\sqrt{\alpha_1}$, then the linear propagation speed can be the parabolic speed or one of the anomalous speeds : s_{para}, s^+_{anom}, and s^-_{anom}.
- If $\epsilon > 1/\sqrt{\alpha_1}$, then the linear propagation speed corresponds to the hyperbolic speed.

In Appendix A, we also verify through numerical simulations that this linear propagation speed is indeed selected for a nonlinear model in a pulled front regime, when initial conditions correspond to Heaviside functions.

4.2.2 Nonlinear speed – Pulled and Pushed regime

The speed of the nonlinear model (4.8) is not necessarily equal to the linear propagation speed. In this section, we use numerical simulations to compare the nonlinear and linear speeds to determine

whether the front is pulled or pushed [40].

For numerical simulations, we employ the numerical scheme presented in the article [202], which is based on the nonlinear flux-limiter schemes developed in the articles [206, 207]. To approximate the wave speed, we use an algorithm based on the LeVeque-Yee formula [208, 209]. In this work, we consider only steep initial data. More specifically, for the model (4.8), we consider initial conditions of the form $p_i^{\pm}(t=0,x) = (p_i^{\star}/2)H(x-x_0)$, for $i=1,2$, where H denotes the Heaviside function and x_0 is a positive constant.

In Figure 4.1, we plot with black dots, for different values of parameter v, the evolution of the critical speed for the nonlinear model normalized by the speed we obtain when $v=1$. For $v=1$, the selected numerical speed corresponds well to the parabolic speed. However, a slight numerical error on the order of 10^{-2} remains due to the inaccuracies of the numerical simulations (mesh, convergence time, etc.). Since this error persists for other values of v, we have chosen to normalize the results by the value calculated at $v=1$ in order to improve the readability of the figure and the comparison with theoretical speeds. The colored curves correspond to the linear propagation speed normalized by the parabolic speed independent of v. We observe two different scenarios separated by a critical threshold v_c. When $v < v_c$, the front is pulled; indeed, the selected numerical speed corresponds to the parabolic linear speed. However, when v becomes greater than the critical threshold v_c, the speed becomes greater than the parabolic linear speed and also greater than all possible linear speeds. Therefore, the front is pushed for $v > v_c$. The hyperbolic speed and the anomalous plus speed are not represented in this figure as they are not admissible for the chosen parameter values.

We performed several additional numerical simulations, not presented in this article, for different parameter values. According to these simulations, it seems that the speed of the nonlinear model can be equal to the parabolic and hyperbolic linear speeds but never equals either of the two anomalous linear speeds. For the model associated with diffusion, numerical results presented in the articles [148, 149] also show these same results. Moreover, when the model is in the pushed regime, the propagation speed appears to always be greater than the linear speed. For single reaction-diffusion equations, the nonlinear speed is always greater than the linear speed; however, in the article [53], the authors presented a counterexample showing that this is not always the case for reaction-diffusion systems.

4.2.3 Optimal invasion strategy

The difference in motility between isolated bacteria and bacterial clusters leads to distinct characteristics regarding their persistence and instantaneous speed. In the article [123], it was shown that bacterial clusters move faster than isolated bacteria. Moreover, based on the contrasting mechanisms of adventurous and social twitching motility [210, 211], we decided to test the case where A motility is more persistent than the other. Therefore, we assume that parameter values are $v > 1$ and $\tau < 1$.

In Figure 4.2, using numerical simulations, we look at the critical speed of the model (4.8) as a function of the values of the couple of parameters linked to the motion characteristics (v, τ). Once again, we normalize this numerical critical speed by the speed calculated at $v=1$ and $\tau=1$. When $v=1$ and $\tau=1$, the front is pulled, and the selected linear speed is the parabolic speed. The intensity of the red color represents the renormalized numerical critical speed. We observe that as either v or

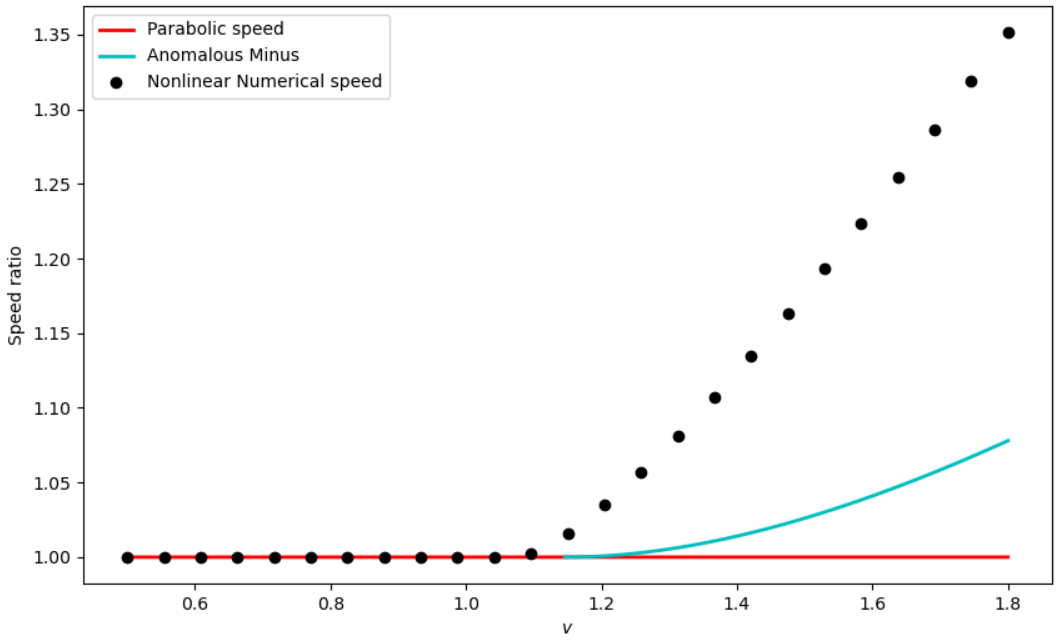

FIGURE 4.1 – **Comparison between the numerical critical speed of the model** (4.8) **and the theoretical linear speed for different values of parameter** v**.** The black points correspond to the numerical critical speed of the model (4.8) normalized by the speed for $v = 1$. The red curve represents the parabolic speed, and the cyan curve represents the anomalous minus speed. For v small enough, the critical speed corresponds to the parabolic speed, indicating a pulled front regime. For $v > v_c \approx 1.1$, the critical speed differs from the possible linear speeds, indicating a pushed front regime. The other parameter values are given by $k = 1$, $\alpha_1 = 1$, $\alpha_2 = 4$, $\tau = 1$, $N_M = 6$, $\epsilon = 0.9$, and $\delta = 2$.

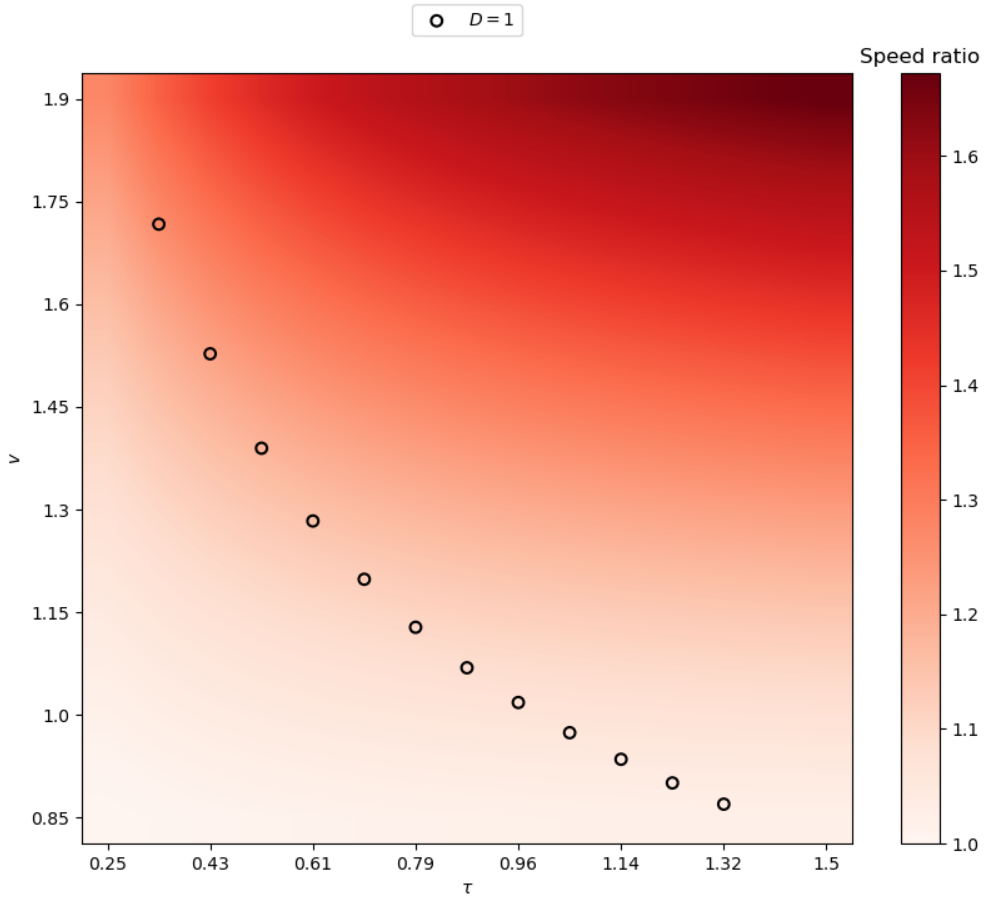

FIGURE 4.2 – **Evolution of the numerical critical speed of the travelling wave as a function of the parameters τ and v for the model** (4.8). The colorimetry represents the intensity of the numerical critical speed obtained from our numerical simulations, divided by the speed at $\tau = 1$ and $v = 1$ (parabolic speed). The circles correspond to the constraint $D := \tau v^2 = 1$. We note that under the constraint $\tau v^2 = 1$, the increase of v and the decrease of τ leads to an increase in the speed ratio. The parameter values are : $\alpha_1 = 0.5$, $\alpha_2 = 4$, $k = 1$, $\epsilon = 0.85$, $\delta = 3$, $N_M = 6$.

τ increases, this speed also increases. Since the instantaneous speed advantage of clusters is offset by a persistence disadvantage, it is also important to study the evolution of the critical speed as one parameter increases and the other decreases.

As mentioned in the introduction, the diffusion coefficient is a combination of persistence and instantaneous speed (4.3). We denote by D the ratio between the coefficient of diffusion associated with bacterial clusters and the diffusion coefficient of isolated bacteria. To focus exclusively on the impact of differences in instantaneous speed and persistence time between clusters and isolated bacteria, we assume that this ratio is equal to 1, i.e., $D := \tau v^2 = 1$. If this ratio differs from 1, for example $D > 1$, this difference could alone influence the propagation speed of the bacteria [148, 149]. We thus define $\mathbf{s}$ as the nonlinear critical speed of the model (4.8), under the constraint $1 = \tau v^2$,

$$\mathbf{s}(\tilde{v}) = s^\star(\tau = 1/\tilde{v}^2, v = \tilde{v}),$$

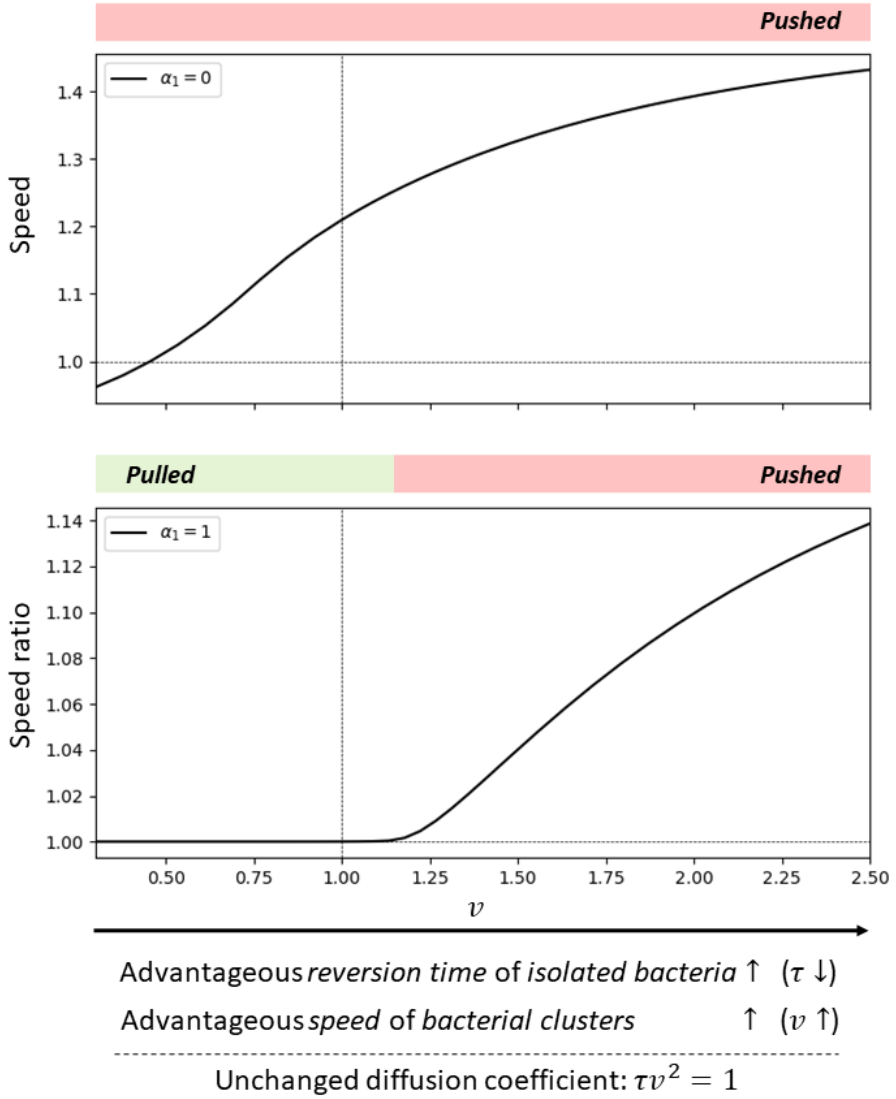

FIGURE 4.3 – **Evolution of the numerical critical speed of the model** (4.8) **under the constraint** $1 = \tau v^2$ **for : Top.** $\alpha_1 = 0$**, Bottom.** $\alpha_1 = 1$**.** The black curves represent the numerical nonlinear speed of the model (4.8). For the bottom figure, we normalize this numerical speed by the speed calculated at $\tau = 1$ and $v = 1$ (parabolic speed). We calculate this speed for different values of v under the constraint $1 = \tau v^2$, so as v increases, the value of the parameter τ, not shown in the figure, will decrease. The rectangles above the two figures illustrate the pushed or pulled regime of the traveling wave. We observe that in both cases, the increase in v coupled with the decrease in τ leads to an increase in the critical speed. The values of the other parameters are given by $\alpha_2 = 4$, $k = 1$, $\epsilon = 0.85$, $N_M = 3$ and $\delta = 2$.

with $s^\star$ the critical nonlinear speed of traveling wave solution of (4.8).

In Figure 4.3, we plot, for two parameter values α_1, the variations of the speed $\mathbf{s}$. Firstly, we assume the extreme case where the division rate of isolated bacteria is zero, which is mathematically expressed as $\alpha_1 = 0$. In this case, we observe that the speed $\mathbf{s}$ is strictly increasing as v increases (and as τ decreases) under the constraint $1 = \tau v^2$. Under the assumption $\alpha_1 = 0$, we lose the linear proliferation term of isolated bacteria, so propagation can only occur through the nonlinear terms.

In the case $\alpha_1 = 1$, we observe two possible scenarios. When v is small enough, the front is pulled, and the critical nonlinear speed always corresponds to the normal critical nonlinear speed in the case $v = 1$ and $\tau = 1$. Indeed, according to our numerical simulations, it is impossible to select an anomalous speed. When v becomes large enough, the front becomes pushed, and the increase in v under the constraint $1 = \tau v^2$ leads to an increase in invasion speed. In this figure, the critical transition between pulled and pushed fronts is close to the value $v_c \approx 1.1$ ($\tau_c = 1/v_c^2$). This critical threshold strongly depends on the parameter values.

More generally, according to our numerical simulations, for $\alpha_1 > 0$, there exists v_c such that : if the advantage of instantaneous speed coupled with the disadvantage of persistence is sufficiently small, i.e., $v < v_c$, the invasion speed is not affected by this difference in speed and persistence. In such a case, the coexistence of both motility systems would not impact the propagation speed of the bacteria. However, if the instantaneous speed v becomes greater than the critical threshold v_c (resulting in $\tau < \tau_c$), in this case, the advantage of clusters leads to an increase in the invasion speed. Thus, the coexistence of both motility systems, adventurous and social, would be a significant advantage for predation.

4.3 Extended model $n > 2$.

In this extended model, the spatially homogeneous null state remains an unstable equilibrium point. The stable steady state is more complex to characterize explicitly, and we use numerical simulations to determine it.

4.3.1 Linear speed

By applying a reasoning similar to the case $n = 2$, by Definition 1, we show in Appendix B that the linear propagation speed, $s^\star_{\text{lin}}$, can take the following possible values :

- The two normal speeds : parabolic and hyperbolic

$$s_{\text{para}} := \frac{2\sqrt{\alpha_1}}{1 + \alpha_1 \epsilon^2}, \qquad s_{\text{hyp}} := \frac{1}{\epsilon}.$$

- The different anomalous speeds : $s^{\pm}_{\text{anom},i}$ for all $i \in \{2, \dots, n\}$, where $s^{\pm}_{\text{anom},i}$ are defined in equation (B.26).

4.3.2 Nonlinear speed – Pulled and Pushed regime

In Figure 4.4, using numerical simulations, we plot, with black dots, the evolution of the critical speed for the nonlinear model (4.4)-(4.5)-(4.6) for different functions v. More precisely, we define v as a threshold function of the following form $v(i) = \mathbf{1}_{i<\lfloor n/2 \rfloor}(i) + \bar{v}\mathbf{1}_{i\geq\lfloor n/2 \rfloor}(i)$, for all $i \in \{2, \dots, n\}$, with

$\bar{v}$ a positive real parameter that we vary in Figure 4.4. For the same reasons as before, we normalize the numerical speed by the speed obtained at $\bar{v} = 1$. To compare with theoretical linear speeds, we also illustrate the parabolic speed by the red curve and the largest of the admissible anomalous speeds by the blue curve, both normalized by the parabolic speed. When $\bar{v}$ is small enough, the speed of the system (4.4)-(4.5)-(4.6) equals the linear prediction. However, when $\bar{v}$ becomes sufficiently large, the speed surpasses the linear speeds, and the front becomes pushed.

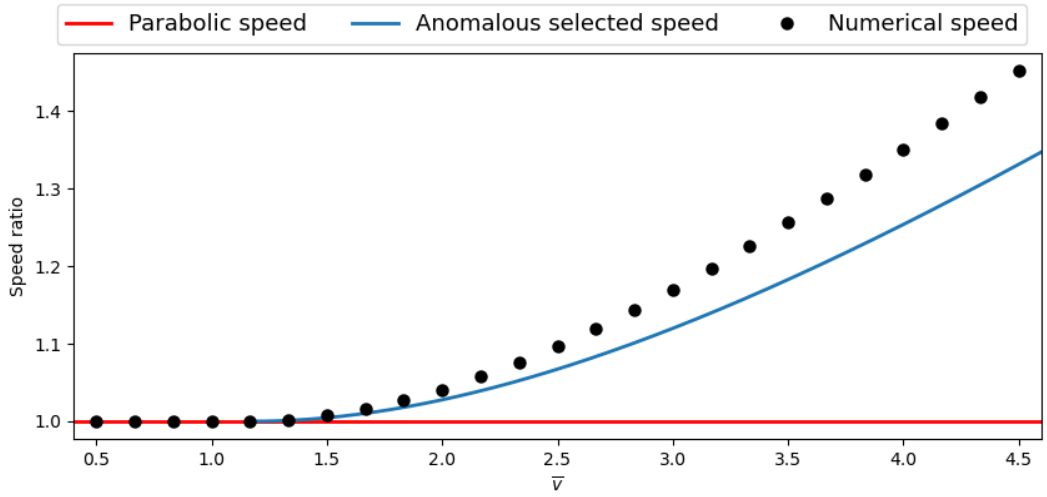

FIGURE 4.4 – **Comparison between the numerical critical speed of the nonlinear model (4.4)-(4.5)-(4.6) and the theoretical linear speed for different values of the parameter $\bar{v}$.** The black points correspond to the numerical critical speed of the nonlinear model (4.4)-(4.5)-(4.6) normalized by the speed for $\bar{v} = 1$. The red horizontal line represents the parabolic linear speed, and the blue curve represents the largest admissible anomalous speeds, both normalized by the parabolic speed. For $\bar{v}$ small enough, the critical speed of the nonlinear model is equal to the linear speed. Then, when $\bar{v}$ becomes large enough, the nonlinear speed becomes strictly greater than the linear speed. The values of the other parameters are given by $\beta = \gamma = \alpha_1 = \alpha_2 = N_M = 1$, $n = 4$, $\epsilon = 0.95$, $\delta = 1.5$, and the functions are given by $\tau(i) = 1$ for all $i \in \{1, 2, 3, 4\}$, $v(2) = 1$.

4.3.3 Biological modeling

Propagation example

In Figure 4.5, we illustrate the traveling wave solution of the model with multiple cluster sizes (4.4)-(4.5)-(4.6). Dotted lines represent the density of clusters of different sizes multiplied by their size at a given time T. The propagation speeds associated with the densities p_i, with $i \in \{1, \dots, n\}$, are always similar. The grey area corresponds to the nutrient density at the same time. Upstream of the front, we only observe the presence of isolated bacteria represented by the black line. These isolated bacteria generate nutrients that subsequently allow the invasion of bacteria clusters. The different cluster sizes are indicated by the following colorimetry : from blue ($i = 2$) to red ($i = n$). We note that the invasion of clusters of different sizes occurs in a staggered and ordered manner based on their size.

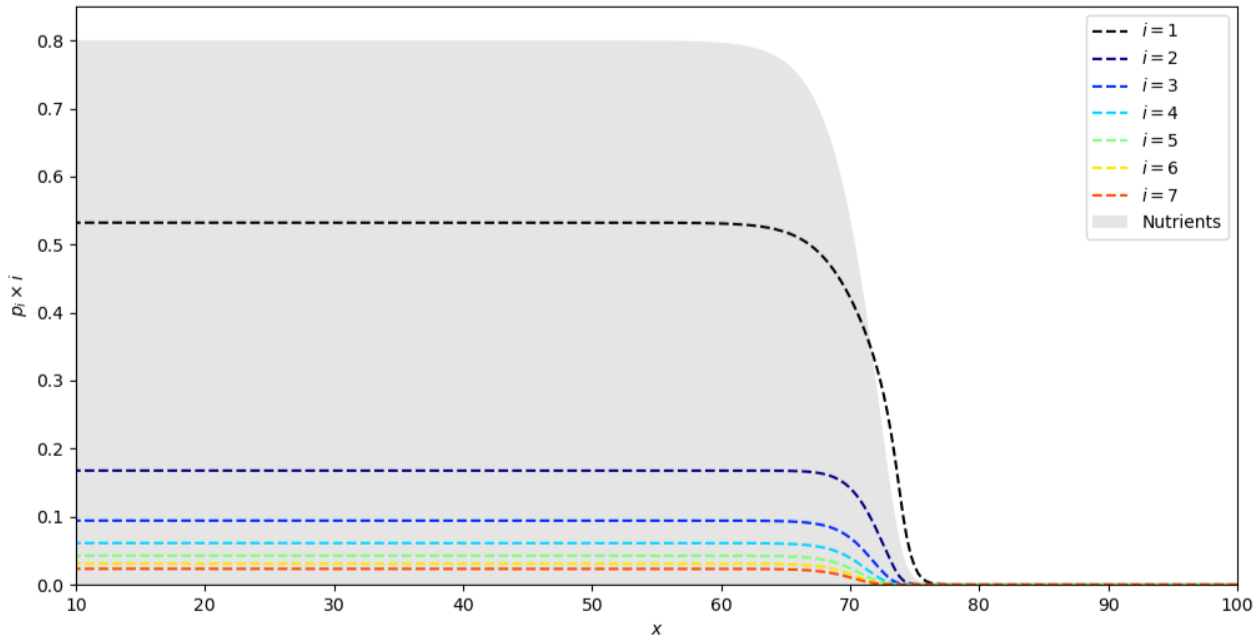

FIGURE 4.5 – **Example of traveling wave solutions of the model** (4.4)-(4.5)-(4.6) **at time** $t = T$**.** The nutrient density, N, is represented in grey. The dashed lines correspond to the densities of different sizes of bacterial clusters multiplied by their size, $p_i(x) \times i$ at time $t = T$. The black line represents isolated bacteria, while the lines from blue to red correspond to bacterial clusters and more precisely, from the cluster of two bacteria in blue to the cluster of n bacteria in red. We observe an invasion of isolated bacteria, leading to the creation of nutrients. In the region where nutrients are present, we see the successive invasion of clusters of increasingly larger sizes. This spatial heterogeneity in the distribution of different cluster sizes has been recently observed biologically in the article [140]. The parameter values are given by $\beta = \gamma = \epsilon = \delta = \alpha_1 = \alpha_2 = N_M = 1$, $n = 10$, and the functions are defined as follows : $v(i) = \tau(i) = 1$ for all $i \in \{2, \dots, n\}$.

After isolated bacteria, we observe the emergence of clusters of two bacteria, then clusters of three bacteria, and so on. This heterogeneity is also observed in biological predation experiments with the bacteria *M. xanthus* [140]. Indeed, at the forefront of the predation front, there are mainly isolated bacteria, called *scouts*. Following this group, clusters of small size, called *loners*, appear. Finally, in the wake of these clusters, the invasion of large clusters, called *swarms*, occurs.

Study of strain invasion speed

In the article [137], the authors investigated the invasion speed of three strains, *Wildtype* ($A+S+$), $A+S-$, and $A-S+$. The *Wildtype* strain has both motility apparatuses, A and S, while the other strains are mutants that have lost one of these systems : the $A+S-$ strain has lost the S apparatus, and the $A-S+$ strain has lost the A apparatus. To do this, the authors conducted three similar predation experiments, one for each strain, which they stopped at the same time to analyze the progress of the bacterial invasion. Their results show that the $A-S+$ strain has significant difficulty invading the prey

compared to the *Wildtype* and $A+S-$ strains. In this section, we adapt our model to the specific case of the $A+S-$ and $A-S+$ strains.

To model the $A+S-$ strain, we remove the transport term for bacterial clusters from the previous model, *i.e.* $v(i) = 0$ for all $i \in \{2, \dots n\}$. Similarly, for the $A-S+$ strain, we remove the transport term of isolated bacteria.

In Figure 4.6, we carry out numerical simulations similar to the biological experiments performed in the article [137]. Specifically, we carry out three independent numerical simulations, one for each strain, which we stop at the same time to compare the invasion of the three strains. The black curve corresponds to the *Wildtype* strain, the red curve to the $A+S-$ strain, and the green curve to the $A-S+$ strain. Our numerical results are consistent with the findings of the biological experiments; the $A-S+$ strain is significantly slower in invading the *E. coli* prey compared to the other strains.

For these parameter values, the invasion speed of the *Wildtype* strain is similar to the invasion speed of the $A+S-$ strain. However, as explained earlier, for other parameter values, the front can be pushed, and in that case, the speed of the *Wildtype* strain would be greater than the speed of the $A+S-$ strain. Regarding the biological experiments performed in the article [137], the $A+S-$ strain is slightly faster in terms of predation than the *Wildtype* strain. Nevertheless, these results are highly variable, and more experiments are needed to conclude a significant difference between these two strains. Note that, in the absence of prey, the *Wildtype* strain propagates significantly faster than both the $A+S-$ and $A-S+$ strains, demonstrating that motilities A and S are used synergistically [212]

Optimal motility strategy for invasion

The interest of the coexistence of the two motility systems is an important question in this field. As explained earlier, these two distinct motility systems lead to significant differences in bacterial movement characteristics. We assume that, for the reasons specified before, the diffusion coefficient remains unchanged for different cluster sizes, and only differences in instantaneous speed and persistence need to be considered. The A motility of isolated bacteria induces a relatively low speed but, in return, a very high persistence in the same direction. In contrast, the social motility of clusters generates a higher speed along one direction but a much lower persistence. To study the impact of these differences on predation speed, we examine the critical speed of the model (4.4)-(4.5)-(4.6) for different couples of functions (v_j, τ_j) under the constraint $v_j^2 \tau_j = 1$, corresponding to the assumption that the diffusion coefficient D is equal to 1 for all cluster sizes (see (4.3)).

Several choices of function families are possible for instantaneous speed/persistence. We particularly study linear functions and Hill functions. First, we assume that the functions v_j are linear. More precisely, we assume that the family of functions $(v_j)_j$ corresponds to the lines connecting the point $(1, 1)$ to the point $(n, \bar{v}_{n,j})$, with $\bar{v}_{n,j} \in \mathbb{R}_+^\star$ corresponding to the speed of clusters of size n. When $\bar{v}_{n,j} < 1$, we have $v_j' < 0$, so the clusters are slower than isolated bacteria but, in return, will have a greater persistence ($\tau_j = 1/v_j^2$). We have the opposite result for $\bar{v}_j > 1$. Moreover, as $\bar{v}_j$ increases compared to 1, the difference in motility between isolated bacteria and clusters becomes more significant. In the top of Figure 4.7, we illustrate the family of functions $(v_j)_j$ (on the left) for different values of

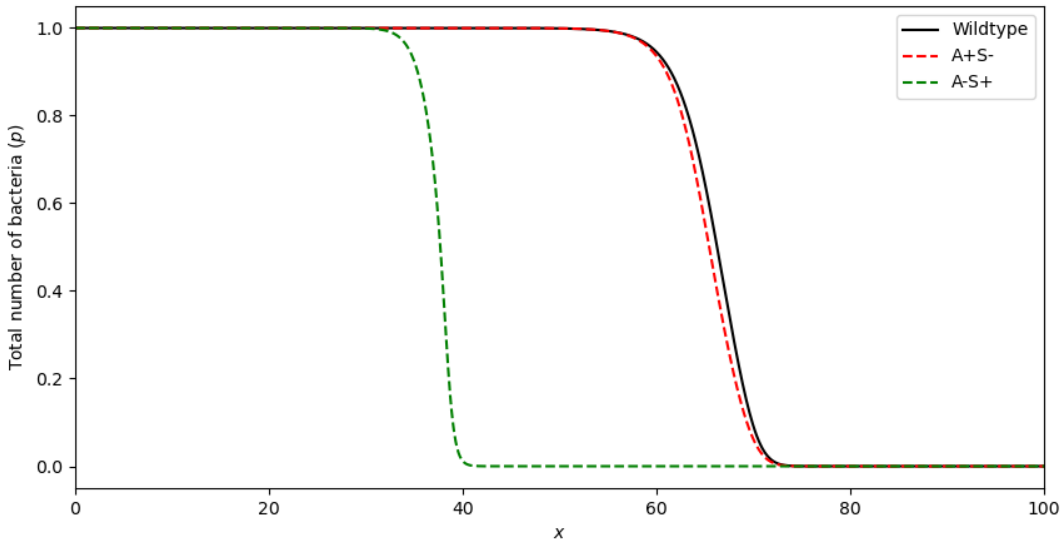

FIGURE 4.6 – **Comparison of the invasion of the three different strains : *Wildtype*, $A+S-$, $A-S+$ at time $t = T$.** The black curve is a numerical solution of the model (4.4)-(4.5)-(4.6) associated with the *Wildtype* strain. The red (respectively green) curve is a numerical solution of the same model but without transport terms for clusters of bacteria (respectively for isolated bacteria) and corresponds to the $A+S-$ strain (respectively $A-S+$ strain). For the *Wildtype* strain and the $A+S-$ strain, the functions v and τ are defined as $v(i) = 1.25$ and $\tau(i) = 1/(1.25^2)$ for all $i \in \{2, \dots, n\}$. For the $A-S+$ strain, the functions v and τ are defined as $v(i) = 0$ and $\tau(i) = 1/(1.25^2)$ for all $i \in \{2, \dots, n\}$. The parameter values are : $n = 10$, $\beta = \gamma = \delta = \alpha_1 = \alpha_2 = N_M = 1$, $\epsilon = 0.5$.

$(\bar{v}_j)_j$, as well as the associated family of functions, $(\tau_j)_j$ (on the right). In the bottom of Figure 4.7, we also plot the critical speed of the model (4.4)-(4.5)-(4.6), for the different couples of functions (v_j, τ_j) as a function of the coefficients $\bar{v}_j$ associated with these couples. The colors of the squares correspond to the color curves of the associated functions v_j and τ_j in the figures above. In Figure 4.8, we follow the same reasoning, but this time taking functions v_j in the form of Hill functions.

For both Figures 4.7 and 4.8, the results on the critical speed are similar. When the difference in instantaneous speed between clusters and isolated bacteria is either a disadvantage or too small an advantage, this difference in instantaneous speed/persistence does not affect the predation speed of bacteria *M. xanthus*. More specifically, in this case, the front is pulled. Indeed, the invasion speed is equal to the linear speed, which, for these parameter values, is the parabolic speed. However, when the speed advantage of bacterial clusters (coupled with the disadvantage of cluster persistence) becomes significant enough, the coexistence of A and S motility enables faster invasion of the prey. In this case, the front is pushed, and the impact on the predation speed is proportional to the difference in instantaneous speed/persistence. In other words, the coexistence of two motility systems either does not affect predation speed, and in this case, the invasion speed is solely influenced by isolated bacteria (pulled front), or it allows faster predation (pushed front). Thus, according to our model, the coexistence of two motility systems is never a disadvantage for predation.

4.4 Conclusion

In this work, we introduce a model concerning the predation of the social bacterium *Myxococcus xanthus*. This model, corresponding to an extension of previous models, aims primarily to model and study the impact of differences between the two motility systems, A and S. For this model, we determine a formula for the linear speed. Particularly, we demonstrate the presence of anomalous speeds caused by the linear coupling between the clusters and the isolated bacteria. Regarding the speed of the nonlinear model, our numerical simulations show the existence of a transition between the pulled-front regime and the pushed-front regime, in which the selected speed exceeds the linear prediction.

From a modelling point of view, the numerical simulations of our model verify characteristics presented in biological experiments. Specifically, our model confirms the spatial distribution of different cluster sizes in the invasion front. It also provides an explanation for biological experiments on the invasion speed of the *Wildtype*, $A+S-$, and $A-S+$ strains. As the experiments showed, the $A-S+$ strain had great difficulty in invading the prey. Furthermore, we use our model to show that the coexistence of the two motility systems, A and S, has either a neutral or a positive effect on faster predation. If the difference in motility does not lead to sufficiently large differences in instantaneous speed and persistence, this coexistence will not influence the propagation speed. Conversely, if this difference is significant enough, it will proportionally induce an increase in the invasion speed.

To determine whether the coexistence of A and S motility has a neutral or positive impact on predation, it is crucial to determine precisely the transition between a pulled-front and a pushed-front regime. However, numerically approximating this transition with high precision is complex. A new numerical method, based on far-field decomposition, makes it possible to approximate this transition

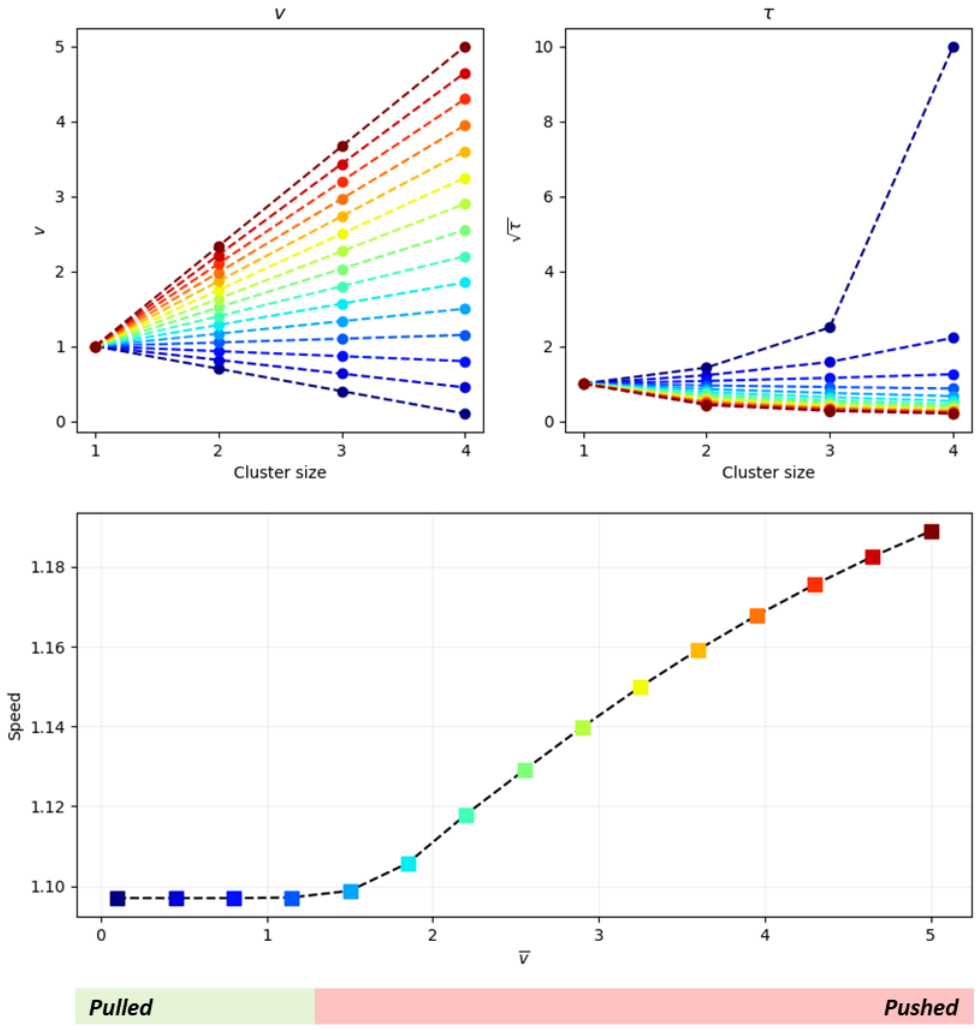

FIGURE 4.7 – **Evolution of the numerical critical speed of the model** (4.4)-(4.5)-(4.6) **under the constraint** $1 = \tau v^2$ **with** v **a linear function. Top.** On the left, we represent a family of instantaneous speed functions v_j. The instantaneous speeds v_j are lines connecting the point $(1, 1)$ to the point $(n, \bar{v}_j)$, with $(\bar{v}_j)$ a uniform discretization of the interval $[0.1, 5]$, represented by the color spectrum from blue ($\bar{v} = 0.1$) to red ($\bar{v} = 5$). On the right, the figure illustrates the functions τ_j associated with instantaneous speeds v_j under the constraint $1 = v_j^2 \tau_j$. **Bottom.** For each couple of functions (v_j, τ_j), we numerically compute the critical speed of the model (4.4)-(4.5)-(4.6) and we indicate the result by a square with the corresponding colour. When $\bar{v}$ is small enough, the critical speeds are equal to the linear speed, and the front is pulled. In this case, the propagation speed is independent of the coefficient $\bar{v}$. However, when the coefficient, $\bar{v}$, becomes large enough, the front becomes pushed and predation of the bacteria is faster. The values of the other parameters are given by $n = 4$, $\epsilon = 0.9$, $\alpha_1 = \alpha_2 = \gamma = \beta = N_M = 1$ and $\delta = 3$.

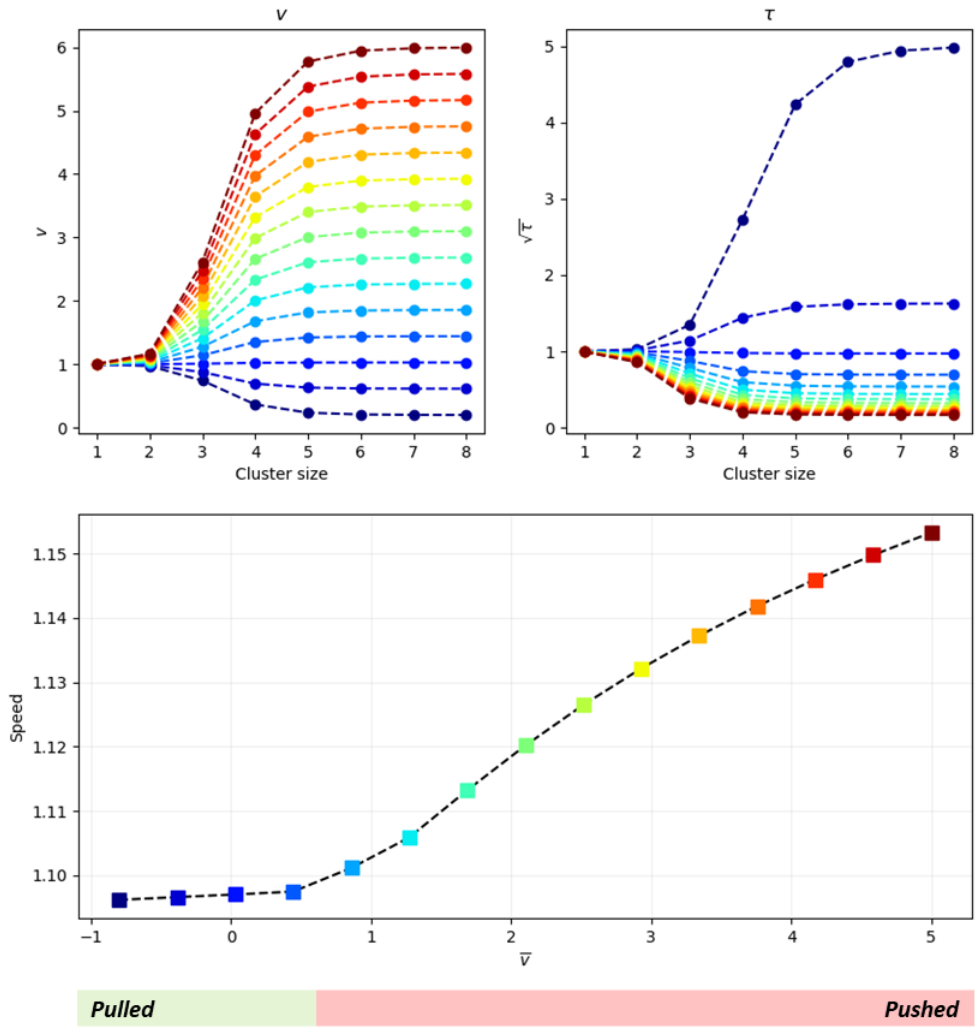

FIGURE 4.8 – **Evolution of the numerical critical speed of the model** (4.4)-(4.5)-(4.6) **under the constraint** $1 = \tau v^2$ **with** v **a Hill function. Top.** On the left, we represent a family of instantaneous speed functions v_j. The functions v_j are of the form $v_j(i) = 1 + \bar{v}_j \cdot h(i)^m/(1 + h(i)^m)$, where h is an affine function given by $h(i) = i \cdot h_1 + h_0$, m is an integer and $(\bar{v}_j)$ a uniform discretization of the interval $[-1, 5]$. On the right, the figure illustrates the functions τ_j associated with instantaneous speeds v_j under the constraint $1 = v_j^2 \tau_j$. **Bottom.** For each couple of functions (v_j, τ_j), we numerically compute the critical speed of the model (4.4)-(4.5)-(4.6) and we indicate the result by a square with the corresponding colour. When $\bar{v}$ is small enough, the critical speeds are equal to the linear speed, and the front is pulled. In this case, the propagation speed is independent of the coefficient $\bar{v}$. However, when the coefficient, $\bar{v}$, becomes large enough, the front becomes pushed and predation of the bacteria is faster. The values of the other parameters are given by $n = 8$, $\epsilon = 0.9$, $\alpha_1 = \alpha_2 = \gamma = \beta = N_M = 1$, $\delta = 3$, $m = 10$, $h_0 \approx 0.28$ and $h_1 \approx 0.21$.

with extreme accuracy for a large family of reaction-diffusion systems [48]. It would be interesting to extend these results to hyperbolic systems. Once this threshold has been precisely calculated, it would be interesting to determine biologically reasonable parameter values in order to determine the associated front regime : pulled or pushed.

In comparison to other bacterial predators specialized in specific prey, *Myxococcus xanthus* stands out as a generalist predator capable of feeding on a wide variety of prey [132]. Due to the vast spectrum of potential prey for *Myxococcus xanthus*, the predation process of this bacterium is likely to be extremely complex, involving various molecular mechanisms acting independently or synergistically to attack different species. It would therefore be relevant to explore, both mathematically and biologically, the variations in the predation process exerted by *M. xanthus* on different prey species. Additionally, some bacterial prey, such as *Bacillus subtilis*, *Pseudomonas fluorescens* and *Escherichia coli*, adopt defensive strategies, including the formation of specific biofilms or the secretion of antibiotics [213, 214, 215, 216]. Therefore, it could also be interesting to study the defensive reactions of prey against the predator.

In this article, we focused on the predation front of *M. xanthus*. In the wake of the invasion front, two main phenomena occur successively : *rippling* and then the formation of fruiting bodies. Following the advance of the predation front, the presence of cellular debris allows *M. xanthus* cells to coordinate their movement by forming accordion-like undulations, similar to the undulations of water [116, 217, 118, 117, 119]. During these undulations, called *ripples*, each wave crest oscillates back and forth without generating a net displacement, although individual cells change their positions. Then, in times of starvation, cells form aggregates, exchanging extracellular chemical signals as well as signals from physical contact, thereby creating multicellular fruiting bodies [115]. The cells involved in fruiting bodies undergo transformation into myxospores, highly resistant to heat [218]. Sporulation has the advantage of enabling survival in hostile environments and increasing germination and growth rates when the cells encounter favourable conditions.

In the literature, there are already several models of different natures aimed at modelling rippling [119, 145, 146], including models with *Run and Tumble* motion [143, 219, 144]. Similarly, numerous models have been introduced to model the formation of fruiting bodies (see, for example, [220, 221, 222]). In order to develop a model encompassing all these phenomena, it would be interesting to extend our hyperbolic model to determine if it can also describe, in the wake of the invasion front, the rippling phenomenon and then, once nutrients are depleted, the formation of fruiting bodies. The existence of periodic solutions in space (formation of fruiting bodies) and/or in time (rippling) are phenomena that have already been extensively studied for hyperbolic equations and systems of equations [223, 224, 225, 226, 227, 228, 229].

A Derivation of the linear propagation speed for $n = 2$

First, we provide the definition of the term *pinched double roots* from [55, Defintion 4.2]

Definition (Pinched double root):
We say $(\nu_\star, \lambda_\star)$ *is a* pinched double root *of the dispersion relation* $D_s(\nu, \lambda)$ *if*

1. Double root : *we have*

$$D_s(\nu_\star, \lambda_\star) = 0, \quad \textit{and}, \quad \partial_\nu D_s(\nu_\star, \lambda_\star) = 0. \tag{A.10}$$

2. Pinching : *there exists a continuous curve* $\lambda(\tau)$*, with* $\tau \in \mathbb{R}_+$ *satisfying :*

- $\mathrm{Re}\ \lambda(\tau)$ *is strictly increasing,*
- $\lambda(0) = \lambda_\star$*,*
- *and* $\mathrm{Re}\ \lambda(\tau) \to \infty$ *as* $\tau \to \infty$*,*

and continuous curves of roots $\nu^\pm(\lambda(\tau))$ *which satisfy*

- $\nu^\pm(\lambda_\star) = \nu_\star$*,*
- *and*

$$\lim_{\tau\to\infty} \mathrm{Re}\ \nu^\pm(\lambda(\tau)) = \pm\infty. \tag{A.11}$$

In this work, we are only interested in time-stationary fronts in the moving frame reference. Consequently, we consider the values $\lambda \in \mathbb{R}^+$, and negative eigenvalues, $\nu \in \mathbb{R}^-$.

Derivation of *normal* speeds. In the decoupled case, $k = 0$, the first two equations (4.9a)-(4.9b) give us the following system

$$\begin{cases} \partial_t p_1^+ + \dfrac{1}{\epsilon}\partial_x p_1^+ = \dfrac{1}{2\epsilon^2}(p_1^- - p_1^+) + \dfrac{\alpha_1}{2}p_1, & \text{(A.12a)} \\ \partial_t p_1^- - \dfrac{1}{\epsilon}\partial_x p_1^- = \dfrac{1}{2\epsilon^2}(p_1^+ - p_1^-) + \dfrac{\alpha_1}{2}p_1, & \text{(A.12b)} \end{cases}$$

which can be expressed as,

$$\epsilon^2\partial_{tt}p_1 + (1 - \alpha_1\epsilon^2)\partial_t p_1 = \partial_{xx}p_1 + \alpha_1 p_1.$$

This linear equation has been extensively studied (See for example [196, 202]). In particular, it has been shown that the associated critical propagation speed is given by the following formula

$$\begin{cases} \dfrac{2\sqrt{\alpha_1}}{1 + \epsilon^2\alpha_1}, & \text{if } \epsilon \le 1/\sqrt{\alpha_1}, \qquad \text{(Parabolic regime)} \\ \dfrac{1}{\epsilon}, & \text{otherwise.} \qquad \text{(Hyperbolic regime)} \end{cases} \tag{A.13}$$

In the parabolic regime, the speed is a perturbation of the critical speed of the Fisher-KPP parabolic equation. While, for the hyperbolic regime, the critical speed corresponds to the maximum possible speed of the wave, which is equal to the coefficient of the transport term.

In the moving frame, $\xi = x - st$, we seek solutions in the exponential form $e^{\lambda t + \nu\xi}\overline{p_1}$, we obtain the following dispersion relation,

$$D_s^{(1)}(\nu, \lambda) = \nu^2 + \nu\frac{s}{1 - \epsilon^2 s^2}(1 - \alpha_1\epsilon^2 - 2\lambda\epsilon^2) + \frac{1}{1 - \epsilon^2 s^2}\left[\alpha_1 - \epsilon^2\lambda^2 - (1 - \alpha_1\epsilon^2)\right],$$

with the two following associated roots,

$$\nu_1^\pm(\lambda, s; \alpha_1, \epsilon) = \frac{s(1 - \alpha_1\epsilon^2) + 2s\epsilon^2\lambda \mp \sqrt{s^2(1 + \alpha_1\epsilon^2)^2 - 4\alpha_1 + 4\lambda(1 - \alpha_1\epsilon^2 + \lambda\epsilon^2)}}{2(\epsilon^2 s^2 - 1)}. \tag{A.14}$$

The dispersion relation has a double root when $\nu_1^+ = \nu_1^-$. Since the speed of $p_1^\pm$ is given by the value $1/\epsilon$, we consider only the range of plausible invasion speeds $s \in]0, 1/\epsilon]$. By performing a Taylor expansion of the eigenvalues as $\lambda \to \infty$, we obtain the following relation

$$\nu_1^\pm(\lambda, s) = \frac{\lambda\epsilon}{(\epsilon s \pm 1)} + \underset{\lambda\to+\infty}{o}(\lambda).$$

Consequently, we have the following limit, $\nu_1^\pm(\lambda, s) \to \pm\infty$ as $\lambda \to +\infty$. The pinching condition is therefore satisfied. The equality $\nu_1^+ = \nu_1^-$ gives us

$$s_1^2(\lambda; \alpha_1, \epsilon) = \frac{4\alpha_1}{(1+\alpha_1\epsilon^2)^2} - \frac{4\lambda(1-\alpha_1\epsilon^2+\lambda\epsilon^2)}{(1+\alpha_1\epsilon^2)^2}. \tag{A.15}$$

To determine the linear propagation speed, we need to minimize the function Λ defined by

$$\Lambda(\lambda; \alpha_1, \epsilon) := \frac{4\lambda(1-\alpha_1\epsilon^2+\lambda\epsilon^2)}{(1+\alpha_1\epsilon^2)^2}.$$

- When $\epsilon \leq 1/\sqrt{\alpha_1}$, the minimum of the function Λ is reached at $\lambda = 0$. In this case, we indeed obtain the parabolic propagation speed.

$$s_1 = s_{\text{para}} := \frac{2\sqrt{\alpha_1}}{1+\epsilon^2\alpha_1},$$

  already demonstrated by Hadeler [196] and Fedotov [198] using completely different methods.
- When $\epsilon > 1/\sqrt{\alpha_1}$, the minimum of the function Λ is reached at $\lambda = \lambda^\star$, with $\lambda^\star := -(1-\alpha_1\epsilon^2)/(2\epsilon^2)$. Substituting this into equation (A.15), we obtain the hyperbolic propagation speed $s_1 = s_{\text{hyp}} := 1/\epsilon$. In this case, the associated $\nu^\star$ is null. Contrary to the pinched double root of the parabolic case, the one of the hyperbolic case is not simple relatively to λ.

Consequently, the concept of pinched double roots allows us to easily obtain the critical linear speed of the system (A.12a)-(A.12b), which was already demonstrated in the article [202] using a different method.

Derivation of *anomalous* speeds. To determine a potential anomalous speed, we now consider equations (4.9c)-(4.9d). Following a similar approach as in the previous analysis, we can derive the pair of eigenvalues associated with the system of two equations (4.9c)-(4.9d). These eigenvalues, denoted as ν_2^- and ν_2^+, are defined by

$$\nu_2^\pm(\lambda, s; \epsilon, v, \tau, k) = \frac{s(1+2\epsilon^2\tau k) + 2\epsilon^2\tau\lambda s \mp \sqrt{4\lambda\tau v^2\left(1+2\epsilon^2\tau k+\epsilon^2\tau\lambda\right) + s^2 + 4k\tau v^2(1+\epsilon^2\tau k)}}{2\tau(\epsilon^2 s^2 - v^2)}. \tag{A.16}$$

The dispersion relation for the complete linear system (4.9a)-(4.9d), due to the triangular structure of the problem, is given by the following formula :

$$D_s(\nu, \lambda) := \left(\nu - \nu_1^+(\lambda, s)\right)\left(\nu - \nu_1^-(\lambda, s)\right)\left(\nu - \nu_2^+(\lambda, s)\right)\left(\nu - \nu_2^-(\lambda, s)\right).$$

This dispersion relation has double roots if one of the equalities $\nu_1^+ = \nu_1^-$, $\nu_2^+ = \nu_2^-$, $\nu_1^+ = \nu_2^-$ and $\nu_1^- = \nu_2^+$ is satisfied. As previously shown, the double root when $\nu_1^+ = \nu_1^-$ is pinched and leads

to parabolic and hyperbolic speeds. The equality $\nu_2^+ = \nu_2^-$ is associated with a complex propagation speed. Let us now consider the equality $\nu_1^- = \nu_2^+$. When ν_2^+ is real, its sign is always positive according to definition (A.16). Therefore, we do not consider this equality. Finally, we examine the last double root $\nu_1^+ = \nu_2^-$. This time, analyzing the signs of the eigenvalues shows that consistent triplets (ν, s, λ) can be obtained. As we have seen before, ν_1^+ tends to $+\infty$ as $\lambda \to +\infty$. Conversely, the expansion of ν_2^- for $\lambda \to +\infty$ is given by the following relation

$$\nu_2^-(\lambda, s) = \frac{\lambda\epsilon}{\epsilon s - v} + \underset{\lambda\to+\infty}{o}(\lambda).$$

Consequently, when $s < v/\epsilon$, we have the limit $\nu_2^- \to -\infty$ as $\lambda \to +\infty$. Here, the possible wave propagation speeds, s, lie between 0 and $\max(1/\epsilon, v/\epsilon)$. Therefore, it is possible to have $s > v/\epsilon$ when $v < 1$. In this case, the root does not satisfy the pinching condition, and no anomalous speed is expected.

The anomalous speed associated with the equality $\nu_1^+ = \nu_2^-$ is a solution of the following polynomial equation,

$$a_4 s^4 + a_2(\lambda)s^2 + a_0(\lambda) = 0, \tag{A.17}$$

with

$$a_0(\lambda) := \left((\lambda + k)\left[1 + \epsilon^2\tau(\lambda + k)\right] - \tau v^2(\lambda - \alpha_1)\left[1 + \epsilon^2\lambda\right]\right)^2, \tag{A.18}$$

$$\begin{aligned} a_2(\lambda) := \big[(1 - \alpha_1\epsilon^2)(1 + 2\epsilon^2\tau k) + 2\alpha_1\tau\epsilon^2 - 2k\epsilon^2(1 + \epsilon^2\tau k)\big] \\ \left\{(\lambda + k)\left[1 + \epsilon^2\tau(\lambda + k)\right] + \tau v^2(\lambda - \alpha_1)\left[1 + \epsilon^2\lambda\right]\right\} \\ - \tau v^2(1 + \alpha_1\epsilon^2)^2(\lambda + k)\left[1 + \epsilon^2\tau(\lambda + k)\right] - (\lambda - \alpha_1)(1 + \lambda\epsilon^2), \end{aligned} \tag{A.19}$$

and,

$$a_4 := \epsilon^2(\alpha_1 + k)(k\epsilon^2 - 1)(\tau[k\epsilon^2 - 1] + 1)(1 + \epsilon^2 k\tau + \alpha_1\epsilon^2\tau). \tag{A.20}$$

Solving equation (A.17) gives us two possibles real positive speeds

$$s^{\pm}(\lambda) := \sqrt{\frac{-a_2(\lambda) \pm \sqrt{a_2^2(\lambda) - 4a_0(\lambda)a_4}}{2a_4}}. \tag{A.21}$$

We define $\Gamma^{\pm}$ as the sets given by

$$\Gamma^{\pm} = \{\lambda \in \mathbb{R}^+ :\ \nu(\lambda, s^{\pm}(\lambda)) \text{ is a pinched double root of } D_s \text{ associated with admissible } (s^{\pm}, \nu)\}.$$

Conjecture 4:
If $\Gamma^+ \cup \Gamma^- \neq \varnothing$*, then* $0 \in \Gamma^+ \cup \Gamma^-$*, and we have the following results :*

- *If* $0 \in \Gamma^+$*, then*

$$s^+(0) \geq \max\left(\max_{\lambda\in\Gamma^+} s^+(\lambda), \max_{\lambda\in\Gamma^-} s^-(\lambda)\right).$$

- *If* $0 \in \Gamma^-$*, then*

$$s^-(0) \geq \max\left(\max_{\lambda\in\Gamma^+} s^+(\lambda), \max_{\lambda\in\Gamma^-} s^-(\lambda)\right).$$

In other words, when there exists a family of admissible pinched double roots associated with the equality $\nu_1^+ = \nu_2^-$ parameterized by λ, the maximum associated speed is given by the one at $\lambda = 0$.

The high complexity of the polynomial coefficients (A.18), (A.19), and (A.20) makes proving such a result challenging. To ensure its validity, we verified that this result holds true for 10^{15} different parameter values, uniformly distributed in the parameter space $(\alpha_1, \epsilon, \tau, v, k) \in [0.05, 10]^5$. For each of these tests, the maximum admissible speed was indeed located at $\lambda = 0$.

Under the assumption of the conjecture 4, we thus define the two anomalous speeds of our problem given by

$$s^{\pm}_{\text{anom}} := s^{\pm}(0) = \sqrt{\frac{-a_2(0) \pm \sqrt{a_2^2(0) - 4a_0(0)a_4}}{2a_4}}. \tag{A.22}$$

Unlike speeds for the parabolic and hyperbolic regimes, these anomalous speeds depend on the parameters v, τ, and k. When $\epsilon = 0$, the term a_4 becomes zero, thus there is only one anomalous speed, which is given by the formula,

$$s^{\pm}_{\text{anom}}(\epsilon = 0) = \alpha_1 \frac{\sqrt{\theta - 1}}{\sqrt{k + \alpha_1}} + \frac{\sqrt{\alpha_1 + k}}{\sqrt{\theta - 1}},$$

with $\theta = \tau v^2$. This equality is in good agreement with the result obtained in the article [54].

To conclude, we obtain the following result :

Proposition 1 (Linear propagation speed for $n = 2$):
We assume conjecture 4. By definition 1, the critical linear propagation speed, $s^\star_{lin}$, can take one of four possible values :

- *The two normal speeds : parabolic and hyperbolic*

$$s_{para} := \frac{2\sqrt{\alpha_1}}{1 + \alpha_1 \epsilon^2}, \qquad s_{hyp} := \frac{1}{\epsilon}.$$

- *The two anomalous speeds :*

$$s^{\pm}_{anom} = s^{\pm}(0) = \sqrt{\frac{-a_2(0) \pm \sqrt{a_2^2(0) - 4a_0(0)a_4}}{2a_4}},$$

with a_0, a_2, and a_4 defined by equations (A.18), (A.19), and (A.20), respectively.

Numerical simulations. In this section, we focus on the selected wave speed for a nonlinear model sharing the same linear part of the model (4.8). More precisely, we introduce a nonlinear model without certain nonlinear terms such as coagulation, in order to have fronts always linearly determined. This allows us to numerically verify whether the linear speed predicted by Proposition 1 is indeed the one selected by a nonlinear model in the pulled front regime.

We consider the following nonlinear model,

$$\begin{cases} \partial_t p_1^+ + \frac{1}{\epsilon}\partial_x p_1^+ = \frac{1}{2\epsilon^2}(p_1^- - p_1^+) + \frac{k}{2}p_2(1-p_1) + \frac{\alpha_1}{2}p_1(1-p_1), & \text{(A.23a)} \\ \partial_t p_1^- - \frac{1}{\epsilon}\partial_x p_1^- = \frac{1}{2\epsilon^2}(p_1^+ - p_1^-) + \frac{k}{2}p_2(1-p_1) + \frac{\alpha_1}{2}p_1(1-p_1), & \text{(A.23b)} \\ \partial_t p_2^+ + \frac{v}{\epsilon}\partial_x p_2^+ = \frac{1}{2\tau\epsilon^2}(p_2^- - p_2^+) - kp_2^+, & \text{(A.23c)} \\ \partial_t p_2^- - \frac{v}{\epsilon}\partial_x p_2^- = \frac{1}{2\tau\epsilon^2}(p_2^+ - p_2^-) - kp_2^-. & \text{(A.23d)} \end{cases}$$

corresponding to an hyperbolic extension of the model presented in the article [54].

In Figure 4.9, we plot the selected speed of the model (A.23a)-(A.23d) using numerical simulations (black points) and the theoretical linear speeds presented in Proposition 1 (colored lines) for various values of the parameter ϵ. We observe that the numerical selected speed indeed corresponds to the predicted linear speed. When ϵ is small enough, the linear speed matches the parabolic speed (red line). As ϵ increases, the selected speed first becomes the *minus* anomalous speed (cyan line) and then the *plus* anomalous speed (magenta line). For other simulations not presented in this article, with different parameter values, we have also observed the possibility to select the hyperbolic speed (green line).

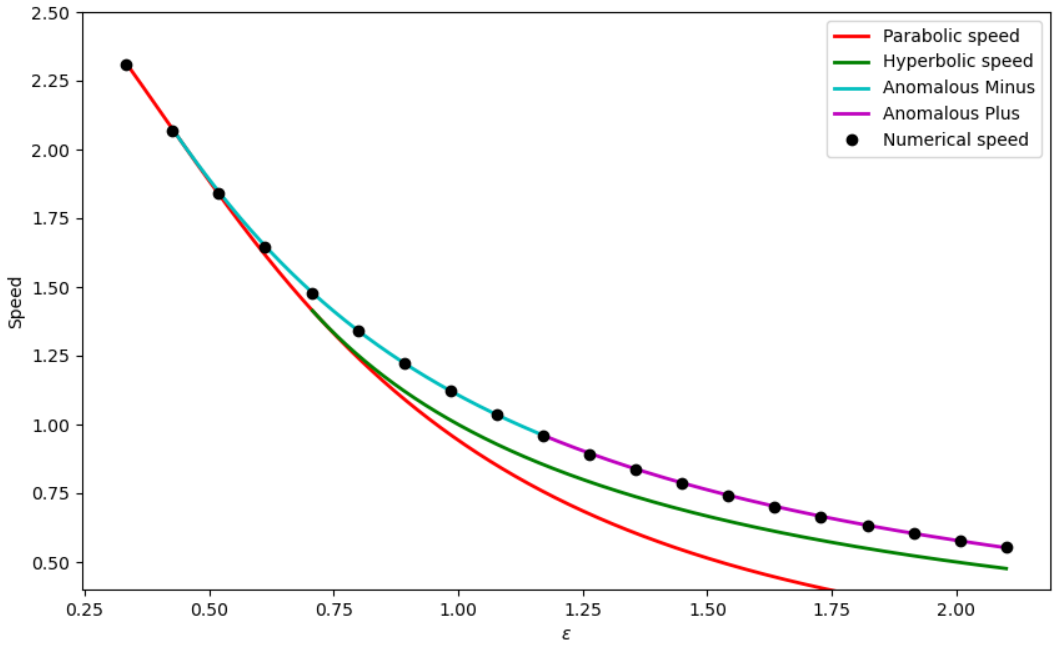

FIGURE 4.9 – **Comparison between the numerical selected speed of the modified model (A.23a)-(A.23d) and various linear speeds for different values of ϵ.** The numerical selected speed of the model (A.23a)-(A.23d) is represented by black points. The theoretical linear speeds are depicted by solid colored lines : red (*parabolic*), green (*hyperbolic*), cyan/magenta (*anomalous minus/plus*). The selected speed of the model (A.23a)-(A.23d) aligns with the linear prediction of Proposition 1. The parameter values are given by : $k = 2$, $\alpha_1 = 2$, $v = 1.5$, $\tau = 1$.

For the parabolic and anomalous regimes, the linear propagation speed is determined by a simple

pinched double root at $\lambda = 0$. In these regimes, our numerical simulations show that the modified nonlinear model indeed selects the marginally stable front. For these initial steep conditions, this scenario is expected and corresponds to the *marginal stability conjecture*. (see [39, 41, 42, 55] for further details). This conjecture was recently proven in the context of higher-order scalar parabolic equations by Avery and Scheel in [45], and later extended to reaction-diffusion systems by Avery [46].

For the hyperbolic regime, the linear propagation speed is induced by a double pinched double root at $\lambda = \lambda^\star > 0$. This type of situation is more complex and has been studied, for instance, in the articles [55, 52, 230]. In this situation, it is possible to overestimate pointwise growth rates and fail to correctly determine the marginally stable front [55, Remark 4.5]. According to our numerical simulations, we observe that this speed can indeed be selected by the model (A.23a)-(A.23d). For example, under the assumption $v < 1$ and $\epsilon > 1/\sqrt{\alpha_1}$, the hyperbolic speed is always selected.

B Derivation of the linear propagation speed for $n > 2$

Linear propagation speed. Linearizing around the zero equilibrium point, we obtain the following linear system

$$\begin{cases} \partial_t p_1^\pm \pm \dfrac{1}{\epsilon}\partial_x p_1^\pm = \pm\dfrac{1}{2\epsilon^2}(p_1^- - p_1^+) + \displaystyle\sum_{j=2}^{n} \beta(j)\eta(j,1)p_j + \frac{\alpha_1}{2}p_1, \\ \partial_t p_i^\pm \pm \dfrac{v(i)}{\epsilon}\partial_x p_i^\pm = \pm\dfrac{1}{2\tau(i)\epsilon^2}(p_i^- - p_i^+) + \displaystyle\sum_{j=i+1}^{n} \beta(j)\eta(j,i)p_j - \beta(i)p_i^\pm, \quad \text{for all } i \in \{2,\dots,n\}. \end{cases} \tag{B.24}$$

The derivation of the linear propagation speed is similar to the case $n = 2$. Due to the triangular structure of the system (B.24), the dispersion relation is given by

$$D_s(\nu,\lambda) = \prod_{i=1}^{n} \left(\nu - \nu_i^+(\lambda,s)\right)\left(\nu - \nu_i^-(\lambda,s)\right), \tag{B.25}$$

where $\nu_i^\pm$ corresponds to the pair of eigenvalues associated with the two equations for clusters of size i, independent of all the other equations, i.e., under the assumption $\beta(j) = 0$ for all $j > i$. Consequently, $\nu_1^\pm$ are the same as previously, explicitly defined by equations (A.14). The eigenvalues $\nu_i^\pm$, for all $i \in \{2,\dots,n\}$, are defined by equation (A.16) in the case $k = \beta(i)$, $v = v(i)$, and $\tau = \tau(i)$.

The pinched double roots of (B.25) associated with an admissible speed and slope can be obtained when $\nu_1^+ = \nu_1^-$ or when one of the equalities $\nu_1^+ = \nu_i^-$ with $i \in \{2,\dots,n\}$ is satisfied. In the first case, the associated speeds are the two normal speeds, while the second case leads to anomalous propagation speeds. For each cluster size $i \in \{2,\dots,n\}$, we assume the equivalent of conjecture 4, allowing us to define the two anomalous speeds for each cluster size.

$$s^\pm_{\text{anom},i} := s_i^\pm(0) = \sqrt{\frac{-a_{2,i}(0) \pm \sqrt{a_{2,i}^2(0) - 4a_{0,i}(0)a_{4,i}}}{2a_{4,i}}}, \quad \text{for } i \in \{2,\dots,n\}. \tag{B.26}$$

where the coefficients $a_{0,i}$, $a_{2,i}$, and $a_{4,i}$ are calculated in the same way as the coefficients a_0, a_2, and a_4, defined respectively by equations (A.18), (A.19), and (A.20).

We thus obtain the following proposition :

Proposition 2 (Critical linear propagation speed for $n > 2$):
We assume conjecture 4 for the different cluster sizes. By definition 1, the critical linear propagation speed, $s^\star_{lin}$, can take the following possible values :

- *The two normal speeds : parabolic and hyperbolic*

$$s_{para} := \frac{2\sqrt{\alpha_1}}{1+\alpha_1\epsilon^2}, \qquad s_{hyp} := \frac{1}{\epsilon}.$$

- *The different anomalous speeds : $s^\pm_{anom,i}$ for all $i \in \{2,\dots,n\}$.*

As before, the linear speed selected among these possible linear speeds corresponds to the maximum of the admissible speeds.

Numerical simulations. As previously, we introduce a nonlinear system that shares the same linear system (B.24), but whose nonlinear terms are chosen to have no impact on the wave speed,

$$\begin{cases} \partial_t p_1^\pm \pm \dfrac{1}{\epsilon}\partial_x p_1^\pm = \pm\dfrac{1}{2\epsilon^2}(p_1^- - p_1^+) + \displaystyle\sum_{j=2}^{n} \beta(j)\eta(j,1)p_j + \frac{\alpha_1}{2}p_1(1-p), \\ \partial_t p_i^\pm \pm \dfrac{v(i)}{\epsilon}\partial_x p_i^\pm = \pm\dfrac{1}{2\tau(i)\epsilon^2}(p_i^- - p_i^+) + \displaystyle\sum_{j=i+1}^{n} \beta(j)\eta(j,i)p_j - \beta(i)p_i^\pm, \quad \forall i \in \{2,\dots,n\}. \end{cases} \tag{B.27}$$

Case $n = 3$. In the first step, we assume that $n = 3$ to simplify the problem. There are six admissible linear speeds : the parabolic speed, the hyperbolic speed, the two anomalous speeds associated with clusters of size 2, and finally the two anomalous speeds associated with clusters of size 3.

In Figure 4.10, we plot the selected speed of the modified model (B.27) using numerical simulations (black points), as well as the admissible theoretical normal and anomalous linear speeds (colored lines) for different parameter values of $v(3)$. The anomalous speed associated with clusters of size 2, $s^\pm_{\text{anom},2}$, is represented in blue while the anomalous speed associated with cluster of size 3, $s^\pm_{\text{anom},3}$, is in yellow. Again, for the numerical simulations, we consider only steep initial data. For this choice of parameter values, the hyperbolic speed is not admissible, and the only normal linear speed is the parabolic speed, represented by the red curve. To illustrate the phenomenon of anomalous speed selection, presented in Definition 1 and Proposition 2, we vary the value of $v(3)$ so that the admissible anomalous speed associated with clusters of three bacteria becomes greater than the admissible anomalous speed associated with clusters of two bacteria. As we can see in Figure 4.10, the selected speed will transition from the anomalous speed associated with clusters of two bacteria to the anomalous speed associated with clusters of size three.

Case $n > 3$. We also perform numerical simulations in the case $n > 3$. In Figure 4.11, we plot the numerical selected speed of the modified model (B.27) using black dots, as well as the theoretical linear speeds for different values of the parameter ϵ and for two different cases, $n = 8$ and $n = 12$. When ϵ is small enough, the linear speed indeed corresponds to the parabolic speed, represented by the red curve. For both figures, the results are similar. When ϵ becomes large enough, the numerical speed becomes the largest of the admissible anomalous speeds represented by the blue curve. We

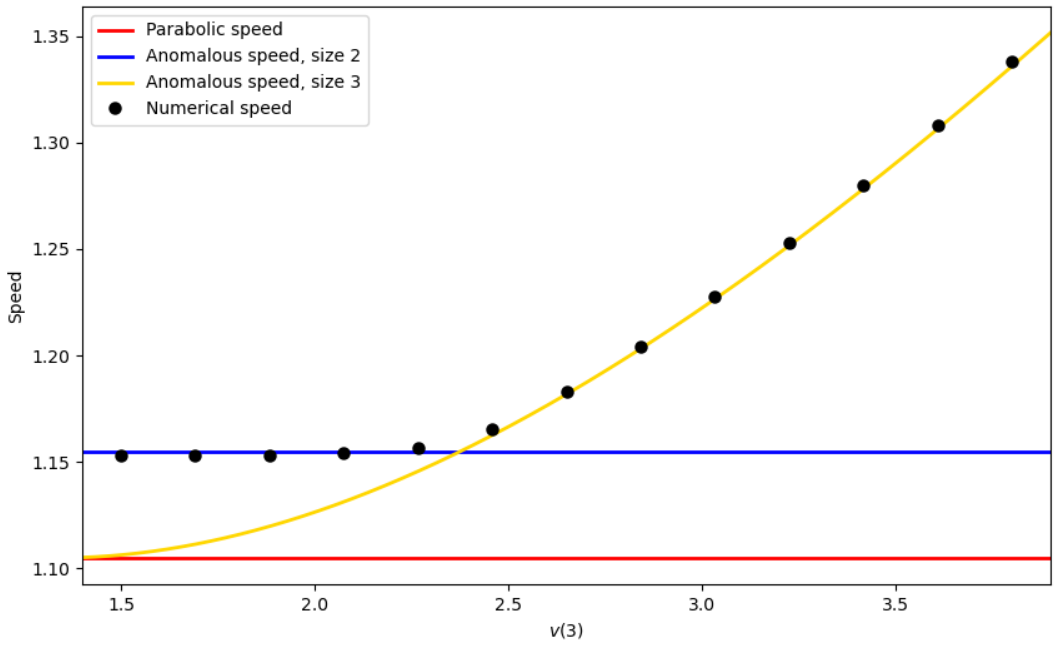

FIGURE 4.10 – **For $n = 3$, comparison between the numerical selected speed of the modified model** (B.27) **and various linear speeds for different values of $v(3)$.** The black dots correspond to the numerical selected speed of the system (B.27). The red curve represents the parabolic speed, the blue curve the anomalous speed associated with cluster of size 2, $s^{\pm}_{\text{anom},2}$, and finally, the yellow curve corresponds to the anomalous speed associated with cluster of size 3, $s^{\pm}_{\text{anom},3}$. For this parameter regime, the hyperbolic speed is not admissible. The parameter values are given by $\beta = 1$, $\alpha_1 = 1$, $\epsilon = 0.9$, and the functions τ and v are given by $\tau(2) = \tau(3) = 1$ and $v(2) = 2$.

also illustrate the hyperbolic speed with the green curve, even though it is never selected for these parameter values. These numerical results are in agreement with the Proposition 2.

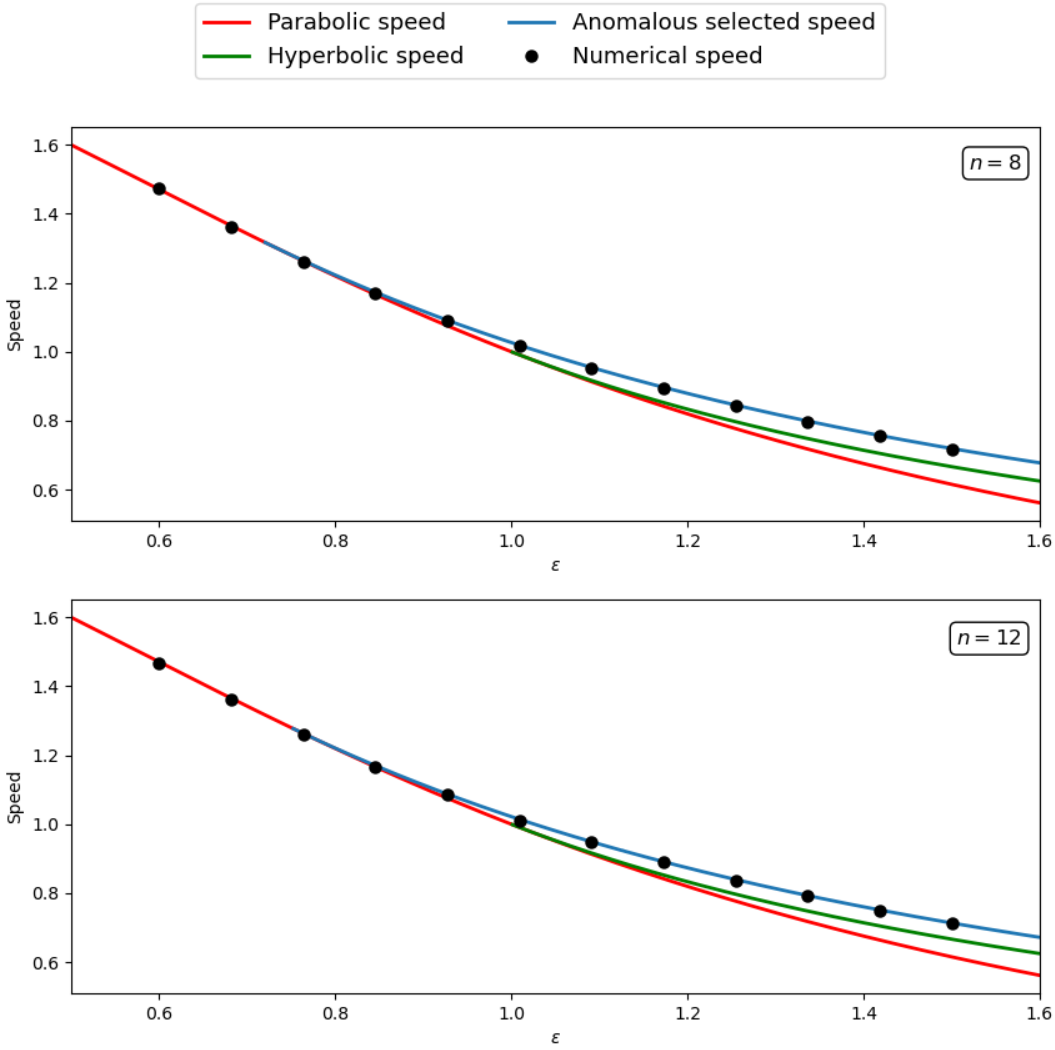

FIGURE 4.11 – **Comparison between the numerical selected speed of the modified model** (B.27) **and the various possible linear speeds for different values of ϵ, and for : Top, $n = 8$; Bottom, $n = 12$.** The black dots represent the numerical selected speed of the system (B.27). The red (resp. green) curve corresponds to the parabolic (resp. hyperbolic) linear speed. The largest of the admissible anomalous speeds is represented by the blue curve. The numerical simulations in the two figures are in agreement with Proposition 2. The values of the other parameters are $\beta = 1$, $\alpha_1 = 1$, and the functions τ and v are given by $\tau(i) = 1$ and (Top) $v(i) = 1 + 1.3 \times \mathbf{1}_{i\leq 4}(i)$, (Bottom) $v(i) = 1 + 1.6 \times \mathbf{1}_{i\leq 6}(i)$ for all $i \in \{2, \dots, n\}$.

Quatrième partie

Modélisation de la dynamique de relaxation des cellules

Introduction

Introduction biologique des expériences de relaxation des cellules

Les expériences de relaxation de cellules consistent à sélectionner une sous-fraction d'une population cellulaire et à observer l'évolution de cette sous-population au cours du temps. Pour des nombreuses expériences, la sous-population de cellules revient à son état de repos ou à son état d'équilibre, ce qui est désigné comme une expérience de relaxation.

Des exemples d'expériences de relaxation sont illustrés dans la figure IV.1. Dans celles-ci, nous partons d'une population de cellules à l'état d'équilibre, que nous étudions en effectuant un marquage par fluorescence pour quantifier la présence d'une certaine protéine. Dans ce travail, nous nous intéressons à l'expression du gène CD34 pressenti pour être un bon marqueur du caractère souche d'une cellule (correspondant, en anglais, à la notion de « *stemness* ») [231]. Suite à ce marquage, nous obtenons une distribution du niveau d'expression du gène au sein de la population et nous pouvons fractionner cette population en des sous-populations dans lesquelles le gène marqué est plus ou moins exprimé. Il est notamment courant d'isoler les cellules ayant une forte expression et celles ayant une faible expression, que nous nommerons respectivement « expérience + » et « expérience - », qui sont illustrées toutes deux dans la figure IV.1.

Des expériences de relaxation ont déjà été réalisées par le passé pour différentes cellules et différents antigènes [232, 233]. Par exemple, dans l'article pionnier de Chang et al. [232], les auteurs ont analysé la distribution de l'antigène Sca-1 à la surface des cellules EML en effectuant trois expériences de relaxation : d'abord avec la population la plus négative en expression de Sca-1, puis avec la population la plus positive, et enfin avec la population intermédiaire. Les expériences biologiques menées montrent que, dans les trois cas, les histogrammes de distribution de Sca-1 se régénèrent, démontrant ainsi que les populations cellulaires reviennent bien à leur état d'équilibre.

Etat de l'art

Dans ce travail, nous nous basons sur le modèle introduit dans l'article [234] que nous détaillons ci-dessous. Nous effectuons les hypothèses de modélisation suivantes :

(H1) La protéine CD34 se dégrade naturellement au cours du temps avec un taux positif d.

(H2) Dans la cellule, le promoteur du gène peut être actif, menant dans ce cas à la synthèse de la protéine avec un taux positif s, ou bien inactif. Le promoteur peut transiter entre ces deux

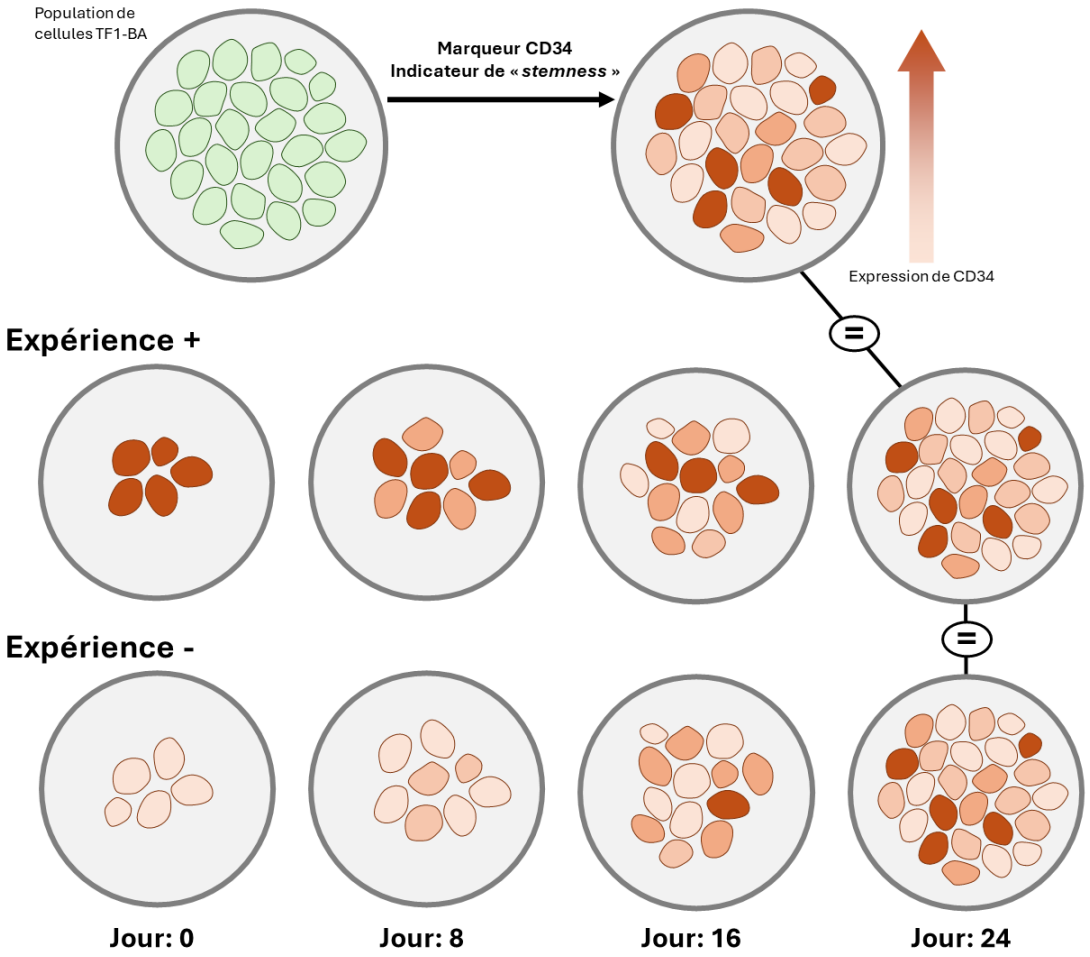

FIGURE IV.1 – **Illustrations d'expériences de relaxation. Haut.** Nous effectuons un marquage par fluorescence de l'antigène CD34 pour une population de cellules TF1-BA. Ce gène est considéré comme un indicateur du caractère souche des cellules. **Bas.** Dans l'expérience + (respectivement -), nous isolons les cellules avec la plus forte (resp. faible) expression de CD34, que l'on nomme $CD34^+$ (resp. $CD34^-$). Nos expériences montrent que les cellules $CD34^-$ sont régénérées à partir des cellules $CD34^+$, comme les biologistes s'y attendent. Nous constatons également que les cellules $CD34^+$ sont régénérées à partir des cellules $CD34^-$. Cette dernière observation peut sembler davantage contre-intuitive, car il est généralement admis que par le renouvellement cellulaire, les cellules fortement souches donnent naissance à des cellules moins souches. Par conséquent, le caractère souche d'une cellule est le résultat d'un système dynamique sous-jacent, comme cela a déjà été démontré dans d'autres systèmes cellulaires.

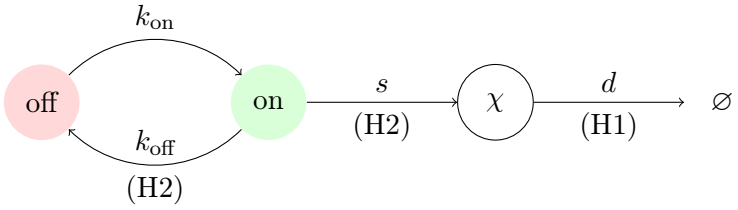

FIGURE IV.2 – **Illustration du processus de Markov déterministe par morceaux (PDMP).**

phases avec des taux k_{on} et respectivement k_{off}.

Le processus de Markov déterministe par morceaux (PDMP), illustré dans la figure IV.2 et associé aux hypothèses (H1-2), est régi par l'équation

$$\frac{\mathrm{d}\chi}{\mathrm{d}t} = s\,E(t) - d\chi(t)$$

où χ correspond au niveau de CD34 dans la cellule au cours du temps. La fonction temporelle, E, représente l'état activé ou désactivé du promoteur, mathématiquement nous définissons $E(t) \in \{0, 1\}$ où 0 correspond à l'état « off » et 1 à l'état « on », permettant ainsi la production de protéines CD34. Comme voulu dans l'hypothèse (H2), cet état va changer au cours du temps avec les taux de transitions k_{on} et k_{off}, ce qui se retranscrit par, $E(t) : 0 \xrightarrow{k_{\text{on}}} 1$, $1 \xrightarrow{k_{\text{off}}} 0$.

Nous nous intéressons maintenant à une population de cellules. Nous introduisons les quantités $n_{\text{on}}(t, \chi)$ et $n_{\text{off}}(t, \chi)$ correspondant aux nombres de cellules ayant un promoteur dans l'état actif (resp. inactif) au temps t avec un niveau d'expression CD34 donné par la variable χ. Nous introduisons également la variable n, représentant le nombre total de cellules, donné par l'égalité $n := n_{\text{on}} + n_{\text{off}}$. Les équations maîtresses associées à ce processus sont données par le système de deux équations suivant,

$$\partial_t n_{\text{on}} + \overbrace{\partial_\chi((s - d\chi)n_{\text{on}})}^{\text{(H1) et (H2)}} = \overbrace{-k_{\text{off}}n_{\text{on}} + k_{\text{on}}n_{\text{off}}}^{\text{(H2)}}, \quad \chi \in]0, s/d[, \tag{IV.1}$$

$$\partial_t n_{\text{off}} + \underbrace{\partial_\chi((-d\chi)n_{\text{off}})}_{\text{(H1)}} = k_{\text{off}}n_{\text{on}} - k_{\text{on}}n_{\text{off}}, \quad \chi \in]0, s/d[. \tag{IV.2}$$

A ces équations, nous rajoutons les conditions aux bords suivantes,

$$n_{\text{on}}(t, \chi = 0) = n_{\text{off}}(t, \chi = s/d) = 0. \tag{IV.3}$$

Une mise à l'échelle de l'espace par s/d nous permet de simplifier le problème de la manière suivante,

$$\begin{cases} \partial_t n_{\text{on}} + d\partial_x((1 - x)n_{\text{on}}) = -k_{\text{off}}n_{\text{on}} + k_{\text{on}}n_{\text{off}}, & x \in]0, 1[, \\ \partial_t n_{\text{off}} + d\partial_x((-x)n_{\text{off}}) = k_{\text{off}}n_{\text{on}} - k_{\text{on}}n_{\text{off}}, & x \in]0, 1[, \\ n_{\text{on}}(t, 0) = n_{\text{off}}(t, 1) = 0. \end{cases} \tag{IV.4}$$

L'état stationnaire du modèle est donné (cf [235] par exemple) par la formule

$$N_{\text{on}}(x) = C(1 - x)^{\frac{k_{\text{off}}}{d} - 1} x^{\frac{k_{\text{on}}}{d}}, \quad N_{\text{off}}(x) = C(1 - x)^{\frac{k_{\text{off}}}{d}} x^{\frac{k_{\text{on}}}{d} - 1},$$

nous donnant ainsi une formule explicite du profil asymptotique d'expression du gène CD34 au sein de la population de cellules, correspondante à une loi bêta,

$$N(x) = N_{\text{on}}(x) + N_{\text{off}}(x) = C(1-x)^{\frac{k_{\text{off}}}{d}-1} x^{\frac{k_{\text{on}}}{d}-1}.$$

Problématique

L'objectif de ce travail est de développer un modèle d'expression génétique capable de décrire avec une grande précision l'évolution temporelle et la dynamique réelle de l'expression du gène CD34 au sein d'une population de cellules. Nous voulons valider rigoureusement ce modèle en le comparant à des données expérimentales issues de différentes expériences de relaxation. De plus, le modèle doit être suffisamment simple pour permettre l'exploration théorique des aspects mathématiques sous-jacents.

Résultats

• Chapitre 5 : Modeling relaxation experiments with a mechanistic model of gene expression.

Ce travail est en collaboration avec les étudiants Marion Dufeu, Grégoire Ranson et les chercheurs Sylvain Lefort, Thibault Voeltzel, Véronique Maguer-Satta, Olivier Gandrillon et Thomas Lepoutre. Ce projet a mené à la publication d'un article dans le journal *BMC Bioinformatics*, dont je suis le premier auteur [236].

Méthodes. D'un point de vue mathématique, nous avons commencé par complexifier le modèle précédent (IV.4) introduit dans l'article [234], en incluant l'hypothèse suivante :

(H3) Les cellules se divisent, entraînant ainsi une prolifération exponentielle de la population cellulaire. Le taux de division est inversement proportionnel au niveau de CD34 : plus l'expression d'une cellule est forte, plus la division cellulaire est rare. En revanche, l'état des promoteurs, lui, n'influence pas la probabilité de division. Nous supposons que les deux cellules filles conservent le même niveau d'expression du gène CD34 ainsi que le même état on/off que leur cellule mère.

Mathématiquement, le modèle étudié est maintenant donné par les équations,

$$\begin{cases} \partial_t n_{\text{on}} + d\partial_x((1-x)n_{\text{on}}) = -k_{\text{off}} n_{\text{on}} + k_{\text{on}} n_{\text{off}} + r(x) n_{\text{on}}(t,x), \quad x \in]0,1[, \\ \partial_t n_{\text{off}} + d\partial_x((-x)n_{\text{off}}) = k_{\text{off}} n_{\text{on}} - k_{\text{on}} n_{\text{off}} + r(x) n_{\text{off}}(t,x), \quad x \in]0,1[, \\ n_{\text{on}}(t,0) = n_{\text{off}}(t,1) = 0, \end{cases} \tag{IV.5}$$

avec r une fonction positive, décroissante, correspondant au taux de prolifération.

Pour déterminer les valeurs des paramètres de ce modèle, nous avons utilisé des données biologiques générées pour ce travail par l'équipe de chercheurs composée de Sylvain Lefort, Thibault Voeltzel et Véronique Maguer-Satta. Ces chercheurs ont effectué, sur des cellules TF1-BA, deux expériences de relaxation, en isolant les 10 % des cellules avec la plus forte expression de CD34 et les 10 % avec la plus faible expression. Une illustration de ces deux expériences, nommées respectivement + et -, est représentée dans la figure IV.1. Grâce à ces données expérimentales, nous connaissons, pour de

nombreux jours, le nombre total de cellules au sein de la population ainsi que la distribution de fluorescence de la protéine CD34 parmi celles-ci. Pour comparer ces données biologiques au modèle théorique, nous avons introduit une distance mathématique adéquate, que nous détaillerons dans la suite de ce travail.

Résultats principaux. Dans ce travail nous obtenons des résultats théoriques ainsi que des résultats de modélisation à l'aide d'outils numériques :

- Concernant les aspects théoriques, sous l'hypothèse d'un taux de prolifération linéaire, $r(x) = r_0 + r_1 x$, nous déterminons le profil exponentiel stable de notre problème. En d'autres termes, nous déterminons une formule explicite de la constante positive λ ainsi que des fonctions N_{on} et N_{off}, dont le vecteur $e^{\lambda t}\left(N_{\text{on}}(x), N_{\text{off}}(x)\right)$ est une solution du problème (IV.5). Notamment, cela nous permet de déterminer une formule explicite du profil asymptotique $N := N_{\text{on}} + N_{\text{off}}$ donnée par l'égalité suivante

$$N(x) = C(1-x)^{\frac{k_{\text{off}}}{d\eta}-1} x^{\frac{k_{\text{on}}\eta}{d}-1} e^{\frac{r_1}{d}x}\left(\eta + (1-\eta)x\right),$$

avec C et η des constantes que nous détaillerons explicitement dans le chapitre qui suit.

- A l'aide des données expérimentales obtenues, nous parvenons à calibrer, de manière robuste, les paramètres de notre modèle. Pour ces valeurs de paramètres trouvées, la dynamique temporelle des cellules est en parfait accord avec les données biologiques générées. En analysant les résultats biologiques des deux expériences de relaxation, nous déterminons une distance de référence entre deux distributions à partir de laquelle deux profils sont présumés similaires. Nous remarquons que, pour les différents jours et pour les différentes expériences, les distances entre les distributions prédites par le modèle et les données biologiques sont toujours relativement proches de cette distance de référence, validant ainsi rigoureusement le choix de notre modèle. Dans l'ensemble, nos résultats soutiennent l'idée que l'expression des gènes doit être considérée et modélisée comme un système dynamique probabiliste.

5 Modeling relaxation experiments with a mechanistic model of gene expression

This chapter corresponds to an article published in the journal *BMC Bioinformatics*, in collaboration with Marion Dufeu, Grégoire Ranson, Sylvain Lefort, Thibault Voeltzel, Véronique Maguer-Satta, Olivier Gandrillon and Thomas Lepoutre [236].

5.1 Background

Cells are neither machines [237] nor simple information processing devices [238, 239]. Their specific complexity sometimes led to the idea that they should be treated differently that classical physico-chemical systems [240]. Nevertheless like all living systems cells are rooted within a physico-chemical reality which they can not escape. We therefore argue that cells should be seen and modelled as probabilistic dynamical systems.

One obvious sign that cells should indeed be seen as such lie in the possibility to perform so-called "relaxation" experiments. This consists in selecting a subfraction of a cell population (potentially down to one cell) and observing the speed at which the entire initial distribution for a given marker is reconstituted. Such relaxation experiments have already been published and analyzed on various cells and antigens.

Arguably the very first report to do so analyzed the distribution of the Sca1 antigen (Stem Cell Antigen 1) at the surface of EML cells, a multipotent mouse haematopoietic cell line. It was shown that it took more than 9 days before the three fractions (most Sca-1 negative, most Sca-1 positive and a central fraction) regenerated Sca-1 histograms similar to that of the parental (unsorted) population [232]. The authors proposed a phenomenological model which point toward discrete transitions in a dynamical system exhibiting multistability to quantitatively predict the relaxation dynamics of the sorted subpopulations [232]. For this they assumed the existence of two stable states, one of low and one of high Sca1 expression. Proliferation was assumed to be equal in both states.

Other studies have adopted a somewhat different approach with the knock-in of fluorescent reporter genes under the control of endogenous promoters [241, 233]. The first targeted promoter was that of Nanog in murine embryonic stem cells [241], an other gene classically considered as a stemness marker. Similarly to [232], the authors demonstrated that, although being in a Nanog low of in a Nanog high state is not biologically equivalent in term of fate, the transition between these two states

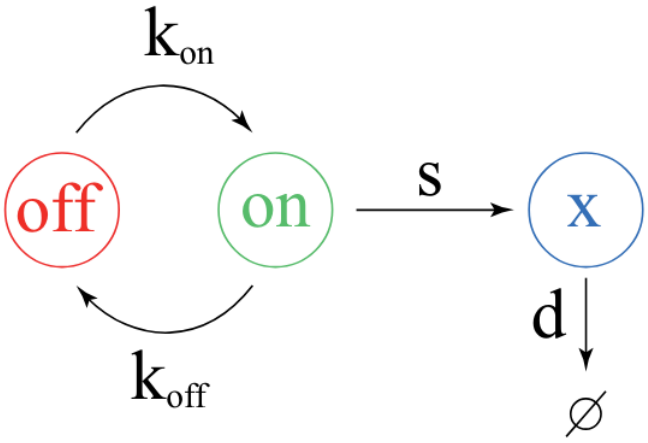

FIGURE 5.1 – The 2-state model of gene expression. The gene opens with a k_{on} rate and closes with a k_{off} rate. Similarly to [244] we only consider protein (x) production (with an s rate) and degradation (with a d rate).

can be adequately modelled using a fully probabilistic model, simulated using a Stochastic Simulation Algorithm [242].

The second targeted promoter was that of Tenascin-C in NIH 3T3 mouse fibroblasts [233]. In that case, the authors first proposed a phenomenological 2-states model, which proved to not correctly capture their data. They then turned toward a Langevin type stochastic differential equation to model the relaxation process. This led to an accurate prediction of the rates at which different phenotypes will arise from an isolated subpopulation of cells [233]. In contrast with [232], the authors assumed that each state had its own proliferation rate.

In the present work, we aimed at using a previously published mechanistic model of gene expression [234] to which we will add a stemness-dependant proliferation term, to fit relaxation data obtained by examining CD34 expression at the surface of TF1-BA cells.

5.2 Methods

5.2.1 Mathematical model

Case without proliferation

Throughout this work, we will use the classical two-state model (Figure 5.1 ; see [234] and references therein), a refinement of the pioneer model introduced by [243].

This is the simplest model that accounts well for the specific nature of single-cell omics data (non-poisonnian [245], well fitted by Gamma distributions [246] and displaying a high proportion of zero counts [247]). More refined models with any number of possible gene configuration have been described [248] but their mathematical complexity makes them cumbersome to use for our purpose.

It is important to stress here that this is a mechanistic model, that differs from the phenomenological 2-states model described upper. Such models only considered a low and a high χ state, without

describing the protein production process. Importantly here stochasticity is described at the core of the modelling and does not need to be introduced as a additional term in the model. We recently proposed a piecewise deterministic Markov process (PDMP) version of that model which rigorously approximates the original molecular model [234]. Furthermore, a moment-based method has been proposed for estimating parameter values from a given experimental distribution assumed to arise from the functioning of a 2-states model [244]. We recall here the mathematical description of the model through the PDMP (piecewise deterministic Markov process) formalism

$$\frac{d}{dt}\chi = s.E(t) - d\chi(t),$$

where $E(t) \in \{0,1\}$ switching from 0 to 1 (resp. 1 to 0) at a rate k_{on} (resp. k_{off}). In this process, the protein quantity $\chi(t)$ is structurally bounded by $X_{max} = s/d$. From this process, we can derive the Chapman Kolmogorov or master equation in the form

$$\begin{cases} \partial_t n_{\text{on}}(t,\chi) + \partial_\chi J_{\text{on}}(t,\chi) = -k_{\text{off}} n_{\text{on}} + k_{\text{on}} n_{\text{off}} \quad \chi \in]0, s/d[, \\ \partial_t n_{\text{off}}(t,\chi) + \partial_\chi J_{\text{off}}(t,\chi) = +k_{\text{off}} n_{\text{on}} - k_{\text{on}} n_{\text{off}} \quad \chi \in]0, s/d[, \\ J_{on}(t,\chi) = (s - d\chi) n_{on}(t,\chi),\ J_{\text{off}}(t,\chi) = -d\chi, \\ J_{\text{on}}(t,0) = J_{\text{off}}(t,0) = J_{\text{on}}(t,s/d) = J_{\text{off}}(t,s/d) = 0. \end{cases} \tag{5.1}$$

see [235, 245, 249] for similar derivations. master equation of the process in the absence of proliferation reads. We recall that the boundary conditions simply reflects the no-flux boundary conditions stating $(s - d\chi)n_{\text{on}}(t,\chi) = -d\chi n_{\text{off}}(t,\chi) = 0$ for $\chi = 0, s/d$. Moreover, because $s - ds/d = -d.0, = 0$, we only specify the boundary conditions when they give constraints on the densities. We define $X_{\max} = s/d$ as the maximum value for the quantity of CD34 in a cell. Scaling the space by $X_{\max}$ allows us to consider the following system

$$\begin{cases} \partial_t n_{\text{on}} + d\partial_x((1-x)n_{\text{on}}) = -k_{\text{off}} n_{\text{on}} + k_{\text{on}} n_{\text{off}}, \quad x \in]0,1[, \\ \partial_t n_{\text{off}} + d\partial_x((-x)n_{\text{off}}) = k_{\text{off}} n_{\text{on}} - k_{\text{on}} n_{\text{off}}, \quad x \in]0,1[, \\ n_{\text{on}}(t,0) = n_{\text{off}}(t,1) = 0. \end{cases} \tag{5.2}$$

with $n_{\text{on}}(t,x)$ being the number of cells with a promoter in the "on" state at time t, with a (scaled) CD34 level x and $n_{\text{off}}(t,x)$ being the number of cells with a promoter in the "off" state. The total number of cells, denoted as $n(t,x)$, is given by $n_{\text{on}}(t,x) + n_{\text{off}}(t,x)$. This is the quantity we considered to be measured.

Steady state of the model. The system is mass preserving and it converges to a steady state $N_{\text{on,off}}$ which is characterized by

$$\begin{cases} d\partial_x((1-x)N_{\text{on}}) = -k_{\text{off}} N_{\text{on}} + k_{\text{on}} N_{\text{off}}, \quad x \in]0,1[, \\ d\partial_x((-x)N_{\text{off}}) = -k_{\text{off}} N_{\text{on}} - k_{\text{on}} N_{\text{off}}, \quad x \in]0,1[, \\ N_{\text{on}}(0) = N_{\text{off}}(1) = 0, \end{cases} \tag{5.3}$$

and the solution is nonnegative. An interesting feature of this system is the fact that we have an explicit solution. We recall here the computations that can be found in [235] because they might help for understanding the computations for the model with proliferation. Indeed, summing up the equations, we get

$$\partial_x((1-x)N_{\text{on}} - xN_{\text{off}}) = 0.$$

Therefore, this quantity is constant on $]0,1[$. Using the boundary condition, we can see that 0 is the only admissible constant. Therefore, in this precise case, we have necessarily

$$(1-x)N_{\text{on}} = xN_{\text{off}}.$$

Injecting in the equation we get

$$d\partial_x((1-x)N_{\text{on}}) = -k_{\text{off}}N_{\text{on}} + k_{\text{on}}\frac{(1-x)N_{\text{on}}}{x} = (1-x)N_{\text{on}}\left(-\frac{k_{\text{off}}}{1-x} + \frac{k_{\text{on}}}{x}\right).$$

From this, we get

$$N_{\text{on}} = C(1-x)^{\frac{k_{\text{off}}}{d}-1}x^{\frac{k_{\text{on}}}{d}}, \quad N_{\text{off}} = C(1-x)^{\frac{k_{\text{off}}}{d}}x^{\frac{k_{\text{on}}}{d}-1}.$$

and quite remarkably, we have

$$N(x) = N_{\text{on}}(x) + N_{\text{off}}(x) = C(1-x)^{\frac{k_{\text{off}}}{d}-1}x^{\frac{k_{\text{on}}}{d}-1}. \tag{5.4}$$

If we choose $C = \dfrac{\Gamma((k_{\text{on}}+k_{\text{off}})/d)}{\Gamma(k_{\text{on}}/d)\Gamma(k_{\text{off}}/d)}$ we normalize this to 1 and get a β law $B(k_{\text{on}}/d, k_{\text{off}}/d)$, so that we end up with

$$(n_{\text{on}}(t,x), n_{\text{off}}(t,x)) \to \left(\int_0^1 n^0_{\text{on}}(x) + n^0_{\text{off}}(x)\right)(N_{\text{on}}(x), N_{\text{off}}(x)).$$

Case with proliferation

HSCs mostly reside in a quiescent state, although they can occasionally divide during homeostasis [250]. We therefore will consider $CD34^+$ TF1-BA cells as immature slowly proliferating cells and $CD34^-$ TF1-BA cells as mature highly proliferating cells. Therefore the proliferation rate will depend on the x variable representing the CD34 content but not on the on/off status.

Moreover, we consider that cells keep their on/off status during a division. This is in line with the demonstration of a memory of transcriptional activity in mammalian cells [251, 252].

$$\begin{cases} \partial_t n_{\text{on}} + d\partial_x((1-x)n_{\text{on}}) = -k_{\text{off}}n_{\text{on}} + k_{\text{on}}n_{\text{off}} + r(x)n_{\text{on}}(t,x), \quad x \in]0,1[, \\ \partial_t n_{\text{off}} + d\partial_x((-x)n_{\text{off}}) = k_{\text{off}}n_{\text{on}} - k_{\text{on}}n_{\text{off}} + r(x)n_{\text{off}}(t,x), \quad x \in]0,1[, \\ n_{\text{on}}(t,0) = n_{\text{off}}(t,1) = 0. \end{cases} \tag{5.5}$$

Since the system is structurally non-conservative, it makes no sense to look for steady state here. However, one can investigate for stable exponential profile, that is to look for positive solutions with shape

$$e^{\lambda t}(N_{\text{on}}(x), N_{\text{off}}(x)).$$

Such solution satisfy the system

$$\begin{cases} \lambda N_{\text{on}} + d\partial_x((1-x)N_{\text{on}}) = -k_{\text{off}}N_{\text{on}} + k_{\text{on}}N_{\text{off}} + r(x)N_{\text{on}}(x), \quad x \in]0,1[, \\ \lambda N_{\text{off}} + d\partial_x((-x)N_{\text{off}}) = k_{\text{off}}N_{\text{on}} - k_{\text{on}}N_{\text{off}} + r(x)N_{\text{off}}(t,x), \quad x \in]0,1[, \\ N_{\text{on}}(0) = N_{\text{off}}(1) = 0, \quad N_{\text{on,off}} > 0. \end{cases} \tag{5.6}$$

In the sequel, we will focus on the normalized representant so that we will assume

$$\int_0^1 \left(N_{\text{on}}(x) + N_{\text{off}}(x)\right)\, dx = 1.$$

We also introduce the adjoint eigenprofile. It can be obtained as exponentially growing solutions for the adjoint differential operators, this is the continuous equivalent of left and right eigenvector for the same eigenvalues in matrix analysis ($MU = \lambda U, v^T M = \lambda V$ or equivalently $M^T V = \lambda V$).

$$\begin{cases} \lambda\phi_{\text{on}} - d(1-x)\partial_x\phi_{\text{on}} = -k_{\text{off}}\phi_{\text{on}} + k_{\text{off}}\phi_{\text{off}} + r(x)\phi_{\text{on}}, \quad x \in]0,1[, \\ \lambda\phi_{\text{off}} - d(-x)\partial_x(\phi_{\text{off}}) = -k_{\text{on}}\phi_{\text{off}} + k_{\text{on}}\phi_{\text{on}} + r(x)\phi_{\text{off}}, \quad x \in]0,1[, \\ \phi_{\text{on,off}} > 0, \quad \displaystyle\int_0^1 \left(N_{\text{on}}\phi_{\text{on}} + N_{\text{off}}\phi_{\text{off}}\right)\, dx = 1. \end{cases} \tag{5.7}$$

We emphasize in particular the following property, for any initial condition of the system, one has

$$\int_0^1 \left(n_{\text{on}}(t,x)\phi_{\text{on}}(x) + n_{\text{off}}(t,x)\phi_{\text{off}}(x)\right)\, dx = e^{\lambda t}\int_0^1 \left(n_{\text{on}}(0,x)\phi_{\text{on}}(x) + n_{\text{off}}(0,x)\phi_{\text{off}}(x)\right)\, dx = C^0 e^{\lambda t},$$

and moreover,

$$\int_0^1 |e^{-\lambda t}n_{\text{on}}(t,.) - C^0 N_{\text{on}}|\phi_{\text{on}}(x)\, dx + \int_0^1 |e^{-\lambda t}n_{\text{off}}(t,.) - C^0 N_{\text{off}}|\phi_{\text{off}}(x)\, dx \to 0.$$

$$e^{-\lambda t}\left(n_{\text{on}}(t,.), n_{\text{off}}(t,.)\right) \to C^0\left(N_{\text{on}}, N_{\text{off}}\right).$$

In the weighted norm $\|(f_{\text{on}}, f_{\text{off}})\|_\phi = \displaystyle\int_0^1 |f_{\text{on}}|\phi_{\text{on}} + |f_{\text{off}}|\phi_{\text{off}}$. In case $\phi_{\text{on,off}}$ is lower bounded, this implies classical L^1 convergence. This lower bound is established below. For more details on this, we refer to [253] for an introduction to eigenvectors in this context. In particular, thanks to our normalization, the triplet (λ, N, ϕ) is uniquely defined. Note that in the conservative case ($r = 0$), $\lambda = 0$, N is given by the renormalized steady state and the adjoint eigenvector is simply the constant vector $(1,1)$. Note also that this guarantees that for any initial data, we have in case $\lambda \geq 0$ and $\phi_{\text{on,off}}$ are lower bounded (as it will be established below)

$$\begin{aligned} \frac{1}{\int_0^1 n_{\text{on}}(t,x) + n_{\text{off}}(t,x)dx}\left(n_{\text{on}}(t,.), n_{\text{off}}(t,.)\right) &= \frac{1}{e^{-\lambda t}\int_0^1 n_{\text{on}}(t,x) + n_{\text{off}}(t,x)dx} e^{-\lambda t}\left(n_{\text{on}}(t,.), n_{\text{off}}(t,.)\right) \\ &\to \frac{1}{C^0} C^0\left(N_{\text{on}}, N_{\text{off}}\right) = \left(N_{\text{on}}, N_{\text{off}}\right). \end{aligned}$$

And regarding the observations of the steady profile in figure 5.2, our normalized asymptotic profile should be $N : x \longmapsto N_{\text{on}}(x) + N_{\text{off}}(x)$.

We assume that, for the initial dimensional system, the proliferation rate is linear, *i.e.* $r : \chi \longmapsto \tilde{r}_0 + \tilde{r}_1\chi$. Scaling again the space by $X_{\max}$, the proliferation term becomes, $r : x \to r_0 + r_1 x$ with $r_0 = \tilde{r}_0$ and $r_1 = \tilde{r}_1 X_{\max}$. We assume that the constant proliferation rate is positive, $r_0 > 0$. Conversely, to model the fact that $CD34^-$ cells divide more frequently than $CD34^+$ cells, we assume that the linear proliferation term, r_1, is negative. However, to preserve the positivity of the proliferation rate, the constant r_1 must satisfy the following condition, $r_1 \in [-r_0, 0]$.

We show in the Results section that, under this proliferation assumption, it is theoretically possible to derive the normalized asymptotic profiles $(N_{\text{on}}, N_{\text{off}})$.

5.2.2 The biological setting

Relaxation experiments

Chronic Myeloid Leukemia (CML) is a myeloproliferative disorder arising at the hematopoietic stem cell (HSC) level. It is associated with the recurrent chromosomal (Philadelphia) translocation t(9 ;22)(q34 ;q11) which leads to the oncogenic chimeric gene that fuses Bcr and Abl genes and results in the expression of a constitutively active unique tyrosine kinase named BCR-ABL [254].

Véronique Maguer-Satta's group has developed the TF1-BA cell line, a unique model of immature human hematopoietic cells (TF1) transformed with BCR-ABL by lentiviral infection. This model was shown to recapitulate early alterations following the BCR-ABL oncogene appearance as identified using primary samples of CML patients at diagnosis and in chronic phase [255].

We decided to analyze the relaxation dynamics for the CD34 antigen at the surface of those TF1-BA cells (Figure 5.2). CD34 is a transmembrane phosphoglycoprotein which is predominantly regarded as a marker of Haematopoietic Stem Cells (HSCs) [231]. We reasoned that CD34 surface expression could therefore be seen as a proxy for stemness of our TF1-BA cells. Interestingly, one observes a relaxation in both directions : $CD34^-$ cells are regenerated from $CD34^+$ cells, as biologists would expect, but one also see that $CD34^+$ cells are regenerated from $CD34^-$ cells, establishing that stemness is not a fixed quality but the result of an underlying dynamical system as previously shown in other cellular systems ([241, 232] ; see upper)

Data processing

Two types of data were collected on days 2, 5, 9, 13, 19, 23, 26 and 30 : cell counts and fluorescence distribution. The cell counts allow us to quantify proliferation whereas the fluorescence measure the distribution of CD34 expression.

Gating. As usual for cytometric data, we initiate the analysis with a gating step. We use SSC-H and FSC-H data to distinguish viable and debris cells. FSC (Forward Scatter) data are generally assimilated to the size of the cells analyzed, and correspond to the light scattered along the laser path. SSC (Side Scattered) data, on the other hand, are usually linked to the granularity and correspond to the light scattered at a 90-degree angle. The "H" stands for Height and is one component of this type of data. Cell debris are characterized by relatively low size and high granularity relative to their size.

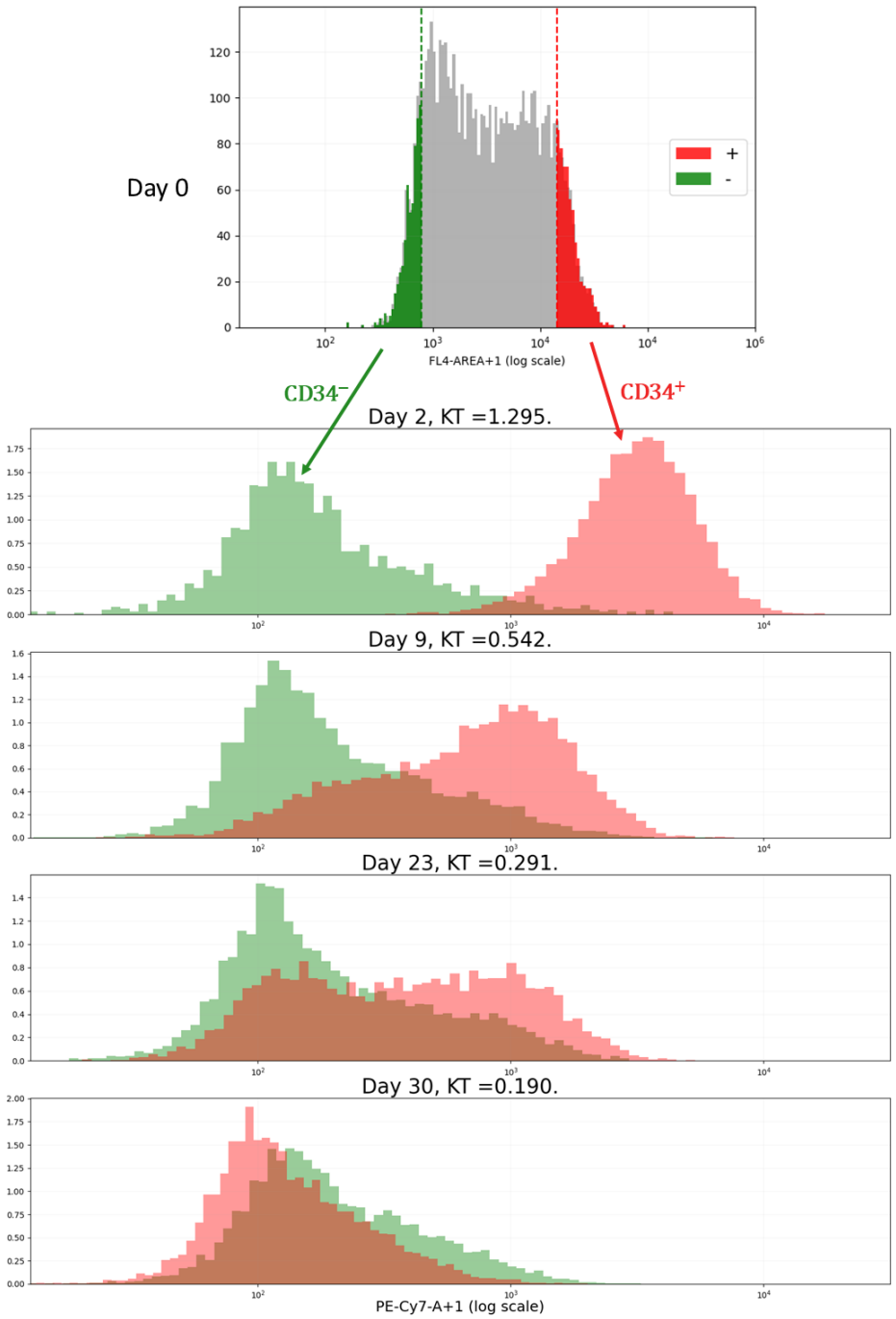

FIGURE 5.2 – **The relaxation experiment.** TF1-BA cells well labelled with an anti-CD34 antibody and FACS-sorted. The 10 percent most CD34 positive and the 10 percent most CD34 negative cells were sorted, grown in culture for the indicated period of time, where the distribution of cell-surface CD34 expression was assessed. KT : the modified Kantorovich-Rubinstein distance, defined by the equation (5.14), between the two distributions [256].

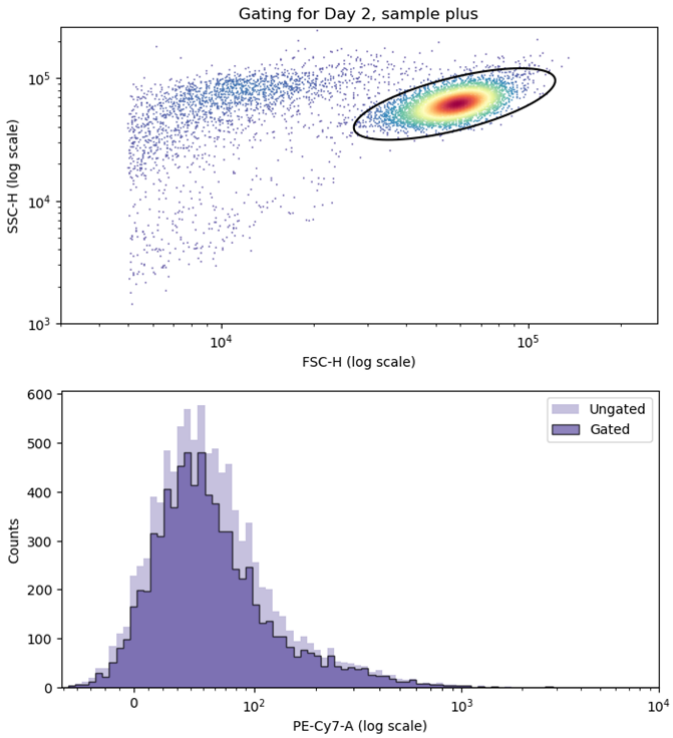

FIGURE 5.3 – **Example of flow cytometry gating.** *Top.* Example of SSC-H along FSC-H plot for raw data from the plus subpopulation on day 2. As the data contain a high proportion of debris cells, we select only those viable cells lying within the black ellipse. *Bottom.* Fluorescence data before gating (*Ungated*) and after gating (*Gated*). For the figures and the ellipse, we used the python package *FlowCal* [257].

To select viable cells, we plot the values of SSC-H along those of FSC-H. An example of such a graph is provided in Figure 5.3 using data from day 2 of the $CD34^+$ cell experiment. Visually, viable cells can be identified as the cluster of points with high FSC-H and SSC-H values. Using the "FlowCal" python package [257], we draw an ellipse as a filter to select only these viable cells. At the bottom of Figure 5.3, we represent fluorescence data with and without the gating phase (*Ungated* and *Gated*, respectively). Note that fluorescence distribution is only slightly affected by the removal of debris cells.

Shifting. Even after gating, some cells exhibit a negative fluorescence level, which is inconsistent as these values are intended to represent the amount of proteins in each cell. To avoid this problem, we added a shifting step. This step occurs immediately after the gating process and consists in subtracting the minimum value of each distribution (for each sub-population and for each day) from all the values, bringing the minimum to 0. This transformation, once again, does not distort the fluorescence distribution. This corresponds to the interpretation of negative values as compensation of a baseline value.

5.2.3 Numerical simulations

Linking data to mathematical model : The cell counts are interpreted as snapshots of the total population $\int_0^{X_{\max}} (n_{\text{on}}(t,x)+n_{\text{off}}(t,x))dx$. The fluorescence distribution is considered as a sample from the distribution $\dfrac{n_{\text{on}}(t,x)+n_{\text{off}}(t,x)}{\int_0^{X_{\max}}(n_{\text{on}}(t,x)+n_{\text{off}}(t,x))dx}$. As we have no information on the repartition on/off for the initial data, we apply the following rule : for t_0, starting of our simulation (DAY 2), we choose the repartition to be the same as in the steady distribution N. More precisely, we fix the proportion with the equation

$$n_{\text{on/off}}(t_0,x) = \underbrace{\frac{N_{\text{on/off}}(x)}{N_{\text{on}}(x)+N_{\text{off}}(x)}}_{\text{parameter dependent}} \underbrace{(n_{\text{on}}(t_0,x)+n_{\text{off}}(t_0,x)}_{\text{data}}. \tag{5.8}$$

Numerical scheme. For the equations (5.5), we use an explicit upwind scheme. Setting $a_{\text{on}} : x \longmapsto d(1-x)$ and $a_{\text{off}} : x \longmapsto -dx$, the scheme is given by

$$\begin{cases} \dfrac{{n_{\text{on}}}_j^{n+1} - {n_{\text{on}}}_j^n}{\Delta t} + \dfrac{{a_{\text{on}}}_{j+1/2}^n {n_{\text{on}}}_j^n - {a_{\text{on}}}_{j-1/2}^n {n_{\text{on}}}_{j-1}^n}{\Delta x} = -k_{\text{off}} {n_{\text{on}}}_j^n + k_{\text{on}} {n_{\text{off}}}_j^n + r_j {n_{\text{on}}}_j^n, \\ \dfrac{{n_{\text{off}}}_j^{n+1} - {n_{\text{off}}}_j^n}{\Delta t} + \dfrac{{a_{\text{off}}}_{j+1/2}^n {n_{\text{off}}}_{j+1}^n - {a_{\text{off}}}_{j-1/2}^n {n_{\text{on}}}_j^n}{\Delta x} = -k_{\text{on}} {n_{\text{off}}}_j^n + k_{\text{off}} {n_{\text{on}}}_j^n + r_j {n_{\text{off}}}_j^n, \end{cases} \tag{5.9}$$

with ${n_{\text{on/off}}}_j^n = n_{\text{on/off}}(j\Delta x, n\Delta t)$, $r_j = r(j\Delta x)$, ${a_{\text{on/off}}}_{j+1/2}^n = (a((j+1)\Delta x, n\Delta t) + a(j\Delta x, n\Delta t))/\Delta x$ and ${a_{\text{on/off}}}_{j-1/2}^n = (a(j\Delta x, n\Delta t) + a((j-1)\Delta x, n\Delta t))/\Delta x$. In the Results section, figure 5.7 illustrates a comparison between the result of the numerical scheme and the theoretical asymptotic profile of equations (5.5).

Estimation of the distance to the data. To calibrate the parameter values of our system, we use our experimental data. Initially, in order to estimate the exponential growth rate of cells, we perform a linear regression analysis on the temporal evolution data of the cell count. To determine the values of other system parameters, we seek values that make our numerical results as close as possible to the experimental data. To characterize this notion of closeness between our numerical results and the data, we introduce the Kantorovich-Rubinstein distance. Given two probability distribution p_1, p_2 on $\mathbb{R}_+$, we define their cumulative distribution function $P_i(x) = Pr(X < x, \text{under distribution } p_i) = \int_0^x p_i(dx)$. Using these functions we can define the Kantorovich Rubinstein (also known as Wasserstein) distance by

$$dist_{\text{KT}}(p_1,p_2) = \int_0^\infty |P_1(x) - P_2(x)|\,\mathrm{d}x. \tag{5.10}$$

In our specific case, we want to compare at each step the (normalized) distribution generated by the model at time t_i (hereby denoted as $model(t_i, dx)$ with cumulative distribution $M(t_i, .)$) and the corresponding distribution of the data at time t_i denoted as $data(t_i, dx)$with cumulative distribution $D(t_i, .)$. We would therefore compute

$$dist_{KT}(t_i) = dist_{\text{KT}}(model(t_i), data(t_i)) = \int_0^\infty |M(t_i,x) - D(t_i,x)|dx.$$

Note that in our case the integral is in fact taken on the finite interval $[0,1]$ for scaled variables.

Considering the distribution profile of the data, we prefer to study this distance on a logarithmic scale. We therefore make the following change of variables $y = \log(xX_{\max}+1)$, and we define the modified Kantorovich-Rubinstein distance as follows

$$dist_{\mathrm{KT}}^{\log}(t) = \int_0^{\log(X_{\max}+1)} \left|\tilde{D}(y,t) - \tilde{M}(y,t)\right| \mathrm{d}y, \tag{5.11}$$

with $\tilde{D}$ and $\tilde{M}$ the two cumulative distribution functions, defined below, in the new logarithmic scale. Note that, following this change of variable, this "distance" can be greater than 1.

We are looking for a function $\tilde{m}$ that satisfies the following relation, for all $b \in [0, \log(1+X_{max})]$

$$\tilde{M}(b,t) = M\left(\frac{e^b-1}{X_{max}}, t\right). \tag{5.12}$$

In particular, the link between the corresponding densities is immediately given by

$$\tilde{m}(b,t) = m\left(\frac{e^b-1}{X_{max}}, t\right)\frac{e^b}{X_{max}}. \tag{5.13}$$

The space $[0,1]$ is discretized uniformly with $J+1$ points, and this sequence is denoted $(x_j)_j$.

$$(x_j)_{j\in\{0,1,\ldots,J\}} :\ x_j = j\Delta x, \qquad \text{with } \Delta x = 1/J.$$

We also define the sequences $(y_j)_{j\in\{0,1,\ldots,J\}}$ and $(\ell_j)_{j\in\{0,1,\ldots,J-1\}}$ as follows

$$(y_j)_{j\in\{0,1,\ldots,J\}} :\ y_j = \log(X_{\max}x_j+1) = \log\left(1+\frac{X_{\max}j}{J}\right),$$

and

$$(\ell_j)_{j\in\{0,1,\ldots,J-1\}} :\ \ell_j = y_{j+1} - y_j.$$

Consequently, the estimator of the cumulative distribution function M is given by

$$\hat{M}(y_j,t) = \frac{1}{\sum_i \tilde{m}(y_i,t)\ell_i}\sum_{i<j}\tilde{m}(y_i,t)\ell_i = \frac{\sum_{i<j} m(x_i,t)\left(\frac{1}{X_{\max}}+x_i\right)\ell_i}{\sum_i m(x_i,t)\left(\frac{1}{X_{\max}}+x_i\right)\ell_i}, \quad \forall j\in\{0,1,\ldots,J\}.$$

where we have used (5.13) to estimate $\tilde{m}$. We need to renormalize to ensure we are comparing probability distributions.

The estimator of the cumulative distribution function D is

$$\hat{D}(y_j,t) = \frac{1}{\#\{d_k(t),\ \forall k\}}\sum_{i<j} h_i, \quad \forall j\in\{0,1,\ldots,J\},$$

with $h_j(t) = \#\{d_i :\ \log(d_i(t)+1)\in[y_{j-1},y_j]\}$, where the operator $\#$ corresponds to the cardinal of a set and the data d_i correspond to the fluorescence data obtained after data processing. These data, d_i, are real numbers between 0 and $X_{\max}$. The term $\#\{d_k(t),\ \forall k\}$ corresponds to the number of cells present in the data on day t after the gating operation.

Therefore, the distance between the experimental data and the mathematical model is as follows

$$\widehat{dist}^{\log}_{\mathrm{KT}}(t;\text{parameters}) = \sum_{j=0}^{J-1} \left| \hat{D}(y_j,t) - \hat{M}(y_j,t;\text{parameters}) \right| \ell_j. \tag{5.14}$$

To calibrate the parameters of our model, we will minimize the sum of the modified Kantorovich-Rubinstein distance for the different days at our disposal and for the two experiments. The distance associated with $\mathrm{CD34}^+$ data is denoted $\widehat{dist}^{\log,+}_{\mathrm{KT}}$, while that associated with $\mathrm{CD34}^-$ data is denoted $\widehat{dist}^{\log,-}_{\mathrm{KT}}$. We also introduce the distance, denoted $\widehat{dist}^{\log,\pm}_{\mathrm{KT}}$, corresponding to the sum of these two distances. Thereby we look for one set of parameters for fitting the two datasets jointly. Mathematically, the optimization problem is given by the following formula

$$\text{parameters}^{\text{opt}} = \underset{\text{parameters}}{\arg\min} \left(\sum_{t\in\text{Days}} \widehat{dist}^{\log,\pm}_{\mathrm{KT}}(t;\text{parameters}) \right). \tag{5.15}$$

The results of this optimization work are detailed in the Results section.

5.3 Results

Mathematical Analysis – derivation of explicit normalized asymptotic profile $(N_{\mathbf{on}}, N_{\mathbf{off}})$

Under the assumption of a linear proliferation rate $r(x) = r_0 + r_1 x$, we obtain the following result

■ **Theorem 3:**
Assume $r(x) = r_0 + r_1 x$. Define the matrix M by

$$\begin{pmatrix} r_1 - k_{off} & k_{on} \\ k_{off} & -k_{on} \end{pmatrix}.$$

Denote $s(M)$ the largest eigenvalue of M, then the left and right eigenvector

$$V^t M = s(M) V^t, \quad MU = s(M) U,$$

can be chosen positive. Moreover, the solution to (5.6) is given by

$$\lambda = r_0 + s(M) = r_0 + \frac{r_1 - k_{on} - k_{off} + \sqrt{(r_1 - k_{on} - k_{off})^2 + 4k_{on}r_1}}{2}. \tag{5.16}$$

And

$$\begin{pmatrix} N_{on}(x) \\ N_{off}(x) \end{pmatrix} = \begin{pmatrix} C(1-x)^{\frac{k_{off}}{d\eta}-1} x^{\frac{k_{on}\eta}{d}} e^{\frac{r_1}{d}x} \\ C\eta(1-x)^{\frac{k_{off}}{d\eta}} x^{\frac{k_{on}\eta}{d}-1} e^{\frac{r_1}{d}x} \end{pmatrix}, \tag{5.17}$$

with C an arbitrary positive constant and η given by $\eta = 1 + s(M)/k_{on}$.
In particular, we have

$$N(x) = C(1-x)^{\frac{k_{off}}{d\eta}-1} x^{\frac{k_{on}\eta}{d}-1} e^{\frac{r_1}{d}x} \left(\eta + (1-\eta)x\right), \tag{5.18}$$

Proof: *We notice that the existence and uniqueness (up to a multiplicative factor) of the triplet $s(M), V, U$ is a straightforward consequence of the classical Perron Frobenius theorem which applies here because the off-diagonal entries of M are positive [258]. We introduce the ration $\eta = \frac{V_{on}}{V_{off}}$ and notice that by construction, we have*

$$\eta = \frac{V_{on}}{V_{off}} = \frac{k_{off}}{s(M) - r_1 + k_{off}} = \frac{s(M) + k_{on}}{k_{on}}. \tag{5.19}$$

Then, consider the system satisfied by $\psi_{on,off} = e^{r_1 x}\phi_{on,off}$, where $\phi_{on/off}$ is the solution of (5.7). We get

$$\begin{cases} \lambda\psi_{on} - d(1-x)\partial_x\psi_{on} = -k_{off}\psi_{on} + k_{off}\psi_{off} + (r_0 + r_1)\psi_{on}(t,x), \quad x \in]0,1[, \\ \lambda\psi_{off} - d(-x)\partial_x(\psi_{off}) = -k_{on}\psi_{off} + k_{on}\psi_{on} + r_0\psi_{off}(x), \quad x \in]0,1[. \end{cases}$$

This system can be summarized as

$$d\begin{pmatrix} -(1-x)\partial_x\psi_{on} \\ -(-x)\partial_x\psi_{off} \end{pmatrix} = \left(\begin{pmatrix} r_0 + r_1 - k_{off} & k_{off} \\ k_{on} & r_0 - k_{on} \end{pmatrix} - \lambda I_2\right)\begin{pmatrix} \psi_{on} \\ \psi_{off} \end{pmatrix}.$$

We recognize the matrix $r_0 + M^t$. Therefore, we have a solution independent on x $\psi_{on,off} = V_{on,off}$ and $\lambda = r_0 + s(M)$ and $\phi_{on,off} = e^{-\frac{r_1}{d}x}V_{on,off}$. Similarly, if we denote $P_{on,off} = e^{-\frac{r_1}{d}x}N_{on,off}$, we obtain

$$\begin{cases} \lambda P_{on} + d\partial_x((1-x)P_{on}) = -k_{off}P_{on} + k_{on}P_{off} + (r_0 + r_1)P_{on}, \quad x \in]0,1[, \\ \lambda P_{off} + d\partial_x((-x)P_{off}) = k_{off}P_{on} - k_{on}P_{off} + r_0 P_{off}, \quad x \in]0,1[, \\ P_{on}(0) = P_{off}(1) = 0, \quad P_{on,off} > 0. \end{cases}$$

This can be condensed into

$$d\partial_x\begin{pmatrix} (1-x)P_{on} \\ -xP_{off} \end{pmatrix} = (r_0 - \lambda + M)\begin{pmatrix} P_{on} \\ P_{off} \end{pmatrix}.$$

We can now proceed as for the conservative case and notice that since $V^t(r_0 - \lambda - M) = 0$ multiplying the equation by V.

$$\partial_x\left(V_{on}(1-x)P_{on}(x) - xV_{off}P_{off}(x)\right) = 0,$$
$$P_{off}(x) = \frac{V_{on}(1-x)}{xV_{off}}P_{on}.$$

After the appropriate substitution, we obtain

$$\begin{aligned} d\partial_x((1-x)P_{on}) &= \left(\frac{-k_{off} + r_0 + r_1 - \lambda}{(1-x)} + \frac{k_{on}V_{on}}{xV_{off}}\right)(1-x)P_{on} \\ &= \left((r_1 - k_{off} - s(M))\frac{1}{(1-x)} + (s(M) + k_{on})\frac{1}{x}\right)(1-x)P_{on}. \end{aligned}$$

This leads to, for a suitable renormalization constant $C > 0$,

$$\begin{cases} P_{on} = C(1-x)^{\frac{k_{off} + s(M) - r_1}{d} - 1}x^{\frac{k_{on} + s(M)}{d}}, \\ P_{off} = C\frac{V_{on}}{V_{off}}(1-x)^{\frac{k_{off} + s(M) - r_1}{d}}x^{\frac{k_{on} + s(M)}{d} - 1}. \end{cases}$$

We introduce then the notation $\eta = \eta(r_1) = \dfrac{V_{on}}{V_{off}}$ *and go back the* N *variables to write*

$$\begin{cases} N_{on} = C(1-x)^{\frac{k_{off}}{d\eta}-1} x^{\frac{k_{on}\eta}{d}} e^{\frac{r_1}{d}x}, \\ N_{off} = C\eta(1-x)^{\frac{k_{off}}{d\eta}} x^{\frac{k_{on}\eta}{d}-1} e^{\frac{r_1}{d}x}. \end{cases} \tag{5.20}$$

In particular, we have

$$N(x) = C(1-x)^{\frac{k_{off}}{d\eta}-1} x^{\frac{k_{on}\eta}{d}-1} e^{\frac{r_1}{d}x} \left(\eta + (1-\eta)x\right).$$

Going back to the definition of η *we notice*

$$k_{on}\eta = k_{on} + s(M), \quad k_{off}/\eta = k_{off} + s(M) - r_1. \tag{5.21}$$

□

5.3.1 Simulation Analysis

Estimation of exponential growth rate. Using experimental data on cell numbers for different days, we estimate the exponential growth rate λ. For both relaxation experiments, we perform a linear regression of the natural logarithm of the number of cells. In the case of $CD34^+$ cell relaxation, the linear regression line is given by the slope $\lambda^+ \approx 0.418$, and for $CD34^-$ cells, the slope is $\lambda^- \approx 0.422$. We estimate the parameter λ by the average of these two slopes, $\lambda \approx 0.42$. Figure 5.4 shows that the estimate of the exponential growth rate is in good agreement with the experimental data.

Calibration of parameters. A study of the maximum for each day and each experiment of the "PE-Cy7-A" fluorescence data reveals an $X_{\max}$ close to 20,000. To reduce the numerical complexity of the 5-parameter optimization $(r_0, r_1, k_{\text{on}}, k_{\text{off}}, d)$, we will use the estimate of λ to reduce our optimization problem to just 4 parameters. Indeed, using the theoretical relationship (5.16) and the previous estimate of λ, we can define the parameter r_0 as a function of the other model parameters,

$$r_0 = s(M) - \hat{\lambda} = s(M) - 0.42.$$

For the estimation of the other parameters r_1, k_{on}, k_{off} and d, we use the modified Kantorovich-Rubinstein distance minimization strategy, presented in the Method section and given by the following formula

$$(r_1^\star, k_{\text{on}}^\star, k_{\text{off}}^\star, d^\star) = \underset{r_1, k_{\text{on}}, k_{\text{off}}, d}{\arg\min} \left(\sum_{t \in \text{Days}} \widehat{dist}_{\text{KT}}^{\log,\pm}(t; r_1, k_{\text{on}}, k_{\text{off}}, d) \right). \tag{5.22}$$

To determine numerically this minimum, we calculate the modified Kantorovich-Rubinstein distance for the two relaxation experiments, for each point on a large grid of parameter values. We then adjust our grid to obtain the location of the minimum of the sum of two distances. This method gives us the following four parameter values $r_1^\star = 0.426$, $k_{\text{on}}^\star = 0.261$, $k_{\text{off}}^\star = 19.178$ and $d^\star = 0.21$. Following this optimization strategy, the optimal choice for the function r is to choose r_1 such that

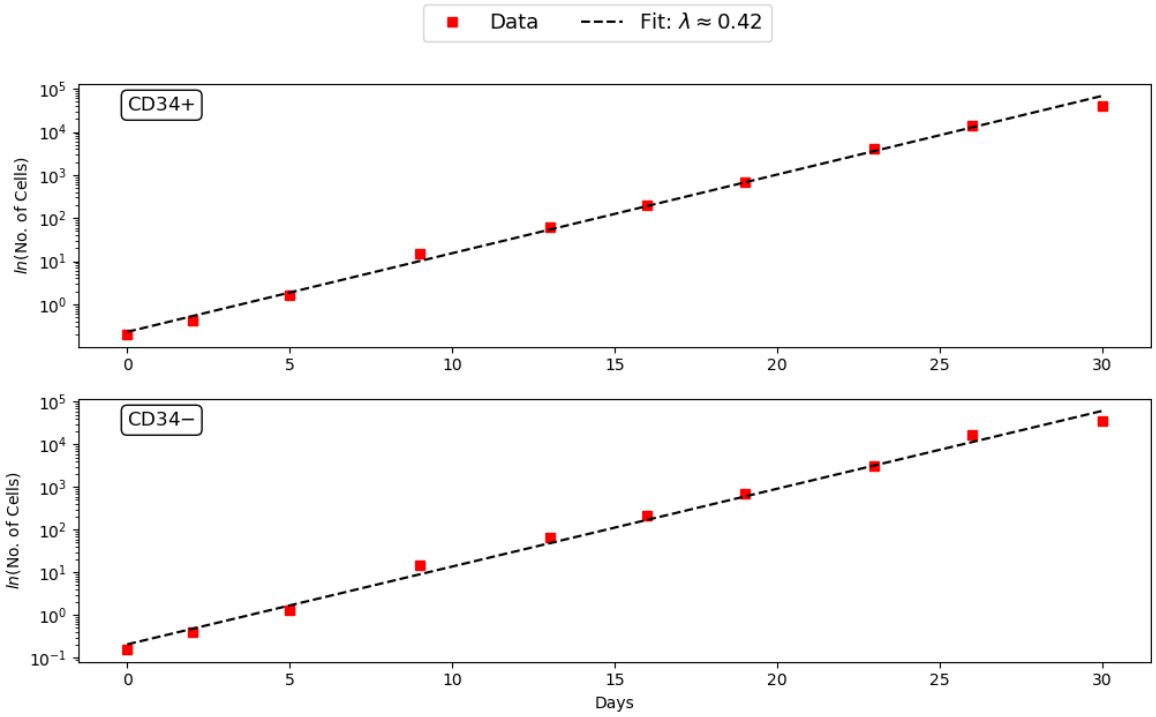

FIGURE 5.4 – **Estimation of the exponential growth rate λ.** The red squares correspond to the number of cells (log scale) at different times for the relaxation experiments : *Top.* $CD34^+$, *Bottom.* $CD34^-$. The dotted line in black illustrates the optimal fit of the experimental data. The average of the slopes of the linear regressions minimizing the two experiments is given by the slope $\lambda \approx 0.42$.

TABLE 5.1 – Estimated parameter values.

Parameter	Value	Units	Description	Estimation Method
$X_{\max}$	2×10^4	proteins	Maximum value for the quantity of CD34 in a cell	Data-driven selection
r_0	0.426	h^{-1}	Constant proliferation rate	Estimating the proliferation rate λ and using the relation (5.16)
r_1	-0.426	h^{-1}	Linear proliferation rate	KT distance minimization (5.22)
k_{on}	0.261	h^{-1}	Rate at which the gene/promoter is turned "on"	KT distance minimization (5.22)
k_{off}	19.178	h^{-1}	Rate at which the gene/promoter is turned "off"	KT distance minimization (5.22)
d	0.21	h^{-1}	Degradation rate	KT distance minimization (5.22)
s	4214	proteins.h^{-1}	Synthesis rate of proteins when gene is on	Relation : $s = dX_{\max}$

$r(x) = r_0 \times (1 - x)$. Nevertheless, we will see in the next section that the choice of r_1 is not decisive for a good fit between the model result and the experimental data.

Finally, using the relation, $s = dX_{\max}$, we can calculate the value of the synthesis rate, $s = 4214$. All parameter value estimates are given in table 5.1.

We compared those values to the litterature. The estimated half-life of CD34 in this model was estimated to be equal to $log(2)/0.261$, that is about 4 hours. This is in the low range of the estimated distribution for proteins half-life [259]. Regarding the $X_{\max}$ estimation, its value is in the range of observed value, slightly over the median that is 1.6×10^4 [259]. The estimated k_{on} value gives an estimated frequency of 4 (1/0.261) bursts per hour on average, which is close from the expected range from a burst every 30 minutes to up to 10 hours [260]. The k_{off} value display the expected ratio ($k_{\text{on}} \ll k_{\text{off}}$ an $d \ll k_{\text{off}}$) in the case of a bursty regime [234]. Altogether all of our estimated parameters are thus in the expected range.

Profile likelihood. To investigate the robustness of our parameter estimates and the significance of each parameter in minimizing the modified Kantorovich-Rubinstein distance, we employ an approach analogous to the *profile likelihood* concept [261, 262] in the context of our optimization problem.

First, we examine the influence of the parameter d. Let d be fixed, we calculate, in the same way, the triplet of parameters $(r_1, k_{\text{on}}, k_{\text{off}})$ that minimizes the modified Kantorovich-Rubinstein distance under the fixed d constraint. These optimal parameters are, therefore, functions dependent on d, denoted as $\widehat{r_1}$, $\widehat{k_{\text{on}}}$, and $\widehat{k_{\text{off}}}$. Mathematically, they are defined by the following relation

$$\left(\widehat{r_1}(d), \widehat{k_{\text{on}}}(d), \widehat{k_{\text{off}}}(d)\right) = \underset{r_1, k_{\text{on}}, k_{\text{off}}}{\arg\min} \left(\sum_{t \in \text{Days}} \widehat{dist}_{\text{KT}}^{\log,\pm}(t; r_1, k_{\text{on}}, k_{\text{off}}, d) \right).$$

Once these functions have been calculated, we can determine the modified Kantorovich-Rubinstein

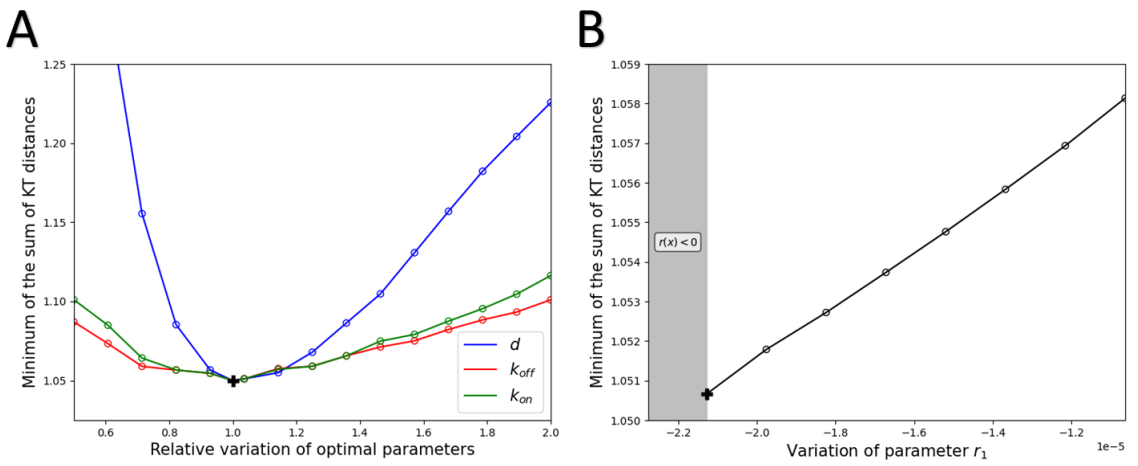

FIGURE 5.5 – **Likelihood profiles for for k_{on}, k_{off} and d in A and for r_1 in B.** A. The blue curve represents the function S_d, the red curve $S_{k_{\text{off}}}$ and the green curve $S_{k_{\text{on}}}$. The function S_d is introduced into equation (5.23). B. The grey area corresponds to the range of parameter values for r_1 such that the function r is non-positive. Compared with the other parameters, variation in the r_1 parameter has a small impact on the minimum Kantorovich-Rubinstein distance.

distance associated with them, denoted by S_d and defined by the following equality,

$$S_d(d/d^\star) = \sum_{t\in\text{Days}} \widehat{dist}_{\text{KT}}^{\log,\pm}\left(t; \widehat{r_1}(d), \widehat{k_{\text{on}}}(d), \widehat{k_{\text{off}}}(d), d\right). \tag{5.23}$$

For the argument of the function, we choose $d/d^\star$, to study the distance associated with the relative variation of the optimal parameter. By definition of the function S_d, it reaches its minimum at $d = 1$, corresponding to $d = d^\star$. Similarly, we can define the functions $S_{k_{\text{on}}}$, $S_{k_{\text{off}}}$, and S_{r_1}.

In figure 5.5.A, we plotted the S_d, $S_{k_{\text{on}}}$ and $S_{k_{\text{off}}}$ functions. The impact of the relative variation of the two transition rates around the optimal value, on the modified Kantorovich-Rubinstein distance is quite similar. For the degradation rate, d, we note that a fine estimate of this is crucial to obtain good accuracy between the data and the mathematical model.

Conversely, the parameter r_1 has a minor impact on the minimum of the modified Kantorovich-Rubinstein distance. Specifically, when r_1 deviates from its optimal value, new optimal parameter values emerge, resulting in distances very close to the optimal distance. This result is illustrated in Figure 5.5.B.

Comparison between model and experimental data. In figure 5.6 we compared data from relaxation experiments with the results of our model for the parameter values presented in table 5.1.

To initialize our model on day 2, we use the equation (5.8), it follows this following initial conditions

$$n_{\text{on/off}}(t_0, x) = \frac{N_{\text{on/off}}(x)}{N_{\text{on}}(x) + N_{\text{off}}(x)} \times \sum_{j=0}^{J-1} h_j \mathbf{1}_{x\in[x_j, x_{j+1}]}(x), \qquad x \in [0,1], \tag{5.24}$$

where h_j corresponds to the number of cells on day 2 with fluorescence between $X_{\max} \times x_j$ and

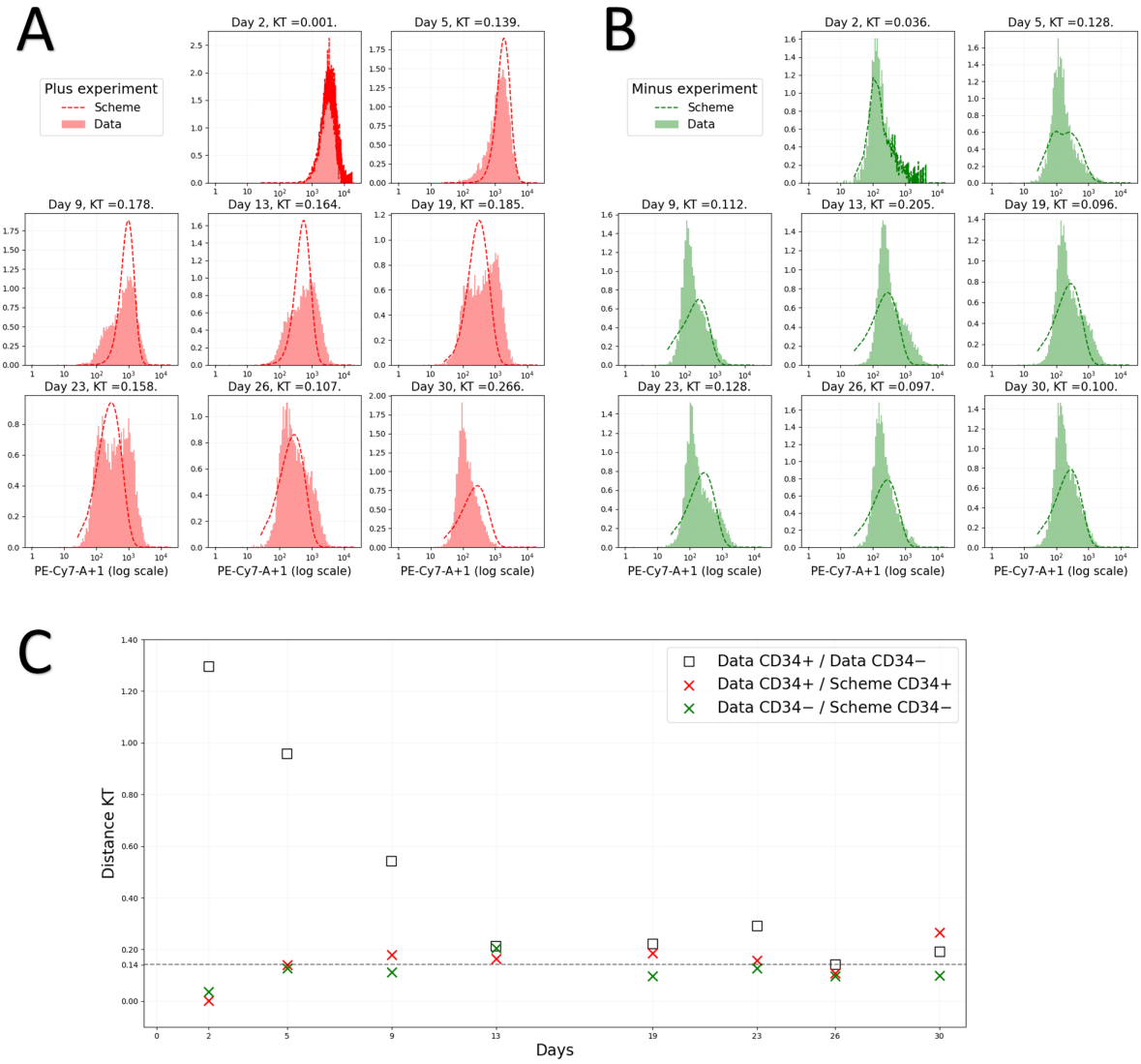

FIGURE 5.6 – **Comparison of model and data.** On the left the fitting of the $CD34^+$ relaxation experiment (in A) and on the right in green of the $CD34^-$ (in B) experiments. Experimental data in logarithmic scale are represented by plain histograms and the numerical results of model (5.5) are represented by the dotted curves. We initialize the model on day 2, using the biological data. The initial condition is given by (5.24). Parameter values are given in table 5.1. KT : the modified Kantorovich-Rubinstein distance, defined by the equation (5.14). C. Time-dependent evolution of the Kantorovich-Rubinstein distance between model and experimental data. For different days of the experiment, the modified Kantorovich-Rubinstein distance between the two relaxation experiments is depicted using black squares. The minimum distance, reached on day 26, is illustrated by a horizontal dotted line. The red crosses correspond to the modified Kantorovich-Rubinstein distance between the model for the parameter values from Table 5.1, and the $CD34^+$ cell relaxation experiment. Similarly, the green crosses represent the distance for the $CD34^-$ cell relaxation experiment.

$X_{\max} \times x_{j+1}$, where $(x_j)_j$ corresponds to the uniform discretization of space $[0, 1]$. That is, the $(h_j)_j$ correspond to the heights of the histogram of the data renormalized by the maximum $X_{\max}$.

Visually, Figure 5.6.A,B reveals a high degree of proximity between the experimental data and the mathematical model. To quantify this closeness, we once again employ the modified Kantorovich-Rubinstein distance. In figure 5.6.C, we represent, by black squares, the temporal evolution of distance between the experimental data of the two relaxation experiments. Due to the antinomic nature of the two experiments, distances are considerable in the early days of the experiment. It then gradually decreases as the two distributions converge towards the stationary distribution. From day 26, both profiles reached the stationary stage. At this point, in the absence of noise, these two distributions are expected to be similar. Therefore, the minimum distance, dist = 0.142 (illustrated by a dotted line), attained on day 26, corresponds to a reference distance to determine the proximity of two distributions.

In this figure, we also illustrate the distance between the model and the two relaxation experiments. The $CD34^+$ cell relaxation experiment is represented by the red crosses, and the $CD34^-$ cell relaxation experiment by the green crosses. To quantitatively assess the proximity of the model to experimental data, we employ the reference distance represented by the horizontal line. For the $CD34^-$ cell relaxation experiment, we observe that the distances are always less than the reference distance, except on day 13 for which the distance is slightly greater. Concerning the $CD34^+$ cell relaxation experiment, this time the distances are more regularly greater than the reference distance, but are still within an acceptable order of magnitude. These results show that our proposed model is very close to the experimental data.

5.4 Discussion

Although we had to infer a number of model parameters which could not be deduced from the literature (like for example the half-life of the CD34 protein), the overall fitting ability of our model proved to be quite satisfactory. Using Kantorovich distances, we indeed observed that the model-to-experiment distance was within the range of the experiment-to-experiment distance, so in the range of experimental variability.

We assumed that the proliferation rate would depend upon the level of expression of the very gene that is being modelled. In our case, that proved to be useful since we wanted to fit relaxation data obtained from CD34 expression. CD34 is a known marker for stemness and we hypothesized that, in line with the existing litterature [231], $CD34^+$ cells would proliferate less that $CD34^-$ more mature cells. We should nevertheless stress that such a behaviour can be true for normal hematopoietic stem cells, but can be questioned regarding cancer stem cells.

The methodology presented in this paper is applicable to any cell systems for which one can perform simultaneously relaxation experiments and proliferation measurements. Biological systems for which the half-life of the protein of interest is known should be preferred, since this will remove the need for estimating an important model parameter.

One of the difficulties we faced when comparing the model's output with experimental data, lies in the need for common units By default, our model output is a value between 0 (no CD34 expressed) and 1 (maximum level of CD34 expression). FACS data are corrected fluorescent values, that can be

negative in the raw acquisition dataset. We therefore processed the data with a gating phase, a shifting phase, and finally normalized them in order to obtain comparable values with the model.

It is crucial to emphasize that within a cell population displaying a stationary distribution of phenotypic states, no cell remains in a permanent state over time. Given a sufficiently long time, one can assume that all cells will have visited all possible states (i.e. all possible values for their surface CD34 expression). In other terms, in the state versus identity long standing debate [263], we clearly side with the view that stemness is an emerging dynamical property

Several points shall be investigated further. The first point that can be enriched is the form of the division rate $r(x) = r_0 - r_1 x$. The linear form ensures the explicit formulation of the stable distribution and facilitates the scaling by $X_{\max}$ but is not necessary for the existence of a profile. Moreover, we made strong assumptions here that the daughter cells have the same concentration of markers than the mother cell and that the division has no impact on the on/off status of the cell. This later is a reasonable assumption in the light of the existence of transcriptional memory [251, 252], but it might be gene-dependent.

One missing aspect of our model is the absence of any explicit death term. On the other hand , an expression independent death rate could immediately be considered by relaxation of the constraint of positive division rate (which would then correspond to a net growth rate). In terms of parameters, this would affect r_0.

Another missing aspect of our model is the fact that the CD34 gene expression is modelled in isolation. It is quite obvious that in cells its expression level will be constrained by its positioning in a complex web of genes-to-genes interactions known as a Gene Regulatory Network (GRN). Inference of such GRNs is a notoriously difficult task (see e.g. [264]), and performing relaxation experiments from such complex objects is yet to be done.

One of the future goal of our work would be to assess its predictive ability. A promising lead would be to go further in the analysis in order to estimate the influence of parameters on the relaxation time. Mathematically, this could be analysed through the spectral gap which is beyond the scope of this work. It would be especially interesting to identify the effects of various parameters on it, in particular the parameter d which represents the degradation rate. Note that in this case, the distribution and the value of λ are expected to change. Interestingly, the model's prediction in this case could be tested experimentally by modifying the endogenous CD34 protein stability.

5.5 Conclusion

In the present work, we proposed a revised two-state probabilistic model for gene expression which explicitly incorporates a proliferation term. This model was analysed and we obtained an analytical solution for our model's steady state. The same model was then used for simulating the transient behavior of FACS-sorted cells leading to the progressive relaxation towards the steady state distribution. Altogether, our work shows that a two-state description for CD34 gene expression is well suited to explain the relaxation experiments. This support the notion that cells should be seen and modeled as probabilistic dynamical systems.

A Supplementary Figures

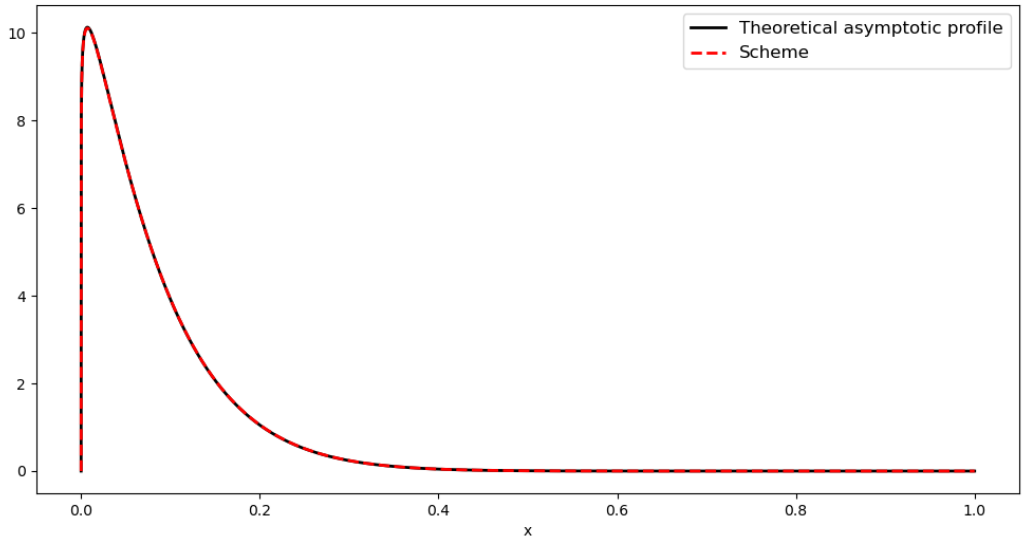

FIGURE 5.7 – **Comparison between the theoretical asymptotic profile N (black line) presented in Theorem 3 and the numerical solution obtained using the numerical scheme (red dotted line) defined by equations (5.9).** Parameter values are given by $r_0 = 3.4$, $r_1 = 3$, $k_{\text{on}} = 0.85$, $k_{\text{off}} = 12.71$, $d = 1$, $X_{\max} = 2 \times 10^4$.

Cinquième partie

Modélisation en lien avec la maladie d'Alzheimer

Introduction

L'agrégation des protéines amyloïdes-β et le rôle de la microglie dans la maladie d'Alzheimer

La maladie d'Alzheimer est une maladie neurodégénérative progressive qui affecte la mémoire, la pensée et le comportement. L'une des principales hypothèses proposées pour expliquer le développement de la maladie est l'agrégation, dans le système nerveux, des protéines amyloïdes-β (notées Aβ), dans ce que l'on nomme des plaques amyloïdes. De nombreuses études montrent que ces agrégats jouent un rôle clé dans les dommages des neurones, entraînant une détérioration progressive et irréversible du cerveau (voir, par exemple, [265, 266, 267, 268, 269]). Comprendre comment ces agrégats se forment et se décomposent pourrait fournir des informations précieuses sur le développement de la maladie d'Alzheimer et sur les stratégies de traitement potentielles.

Comment se créent et évoluent les protéines Aβ ? Les neurones produisent des monomères Aβ qui commencent presque instantanément à se regrouper en petites structures appelées *proto-oligomères*. Ces proto-oligomères peuvent soit s'assembler pour former des structures plus grandes, soit se décomposer en plus petites structures. Lorsqu'ils atteignent une certaine taille critique, ils deviennent des oligomères Aβ stables, qui ne peuvent plus se transformer en d'autres structures [270, 271]. Ce processus d'agrégation des monomères en oligomères est connu sous le nom d'hypothèse de la *cascade amyloïde*. Les oligomères libres peuvent ensuite s'assembler pour former des plaques amyloïdes, où ils deviennent complètement inertes. Ces plaques sont réparties de manière hétérogène dans le cerveau, comme illustré à la figure 6.1 du chapitre 6. Ce mécanisme est largement considéré comme un facteur clé des dommages neuronaux observés chez les patients atteints de la maladie d'Alzheimer.

L'interaction entre la microglie et les protéines Aβ. Outre le mécanisme de polymérisation, les oligomères interagissent avec les cellules microgliales, considérées comme des cellules auxiliaires du système nerveux régulant le développement cérébral. Tout d'abord, ces cellules déclenchent une réaction inflammatoire en libérant des interleukines par le biais d'une cascade chimique [272, 273]. Les interleukines vont ensuite signaler aux neurones d'augmenter la production de monomères Aβ. Cependant, si la concentration d'oligomères Aβ devient trop élevée, une réaction de stress appelée

Unfolded protein response (UPR) [268] est déclenchée, ce qui entraîne une diminution de la production de monomères Aβ. Les cellules microgliales auront également un rôle clé dans le transfert des oligomères libres vers les plaques amyloïdes inertes.

Etat de l'art

Ce projet s'inscrit comme une suite directe et naturelle de l'article [274], dans lequel Ciuperca, Pujo-Menjouet, Matar-Tine, Torres et Volpert introduisent un système modélisant le rôle de la microglie, des interleukines et des protéines Aβ dans la maladie d'Alzheimer, tel que décrit ci-dessus.

Présentation du modèle introduit dans l'article [274]. Plus précisément, dans cet article, les auteurs introduisent un système d'équations aux dérivées partielles faisant interagir les éléments suivants

- Les monomères Aβ : m.
- Les protos-oligomères Aβ de taille $i \in \{2, \dots, i_0 - 1\}$: u_i.
- Les oligomères libres Aβ : u.
- Les oligomères dans les plaques inertes : u_p.
- Les cellules microgliales : M.
- Les interleukines : I.

Pour aborder ce modèle complexe, les auteurs proposent de simplifier le problème en supposant que la nucléation de deux monomères ne produit pas un proto-oligomère de taille 2 mais directement un oligomère libre ($m + m \to u$). Dans cette situation, ils négligent la modélisation des proto-oligomères. Etant donné que la structure en taille est omise, ils supposent que lorsqu'un monomère se fixe à un oligomère, la structure résultante reste un oligomère et le monomère est consommé ($u + m \to u$). Les équations du système sont les suivantes :

$$\begin{cases} \partial_t u = \nu_2 \Delta u + r_1 m^2 - \gamma(M) u - \tau_0 u, \\ \partial_t u_p = \gamma(M) u - \tau_p u_p, \\ \partial_t m = \nu_1 \Delta m + S(I, u) - dm - r_2 u m - r_1 m^2, \\ \partial_t M = D_1 \Delta M - \alpha \nabla \cdot (M \nabla u) + G(u)(\hat{M} - M) M - \sigma M + \lambda_M, \\ \partial_t I = D_I \Delta I + F(u) M - \tau_3 I, \end{cases} \tag{V.1}$$

considérées sur un domaine ouvert borné $\Omega \subset \mathbb{R}^3$, représentant une partie du cerveau, avec des conditions de Neumann aux bords. Pour chaque acteur du système, les auteurs supposent un terme de dégradation naturelle avec un certain taux respectif. Les monomères, oligomères libres et les interleukines sont également supposés diffuser avec leur propre coefficient de diffusion. En revanche, les oligomères dans les plaques amyloïdes sont considérés comme inertes, donc sans capacité de mouvement ; tandis que les cellules microgliales ont un mouvement de diffusion biaisé par les fortes concentrations d'oligomères, modélisé par la combinaison d'un terme de diffusion et de chimiotaxie. Les autres termes de réaction seront détaillés ci-dessous, équation par équation :

- Dans le système (V.1), l'équation des *monomères* est donnée par

$$\partial_t m = \underbrace{\nu_1 \Delta m}_{\text{Diffusion}} + \underbrace{S(I,u)}_{\text{Création}} \underbrace{-r_2 u m - r_1 m^2}_{\text{Polymérisation}} \underbrace{-dm}_{\text{Dégradation}} \quad ,$$

avec la fonction $S(I,u)$ représentant le terme de création des monomères par les neurones, donnée par la formule $S(I,u) := I\tau_S/(1+Cu^n)$. Les auteurs supposent que la création est proportionnelle à la concentration locale d'interleukines I, mais que la quantité créée dépend également de la concentration locale d'oligomères. Lorsque la concentration d'oligomères est faible ($u \approx 0$), la production est proportionnelle à I ; en revanche, lorsque la concentration est élevée, le terme source $S(I,u)$ tend vers 0, modélisant ainsi le processus de stress appelé *Unfolded protein response*. Les deux termes de polymérisation correspondent respectivement au cas, $u+m \to u$, et à la nucléation de deux monomères donnant un oligomère, $m+m \to u$, provenant de l'hypothèse simplificatrice énoncée ci-dessus.

- L'équation relative aux *oligomères libres* est formulée comme suit

$$\partial_t u = \underbrace{\nu_2 \Delta u}_{\text{Diffusion}} \underbrace{-\gamma(M)}_{u \to u_p} u \quad \underbrace{+r_1 m^2}_{\text{Polymérisation}} \quad \underbrace{-\tau_0 u}_{\text{Dégradation}} \quad ,$$

avec, $\gamma(M)u$, correspondant au terme de recrutement des oligomères libres dans les plaques amyloïdes, dont le taux est donné par la fonction γ, qui dépend de la concentration locale de cellules microgliales. Plus la concentration de cellules est élevée, plus le recrutement est important. Les auteurs ont choisi une fonction de type Michaelis-Menten, $\gamma(M) := \gamma_0 + \gamma_1 M/(1+\gamma_2 M)$.

- L'équation décrivant la concentration des *oligomères dans les plaques inertes* est définie par

$$\partial_t u_p = \underbrace{\gamma(M)u}_{u \to u_p} \quad \underbrace{-\tau_p u_p}_{\text{Dégradation}} \quad .$$

- L'équation qui régit la concentration des *cellules microgliales* est donnée par

$$\partial_t M = \underbrace{D_1 \Delta M}_{\text{Diffusion}} \underbrace{-\alpha \nabla \cdot (M \nabla u)}_{\text{Chimiotaxie}} + \underbrace{G(u)(\hat{M} - M)M}_{\text{Prolifération}} + \underbrace{\lambda_M}_{\text{Création}} \quad \underbrace{-\sigma M}_{\text{Dégradation}} \quad .$$

La production de nouvelles cellules microgliales résulte soit de la prolifération cellulaire, soit d'un terme source λ_M. Le terme de prolifération est supposé logistique, avec un taux de prolifération donné par la fonction G dépendant de u et ayant une forme de type Michaelis-Menten. Le mouvement des cellules microgliales n'est pas parfaitement brownien. Les auteurs supposent qu'il existe un biais vers les fortes concentrations d'oligomères libres, modulé par le coefficient de chimiotaxie α, qui sera particulièrement étudié dans le chapitre suivant.

- L'équation de la concentration des *interleukines* est définie comme suit

$$\partial_t I = \underbrace{D_I \Delta I}_{\text{Diffusion}} + \underbrace{F(u)M}_{\text{Création}} \quad \underbrace{-\tau_3 I}_{\text{Dégradation}} \quad ,$$

où, $F(u)M$, représente la création de nouvelles interleukines par les cellules microgliales. Ce terme source dépend également de la concentration locale d'oligomères libres via la fonction F, définie par la fonction de Michaelis-Menten suivante : $F(u) := \tau_1 u/(1+\tau_2 u)$. Cette dépendance modélise le fait que les oligomères libres activent les cellules microgliales, permettant ainsi la production d'interleukines.

Analyse du modèle (V.1) **sans espace.** Dans l'article [274], Torres et al. ont également étudié les états stationnaires spatialement homogènes du modèle (V.1). Pour simplifier les notations, nous considérons le vecteur $\mathbf{V} = (u, u_p, m, M, I)$. Tout d'abord, le point $\mathbf{V}_0 := (0, 0, 0, \lambda_M/\sigma, 0)$ est toujours un point d'équilibre du système, correspondant à l'équilibre sans plaque ni inflammation. Sous la condition, $\sigma\gamma_0\tau_3 < \tau_1\tau_S\lambda_M$, que nous supposons satisfaite, il existe une valeur critique d_m telle que pour $d < d_m$, le modèle admet deux autres états homogènes positifs, notés respectivement $\mathbf{V}_u$ et $\mathbf{V}_s$. En l'absence des mouvements spatiaux, le point $\mathbf{V}_s$ est stable tandis que le point $\mathbf{V}_u$ est instable. Lorsque $d > d_m$, il n'existe aucun point d'équilibre positif.

Problématique

L'idée de ce travail est d'étendre les recherches précédentes en étudiant ce modèle avec, cette fois-ci, la composante spatiale. Notre objectif est de répondre à la question centrale suivante :

Pouvons-nous obtenir des motifs spatiaux stationnaires ? Sous quelles conditions ?

Une fois ces questions traitées, nous analyserons les caractéristiques de ces motifs en fonction des paramètres du modèle, telles que leur forme ou leur nombre de plaques.

Résultats

• **Chapitre 6 : Spatial pattern analysis of a Aβ-monomer model with inflammation processes for Alzheimer's disease.**

Ce travail, réalisé en collaboration avec Nicolas Torres Escorza, Julien Blohm et Laurent Pujo-Menjouet, fait l'objet d'une prépublication.

Méthodes. Dans cet article, nous avons effectué une analyse linéaire pour les deux points d'équilibre stables, selon les termes de réaction. Nous montrons que le point d'équilibre $\mathbf{V}_0$ ne peut pas être déstabilisé par l'ajout de la diffusion et de la chimiotaxie, et qu'il est donc stable face aux perturbations spatialement hétérogènes. En revanche, le point d'équilibre positif $\mathbf{V}_s$ peut être, lui, déstabilisé pour un α suffisamment grand. Le seuil critique, noté α_c, correspond au zéro d'une fonction que nous avons calculée explicitement.

A l'aide de simulations numériques, nous constatons que, même à proximité de la valeur critique α_c, les motifs stationnaires généralement sélectionnés sont fortement non-linéaires. Pour étudier ces motifs complexes, nous utilisons le package Matlab `pde2path` [104, 106, 105] pour réaliser un diagramme de bifurcation complet de notre modèle. Pour détecter les branches de motifs loin de l'équilibre, nous poursuivons les branches bifurcantes de l'état stationnaire $\mathbf{V}_s$ ainsi que toutes les sous-branches qui en émanent. Étant donné que chaque branche peut générer de nouvelles bifurcations, nous décidons d'arrêter la continuation lorsque toutes les branches stables importantes nous semblent être trouvées. Pour identifier ces branches stables, nous effectuons de nombreuses simulations numériques pour différentes valeurs de paramètres, en les initialisant à l'état homogène $\mathbf{V}_s$ légèrement bruité. Une fois les résultats obtenus, nous recensons et classifions automatiquement les différents motifs. Selon nos

simulations numériques, pour les domaines étudiés, tous les motifs sélectionnés correspondent bien à des branches stables poursuivies dans notre diagramme de bifurcation.

La mise en œuvre simultanée de ces deux méthodes nous permet d'estimer la *sélectivité* de nos branches stables. Certaines branches, dans un certain sens, sont plus stables que d'autres. Ici, dans le contexte des équations à dérivées partielles, la notion de bassin d'attraction est plus difficile à définir et à mesurer. Cette notion de sélectivité dépend fortement des conditions initiales. Nous constatons que de très légères fluctuations de la donnée initiale, de l'ordre de 10^{-5}, suffisent à changer de bassin d'attraction. Nous remarquons également la présence de branches stables de motifs que nous ne sélectionnons jamais avec notre choix de conditions initiales.

Résultats principaux. Dans le régime bistable ($d < d_m$), selon notre diagramme de bifurcation nous obtenons bien une bifurcation de Turing à la localisation prédite par l'analyse linéaire. La branche de motifs créée, associée aux motifs de faible amplitude, perd rapidement sa stabilité, voire est directement instable. De plus, comme l'illustrent nos diagrammes de bifurcation, des branches de motifs de forte amplitude coexistent dans ces régimes de valeurs de paramètre ($\alpha \approx \alpha_c$). En pratique, pour les paramètres que nous avons étudiés, il est très difficile de sélectionner des motifs de faible amplitude. Nous nous concentrons ainsi sur les motifs loin de l'équilibre.

A la suite d'une analyse linéaire, même si l'étude est purement locale, nous prédisons généralement que pour $\alpha > \alpha_c$, la solution doit converger vers des motifs spatialement hétérogènes. Cependant, nos résultats montrent que ce n'est pas toujours le cas. Dans notre modèle, il est important de noter que le point d'équilibre $\mathbf{V}_0$ est toujours stable. Par conséquent, il y a une compétition entre $\mathbf{V}_0$ et $\mathbf{V}_s$ lorsque $\alpha < \alpha_c$, et une compétition entre $\mathbf{V}_0$ et les branches de motifs stables lorsque $\alpha > \alpha_c$. Il n'est donc pas surprenant d'obtenir des simulations numériques convergeant vers l'état d'équilibre $\mathbf{V}_0$ homogène en espace.

La probabilité de convergence vers $\mathbf{V}_0$ dépend fortement de la valeur de α : plus la valeur de α augmente, plus cette probabilité devient élevée. De plus, nos simulations numériques montrent qu'à partir d'un certain seuil, noté α_0, aucune branche de motif n'est stable. Dans cette situation, les solutions numériques convergent toujours vers l'état d'équilibre $\mathbf{V}_0$. Cette question a également été traitée dans le même temps que nos travaux par Krause et al. dans l'article [8]. Dans ce travail, les auteurs, à travers de nombreux exemples de modèles, montrent à l'aide de simulations numériques que la multi-stabilité des états homogènes peut altérer la prédiction de l'analyse linéaire. En effet, ils observent que, comme pour notre modèle, la solution peut converger vers un état homogène stable, même si les valeurs des paramètres sont dans l'espace de Turing.

En plus de montrer que toutes les branches perdent, un moment, leur stabilité, nous constatons que cette perte de stabilité dépend du motif associé à chaque branche. En effet, près du seuil α_c, nous observons une forte multi-stabilité de plusieurs branches de motifs, chacune associée à différents nombres de pics. Lorsque α croît, les branches perdent progressivement leur stabilité, et cela selon un ordre décroissant de leur nombre de pics. Les résultats des simulations numériques corroborent cette observation : plus α augmente, plus le nombre moyen de pics semble décroître. Concernant cette fonction théorique du nombre moyen de pics, nous nous attendons à une fonction décroissante, possiblement discontinue par morceaux, avec des discontinuités correspondant aux pertes de stabilités

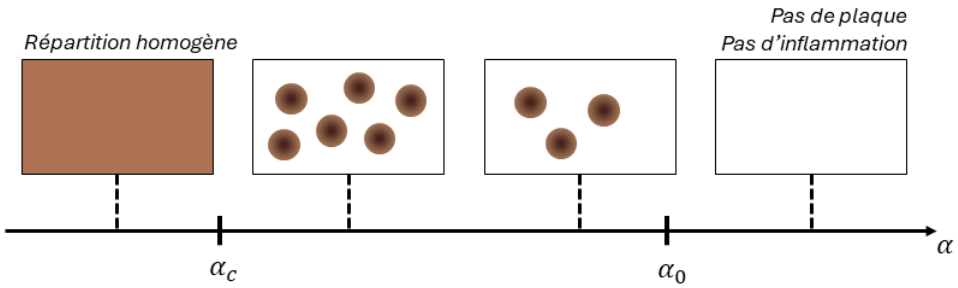

FIGURE V.1 – **Illustration de la dynamque des plaques amyloïdes en fonction du coefficient de chimiotaxie α.**

soudaines des branches.

Cette caractérisation poussée du comportement des plaques amyloïdes et de l'inflammation nous permet d'obtenir des résultats intéressants de modélisation. Selon nos résultats, si le coefficient de sensibilité des cellules migrogliales vers les oligomères, α, est suffisamment élevé, nous prédisons l'absence d'inflammation et de plaques. De manière plus générale, plus ce coefficient augmente, plus les plaques se raréfient, réduisant peu à peu les zones de forte inflammation, jusqu'à, un moment donné, disparaître totalement. Grâce à nos méthodes, nous étendons les résultats précédents de l'article [274], qui visaient à identifier un seuil critique sur les conditions initiales permettant de déterminer la persistance ou non des plaques, mais uniquement pour le modèle sans espace.

La dynamique des motifs en fonction du paramètre α, décrite ci-dessus, est résumée dans la figure V.1. Les valeurs des seuils critiques dépendent des paramètres du système. Nous déterminons notamment l'effet du paramètre d représentant la dégradation des monomères.

6 Spatial pattern analysis of a Aβ-monomer model with inflammation processes for Alzheimer's disease.

This chapter corresponds to a preprint written in collaboration with Nicolas Torres Escorza, Julien Blohm, and Laurent Pujo-Menjouet.

6.1 Introduction

Alzheimer's disease (AD) is a progressive neurodegenerative disorder that affects memory, thinking, and behavior. The pathogenesis of AD is multifactorial and involves several risk factors such as age, genetics, head injuries, vascular diseases, infections, and environment. One of the main hypotheses proposed to explain the disease's pathogenesis is the misfolding and aggregation of amyloid β-proteins in the nervous system.

Amyloid-beta (Aβ) is a peptide that forms the primary component of the amyloid plaques found in the brains of Alzheimer's disease patients (see figure 6.1). Aβ peptides are intrinsically disordered in their monomeric form and assemble into stable structures such as oligomers and fibrils via a nucleation-dependent pathway. Many studies point to a key role for these Aβ-aggregates in neurotoxicity, leading to progressive, irreversible neuronal damage (see, for example, [265, 266, 267, 268, 269]). Understanding the role of Aβ aggregates and the mechanisms of their formation and degradation could provide valuable insights into the pathogenesis of Alzheimer's disease and potential therapeutic strategies.

Neurons produce Aβ-monomers that almost instantaneously start to polymerize into proto-oligomers. In this aggregation process, proto-oligomers can polymerize or depolymerize, and once they reach a critical size, they become stable in the form of Aβ-oligomers. These latter are assumed to be completely stable in the sense that neither polymerization nor depolymerization is possible for Aβ-oligomers in equilibrium [270, 271]. This mechanism involving Aβ-oligomers is known as the amyloid cascade hypothesis, and there is a consensus that it is a key factor in AD progression.

The role of microglia, the primary immune cells in the brain, in the progression of Alzheimer's disease is also significant. They induce an inflammatory reaction through a chemical cascade in microglial cells, releasing interleukins [272, 273, 275, 276]. These interleukins then activate an increase in Aβ-monomer production from neurons. However, if the concentration of Aβ-oligomers is high en-

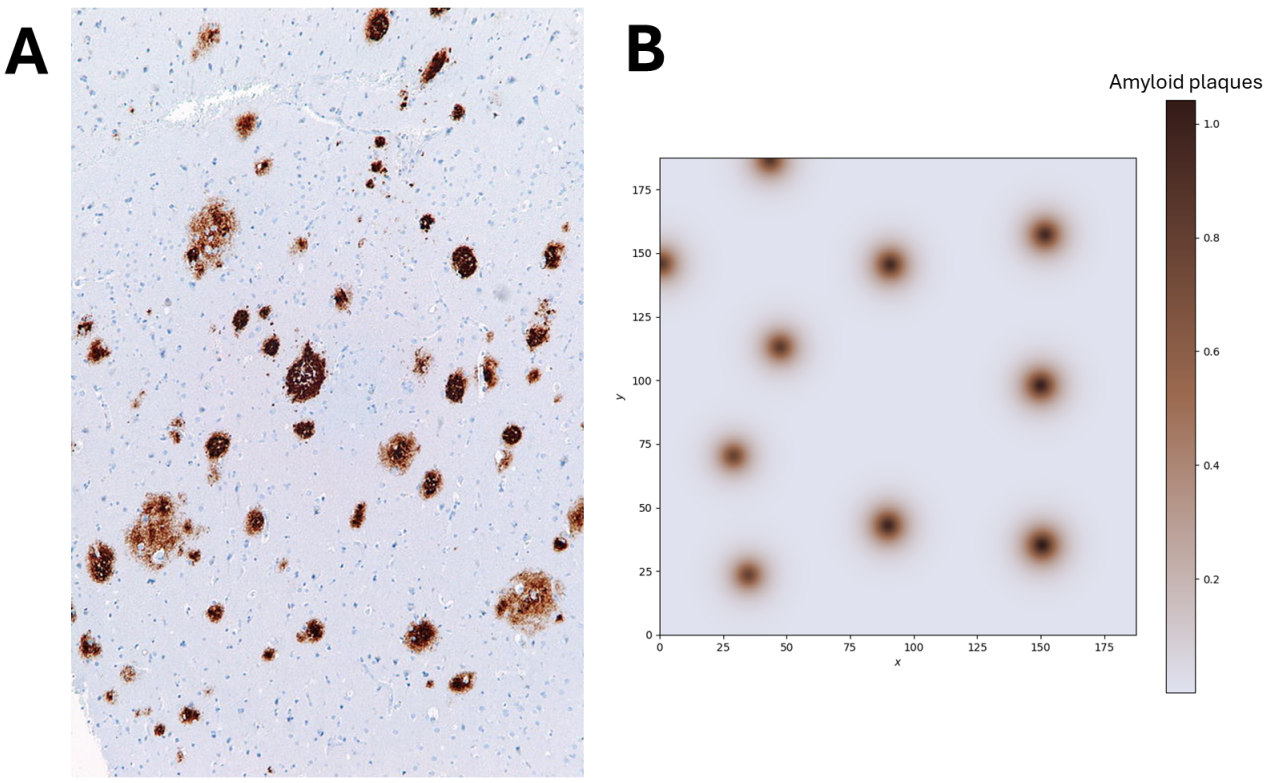

FIGURE 6.1 – **A.** A picture of Aβ amyloid plaques in the brain.[1] **B.** Stationary patterns of our mathematical model.

ough, a stress reaction called the unfolded protein response (UPR) [268] is triggered, which leads to a decrease in Aβ-monomer production. At the same time, the remaining oligomers diffuse into the neuronal environment. In this context, two opposing mechanisms of stimulation and inhibition determine whether AD persists. Moreover, microglial cells also play a role in the transfer of oligomers to amyloid plaques, where these oligomers become inert elements (no diffusion, polymerization, or de-polymerization) [277, 278, 279].

From a mathematical point of view, previous works on partial differential equations on AD include the works of Andrade *et al.* [280] on a space-dependent model for the polymerization of Aβ-proteins, Ciuperca *et al.* [281] which takes into account the formation of Aβ-oligomers and fibrils through a continuous size model based on Lifshitz–Slyozov equations and Hao *et al.* [282] on a multi-component model taking into account astrocytes, microglia cells and peripheral cell population, besides the Aβ-oligomers (for other works on reaction-diffusion models see also [283, 284, 285]).

In this article, we study the bi-monomeric model introduced in the work of [274], which is given by the following reaction-diffusion system in a bounded domain Ω,

1. Source : Copyright © 2011 Michael Bonert, MD, FRCPC (https://commons.wikimedia.org/wiki/User:Nephron, https://experts.mcmaster.ca/display/bonertm). You are free to share and adapt this image as per the CC BY-SA 3.0 (https://creativecommons.org/licenses/by-sa/3.0/legalcode).

$$\begin{cases} \dfrac{\partial u}{\partial t} &= \nu_2 \Delta u + r_1 m^2 - \gamma_0 u, \\ \dfrac{\partial u_p}{\partial t} &= \gamma_0 u - \tau_p u_p, \\ \dfrac{\partial m}{\partial t} &= \nu_1 \Delta m + \dfrac{\tau_S}{1+Cu^n} I - dm - r_2 um - r_1 m^2, \\ \dfrac{\partial M}{\partial t} &= D_1 \Delta M - \alpha \nabla \cdot [M \nabla u] + \dfrac{\alpha_1 u}{1+\alpha_2 u}(\hat{M} - M)M - \sigma M + \lambda_M, \\ \dfrac{\partial I}{\partial t} &= D_I \Delta I + \dfrac{\tau_1 u}{1+\tau_2 u} M - \tau_3 I. \end{cases} \tag{6.1}$$

The term u corresponds to the concentration of the oligomers, while the term m represents the concentration of the monomers. In this model, we simplify the assumption that oligomers correspond to the aggregate of two monomers, as in [274]. The term u_p corresponds to the concentration of oligomers in amyloid plaques and is the main focus of our study. Finally, the terms M and I correspond to the concentration of microglial cells and interleukins respectively.

To simplify notation, we define the vector $\mathbf{V}(x,t)$ as follows

$$\mathbf{V}(t,x) = (u(t,x), u_p(t,x), m(t,x), M(t,x), I(t,x)) .$$

We study this problem in the one-dimensional case, *i.e.* $\Omega = [0, L]$, and also in the two-dimensional case, *i.e.* $\Omega = [0, L] \times [0, L]$, where $L > 0$ represents the size of the domain. Concerning the boundary conditions, we assume Neumann boundary conditions, *i.e.*

$$\partial_{\mathbf{n}} \mathbf{V}(y) = 0, \quad \text{for all } y \in \partial\Omega, \text{ where } \mathbf{n} \text{ denotes the normal to the boundary } \partial\Omega.$$

In the article [274], the authors studied the spatially homogeneous steady states of the model (6.1). In particular, the point $(0, 0, 0, \lambda_M/\sigma, 0)$ is always an equilibrium point for the model (6.1), corresponding to the disease-free equilibrium, which we denote as $\tilde{0}$. Moreover, when the following condition is satisfied

$$\sigma\gamma_0\tau_3 < \tau_1\tau_S\lambda_M, \tag{6.2}$$

there is a critical threshold for the monomer degradation, denoted d_m, so that for $d < d_m$ the model (6.1) admits two other positive spatially-homogeneous steady states, denoted $\mathbf{V}_u$ and $\mathbf{V}_s$. In the absence of chemotaxis and diffusion, the first positive equilibrium $\mathbf{V}_u$ is unstable and the second one $\mathbf{V}_s$ is stable.

In this article, we focus on the emergence of spatially periodic patterns corresponding biologically to the emergence of amyloid plaques. To achieve this goal, we study the possible instability of the positive equilibrium $\mathbf{V}_s$ when the chemotaxis parameter α is strictly positive. First, we use a linear analysis to study the impact of the chemotaxis parameter on the stability of the equilibria in our problem. In particular, we prove in section 6.2 that the disease-free equilibrium is linearly asymptotically stable. Conversely, the positive equilibrium $\mathbf{V}_s$ becomes unstable when the chemotaxis parameter is large enough. Secondly, we use numerical simulations to study the spatial patterns of the model (6.1). These patterns correspond to successions of zones of high and low oligomers concentration in the plaques.

We focus on the bistable regime of the model (6.1). Even if the analysis of the patterns of bistable systems is less studied, this type of numerical analysis has already been carried out for several bistable reaction-diffusion systems, notably for predatory prey systems or for systems describing chemical processes (see for example [286, 287, 288, 289]).

In the bistable regime, stable pattern branches compete with the stable homogeneous state. Therefore, it is not surprising to observe a convergence towards the stable equilibrium point. In the article by Krause *et al.* [8], the authors prove, through numerous examples, that multistability can significantly alter the predictions made by linear analysis. Indeed, they observe that the solution may converge towards a stable homogeneous state, even though the parameter values within the Turing space suggest the emergence of patterns. This phenomenon is also illustrated in [290], where Al-Karkhi *et al.* study the patterns of a predator-prey model with multiple stable homogeneous equilibria without diffusion. By conducting a bifurcation diagram, they show that the pattern branches can all lose their stability, thus explaining the absence of convergence towards a spatially heterogeneous pattern. In this article, we also observe and numerically analyze this phenomenon.

In the one-dimensional case, we find several possible scenarios : low-amplitude or high-amplitude stationary patterns, time-oscillating patterns, and convergence to the disease-free equilibrium. In the two-dimensional case, numerical simulations revealed the following phenomena : the emergence of stripe patterns, dots, complex stationary patterns between stripes and dots, and convergence to the disease-free equilibrium.

To study the existence and stability of these different possible patterns, we perform several bifurcation diagrams for the chemotaxis parameter α, using the package `pde2path` [104, 105]. We notice a difference between these bifurcation diagrams and the typical ones, which are generally obtained for a monostable reaction-diffusion system. Generally, close enough to the Turing bifurcation, the only stable pattern is the one associated with the admissible critical frequency. Then moving away from this bifurcation, several other frequencies gradually become admissible and thus several stable branches emerge and coexist. In general, linear analysis shows that close to the Turing bifurcation, only a single mode can be destabilized, thereby predicting a stationary pattern with a spatial period corresponding to the critical frequency. Moving further away from this bifurcation, the study of the dispersion relation shows that several other modes progressively become admissible, and thus, several stable branches associated with these modes emerge and coexist. For our model (6.1), we notice an inverse trend : initially, several branches of stable patterns coexist, and the further we move away from the critical Turing threshold, the more the branches lose their stability, to the point where they all lose their stability. The result predicted by our numerical simulations is presented in the following conjecture :

Conjecture 5 (Selection of disease-free equilibrium for α large enough):
We assume that the condition (6.2) *is satisfied.*
Then there exists $\alpha_0 > 0$ *such that for all* $\alpha > \alpha_0$,

$$\lim_{t\to\infty} \mathbf{V}(x,t) \to \tilde{0}, \text{ uniformly for all } x \in \Omega.$$

From a modeling point of view, this means counterintuitively that when the chemotaxis coefficient is large enough the system converges to the disease-free equilibrium without any amyloid plaques or inflammation.

In the case where $d > d_m$, the disease-free equilibrium is the only stable steady state and it is a global attractor for all initial data. Therefore, the value of α does not influence the selection of the final stationary state and we have $\alpha_0 = 0$. In the case where $d \leq d_m$, the spatially homogeneous states have bistable dynamics and there is a critical threshold α_c for which the equilibrium $\mathbf{V}_s^\star$ loses its stability. We observe numerically that there exists a $\alpha_0 \geq \alpha_c$ such that for $\alpha > \alpha_0$ the solution converges, independently of the slight noise, to the disease-free equilibrium. This threshold α_0 depends on the values of the rest of the parameters in the model but also depends on the size of the domain Ω. In particular, we also note that $\alpha_0 \to \alpha_c$ when $d \to d_m$.

Therefore, in the context of modeling, the parameter d, representing the natural degradation rate of monomers, is a reliable indicator of disease progression. When this parameter is sufficiently large ($d > d_m$), natural degradation is sufficient to prevent the formation of amyloid plaques. In this case, the individual can be considered healthy or in a pre-symptomatic stage where the disease has not yet manifested. Conversely, when natural degradation is insufficient ($d < d_m$), plaque formation becomes possible, with a probability that depends on its value : the lower the value of d, the wider the range of parameter values for which plaques form and persist.

Our numerical simulations reveal that the stability range of pattern branches seems to be correlated with the frequencies of these patterns. For the examples given, we notice that the greater the number of peaks in a pattern, the faster its associated branch tends to lose stability as α increases. Based on these numerical results, we propose the following conjecture :

Conjecture 6 (Decrease in the average number of amyloid plaques when α increases):
We assume that the condition (6.2) *is satisfied. Let* $\mathbf{V}_0$ *be an initial data corresponding to a slight Gaussian noise from the positive equilibrium* $\mathbf{V}_s$.
We assume that $\alpha > \alpha_c$, *we denote* $\#\max(\alpha)$ *the number of local maxima of the final stationary solution of the system* (6.1), *with* $\#\max$ *defined as 0 in the spatially homogeneous case. The average of* $\#\max(\alpha)$ *over several independent realizations for different noisy initial conditions is denoted with some abuse of notation* $\mathbb{E}\#\max(\alpha)$. *In this setting, we find the following property :*

$$\text{the function } \mathbb{E}\#\max(\alpha) \text{ is non-increasing with respect to } \alpha.$$

From a modeling perspective, this implies that as the chemotaxis coefficient increases, the number of amyloid plaques decreases.

The plan of the paper is the following : in Section 2, we begin with a linear analysis of the model (6.1) to obtain the conditions for pattern emergence, and in Section 3 we numerically study the stationary patterns generated by the model (6.1) in the one-dimensional case and the two-dimensional case.

6.2 Stability Analysis

6.2.1 Linear stability analysis of the disease-free equilibrium

We start by studying the stability of the disease-free equilibrium. The linearization around this steady state can be rewritten in a system of the form

$$\frac{\partial \tilde{\omega}}{\partial t} = D\Delta\tilde{\omega} + J\tilde{\omega}, \tag{6.3}$$

where $\tilde{\omega} = (\tilde{u}, \tilde{u}_p, \tilde{m}, \tilde{M}, \tilde{I})^\top$ is a vector for a small perturbation of the steady state $(0, 0, 0, \frac{\lambda}{\sigma}, 0)$ with Neumann boundary conditions and

$$D = \begin{pmatrix} \nu_2 & 0 & 0 & 0 & 0 \\ 0 & 0 & 0 & 0 & 0 \\ 0 & 0 & \nu_1 & 0 & 0 \\ -\alpha\frac{\lambda}{\sigma} & 0 & 0 & D_1 & 0 \\ 0 & 0 & 0 & 0 & D_I \end{pmatrix}, \; J = \begin{pmatrix} -\gamma_0 & 0 & 0 & 0 & 0 \\ \gamma_0 & -\tau_p & 0 & 0 & 0 \\ 0 & 0 & -d & 0 & \tau_S \\ \left(\hat{M} - \frac{\lambda}{\sigma}\right)\frac{\lambda}{\sigma} & 0 & 0 & -\sigma & 0 \\ \tau_1\frac{\lambda}{\sigma} & 0 & 0 & 0 & -\tau_3 \end{pmatrix}.$$

In this setting, the corresponding eigenvalue problem is given by

$$\lambda\tilde{\omega} = D\Delta\tilde{\omega} + J\tilde{\omega}. \tag{6.4}$$

Concerning the stability, we have the following result.

Proposition 3 (Disease-free equilibrium is asymptotically-stable):
The eigenvalue problem (6.4) has a countable set of eigenvalues that are all strictly negative. Therefore the disease-free equilibrium of the system (6.1) is linearly asymptotically stable.

Proof: *Consider the following eigenvalue problem*

$$\begin{aligned} \Delta\varphi &= \lambda\varphi \quad in\, \Omega, \\ \nabla\varphi \cdot \hat{n} &= 0 \quad on\, \partial\Omega, \end{aligned} \tag{6.5}$$

which has a set of eigenvalues $\{\lambda_k\}_{k\in\mathbb{N}}$ with $\lambda_k \leq 0$ and $\lambda_k \to -\infty$ when $k \to \infty$. Let φ_k be the corresponding eigenfunction.

We prove that the eigenvalues of problem (6.4) are strictly negative.

From Equation (6.5)*, we deduce that the solution of the first equation of the eigenvalue problem* (6.4) *given by*

$$\begin{aligned} \Delta\varphi &= \lambda\varphi \quad in\,\Omega, \\ \nabla\varphi\cdot\hat{n} &= 0 \quad on\,\partial\Omega, \end{aligned} \tag{6.6}$$

is of the form $\tilde{u}=\varphi_k$ *with* $\lambda=\nu_2\lambda_k-\gamma_0<0$ *and thus the system* (6.4) *has a solution for the corresponding eigenvector (take for instance* $(\varphi_k,0,0,0,0)^\top$*).*

Assume now that $\lambda\neq\nu_2\lambda_k-\gamma_0$*. From the theory of elliptic operators [291], we get that* $\tilde{u}\equiv 0$ *and the system* (6.4) *is reduced as follows*

$$\begin{cases} (\lambda+\tau_p)\tilde{u}_p=0, \\ \nu_1\Delta\tilde{m}=(\lambda+d)\tilde{m}-\tau_S\tilde{I}, \\ D_1\Delta\tilde{M}=(\lambda+\sigma)\tilde{M}, \\ D_I\Delta\tilde{I}=(\lambda+\tau_3)\tilde{I}. \end{cases} \tag{6.7}$$

By applying the same argument used for $\tilde{u}$ *to rest of components of* $\tilde{\omega}$ *(first for* $\tilde{u}_p$*,* $\tilde{M}$*,* $\tilde{I}$ *and then for* $\tilde{m}$*), we conclude that set of eigenvalues* $\mathcal{E}$ *is given by*

$$\mathcal{E}=\{-\tau_p\}\cup\bigcup_{k\in\mathbb{N}}\{\nu_1\lambda_k-d,\nu_2\lambda_k-\gamma_0,D_1\lambda_k-\sigma,D_I\lambda_k-\tau_3\}\subset(-\infty,0).$$

This proves the desired result. From the theory of elliptic equations [291], we remark that the spectrum of the linear operator determined by the system (6.4) *consists only of eigenvalues.*

□

6.2.2 Linear stability analysis of the positive equilibrium $\mathbf{V}_s$

The corresponding linearization around the point $\mathbf{V}_s$ gives the following equation

$$\frac{\partial\tilde{\omega}}{\partial t}=D\Delta\tilde{\omega}+J\tilde{\omega}, \tag{6.8}$$

where $\tilde{\omega}=(\tilde{u},\tilde{u}_p,\tilde{m},\tilde{M},\tilde{I})^\top$ is a vector that corresponds to a small perturbation of the equilibrium $\mathbf{V}_s$ with

$$D=\begin{pmatrix} \nu_2 & 0 & 0 & 0 & 0 \\ 0 & 0 & 0 & 0 & 0 \\ 0 & 0 & \nu_1 & 0 & 0 \\ -\alpha M_0 & 0 & 0 & D_1 & 0 \\ 0 & 0 & 0 & 0 & D_I \end{pmatrix},$$

and, $J=\begin{pmatrix} -\gamma_0 & 0 & 2r_1m_0 & 0 & 0 \\ \gamma_0 & -\tau_p & 0 & 0 & 0 \\ -r_2m_0-I_0\tau_S\dfrac{nCu_0^{n-1}}{(1+Cu_0^n)^2} & 0 & -d-r_2u_0-2r_1m_0 & 0 & \dfrac{\tau_S}{1+Cu_0^n} \\ (\hat{M}-M_0)M_0\dfrac{\alpha_1}{(1+\alpha_2u_0)^2} & 0 & 0 & \dfrac{\alpha_1u_0}{1+\alpha_2u_0}(\hat{M}-2M_0)-\sigma & 0 \\ M_0\dfrac{\tau_1}{(1+\tau_2u_0)^2} & 0 & 0 & \dfrac{\tau_1u_0}{1+\tau_2u_0} & -\tau_3 \end{pmatrix}$.

The solution of (6.8) with the form $\tilde{\omega} = e^{ikx+\lambda t}$ leads to the following equation,

$$\lambda\tilde{\omega} = (J - k^2 D)\tilde{\omega}, \tag{6.9}$$

where $\lambda \in \mathbb{C}$ is the eigenvalue and $k \in \mathbb{R}$ corresponds to the wavenumber. We denote P_{J-k^2D}, the characteristic polynomial associated with the problem (6.9). We obtain the following factorization, $P_{J-k^2D}(\lambda) = (-\tau_p - \lambda)Q_{J-k^2D}(\lambda)$. From this, we derive the first eigenvalue of the problem, equals to $\lambda_0 = -\tau_p < 0$ and the polynomial Q_{J-k^2D} is given by the following relation

$$Q_{J-k^2D}(\lambda) = \lambda^4 + a_1\lambda^3 + a_2\lambda^2 + a_3\lambda + a_4,$$

with

$$\begin{cases} a_1 = & A + F + I + P, \\ a_2 = & -BE + A(F + I + P) + F(I + P) + IP, \\ a_3 = & -BGW + BE(I + P) - AFI - AFP - AIP - FIP, \\ a_4 = & AFIP - BEIP + BGIW - BGKH(\alpha), \end{cases}$$

and where the constants are given by

$$A = -\gamma_0 - k^2\nu_2, \qquad B = 2r_1 m_0, \qquad E = -r_2 m_0 - I_0\tau_S \frac{nCu_0^{n-1}}{(1 + Cu_0^n)^2}, \qquad F = -d - r_2 u_0 - 2r_1 m_0 - k^2\nu_1,$$

$$G = \frac{\tau_S}{1 + Cu_0^n}, \qquad H(\alpha) = (\hat{M} - M_0)M_0 \frac{\alpha_1}{(1 + \alpha_2 u_0)^2} + \alpha M_0 k^2, \qquad I = \frac{\alpha_1 u_0}{1 + \alpha_2 u_0}(\hat{M} - 2M_0) - \sigma - k^2 D_1,$$

$$K = \frac{\tau_1 u_0}{1 + \tau_2 u_0}, \qquad P = -\tau_3 - k^2 D_I, \qquad W = M_0 \frac{\tau_1}{(1 + \tau_2 u_0)^2}.$$

To study Turing bifurcation we first prove the following lemma.

Proposition 4:
Assume that there is a Turing bifurcation. Then the positive equilibrium $\mathbf{V}_s$ *becomes unstable when* $\det(J - k^2 D) > 0$ *holds for at least one* $k > 0$ *and it remains stable when* $\det(J - k^2 D) < 0$ *holds for all* $k \geq 0$.

Proof: *Using the Routh-Hurwitz criterion, we state that all eigenvalues have strictly negative real parts if and only if these five conditions hold*

$$a_i > 0 \text{ for all } i \in \{1, 2, 3, 4\} \text{ and } a_1 a_2 a_3 > a_3^2 + a_1^2 a_4.$$

We assume that $(\lambda_i)_{i\in\{1,2,3,4\}}$ *represent the roots of the characteristic equation and accordingly to the characteristic equation, we obtain*

$$-a_1 = \lambda_1 + \lambda_2 + \lambda_3 + \lambda_4, \qquad a_2 = \lambda_1\lambda_2 + \lambda_1\lambda_3 + \lambda_1\lambda_4 + \lambda_2\lambda_3 + \lambda_2\lambda_4 + \lambda_3\lambda_4,$$

$$-a_3 = \lambda_1\lambda_2\lambda_3 + \lambda_1\lambda_2\lambda_4 + \lambda_1\lambda_3\lambda_4 + \lambda_2\lambda_3\lambda_4, \qquad a_4 = \lambda_1\lambda_2\lambda_3\lambda_4.$$

Turing instability emerges when the real part of one eigenvalue passes through zero and the remaining eigenvalues have negative real parts. We denote k_c as the critical wavenumber. Thus, at this critical wavenumber $k = k_c$ we can assume without any loss of generality that $\lambda_1(k_c) = 0$ and $\lambda_2, \lambda_3, \lambda_4 < 0$.

Under this assumption, it follows that $a_1(k_c) > 0$, $a_2(k_c) > 0$, $a_3(k_c) > 0$ and $a_1(k_c)a_2(k_c) > a_3(k_c)$. However, for $k = k_c$, we obtain $a_4(k_c) = 0$. Thus, if there is a Turing bifurcation, that comes from the nullity of the term a_4 which also corresponds to the nullity of the determinant of the matrix $J - k^2 D$. □

The condition $a_4 < 0$ is equivalent to the following inequality

$$\alpha > \frac{AFIP - BEIP + BGIW}{BGKM_0k^2} - \frac{(\hat{M} - M_0)\frac{\alpha_1}{(1+\alpha_2 u_0)^2}}{k^2}, \tag{6.10}$$

by positivity of terms B, G, K and M_0. Therefore, a spatial pattern appears on a discrete domain and for a large enough chemotaxis parameter.

The term a_4 can be rewritten as a polynomial function of degree 4 in terms of k^2,

$$a_4(k^2) = b_1\,(k^2)^4 + b_2\,(k^2)^3 + b_3\,(k^2)^2 + b_4(\alpha)\,k^2 + b_5,$$

with functions b_i, $i = 1, 2, 3, 4$, which have cumbersome expressions not reported in this work. We determine k_{min} the frequency for which the a_4 function reaches its minimum. This term depends on the system parameters, particularly the chemotaxis parameter α. The critical frequency k_c is given by $a_4(k_c) = \min_{k'} a_4(k') = 0$. Thus, Turing bifurcation can occur at the critical value α_c, defined by a root of the function

$$\alpha \longmapsto b_1\,(k^2_{\min}(\alpha))^4 + b_2\,(k^2_{\min}(\alpha))^3 + b_3\,(k^2_{\min}(\alpha))^2 + b_4(\alpha)\,k^2_{\min}(\alpha) + b_5. \tag{6.11}$$

We compute this root using numerical tools. The results of these calculations are consistent with the numerical simulations and bifurcation diagrams performed in the next section.

6.3 Pattern analysis

In this section, we use numerical tools to study the patterns induced by the loss of stability of the equilibrium $\mathbf{V}_s$. The parameter values used in these simulations are similar to those presented in the article [274], whose orders of magnitude respect biological laws. These parameter values are given in Table 6.1. In this study, we only investigate the influence of the following variable parameters : chemotaxis coefficient, α, and monomer degradation, d. First, we work on the domain $\Omega = [0, L]$ and then we perform a numerical study of the patterns for the two-dimensional square domain, $\Omega = [0, L] \times [0, L]$, $L > 0$.

The initial conditions chosen for our numerical simulations play a crucial role in pattern selection. Moreover, adding noise in these initial conditions is necessary for consistent modeling. Throughout this article, except for the Section 6.3.4, we choose a weak perturbation of the positive equilibrium state $\mathbf{V}_s$, described in the remark below.

Remark 1 (Choice of the noisy initial condition):

- *For a one-dimensional domain, we discretize the space into the points* $(x_i)_{i\in I}$ *and for each grid point we add a slight Gaussian noise,*

$$\mathbf{V}_0(x_i) = \mathbf{V}_s + \epsilon\mathcal{N}^i,$$

where $\mathcal{N}^i$ *corresponds to a Gaussian vector of dimension 5 and* ϵ *corresponds to a positive constant (e.g.* $\epsilon = 10^{-5}$*) small enough to preserve positivity.*

- *For the two-dimensional domain, we use the same initial conditions, but this time on the* $(x_i, y_j)_{i\in I,\, j\in J}$ *grid.*

TABLE 6.1 – **Parameter values for the numerical simulations of the system** (6.1)**.**

Parameter	Value	Units	Description
r_1	10^{-1}	$L\,(\text{mol})^{-1}(\text{months})^{-1}$	Bi-monomeric polymerization rate
r_2	10^{-1}	$L\,(\text{mol})^{-1}(\text{months})^{-1}$	Polymerization rate of monomers attaching to oligomers
d	Variable	$(\text{month})^{-1}$	Degradation rate of monomers
γ_0	5×10^{-2}	$(\text{month})^{-1}$	Recruitment rate of oligomers to the amyloid plaques
τ_1	1	$L\,(\text{mol})^{-1}(\text{months})^{-1}$	Production coefficient of interleukins interacting with oligomers
τ_2	1	$L\,(\text{mol})^{-1}$	Production coefficient of interleukins interacting with oligomers
τ_3	1	$(\text{months})^{-1}$	Degradation rate of interleukins
τ_p	3×10^{-2}	$(\text{months})^{-1}$	Degradation rate of oligomers in the amyloid plaques
τ_S	1	$(\text{months})^{-1}$	Coefficient of neural stress
C	1	$L^n\,(\text{mol})^{-n}$	Coefficient of neural stress function
n	2	-	Power coefficient of neural stress function
α_1	1	$L^2\,(\text{mol})^{-2}(\text{months})^{-1}$	Proliferation coefficient of microglial cells interacting with oligomers
α_2	1	$L\,(\text{mol})^{-1}$	Proliferation coefficient of microglial cells interacting with oligomers
λ_M	10^{-3}	$\text{mol}\,L^{-1}(\text{months})^{-1}$	Source term of microglial cells
$\hat{M}$	1	$\text{mol}\,L^{-1}$	Carrying capacity of microglial cells
σ	10^{-3}	$(\text{months})^{-1}$	Degradation rate of microglial cells
D_1	1	$m^2\,(\text{months})^{-1}$	Diffusion coefficient of microglial cells
D_I	1	$m^2\,(\text{months})^{-1}$	Diffusion coefficient of interleukins
ν_1	1	$m^2\,(\text{months})^{-1}$	Diffusion coefficient of monomers
ν_2	1	$m^2\,(\text{months})^{-1}$	Diffusion coefficient of oligomers
α	Variable	$m^2\,L\,(\text{mol})^{-1}$	Coefficient of chemotaxis

6.3.1 Numerical simulation in the one-dimensional case

Low and high amplitude patterns

For the one-dimensional domain, we numerically observe the existence of two different stationary pattern profiles. When the Turing bifurcation is supercritical, we notice the presence of *low-amplitude* patterns. In this case, the pattern corresponds to a sinusoidal perturbation of the positive equilibrium state with the critical frequency k_c. The amplitude of this perturbation increases with distance from

the bifurcation. However, the stable branch associated with this pattern rapidly loses its stability. An example of a low-amplitude pattern is shown in figure 6.2 (left). When the bifurcation is subcritical, we notice the emergence of an unstable branch as expected. For our system and the parameter values tested, this branch remains unstable. Note that a weakly nonlinear analysis could be applied to approximate the stationary pattern in the supercritical case. This method can also determine the parameter values for which the bifurcation is sub- or supercritical (see, for example, [9, 10, 13]).

The nonlinear interactions of the system (6.1) can cause the emergence of large amplitude patterns. These correspond to higher peaks, distributed periodically in space, according to a certain frequency which is not the expected one and it is not even necessarily an admissible frequency according to the linear study. In figure 6.2 (right) we represent an example of high amplitude patterns. These high amplitude patterns are similar to biological images of amyloid plaques in the human brain, with the sequence of areas of high concentration and areas with the absence of beta-amyloid proteins. Note that these two types of low and high amplitude patterns can mathematically coexist.

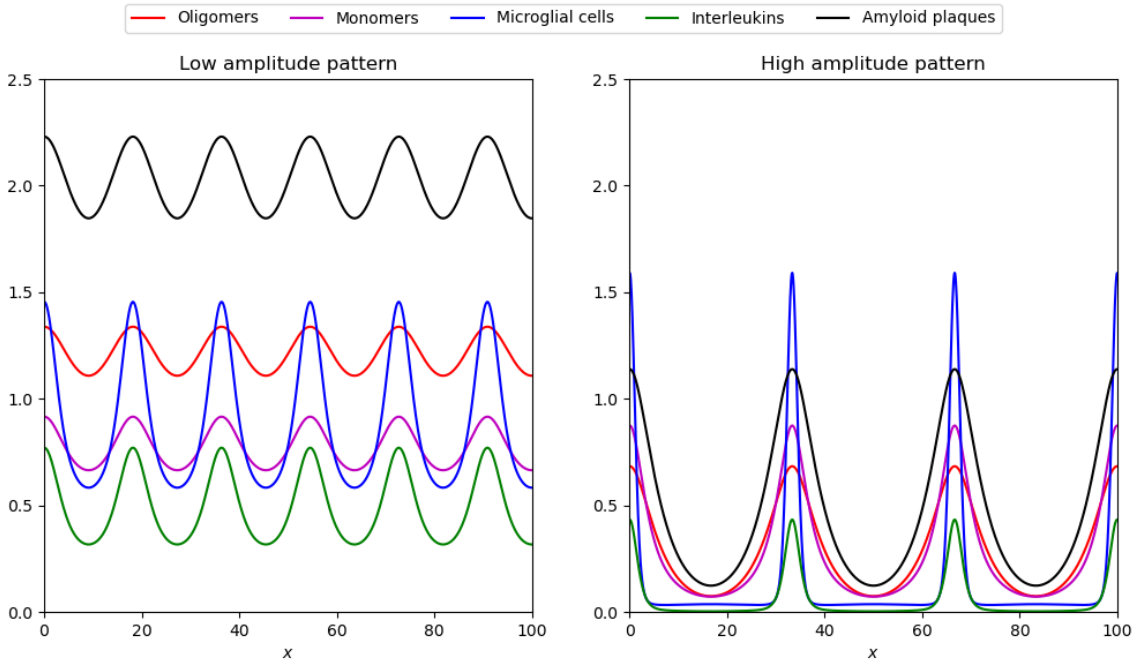

FIGURE 6.2 – **Examples of final stationary patterns of the system** (6.1)**. Left.** Example of a low-amplitude pattern. **Right** Example of a high-amplitude pattern. The concentration of oligomers is shown in red, the concentration of monomers in magenta, the concentration of microglial cells in blue, the concentration of interleukins in green, and the concentration of oligomers in amyloid plaques in black. Parameter values are those given in Table 6.1, with $d = 0.05$ and $\alpha = 21.7$ for the figure on the left and $\alpha = 28$ for the figure on the right.

Time-oscillating patterns

We also notice the presence of heterogeneous patterns in space oscillating in time. Time-oscillating patterns have already been studied for classical reaction-diffusion systems [292, 293], for a prey-predator model [294], with a cross-diffusion term [295, 73, 32] and as well as for bistable reaction-diffusion models [287, 288].

An example of a time-periodic oscillating pattern is shown in figure 6.3A. This figure illustrates the evolution of oligomers concentration in amyloid plaques in space and time. The solution becomes periodic and oscillates between low-amplitude and high-amplitude patterns. In figure 6.3B, we illustrate the phase portrait of the concentration of oligomers at $x = 20$ as a function of the concentration of oligomers in the amyloid plaques. At the same time, we notice the emergence of a limit cycle in agreement with the periodicity in time of the solution. The dots shown in black and red correspond to the phase portrait at time $t = t_1$ and $t = t_2$ respectively and these two-time points are accordingly represented by two vertical lines of the same color in figure 6.3A. In figure 6.3C, we illustrate an example of the high amplitude in the oscillating pattern. This corresponds to the solution shown in figure 6.3A at time $t = t_1$. The solid curve shows the spatial distribution of oligomers concentration in amyloid plaques, while the dotted curve shows the evolution of microglial cell concentration. Finally, we also illustrate a low-amplitude pattern in figure 6.3D, taking a solution at time $t = t_2$. We compare it with the high-amplitude pattern, shown here in red.

Like in other articles (e.g. [295, 292]), we also notice the presence of quasi-periodicity and chaotic oscillations. For example, for a slightly larger value of α we notice the emergence of a torus in the phase portrait shown in figure 6.15 in Appendix A. Biologically speaking, to our knowledge, there is no evidence of temporal oscillation in amyloid plaque formation. Thus, we do not develop the study of time-oscillating patterns in this work.

According to our numerical simulations, time-oscillating and low-amplitude exist only very close to the Turing bifurcation, which occurs at $\alpha = \alpha_c$. Therefore we mainly study the patterns for α assumed to be large enough to obtain only high amplitude. In the following section, we study in particular the influence of the parameter d on stationary patterns.

Influence of monomer degradation on high-amplitude patterns

We successively study the formation of high-amplitude for the following parameter values : $d = 0.15$, $d = 0.35$ and $d = 0.45$.

• **For $d = 0.15$.** To study the stationary patterns of the system (6.1), we perform a bifurcation shown in figure 6.4 diagram by using the `pde2path` package [104, 105] and more specifically the code presented in the article [106] for a reaction-diffusion system including a chemotaxis term. Stable branches are represented by a thick line, while unstable branches are represented by a thin line and the black horizontal branch corresponds to the positive steady state $\mathbf{V}_s$. As predicted in the section above, this branch loses its stability for $\alpha \geq \alpha_c$. At this Turing bifurcation, a branch is created which is associated with a periodic pattern in space. For $d = 0.15$, we notice that the Turing bifurcation is supercritical, indeed the branch is initially stable and associated with low amplitude. This branch rapidly loses its

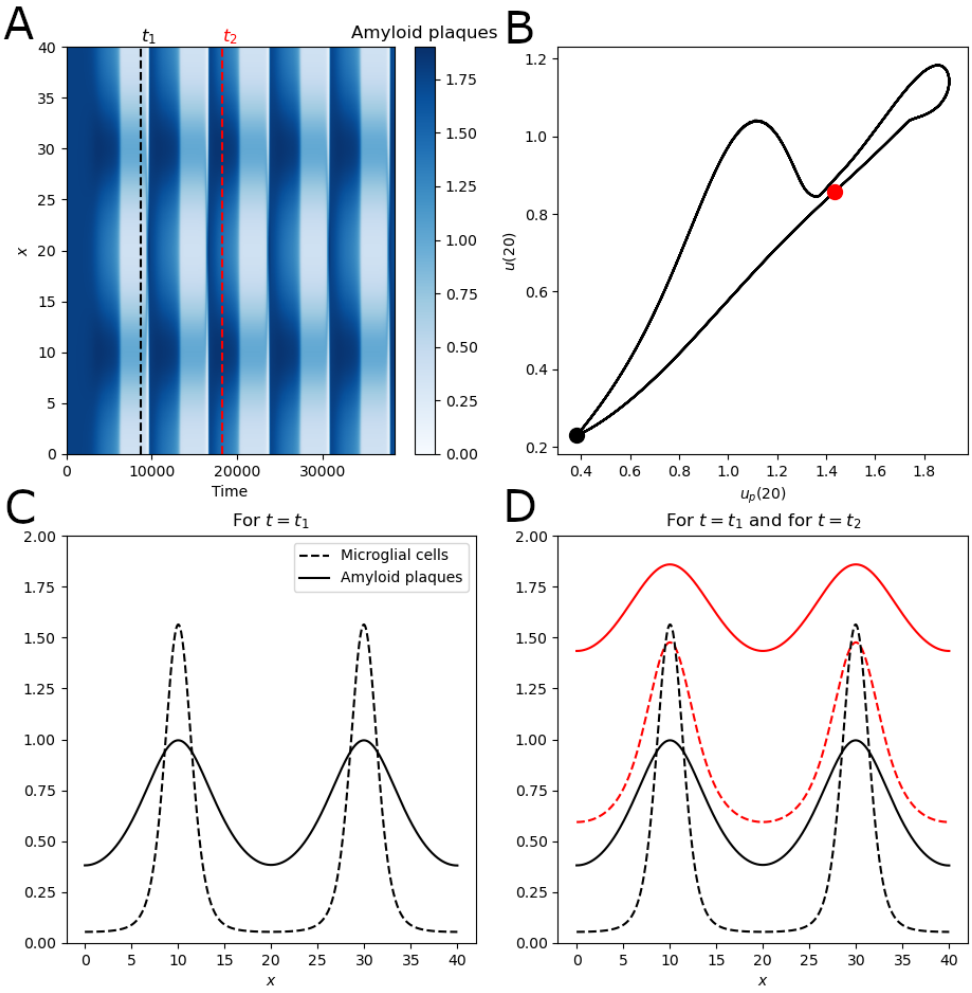

FIGURE 6.3 – **Spatially heterogeneous patterns that also exhibit regular oscillations in time. A.** Concentration of oligomers in amyloid plaques over time and space. **B.** Evolution over time of the concentration of oligomers at $x = 20$ compared to the concentration of oligomers in the amyloid plaques also at $x = 20$. The black dot corresponds to time $t = t_1$, while the red dot corresponds to time $t = t_2$. **C.** Concentration of microglial cells and oligomers in amyloid plaques at time $t = t_1$. (dotted black line in sub-figure A.). **D.** Concentration of microglial cells (dotted line) and oligomers in amyloid plaques (solid line) at time $t = t_1$ in black and at time $t = t_2$ in red (vertical dotted red line in sub-figure A.).

stability as the α parameter increases. Nevertheless, following several other bifurcations of this branch, we obtain new stable branches associated with high amplitude. First of all, we note the stability, over a short interval, of the branch associated with the pattern *One peak in the middle and one peak on the edge* represented by the blue line in figure 6.4. Then we notice two similar branches for the L^1 norm, associated respectively with the patterns *Middle peak* and *Two peaks at the edges*. The pattern with a middle peak can be seen as a reorganization of the pattern with two half-peaks at the edges, where each half-peak is shifted towards the center of the domain to form a complete, centered peak. Finally,

we also notice the stability of the branch in magenta, corresponding to the pattern *One peak at the edge*. This diagram shows that for a wide range of α, the system admits multi-stability of different branches, which is expected for models with a Turing-type bifurcation.

We notice that the size of the stability domain of the different branches of high amplitude decreases when the number of peaks or half-peaks (peaks on the edge) increases. Moreover, we notice that these domains of stability are finite and that for a large enough α, none of the branches that we have detected is stable. For this bifurcation diagram, we have assumed a relatively small domain for the spatial variable, $\Omega = [0, 40]$, to have fewer possible stable patterns. For a larger domain, we notice again this negative correlation between the number of peaks and the length of the stability domain. Note that in addition to the stable branches shown in figure 6.4, the disease-free equilibrium is also stable and can be an attractor.

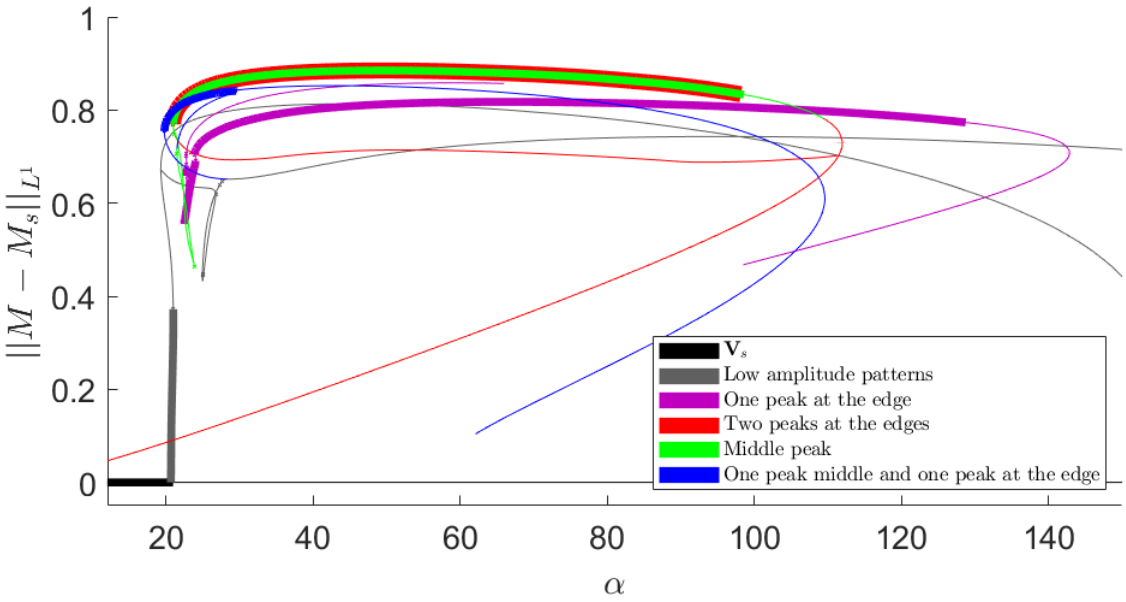

FIGURE 6.4 – **Bifurcation diagram for $d = 0.15$.** his bifurcation diagram is obtained using the package `pde2path` [104, 105]. Thick lines indicate stable branches, while thin lines indicate unstable branches. The horizontal branch in black corresponds to the stationary state $\mathbf{V}_s$, which loses its stability in α_c. For $d = 0.15$, this bifurcation point is supercritical, giving rise to a stable branch associated with a low-amplitude pattern. Following several bifurcations, we obtain the presence of other stable branches, associated with high-amplitude patterns described in the legend on the right. The term M_s corresponds to the microglial cell concentration component of the positive equilibrium $\mathbf{V}_s$. Parameter values are given in Table 6.1.

In addition to the bifurcation diagram, which exhibits a multi-stability of different branches of possible patterns, we illustrate the probability of selection of these different stable structures in figure 6.5 by performing 200 independent simulations for different values of parameter α. Pattern selection is highly dependent on the energy of each branch and the choice of initial condition. In our case, we choose an initial condition presented in Remark 1 with a very slight noise with an order of magnitude 10^{-5}.

Despite this relatively low noise level, we find at least once, a wide disparity. Indeed for several values of parameter α, we notice three patterns out of the four determined using the bifurcation diagram. When α is relatively close to the critical threshold α_c the pattern *Two peaks at the edges* seems to be strongly selected. Then when α is between $\alpha = 40$ and $\alpha = 90$ the probabilities of selection of the *Two peaks at the edges*, *One peak at the edge* and *Middle peak* are in the same order of magnitude. Finally for $\alpha > 120$, in agreement with the Conjecture 5, the only possible stationary solution is the disease-free equilibrium.

In the top panel of figure 6.5, we also illustrate the domains where stationary solutions are stable. These domains corroborate the results shown at the bottom panel, obtained independently. Indeed, no pattern was selected outside its stability zone determined by the bifurcation diagram.

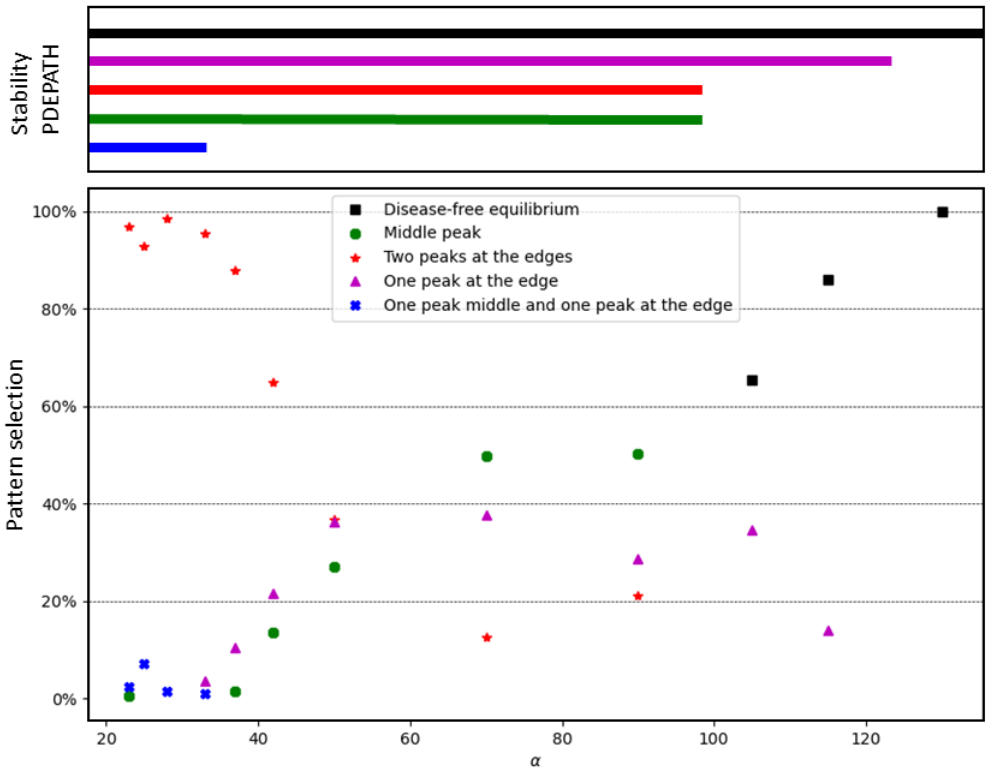

FIGURE 6.5 – **Pattern Selection for $d = 0.15$. Top.** Stability of the different branches of stationary patterns obtained using the package `pde2path` for different values of parameter α (See figure 6.4), for $d = 0.15$. The black branch corresponds to the disease-free equilibrium, this branch is stable for all $\alpha \in \mathbb{R}$. **Bottom.** Percentage of obtaining the different stationary patterns following 200 numerical simulations independent of the (6.1) system. The noisy initial conditions used are described in Remark 1. This process was repeated for different values of parameter α. The bifurcation diagram shown in figure 6.4 is consistent with our independent numerical simulations. Other parameter values are given in the Table 6.1.

In figure 6.6, we plot the average number of peaks in the final pattern associated with the numerical simulations in figure 6.5. We note that this average number of peaks tends to decrease as the chemotaxis

coefficient, α, increases. In particular, we note a strong discontinuity linked to the loss of stability of the *Two peaks at the edges* and *Middle peak* branches. These results are in agreement with the Conjecture 6.

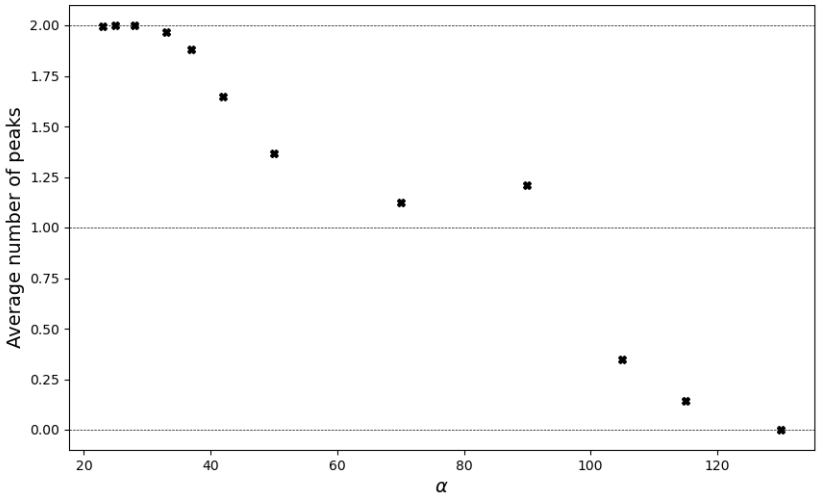

FIGURE 6.6 – **Average Number of peaks for $d = 0.15$.** Average number of amyloid plaques for the final stationary pattern for 200 independent numerical simulations of the system (6.1), on the domain $\Omega = [0.40]$, for different values of the parameter α. The noisy initial conditions used are described in Remark 1. The other parameter values are given in the Table 6.1.

• **For $d = 0.35$.** We now assume that the degradation coefficient of the monomers is equal to $d = 0.35$ and we perform the same analysis as before. The bifurcation diagram is shown in figure 6.7. This diagram has strong similarities with the previous diagram in figure 6.4. Again, close to the Turing-type bifurcation, we notice a strong multi-stability of different branches associated with different spatially heterogeneous patterns. The red branch corresponds to a pattern with two peaks on the edges, the green branch with one peak in the middle, and finally the blue branch corresponds to a single peak on the edge. As before, we notice that the length of the domains of stability is correlated with the number of half-peaks.

The main difference between the bifurcation diagram in figure 6.7 and the previous bifurcation diagram shown in figure 6.4, concerns the length of the stable domains of the branches. In particular, we notice that the last branch to lose its stability, loses its stability close to $\alpha = 22$, much less than in the previous case.

To determine the probability of selection of these different possible patterns, we perform 50 simulations with a slightly noisy initial condition (see Remark 1), and the results are shown in figure 6.8. When the branch *Two peaks at the edges* is stable, we always select it even if other branches are also stable. As soon as the red branch loses stability, the blue branch *One peak at the edge*, becomes predominant in the selection of the stationary pattern. But in this range of value of α the solution can also, with low probability, converge towards the disease-free equilibrium. According to our bifurcation diagram, once the blue branch loses its stability, no branch associated with a spatially heterogeneous

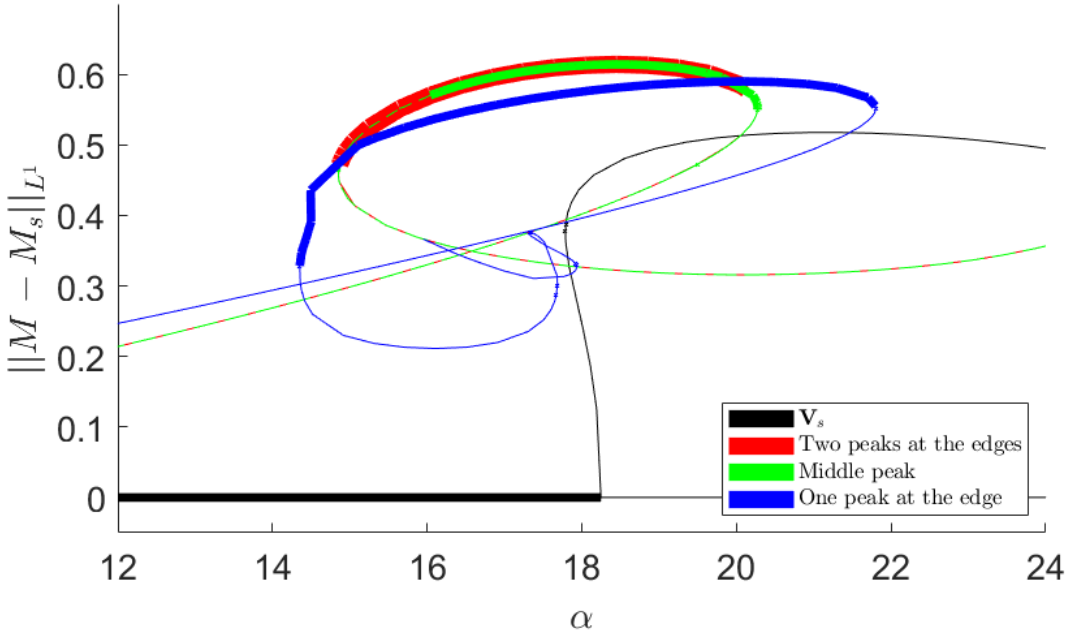

FIGURE 6.7 – **Bifurcation diagram for $d = 0.35$.** This bifurcation diagram is obtained using the package `pde2path` [104, 105]. Thick lines indicate stable branches, while thin lines indicate unstable branches. The horizontal branch in black corresponds to the stationary state $\mathbf{V}_s$, which loses its stability in α_c. For $d = 0.35$, this bifurcation point is subcritical. Following several bifurcations, we obtain the presence of other branches, which are stable, and associated with high-amplitude patterns described in the legend on the right. The term M_s corresponds to the microglial cell concentration component of the positive equilibrium $\mathbf{V}_s$. Parameter values are given in Table 6.1.

pattern is stable and this result agrees with our numerical simulations of figure 6.8. For parameter values $\alpha = 22$, 22.5, and 23, we systematically select the disease-free equilibrium.

The *Middle peak* structure was never selected in our simulations, despite its stability. Note that the noise is again chosen to be very low. For initial values with a larger variance, the results could differ greatly.

In the top panel of figure 6.8, we illustrate the average of the peaks of the selected stationary patterns presented in figure 6.7. As expected, we obtain a decreasing function as a function of α, which is close to a step function, where the discontinuity comes from the loss of stability of a stable branch. For a larger domain, for example, $\Omega = [0, 100]$, more patterns are theoretically eligible. In this case, we notice that the decrease in the average of the peaks is less discontinuous than before (see the bottom panel of the figure 6.8).

• **For $d = 0.45$.** We finally study the case $d = 0.45$. For this parameter value, we are still in the bistable domain of the model 6.1, so there is a Turing type bifurcation such that for $\alpha > \alpha_c$ the stable equilibrium without chemotaxis $\mathbf{V}_s$, becomes unstable. This bifurcation gives rise to a branch of spatially heterogeneous patterns. However, according to our bifurcation diagram and independent

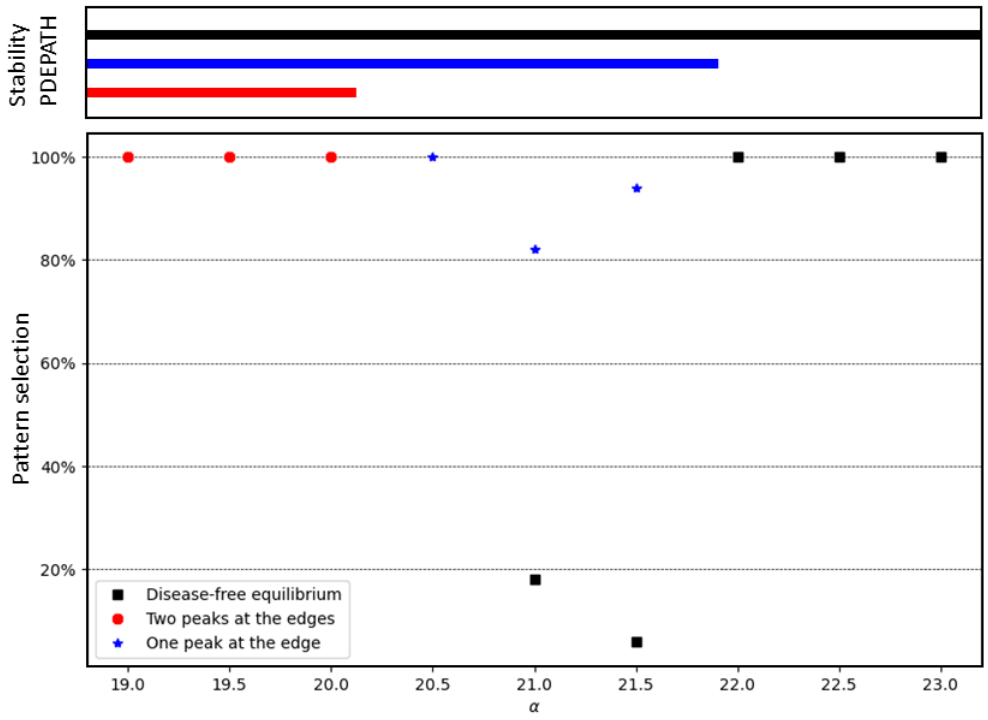

FIGURE 6.8 – **Pattern Selection for $d = 0.35$. Top.** Stability of the different branches of stationary patterns obtained using the package `pde2path` for different values of the parameter α (See figure 6.7), for $d = 0.35$. The black branch corresponds to the disease-free equilibrium, this branch is stable for all $\alpha \in \mathbb{R}$. **Bottom.** Percentage of obtaining the different stationary patterns following 50 independent numerical simulations of the system (6.1). The noisy initial conditions used are described in Remark 1. This process was repeated for different values of parameter α. The bifurcation diagram shown in figure 6.4 is consistent with our independent numerical simulations. Other parameter values are given in the Table 6.1.

numerical simulations, this branch is always unstable. So when the equilibrium $\mathbf{V}_s$ loses its stability, the problem becomes monostable, and the solution of the model (6.1) converges towards the disease-free equilibrium.

6.3.2 Numerical simulation in the two-dimensional case

Stripes and dots

We now study spatially heterogeneous patterns in a two-dimensional square domain, $\Omega = [0, L] \times [0, L]$. In this case, we can obtain many families such as stripes, dots, and hexagons, or even more complex ones, such as mazes.

Again we notice the presence of low-amplitude and high-amplitude. These low-amplitude, corres-

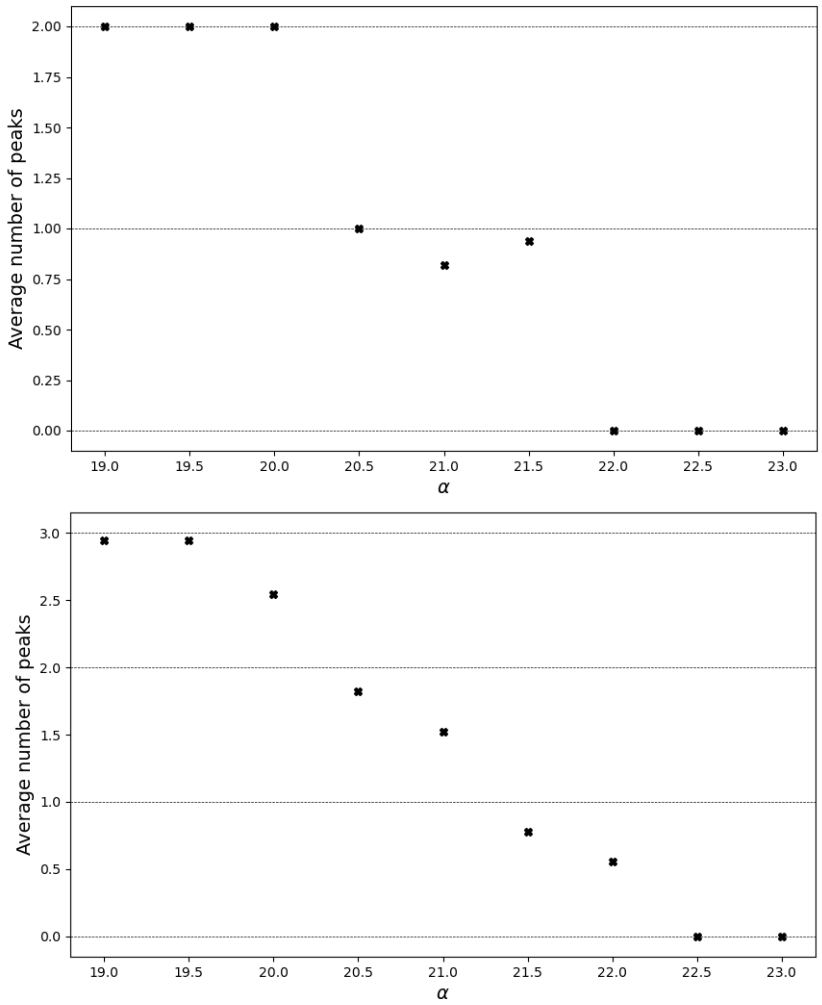

FIGURE 6.9 – **Average Number of peaks for** $d = 0.35$**.** Average number of amyloid plaques for the final stationary pattern for 50 independent numerical simulations of the system (6.1), for different values of the parameter α and for the following domain : **Top.** $\Omega = [0, 40]$ and **Bottom.** $\Omega = [0, 100]$. The noisy initial conditions used are described in Remark 1. The other parameter values are given in the Table 6.1.

pond to weak perturbations of the positive steady state $\mathbf{V}_s$ and exist only for α very close to the critical threshold α_c. Note that the weakly nonlinear analysis is a tool to theoretically determine the family of low-amplitude [11, 71]. However, as in the previous section, we focus only on high amplitude. Our numerical simulations reveal several possible high amplitudes, including stripes and dots. These two types are illustrated in figure 6.10 and can coexist for certain ranges of parameter values. Note also that we obtain complex stationary patterns corresponding to a structure between dots and stripes. For a large enough α, we only notice the presence of a dot. Subsequently, we focus on those which are more reasonable in terms of modeling. Indeed, biologically, amyloid plaques form spots distributed heterogeneously in space (see figure 6.1).

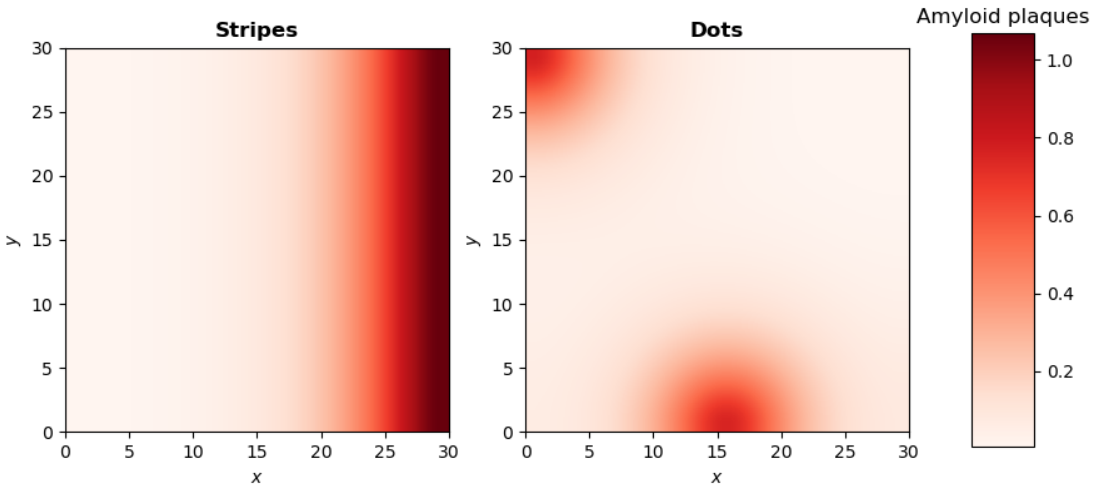

FIGURE 6.10 – **Examples of high-amplitude final stationary patterns for the system** (6.1)**. Top.** Stripe pattern. **Bottom.** Dot pattern. The parameter values are those shown in the Table 6.1, with $d = 0.15$ and $\alpha = 24$.

Pattern selection

In the two-dimensional case, there are many more possible structures. Therefore, it is difficult to detect all stable branches using a continuation method. In particular, there is a good chance of forgetting branches that are difficult to select but theoretically stable. Thus for the square domain $\Omega = [0, L] \times [0, L]$ we only work with successive independent numerical simulations.

In figure 6.11 we plot the evolution of the average number of peaks for 50 independent simulations of the model (6.1). The choice of the initial conditions is detailed in Remark 1. Since it is impossible to quantify the number of peaks for stripe patterns, we study the average only for $\alpha > 25$. For these values of α we always obtained stationary dot patterns. As for the study in the one-dimensional case, presented above, the average number of peaks tends to decrease when the chemotaxis parameter increases. From a certain stage, this average number of peaks is equal to 0. These results are in agreement with the Conjecture 6.

6.3.3 Parameter value ranges without amyloid plaque

For modeling reasons, it is interesting to determine the zones of parameters for which it is *a priori* impossible to observe the emergence and persistence of amyloid plaques. In other words, for the initial conditions presented in Remark 1, we want to determine a threshold α_0 such that for any $\alpha > \alpha_0$, the solution of the system (6.1) converges to the disease-free equilibrium independently of the noise of the initial condition.

We approach this threshold α_0 using numerical simulations. We discretize the possible values of α and look for the smallest possible point such that for any α greater than this point the n independent simulations have led to convergence to the disease-free equilibrium. Our algorithm first explores a possible candidate and then refines this candidate to obtain a precise approximation of the threshold

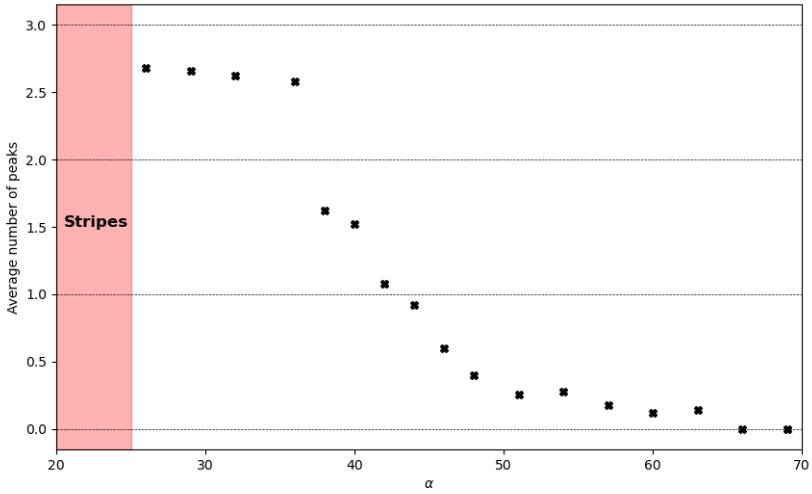

FIGURE 6.11 – **Average Number of peaks for $d = 0.15$ and $\Omega = [0, 40] \times [0, 40]$.** Average number of amyloid plaques for the final stationary pattern for 50 independent numerical simulations of the system (6.1), for different values of the parameter α. For $\alpha > 25$, we did not obtain any stripes pattern for our various numerical simulations. The noisy initial conditions used are described in Remark 1. The other parameter values are given in the Table 6.1.

α_0. We apply this algorithm for different values of parameter d and obtain an approximation of the threshold $\alpha_0^{\exp}(d)$. For $d < d_m$, and if we assume that d is large enough, the threshold α_0 is equal to the critical threshold α_c. Conversely, for d small enough, we observe a strong increase in the α_0 threshold.

In the one-dimensional case, we represent the approximation obtained using our algorithm, $\alpha_0^{\exp}(d)$, by the dotted red line marked by the red arrow in figure 6.12. In the bistable domain, we note that this curve separates two distinct parts. The first part corresponds to parameter values for which the solutions of our n consecutive independent simulations have converged toward the disease-free equilibrium. We therefore assume that for these parameter values, we always converge to the disease-free equilibrium. Note that in theory, this assumption could turn out to be wrong, especially for small parameter values d where the threshold seems very high. We denote $\mathbf{P}_d(\alpha)$ the probability that the solution does not converge to the equilibrium without disease. Even if this probability is positive for any $\alpha > 0$, we theoretically get the existence of $\alpha_0^{\exp}$. Nevertheless, the bifurcation diagrams presented in section 6.3.1 show that pattern branches lose their stability for a large enough α ; this motivates and justifies the choice of such an assumption. From a modeling point of view, this zone of parameter values corresponds to a zone where, after a certain time t, no amyloid plaques are present.

In the second part, shown in red, there are several possible phenomena. In particular for $\alpha < \alpha_c$, for very slightly noisy initial conditions around $\mathbf{V}_s$, we converge to the positive homogeneous stationary state $\mathbf{V}_s$. When α is between α_c and $\alpha_0^{\exp}$, there are plenty of possibilities, including convergence to a spatially heterogeneous stationary pattern, convergence to a time oscillating pattern and convergence

to the disease-free equilibrium. Nevertheless, according to our numerical simulations, we obtained at least once a solution that is not the disease-free equilibrium.

In the monostable domain ($d > d_m$), the positive equilibrium $\mathbf{V}_s$ does not exist. For this range of parameter values, only the disease-free equilibrium is stable. Consequently, we converge, regardless of the chemotaxis parameter value and independently of the noise of the initial condition, to this disease-free equilibrium. In the two-dimensional case, *i.e.* for $\Omega = [0, L] \times [0, L]$ we obtain a similar result, which is represented in the figure 6.16 in Appendix A.

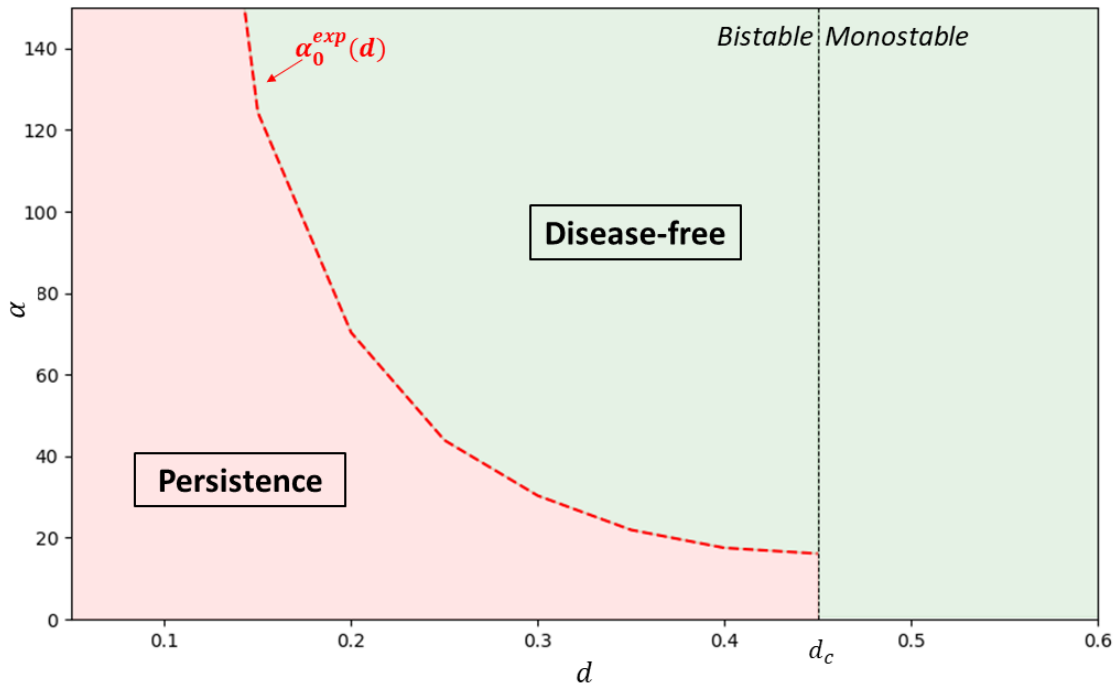

FIGURE 6.12 – **Asymptotic behavior of the solutions of system (6.1) as a function of the degradation of monomers d and the chemotaxis parameter α, for the domain $\Omega = [0.40]$.** For $d > d_m$, there is only one equilibrium which is the disease-free equilibrium. From the stability of this equilibrium, the solutions of the system converge towards it. For $d < d_m$, it is possible to converge to the disease-free equilibrium, the positive equilibrium $\mathbf{V}_s$, and a spatially heterogeneous (possibly time-oscillating) pattern. The red zone represents an area of parameter values for which we have noticed, at least once, convergence towards a stationary solution other than the disease-free equilibrium. The green zone corresponds to parameter values for which we systematically converge towards the disease-free equilibrium. This result is highly dependent on the chosen initial conditions. The choice of the noisy initial condition is described in Remark 1.

6.3.4 Influence of the initial data

We assume that the initial concentrations of monomers, oligomers, and microglial cells are initially uniformly distributed in space and there is a complete absence of amyloid plaques. In this section, we investigate the influence of initial inflammation on the final pattern. The initial data is provided in

Table 6.2.

TABLE 6.2 – **Initial data used in Section 6.3.4**

Parameter	Value	Units	Description
u_0	10^{-4}	$\mathrm{mol}\,L^{-1}$	Concentration of free oligomers
u_p	0	$\mathrm{mol}\,L^{-1}$	Concentration of oligomers in the amyloid plaques
m_0	10^{-3}	$\mathrm{mol}\,L^{-1}$	Concentration of monomers
M_0	1	$\mathrm{mol}\,L^{-1}$	Concentration of microglial cells
I_0	Variable	$\mathrm{mol}\,L^{-1}$	Concentration of interleukins

Initial homogeneous inflammation in space

First, we assume that the inflammation, corresponding to the interleukin concentration, is initially uniformly distributed in space with a certain quantity I_0 that we vary.

In figure 6.13, we follow a similar approach as previously done to identify parameter regions where the persistence of amyloid plaques is not observed. Here, we examine the influence of monomer degradation d and the initial value of interleukin concentration I_0. The algorithm used to obtain this figure is similar to the one presented in Section 6.3.3. In the monostable case ($d > d_m$), where the only equilibrium is the disease-free equilibrium, all the solutions of the system (6.1) converge to this equilibrium, while in the bistable case ($d < d_m$), the steady-state solution can be either homogeneous or spatially heterogeneous. The green region corresponds to parameter values for which the steady-state solution of the model (6.1) coincides with the disease-free equilibrium. In contrast, the red region represents other possibilities, namely a homogeneous solution equal to the other positive equilibrium or a spatially heterogeneous solution. The dichotomy observed in figure 6.13 is similar to the results presented in the article [274].

Initial heterogeneous inflammation in space

We now assume that the initial concentration of interleukins is heterogeneous in space. More precisely, we assume that the interleukin concentration is initially distributed in three Gaussians evenly spaced across the domain $[0, 40]$. Mathematically, the initial data is defined by the following family of functions,

$$I_0^\eta(x) = \frac{1}{\eta\sqrt{2\pi}} e^{-\frac{(x-10)^2}{2\eta^2}} + \frac{1}{\eta\sqrt{2\pi}} e^{-\frac{(x-20)^2}{2\eta^2}} + \frac{1}{\eta\sqrt{2\pi}} e^{-\frac{(x-30)^2}{2\eta^2}}, \tag{6.12}$$

dependent on the variable $\eta > 0$, which corresponds to the variance of the Gaussians. Note that the initial mass of the interleukin concentration, $\int I_0$, is independent of the variable η.

In figure 6.14, we investigate the impact of the variance η on the potential persistence of inflammation. In the left panel, we illustrate four different initial data of interleukin concentration, each associated with different variances, according to the formula (6.12). In the right panel, we depict the final steady-state solution associated with the corresponding initial data on the left. When the

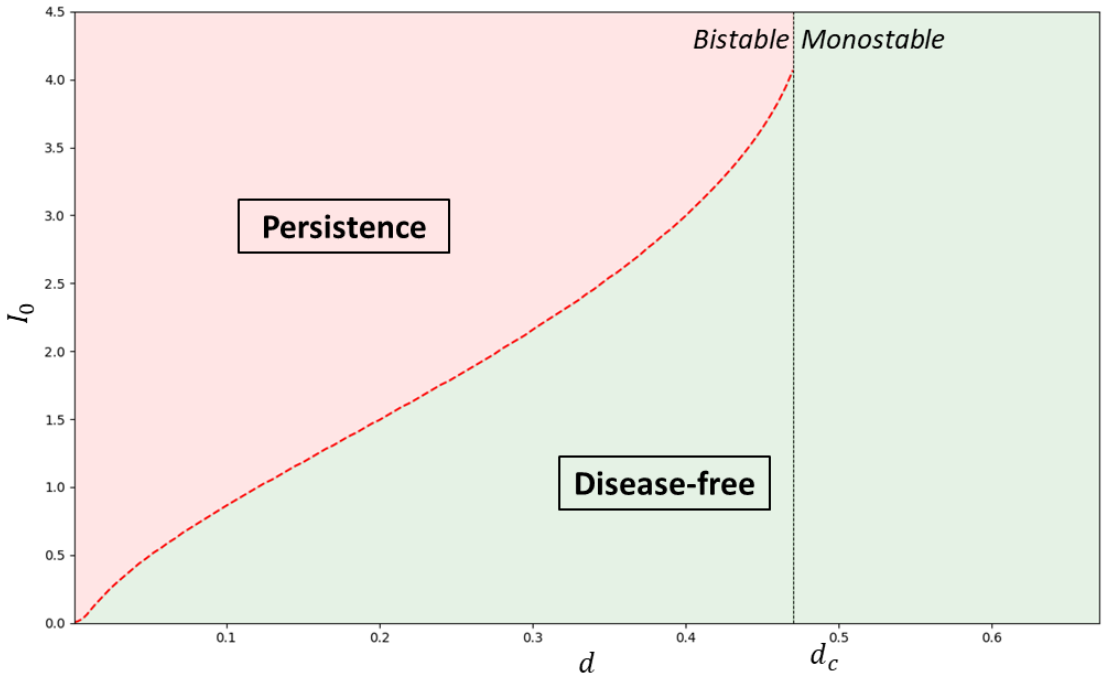

FIGURE 6.13 – **Asymptotic behavior of the solutions of system (6.1) as a function of the degradation of the monomers d and the initial concentration of interleukin I_0.** For $d > d_m$, there is only one equilibrium which is the disease-free equilibrium. By stability of this equilibrium, the solutions of the system converge towards this steady state. For $d < d_m$ it is possible to converge to the disease-free equilibrium, the positive equilibrium $\mathbf{V}_s$, and a spatially heterogeneous (possibly time-oscillating) pattern. The red zone represents an area of parameter values for which we have noticed at least one convergence towards a stationary solution other than the disease-free equilibrium. The green zone corresponds to parameter values for which we systematically converge towards the disease-free equilibrium. This result is very similar to the one obtained in the article [274]. The other parameter values are given in Table 6.1 and the initial data is provided in Table 6.2.

variance η is small, the initial data corresponds to very narrow Gaussian curves, resulting in highly concentrated inflammation in small spatial regions. In this case, we observe that the solutions of the model (6.1) converge towards the disease-free equilibrium. Conversely, when the variance η is larger, the initial inflammation is more dispersed than before but with less amplitude. We notice that in this case the steady-state solutions of the model (6.1) correspond to spatially positive heterogeneous solutions and the initial inflammation leads to a persistent inflammation over time.

The result presented in figure 6.14 is in some sense quite similar to the proposition outlined in Conjecture 5. As α increases, heterogeneous steady-state solutions are more prone to converge to asymptotic Dirac masses. In other words, as α grows, the heterogeneous spatial concentration of interleukins becomes increasingly strong but also more concentrated in small regions of space, leaving a significant portion of space with an almost negligible interleukin density. In the previous sections, through numerical simulations, we proved that these spatially heterogeneous solutions lose their sta-

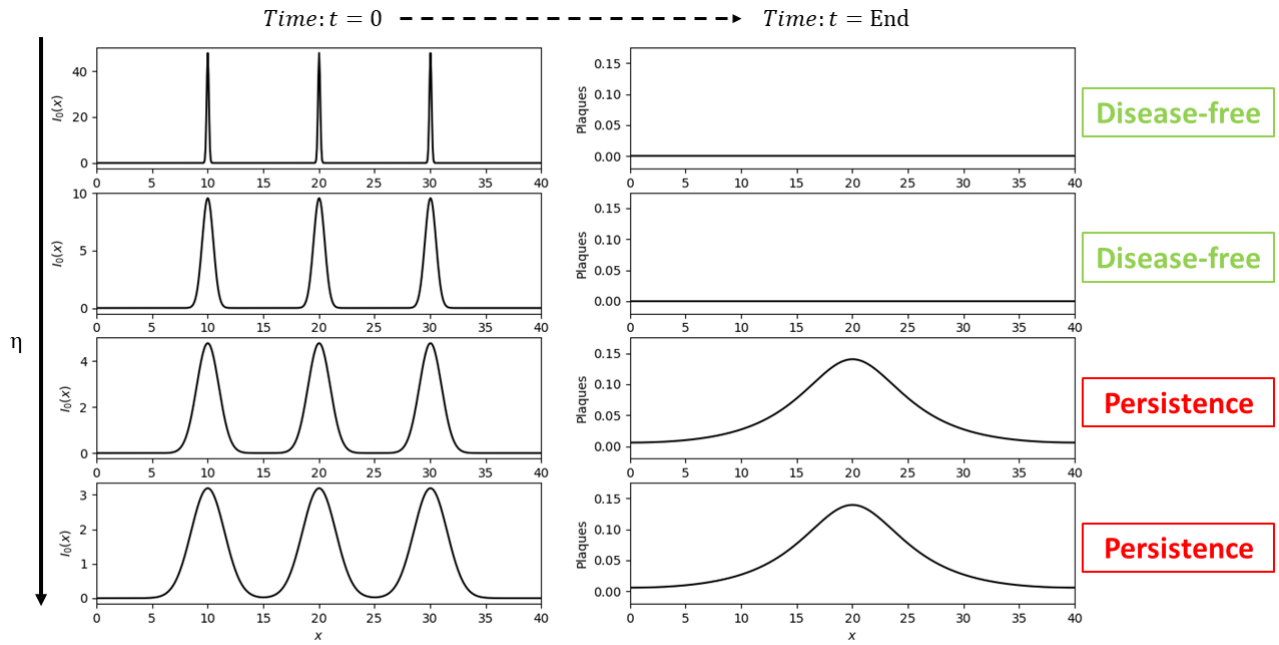

FIGURE 6.14 – **Steady-state solutions of the model (6.1) for various initial data corresponding to sums of Gaussians. Left.** Different initial data for interleukin concentration given by the equation (6.12), associated with different variances from lower ones (Top) to higher ones (Bottom). **Right.** Steady-state solutions of the model (6.1) associated with the initial data from the left panel. The parameter values are listed in Table 6.1, and the remaining initial data is given in Table 6.2.

bility when α becomes excessively large ($\alpha > \alpha_0$), meaning when inflammation is too concentrated in a small fraction of space.

In terms of modeling, it is, therefore, simpler to eliminate inflammation if it is highly concentrated in a small part of the space, preserving a large part of the healthy tissue, rather than to treat milder inflammation spread over a wider area.

6.4 Conclusion and perspectives

In this work, we have extended the research presented in the article by Ciuperca *et al.* [274] by studying the model (6.1) with its spatial components. Our linear analysis shows that the equilibrium point $\mathbf{V}_s$ is unstable to spatially heterogeneous perturbations when $\alpha > \alpha_c$, with α_c being a critical threshold corresponding to a root of the function defined by (6.11). To study pattern formation, we plotted numerous bifurcation diagrams using the `pde2path` package, revealing a wide variety of patterns. We also performed numerous independent numerical simulations to ensure that all branches were found. With this complete bifurcation diagram, we can predict interesting modeling results. For instance, according to our model, the higher the coefficient α, corresponding to the intensity of the attraction of microglial cells to oligomers, the fewer plaques are expected. Additionally, when α is sufficiently large, neither plaques nor inflammation are expected. This phenomenon also depends on other parameters ; we specifically study the influence of the parameter d, representing the natural

degradation rate of monomers.

However, to confirm or refute these predictions, it would be necessary to obtain brain images at different stages of plaque formation dynamics, as well as methods to modify parameters present in our system, such as the administration of anti-inflammatory drugs.

In our diagrams, we have highlighted that for sufficiently large values of α, all pattern branches become unstable. This unusual behavior appears to be a consequence of the bistability of our model [8]. Similar results, showing a total loss of branch stability, were presented in the article by Al-Karkhi *et al.* [290]. Additionally, our bifurcation diagrams reveal that the loss of branch stability strongly depends on their associated pattern : the higher the number of peaks, the faster the loss of stability. It would be particularly interesting to theoretically study how bistability can be responsible for such phenomena.

The model (6.1) introduced in the article [274] is a simplified subsystem of a more complex model, also introduced in the same article, which also models proto-oligomer structures of different sizes. Therefore, it would be interesting to study whether our results extend to the more general model. Additionally, the model was initially introduced for a study on a bounded open domain $\Omega \subset \mathbb{R}^3$. In this work, we performed analyses only in one and two dimensions, as these dimensions are simpler to handle. A three-dimensional analysis, although more complex, would be particularly interesting and is also made possible by the Matlab package `pde2path` (see, for example, [296]).

A direct application of our model is to study the effects of different therapeutic strategies. In this work, we have highlighted that microglial cells play a key role in plaque aggregation, particularly through the influence of the coefficient α. Therefore, it would be interesting to identify factors, such as molecules, able to influence plaque structuring via microglial cells.

Anti-inflammatory treatments can also be studied using our model. As proven in the article [274], we show that initial inflammation may or may not lead to plaque formation. We also highlight that inflammation concentrated in a specific tissue area does not have the same impact as more diffuse inflammation. Given the strong multistability observed in this model, it is obvious that the administration of anti-inflammatory drugs induces transitions between different stable branches. Anti-inflammatory treatment has already been tested for Alzheimer's disease. In the article by Rivers-Auty *et al.* [297], the authors indicated that diclofenac could slow cognitive decline and offer promising prospects for the progression of Alzheimer's disease. However, rigorous clinical trials have failed to confirm the efficacy of these anti-inflammatory treatments [298, 299, 300]. In contrast, other studies suggest that the effectiveness of these treatments could be significant if administered well before the onset of clinical symptoms [301, 302].

A Supplementary Figures

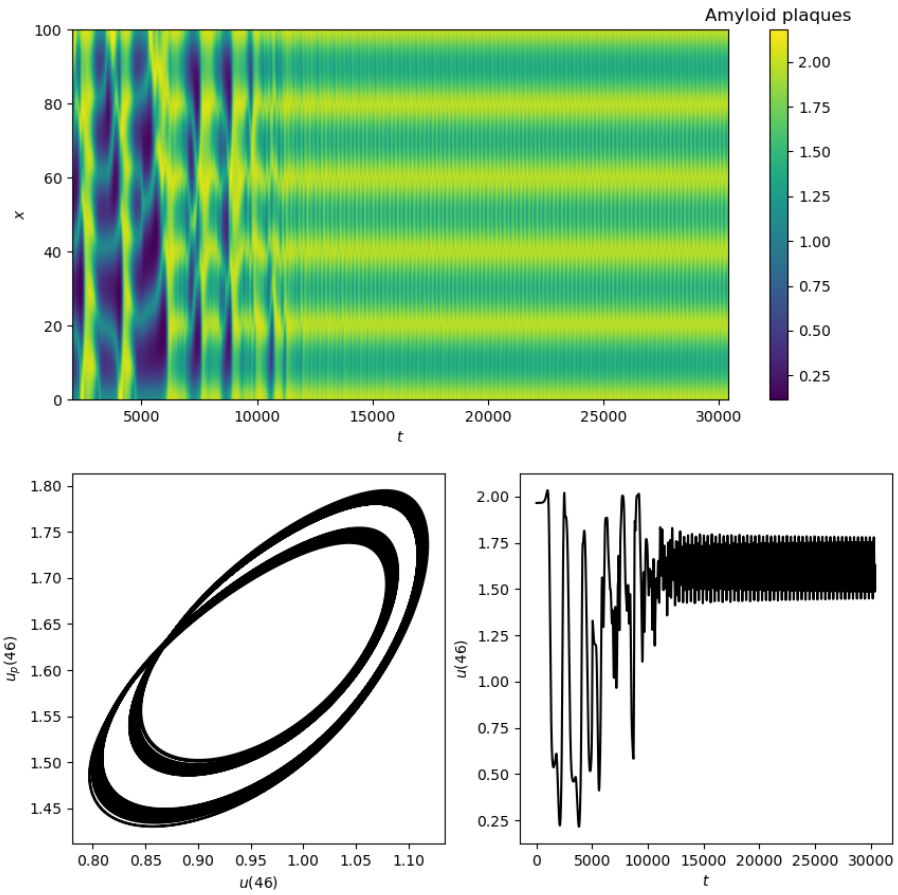

FIGURE 6.15 – **Heterogeneous patterns in space with quasi-periodic oscillations in time. Top.** Concentration of amyloid plaques over time. **Bottom-left.** Evolution over time of the concentration of oligomers at $x = 46$ as a function of the concentration of amyloid plaques also at $x = 46$. **Bottom-right.** Concentration of oligomers at $x = 46$ over time.

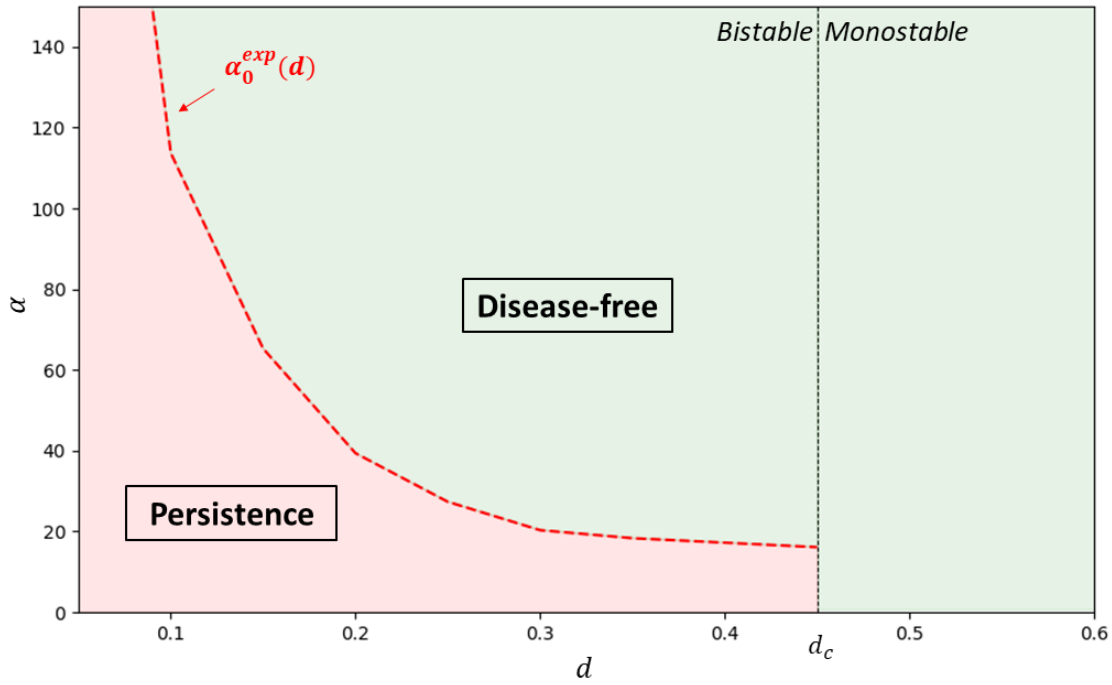

FIGURE 6.16 – **Asymptotic behavior of the solutions of system** (6.1) **as a function of the degradation of the monomers** d **and the chemotaxis parameter** α**, for the domain** $\Omega = [0, 30] \times [0, 30]$. For $d > d_m$, there is only one equilibrium which is the disease-free equilibrium. By stability of this equilibrium, the solutions of the system converge towards it. For $d < d_m$, it is possible to converge to the disease-free equilibrium, the positive equilibrium $\mathbf{V}_s$, and a spatially heterogeneous (possibly time-oscillating) pattern. The red zone represents an area of parameter values for which we have noticed, at least once, convergence towards a stationary solution that is not the disease-free equilibrium. The green zone corresponds to parameter values for which we systematically converge towards the disease-free equilibrium. This result is highly dependent on the chosen initial conditions. The choice of the noisy initial condition is described in Remark 1.

Bibliographie

[1] K. J. Painter, M. Ptashnyk et D. J. Headon. « Systems for intricate patterning of the vertebrate anatomy ». In : *Philosophical Transactions of the Royal Society A : Mathematical, Physical and Engineering Sciences* 379.2213 (2021). doi : 10.1098/rsta.2020.0270.

[2] M. C. Milinkovitch, E. Jahanbakhsh et S. Zakany. « The Unreasonable Effectiveness of Reaction Diffusion in Vertebrate Skin Color Patterning ». In : *Annual Review of Cell and Developmental Biology* 39.1 (2023). doi : 10.1146/annurev-cellbio-120319-024414.

[3] S. Kondo, M. Watanabe et S. Miyazawa. « Studies of Turing pattern formation in zebrafish skin ». In : *Philosophical Transactions of the Royal Society A : Mathematical, Physical and Engineering Sciences* 379.2213 (2021). doi : 10.1098/rsta.2020.0274.

[4] C. Konow, M. Dolnik et I. R. Epstein. « Insights from chemical systems into Turing-type morphogenesis ». In : *Philosophical Transactions of the Royal Society A : Mathematical, Physical and Engineering Sciences* 379.2213 (2021). doi : 10.1098/rsta.2020.0269.

[5] A. L. Krause et al. « Modern perspectives on near-equilibrium analysis of Turing systems ». In : *Philosophical Transactions of the Royal Society A : Mathematical, Physical and Engineering Sciences* 379.2213 (2021). doi : 10.1098/rsta.2020.0268.

[6] J. D. Murray, éd. *Mathematical Biology : II : Spatial Models and Biomedical Applications*. T. 18. Interdisciplinary Applied Mathematics. New York, NY : Springer New York, 2003. doi : 10.1007/b98869.

[7] H. Meinhardt et A. Gierer. « Pattern formation by local self-activation and lateral inhibition ». In : *BioEssays* 22.8 (2000). doi : 10.1002/1521-1878(200008)22:8<753::AID-BIES9>3.0.CO;2-Z.

[8] A. L. Krause et al. *Turing instabilities are not enough to ensure pattern formation*. Version Number : 2. 2023. doi : 10.48550/ARXIV.2308.15311.

[9] M. C. Cross et P. C. Hohenberg. « Pattern formation outside of equilibrium ». In : *Reviews of Modern Physics* 65.3 (1993). doi : 10.1103/RevModPhys.65.851.

[10] D. J. Wollkind, V. S. Manoranjan et L. Zhang. « Weakly Nonlinear Stability Analyses of Prototype Reaction-Diffusion Model Equations ». In : *SIAM Review* 36.2 (1994). doi : 10.1137/1036052.

[11] B. Ermentrout. « Stripes or spots ? Nonlinear effects in bifurcation of reaction—diffusion equations on the square ». In : *Proceedings of the Royal Society of London. Series A : Mathematical and Physical Sciences* 434.1891 (1991). doi : 10.1098/rspa.1991.0100.

[12] B. Bozzini et al. « Weakly nonlinear analysis of Turing patterns in a morphochemical model for metal growth ». In : *Computers & Mathematics with Applications* 70.8 (2015). doi : 10.1016/j.camwa.2015.08.019.

[13] G. Gambino, M. Lombardo et M. Sammartino. « Turing instability and traveling fronts for a nonlinear reaction–diffusion system with cross-diffusion ». In : *Mathematics and Computers in Simulation* 82.6 (2012). doi : 10.1016/j.matcom.2011.11.004.

[14] A. Gierer et H. Meinhardt. « A theory of biological pattern formation ». In : *Kybernetik* 12.1 (1972). doi : 10.1007/BF00289234.

[15] J. Schnakenberg. « Simple chemical reaction systems with limit cycle behaviour ». In : *Journal of Theoretical Biology* 81.3 (1979). doi : 10.1016/0022-5193(79)90042-0.

[16] P. Gray et S. Scott. « Autocatalytic reactions in the isothermal, continuous stirred tank reactor ». In : *Chemical Engineering Science* 39.6 (1984). doi : 10.1016/0009-2509(84)87017-7.

[17] R. A. Satnoianu, M. Menzinger et P. K. Maini. « Turing instabilities in general systems ». In : *Journal of Mathematical Biology* 41.6 (2000). doi : 10.1007/s002850000056.

[18] L. Marcon et al. « High-throughput mathematical analysis identifies Turing networks for patterning with equally diffusing signals ». In : *eLife* 5 (2016). doi : 10.7554/eLife.14022.

[19] X. Diego et al. « Key Features of Turing Systems are Determined Purely by Network Topology ». In : *Physical Review X* 8.2 (2018). doi : 10.1103/PhysRevX.8.021071.

[20] G. Gambino et al. « Turing pattern formation in the Brusselator system with nonlinear diffusion ». In : *Physical Review E* 88.4 (2013). doi : 10.1103/PhysRevE.88.042925.

[21] G. Gambino, M. C. Lombardo et M. Sammartino. « Turing Instability and Pattern Formation for the Lengyel–Epstein System with Nonlinear Diffusion ». In : *Acta Applicandae Mathematicae* 132.1 (2014). doi : 10.1007/s10440-014-9903-2.

[22] B. I. Henry et S. L. Wearne. « Existence of Turing Instabilities in a Two-Species Fractional Reaction-Diffusion System ». In : *SIAM Journal on Applied Mathematics* 62.3 (2002). doi : 10.1137/S0036139900375227.

[23] B. I. Henry, T. A. M. Langlands et S. L. Wearne. « Turing pattern formation in fractional activator-inhibitor systems ». In : *Physical Review E* 72.2 (2005). doi : 10.1103/PhysRevE.72.026101.

[24] T. A. M. Langlands, B. I. Henry et S. L. Wearne. « Turing pattern formation with fractional diffusion and fractional reactions ». In : *Journal of Physics : Condensed Matter* 19.6 (2007). doi : 10.1088/0953-8984/19/6/065115.

[25] D. M. Busiello et al. « Pattern formation for reactive species undergoing anisotropic diffusion ». In : *The European Physical Journal B* 88.9 (2015). doi : 10.1140/epjb/e2015-60269-0.

[26] H. Shoji et al. « Directionality of Stripes Formed by Anisotropic Reaction–Diffusion Models ». In : *Journal of Theoretical Biology* 214.4 (2002). doi : 10.1006/jtbi.2001.2480.

[27] H. Shoji et al. « Origin of directionality in the fish stripe pattern ». In : *Developmental Dynamics* 226.4 (2003). doi : 10.1002/dvdy.10277.

[28] H. Shoji et al. « Bifurcation Points of Periodic Triangular Patterns Obtained in Reaction-Diffusion System with Anisotropic Diffusion ». In : *Journal of Applied Mathematics and Physics* 10.07 (2022). doi : 10.4236/jamp.2022.107159.

[29] D. Fanelli, C. Cianci et F. Di Patti. « Turing instabilities in reaction-diffusion systems with cross diffusion ». In : *The European Physical Journal B* 86.4 (2013). doi : 10.1140/epjb/e2013-30649-7.

[30] A. Madzvamuse, H. S. Ndakwo et R. Barreira. « Cross-diffusion-driven instability for reaction-diffusion systems : analysis and simulations ». In : *Journal of Mathematical Biology* 70.4 (2015). doi : 10.1007/s00285-014-0779-6.

[31] G. Gambino et al. « Cross-diffusion effects on stationary pattern formation in the FitzHugh-Nagumo model ». In : *Discrete and Continuous Dynamical Systems - B* 27.12 (2022). doi : 10.3934/dcdsb.2022063.

[32] N. Mukherjee, S. Ghorai et M. Banerjee. « Cross-Diffusion Induced Turing and non-Turing Patterns in Rosenzweig–MacArthur Model ». In : *Letters in Biomathematics* 6.1 (2019). doi : 10.30707/LiB6.1Mukherjee.

[33] E. Tulumello, M. C. Lombardo et M. Sammartino. « Cross-Diffusion Driven Instability in a Predator-Prey System with Cross-Diffusion ». In : *Acta Applicandae Mathematicae* 132.1 (2014). doi : 10.1007/s10440-014-9935-7.

[34] G. Gambino et al. « Super-critical and sub-critical bifurcations in a reaction-diffusion Schnakenberg model with linear cross-diffusion ». In : *Ricerche di Matematica* 65.2 (2016). doi : 10.1007/s11587-016-0267-y.

[35] J. Swift et P. C. Hohenberg. « Hydrodynamic fluctuations at the convective instability ». In : *Physical Review A* 15.1 (1977). doi : 10.1103/PhysRevA.15.319.

[36] J. W. Cahn et J. E. Hilliard. « Free Energy of a Nonuniform System. I. Interfacial Free Energy ». In : *The Journal of Chemical Physics* 28.2 (1958). doi : 10.1063/1.1744102.

[37] T. Hillen et K. J. Painter. « A user's guide to PDE models for chemotaxis ». In : *Journal of Mathematical Biology* 58.1-2 (2009). doi : 10.1007/s00285-008-0201-3.

[38] A. Bers. « Space-time evolution of plasma instabilities-absolute and convective ». In : *Basic plasma physics. 1.* 1983.

[39] G. Dee et J. S. Langer. « Propagating Pattern Selection ». In : *Physical Review Letters* 50.6 (1983). doi : 10.1103/PhysRevLett.50.383.

[40] W. Van Saarloos. « Front propagation into unstable states ». In : *Physics Reports* 386.2-6 (2003). DOI : 10.1016/j.physrep.2003.08.001.

[41] W. Van Saarloos. « Front propagation into unstable states : Marginal stability as a dynamical mechanism for velocity selection ». In : *Physical Review A* 37.1 (1988). DOI : 10.1103/PhysRevA.37.211.

[42] W. Van Saarloos. « Front propagation into unstable states. II. Linear versus nonlinear marginal stability and rate of convergence ». In : *Physical Review A* 39.12 (1989). DOI : 10.1103/PhysRevA.39.6367.

[43] J. P. Eckmann et C. E. Wayne. « Propagating fronts and the center manifold theorem ». In : *Communications in Mathematical Physics* 136.2 (1991). DOI : 10.1007/BF02100026.

[44] P. Collet et J. P. Eckmann. « The existence of dendritic fronts ». In : *Communications in Mathematical Physics* 107.1 (1986). DOI : 10.1007/BF01206953.

[45] M. Avery et A. Scheel. « Universal selection of pulled fronts ». In : *Communications of the American Mathematical Society* 2.5 (2022). DOI : 10.1090/cams/8.

[46] M. Avery. *Front selection in reaction-diffusion systems via diffusive normal forms*. arXiv :2211.11829 [nlin]. 2023.

[47] M. Avery, M. Holzer et A. Scheel. *Pushed and pulled fronts in a logistic Keller-Segel model with chemorepulsion*. arXiv :2308.01754 [math]. 2023.

[48] M. Avery, M. Holzer et A. Scheel. « Pushed-to-Pulled Front Transitions : Continuation, Speed Scalings, and Hidden Monotonicty ». In : *Journal of Nonlinear Science* 33.6 (2023). DOI : 10.1007/s00332-023-09957-3.

[49] M. Avery et L. Garénaux. « Spectral stability of the critical front in the extended Fisher-KPP equation ». In : *Zeitschrift für angewandte Mathematik und Physik* 74.2 (2023). DOI : 10.1007/s00033-023-01960-8.

[50] G. Faye et G. Peltier. « Anomalous invasion speed in a system of coupled reaction-diffusion equations ». In : *Communications in Mathematical Sciences* 16.2 (2018). DOI : 10.4310/CMS.2018.v16.n2.a7.

[51] G. Faye et M. Holzer. « Modulated traveling fronts for a nonlocal Fisher-KPP equation : A dynamical systems approach ». In : *Journal of Differential Equations* 258.7 (2015). DOI : 10.1016/j.jde.2014.12.006.

[52] G. Faye, M. Holzer et A. Scheel. « Linear spreading speeds from nonlinear resonant interaction ». In : *Nonlinearity* 30.6 (2017). DOI : 10.1088/1361-6544/aa6c74.

[53] M. Holzer et A. Scheel. « A slow pushed front in a Lotka–Volterra competition model ». In : *Nonlinearity* 25.7 (2012). DOI : 10.1088/0951-7715/25/7/2151.

[54] M. Holzer. « Anomalous spreading in a system of coupled Fisher–KPP equations ». In : *Physica D : Nonlinear Phenomena* 270 (2014). DOI : 10.1016/j.physd.2013.12.003.

[55] M. Holzer et A. Scheel. « Criteria for Pointwise Growth and Their Role in Invasion Processes ». In : *Journal of Nonlinear Science* 24.4 (2014). doi : 10.1007/s00332-014-9202-0.

[56] S. Tobias, M. Proctor et E. Knobloch. « Convective and absolute instabilities of fluid flows in finite geometry ». In : *Physica D : Nonlinear Phenomena* 113.1 (1998). doi : 10.1016/S0167-2789(97)00141-3.

[57] B. Sandstede et A. Scheel. « Absolute and convective instabilities of waves on unbounded and large bounded domains ». In : *Physica D : Nonlinear Phenomena* 145.3-4 (2000). doi : 10.1016/S0167-2789(00)00114-7.

[58] J. A. Sherratt, A. S. Dagbovie et F. M. Hilker. « A Mathematical Biologist's Guide to Absolute and Convective Instability ». In : *Bulletin of Mathematical Biology* 76.1 (2014). doi : 10.1007/s11538-013-9911-9.

[59] R. A. Fisher. « The wave of advance of advantageous genes ». In : *Annals of Eugenics* 7.4 (1937). doi : 10.1111/j.1469-1809.1937.tb02153.x.

[60] A. N. Kolmogorov. « A study of the equation of diffusion with increase in the quantity of matter, and its application to a biological problem ». In : *Moscow University Bulletin of Mathematics* 1 (1937).

[61] H. F. Weinberger, M. A. Lewis et B. Li. « Anomalous spreading speeds of cooperative recursion systems ». In : *Journal of Mathematical Biology* 55.2 (2007). doi : 10.1007/s00285-007-0078-6.

[62] J. Garnier et al. « Inside dynamics of pulled and pushed fronts ». In : *Journal de Mathématiques Pures et Appliquées* 98.4 (2012). doi : 10.1016/j.matpur.2012.02.005.

[63] K. P. Hadeler et F. Rothe. « Travelling fronts in nonlinear diffusion equations ». In : *Journal Of Mathematical Biology* 2.3 (1975). doi : 10.1007/BF00277154.

[64] E. Ben-Jacob et al. « Pattern propagation in nonlinear dissipative systems ». In : *Physica D : Nonlinear Phenomena* 14.3 (1985). doi : 10.1016/0167-2789(85)90094-6.

[65] W. Van Saarloos et P. Hohenberg. « Fronts, pulses, sources and sinks in generalized complex Ginzburg-Landau equations ». In : *Physica D : Nonlinear Phenomena* 56.4 (1992). doi : 10.1016/0167-2789(92)90175-M.

[66] M. R. Myerscough et J. D. Murray. « Analysis of propagating pattern in a chemotaxis system ». In : *Bulletin of Mathematical Biology* 54.1 (1992). doi : 10.1007/BF02458621.

[67] K. Tarumi et E. Mueller. « Wavelength selection mechanism in the gierer-meinhardt model ». In : *Bulletin of Mathematical Biology* 51.2 (1989). doi : 10.1016/S0092-8240(89)80068-0.

[68] P. Collet et J.-P. Eckmann. *Instabilities and Fronts in Extended Systems :* Princeton University Press, 1990. doi : 10.1515/9781400861026.

[69] M. Avery. *Front propagation close to the onset of instability.* Version Number : 1. 2023. doi : 10.48550/ARXIV.2310.13602.

[70] V. Klika, E. A. Gaffney et P. K. Maini. *On the speed of propagation in Turing patterns for reaction-diffusion systems*. arXiv :2403.09247 [nlin]. 2024.

[71] G. Gambino, M. Lombardo et M. Sammartino. « Pattern formation driven by cross-diffusion in a 2D domain ». In : *Nonlinear Analysis : Real World Applications* 14.3 (2013). doi : 10.1016/j.nonrwa.2012.11.009.

[72] M. Ma, M. Gao et R. Carretero-González. « Pattern formation for a two-dimensional reaction-diffusion model with chemotaxis ». In : *Journal of Mathematical Analysis and Applications* 475.2 (2019). doi : 10.1016/j.jmaa.2019.03.060.

[73] V. Giunta, M. C. Lombardo et M. Sammartino. « Pattern Formation and Transition to Chaos in a Chemotaxis Model of Acute Inflammation ». In : *SIAM Journal on Applied Dynamical Systems* 20.4 (2021). doi : 10.1137/20M1358104.

[74] R. Hoyle. *Pattern Formation : An Introduction to Methods*. 1re éd. Cambridge University Press, 2006. doi : 10.1017/CBO9780511616051.

[75] R. Bailleul et al. « Symmetry breaking in the embryonic skin triggers directional and sequential plumage patterning ». In : *PLOS Biology* 17.10 (2019). Sous la dir. de C. S. Hill. doi : 10.1371/journal.pbio.3000448.

[76] D. Dhouailly. « A new scenario for the evolutionary origin of hair, feather, and avian scales ». In : *Journal of Anatomy* 214.4 (2009). doi : 10.1111/j.1469-7580.2008.01041.x.

[77] A. Diez et al. « Turing Pattern Formation in Reaction-Cross-Diffusion Systems with a Bilayer Geometry ». In : *Bulletin of Mathematical Biology* 86.2 (2024). doi : 10.1007/s11538-023-01237-1.

[78] C.-C. Tseng et al. « Gap junctions in Turing-type periodic feather pattern formation ». In : *PLOS Biology* 22.5 (2024). Sous la dir. de G. S. Barsh. doi : 10.1371/journal.pbio.3002636.

[79] F. Michon et al. « BMP2 and BMP7 play antagonistic roles in feather induction ». In : *Development* 135.16 (2008). doi : 10.1242/dev.018341.

[80] K. J. Painter, W. Ho et D. J. Headon. « A chemotaxis model of feather primordia pattern formation during avian development ». In : *Journal of Theoretical Biology* 437 (2018). doi : 10.1016/j.jtbi.2017.10.026.

[81] N. A. Barnafi et al. « Coupling Chemotaxis and Growth Poromechanics for the Modelling of Feather Primordia Patterning ». In : *Mathematics* 10.21 (2022). doi : 10.3390/math10214096.

[82] W. K. W. Ho et al. « Feather arrays are patterned by interacting signalling and cell density waves ». In : *PLOS Biology* 17.2 (2019). Sous la dir. de G. S. Barsh. doi : 10.1371/journal.pbio.3000132.

[83] A. Nakamasu et al. « Interactions between zebrafish pigment cells responsible for the generation of Turing patterns ». In : *Proceedings of the National Academy of Sciences* 106.21 (2009). doi : 10.1073/pnas.0808622106.

[84] L. Manukyan et al. « A living mesoscopic cellular automaton made of skin scales ». In : *Nature* 544.7649 (2017). doi : 10.1038/nature22031.

[85] A. Sadier et al. « Modeling Edar expression reveals the hidden dynamics of tooth signaling center patterning ». In : *PLOS Biology* 17.2 (2019). Sous la dir. de C. S. Hill. doi : 10.1371/journal.pbio.3000064.

[86] A. D. Economou, N. A. M. Monk et J. B. A. Green. « Perturbation analysis of a multi-morphogen turing reaction-diffusion stripe patterning system reveals key regulatory interactions ». In : *Development* (2020). doi : 10.1242/dev.190553.

[87] M. Ma et al. « Chemotaxis-driven pattern formation for a reaction–diffusion–chemotaxis model with volume-filling effect ». In : *Computers & Mathematics with Applications* 72.5 (2016). doi : 10.1016/j.camwa.2016.06.039.

[88] A. M. Turing. « The chemical basis of morphogenesis ». In : *Bulletin of Mathematical Biology* 52.1-2 (1990). doi : 10.1007/BF02459572.

[89] C. Mou et al. « Generation of the primary hair follicle pattern ». In : *Proceedings of the National Academy of Sciences* 103.24 (2006). doi : 10.1073/pnas.0600825103.

[90] J. D. Glover et al. « Hierarchical patterning modes orchestrate hair follicle morphogenesis ». In : *PLOS Biology* 15.7 (2017). Sous la dir. de C. Hill. doi : 10.1371/journal.pbio.2002117.

[91] P. Kulesa et al. « On a Model Mechanism for the Spatial Patterning of Teeth Primordia in the Alligator ». In : *Journal of Theoretical Biology* 180.4 (1996). doi : 10.1006/jtbi.1996.0103.

[92] R. L. Cooper et al. « An ancient Turing-like patterning mechanism regulates skin denticle development in sharks ». In : *Science Advances* 4.11 (2018). doi : 10.1126/sciadv.aau5484.

[93] M. N. Evanitsky et S. Di Talia. « An active traveling wave of Eda/NF-kappaB signaling controls the timing and hexagonal pattern of skin appendages in zebrafish ». In : *Development* 150.18 (2023). doi : 10.1242/dev.201866.

[94] A. Sadier et al. « Bat teeth illuminate the diversification of mammalian tooth classes ». In : *Nature Communications* 14.1 (2023). doi : 10.1038/s41467-023-40158-4.

[95] A. C. Tzika et al. « Somitic positional information guides self-organized patterning of snake scales ». In : *Science Advances* 9.24 (2023). doi : 10.1126/sciadv.adf8834.

[96] E. Jahanbakhsh et M. C. Milinkovitch. « Modeling convergent scale-by-scale skin color patterning in multiple species of lizards ». In : *Current Biology* 32.23 (2022). doi : 10.1016/j.cub.2022.10.044.

[97] J. Zheng et al. « A new result for global existence and boundedness of solutions to a parabolic–parabolic Keller–Segel system with logistic source ». In : *Journal of Mathematical Analysis and Applications* 462.1 (2018). doi : 10.1016/j.jmaa.2018.01.064.

[98] Y. Liu, P. K. Maini et R. E. Baker. « Control of diffusion-driven pattern formation behind a wave of competency ». In : *Physica D : Nonlinear Phenomena* (2022). Publisher : Elsevier.

[99] C. Fraga Delfino Kunz et al. « Novel Aspects in Pattern Formation Arise from Coupling Turing Reaction–Diffusion and Chemotaxis ». In : *Bulletin of Mathematical Biology* 86.1 (2024). doi : 10.1007/s11538-023-01225-5.

[100] C. Curantz et al. « Cell shape anisotropy contributes to self-organized feather pattern fidelity in birds ». In : *PLOS Biology* 20.10 (2022). Sous la dir. de M. E. Bronner. doi : 10.1371/journal.pbio.3001807.

[101] R. Han et B. Dai. « Cross-diffusion induced Turing instability and amplitude equation for a toxic-phytoplankton–zooplankton model with nonmonotonic functional response ». In : *International Journal of Bifurcation and Chaos* 27.06 (2017). Publisher : World Scientific.

[102] Y. Han et al. « Wavefront invasion for a volume-filling chemotaxis model with logistic growth ». In : *Computers & Mathematics with Applications* 71.2 (2016). Publisher : Elsevier.

[103] Y. Han et al. « Pattern formation for a volume-filling chemotaxis model with logistic growth ». In : *Journal of Mathematical Analysis and Applications* 448.2 (2017). Publisher : Elsevier.

[104] H. Uecker, D. Wetzel et J. D. M. Rademacher. *pde2path - A Matlab package for continuation and bifurcation in 2D elliptic systems*. arXiv :1208.3112 [math]. 2012.

[105] H. Uecker. *Numerical continuation and bifurcation in nonlinear PDEs*. Other Titles 174. Philadelphia : Society for Industrial et Applied Mathematics, 2021.

[106] H. Uecker. *Pattern formation with pde2path – a tutorial*. Version Number : 3. 2019. doi : 10.48550/ARXIV.1908.05211.

[107] W. v. Saarloos, M. v. Hecke et P. Hohenberg. « Amplitude equations for pattern forming systems ». In : (1994).

[108] Z. R. Sudderick et J. D. Glover. « Periodic pattern formation during embryonic development ». In : *Biochemical Society Transactions* 52.1 (2024). doi : 10.1042/BST20230197.

[109] G. C. Cruywagen, J. D. Murray et P. K. Maini. « Biological pattern formation on two-dimensional spatial domains : a nonlinear bifurcation analysis ». In : *SIAM Journal on Applied Mathematics* 57.6 (1997). Publisher : SIAM.

[110] R. Goh et A. Scheel. « Triggered fronts in the complex Ginzburg Landau equation ». In : *Journal of Nonlinear Science* 24.1 (2014). Publisher : Springer.

[111] R. Goh et A. Scheel. « Pattern formation in the wake of triggered pushed fronts ». In : *Nonlinearity* 29.8 (2016). Publisher : IOP Publishing.

[112] M. Avery et al. « Growing Stripes, with and without Wrinkles ». In : *SIAM Journal on Applied Dynamical Systems* 18.2 (2019). doi : 10.1137/18M1221989.

[113] R. Goh et A. Scheel. « Pattern-forming fronts in a Swift–Hohenberg equation with directional quenching — parallel and oblique stripes ». In : *Journal of the London Mathematical Society* 98.1 (2018). doi : 10.1112/jlms.12122.

[114] R. Goh et A. Scheel. « Growing patterns ». In : *Nonlinearity* 36.10 (2023). doi : 10.1088/1361-6544/acf265.

[115] D. Kaiser. « Signaling in myxobacteria ». In : *Annual Review of Microbiology* 58.1 (2004). doi : 10.1146/annurev.micro.58.030603.123620.

[116] J. Pérez et al. « Rhizobial galactoglucan determines the predatory pattern of Myxococcus xanthus and protects Sinorhizobium meliloti from predation ». In : *Environmental Microbiology* 16.7 (2014). doi : 10.1111/1462-2920.12477.

[117] J. E. Berleman et al. « Rippling Is a Predatory Behavior in *Myxococcus xanthus* ». In : *Journal of Bacteriology* 188.16 (2006). doi : 10.1128/JB.00559-06.

[118] B. Sager et D. Kaiser. « Intercellular C-signaling and the traveling waves of Myxococcus. » In : *Genes & Development* 8.23 (1994). doi : 10.1101/gad.8.23.2793.

[119] O. Sliusarenko et al. « Accordion waves in *Myxococcus xanthus* ». In : *Proceedings of the National Academy of Sciences* 103.5 (2006). doi : 10.1073/pnas.0507720103.

[120] L. M. Faure et al. « The mechanism of force transmission at bacterial focal adhesion complexes ». In : *Nature* 539.7630 (2016). doi : 10.1038/nature20121.

[121] R. Mercier et al. « The polar Ras-like GTPase MglA activates type IV pilus via SgmX to enable twitching motility in *Myxococcus xanthus* ». In : *Proceedings of the National Academy of Sciences* 117.45 (2020). doi : 10.1073/pnas.2002783117.

[122] J. Hodgkin et D. Kaiser. « Genetics of gliding motility in Myxococcus xanthus (Myxobacterales) : Two gene systems control movement ». In : *Molecular and General Genetics MGG* 171.2 (1979). doi : 10.1007/BF00270004.

[123] H. Bloch et al. « Modelling, analysis, and simulation of traffic jam in colonies of Myxococcus xanthus (In preparation) ». In : *In preparation* (2023).

[124] B. D. Blackhart et D. R. Zusman. « "Frizzy" genes of Myxococcus xanthus are involved in control of frequency of reversal of gliding motility. » In : *Proceedings of the National Academy of Sciences* 82.24 (1985). doi : 10.1073/pnas.82.24.8767.

[125] M. Dworkin. « Tactic behavior of Myxococcus xanthus ». In : *Journal of Bacteriology* 154.1 (1983). doi : 10.1128/jb.154.1.452-459.1983.

[126] R. Mercier et T. Mignot. « Regulations governing the multicellular lifestyle of Myxococcus xanthus ». In : *Current Opinion in Microbiology* 34 (2016). doi : 10.1016/j.mib.2016.08.009.

[127] M. Dworkin et D. Eide. « *Myxococcus xanthus* Does Not Respond Chemotactically to Moderate Concentration Gradients ». In : *Journal of Bacteriology* 154.1 (1983). doi : 10.1128/jb.154.1.437-442.1983.

[128] E. Rosenberg et M. Varon. « Antibiotics and Lytic Enzymes ». In : *Myxobacteria*. Sous la dir. d'A. Rich et E. Rosenberg. Series Title : Springer Series in Molecular Biology. New York, NY : Springer New York, 1984. doi : 10.1007/978-1-4613-8280-5_5.

[129] A. D. Morgan et al. « Comparative Analysis of *Myxococcus* Predation on Soil Bacteria ». In : *Applied and Environmental Microbiology* 76.20 (2010). doi : 10.1128/AEM.00414-10.

[130] J. Muñoz-Dorado et al. « Myxobacteria : Moving, Killing, Feeding, and Surviving Together ». In : *Frontiers in Microbiology* 7 (2016). DOI : 10.3389/fmicb.2016.00781.

[131] J. E. Berleman et al. « Predataxis behavior in *Myxococcus xanthus* ». In : *Proceedings of the National Academy of Sciences* 105.44 (2008). DOI : 10.1073/pnas.0804387105.

[132] S. Thiery et C. Kaimer. « The Predation Strategy of Myxococcus xanthus ». In : *Frontiers in Microbiology* 11 (2020). DOI : 10.3389/fmicb.2020.00002.

[133] J. E. Berleman et J. R. Kirby. « Deciphering the hunting strategy of a bacterial wolfpack ». In : *FEMS Microbiology Reviews* 33.5 (2009). DOI : 10.1111/j.1574-6976.2009.00185.x.

[134] Y. Xiao et al. « Antibiotic Production by Myxobacteria Plays a Role in Predation ». In : *Journal of Bacteriology* 193.18 (2011). DOI : 10.1128/JB.05052-11.

[135] S. Thiery et al. « The predatory soil bacterium Myxococcus xanthus combines a Tad- and an atypical type 3-like protein secretion system to kill bacterial cells ». In : *Cell Reports* 40.11 (2022). DOI : 10.1016/j.celrep.2022.111340.

[136] W. Zhang et al. « Dynamics of Solitary Predation by Myxococcus xanthus on Escherichia coli Observed at the Single-Cell Level ». In : *Applied and Environmental Microbiology* 86.3 (2020). Sous la dir. de H. Nojiri. DOI : 10.1128/AEM.02286-19.

[137] S. Seef et al. « A Tad-like apparatus is required for contact-dependent prey killing in predatory social bacteria ». In : *eLife* 10 (2021). DOI : 10.7554/eLife.72409.

[138] E. Rosenberg, K. H. Keller et M. Dworkin. « Cell density-dependent growth of Myxococcus xanthus on casein ». In : *Journal of Bacteriology* 129.2 (1977). DOI : 10.1128/jb.129.2.770-777.1977.

[139] S. Panigrahi et al. « Misic, a general deep learning-based method for the high-throughput cell segmentation of complex bacterial communities ». In : *eLife* 10 (2021). DOI : 10.7554/eLife.65151.

[140] S. Rombouts et al. « Multi-scale dynamic imaging reveals that cooperative motility behaviors promote efficient predation in bacteria ». In : *Nature Communications* 14.1 (2023). DOI : 10.1038/s41467-023-41193-x.

[141] A. Gallegos, B. Mazzag et A. Mogilner. « Two continuum models for the spreading of myxobacteria swarms ». In : *Bulletin of Mathematical Biology* 68.4 (2006). DOI : 10.1007/s11538-005-9031-2.

[142] P. Patra et al. « Colony Expansion of Socially Motile Myxococcus xanthus Cells Is Driven by Growth, Motility, and Exopolysaccharide Production ». In : *PLOS Computational Biology* 12.6 (2016). Sous la dir. de C. V. Rao. DOI : 10.1371/journal.pcbi.1005010.

[143] Lutscher et Stevens. « Emerging Patterns in a Hyperbolic Model for Locally Interacting Cell Systems ». In : *Journal of Nonlinear Science* 12.6 (2003). DOI : 10.1007/s00332-002-0510-4.

[144] A. Manhart. « Counter-propagating wave patterns in a swarm model with memory ». In : *Journal of Mathematical Biology* 78.3 (2019). DOI : 10.1007/s00285-018-1287-x.

[145] O. A. Igoshin et al. « Pattern formation and traveling waves in myxobacteria : Theory and modeling ». In : *Proceedings of the National Academy of Sciences* 98.26 (2001). DOI : 10.1073/pnas.221579598.

[146] O. A. Igoshin et al. « Waves and aggregation patterns in myxobacteria ». In : *Proceedings of the National Academy of Sciences* 101.12 (2004). DOI : 10.1073/pnas.0400704101.

[147] S. Hittmeir et al. *Kinetic Modelling of Colonies of Myxobacteria*. Version Number : 2. 2020. DOI : 10.48550/ARXIV.2001.02711.

[148] V. Calvez et al. « Regime switching on the propagation speed of travelling waves of some size-structured Myxobacteriapopulation models ». In : *In preparation* (2023).

[149] M. Estavoyer et T. Lepoutre. « Travelling waves for a fast reaction limit of a discrete coagulation–fragmentation model with diffusion and proliferation ». In : *Journal of Mathematical Biology* 89.1 (2024). DOI : 10.1007/s00285-024-02099-4.

[150] S. Focant et T. Gallay. « Existence and stability of propagating fronts for an autocatalytic reaction-diffusion system ». In : *Physica D : Nonlinear Phenomena* 120.3-4 (1998). DOI : 10.1016/S0167-2789(98)00096-7.

[151] J. A. Shapiro. « Thinking about bacterial populations as multicellular organisms ». In : *Annual Review of Microbiology* 52.1 (1998). DOI : 10.1146/annurev.micro.52.1.81.

[152] S. V. Avery. « Microbial cell individuality and the underlying sources of heterogeneity ». In : *Nature Reviews Microbiology* 4.8 (2006). DOI : 10.1038/nrmicro1460.

[153] Y. Zhang et al. « From individual cell motility to collective behaviors : insights from a prokaryote, *Myxococcus xanthus* ». In : *FEMS Microbiology Reviews* 36.1 (2012). DOI : 10.1111/j.1574-6976.2011.00307.x.

[154] A. Ducrot et P. Magal. « Travelling wave solutions for an infection-age structured model with diffusion ». In : *Proceedings of the Royal Society of Edinburgh : Section A Mathematics* 139.3 (2009). DOI : 10.1017/S0308210507000455.

[155] E. Bouin et V. Calvez. « Travelling waves for the cane toads equation with bounded traits ». In : *Nonlinearity* 27.9 (2014). DOI : 10.1088/0951-7715/27/9/2233.

[156] M. Alfaro, J. Coville et G. Raoul. « Travelling Waves in a Nonlocal Reaction-Diffusion Equation as a Model for a Population Structured by a Space Variable and a Phenotypic Trait ». In : *Communications in Partial Differential Equations* 38.12 (2013). DOI : 10.1080/03605302.2013.828069.

[157] Q. Griette. « Singular measure traveling waves in an epidemiological model with continuous phenotypes ». In : *Transactions of the American Mathematical Society* 371.6 (2018). DOI : 10.1090/tran/7700.

[158] R. Keane et J. Berleman. « The predatory life cycle of Myxococcus xanthus ». In : *Microbiology* 162.1 (2016). DOI : 10.1099/mic.0.000208.

[159] K. L. Hillesland, G. J. Velicer et R. E. Lenski. « Experimental evolution of a microbial predator's ability to find prey ». In : *Proceedings of the Royal Society B : Biological Sciences* 276.1656 (2009). doi : 10.1098/rspb.2008.1098.

[160] M. J. McBride et D. R. Zusman. « Behavioral analysis of single cells of *Myxococcus xanthus* in response to prey cells of *Escherichia coli* ». In : *FEMS Microbiology Letters* 137.2-3 (1996). doi : 10.1111/j.1574-6968.1996.tb08110.x.

[161] M. Osborne. « On shooting methods for boundary value problems ». In : *Journal of Mathematical Analysis and Applications* 27.2 (1969). doi : 10.1016/0022-247X(69)90059-6.

[162] P. Degond, J.-G. Liu et R. L. Pego. « Coagulation–Fragmentation Model for Animal Group-Size Statistics ». In : *Journal of Nonlinear Science* 27.2 (2017). doi : 10.1007/s00332-016-9336-3.

[163] P. Laurençot. « Stationary solutions to coagulation-fragmentation equations ». In : (2019). doi : 10.48550/ARXIV.1904.01868.

[164] S. Rombouts. « Advanced microscopies for the study of motility behavior in predating Myxococcus xanthus ». PhD Thesis. Université Montpellier, 2021.

[165] E. Bouin, V. Calvez et G. Nadin. « Propagation in a Kinetic Reaction-Transport Equation : Travelling Waves And Accelerating Fronts ». In : *Archive for Rational Mechanics and Analysis* 217.2 (2015). doi : 10.1007/s00205-014-0837-7.

[166] J. A. Carrillo, L. Desvillettes et K. Fellner. « Rigorous Derivation of a Nonlinear Diffusion Equation as Fast-Reaction Limit of a Continuous Coagulation-Fragmentation Model with Diffusion ». In : *Communications in Partial Differential Equations* 34.11 (2009). doi : 10.1080/03605300903225396.

[167] L. Desvillettes et K. Fellner. « Large Time Asymptotics for a Continuous Coagulation-Fragmentation Model with Degenerate Size-Dependent Diffusion ». In : *SIAM Journal on Mathematical Analysis* 41.6 (2010). doi : 10.1137/090752602.

[168] M. Aizenman et T. A. Bak. « Convergence to equilibrium in a system of reacting polymers ». In : *Communications in Mathematical Physics* 65.3 (1979). doi : 10.1007/BF01197880.

[169] D. Aronson et H. Weinberger. « Multidimensional nonlinear diffusion arising in population genetics ». In : *Advances in Mathematics* 30.1 (1978). doi : 10.1016/0001-8708(78)90130-5.

[170] M. Holzer. « A proof of anomalous invasion speeds in a system of coupled Fisher-KPP equations ». In : (2014). Publisher : arXiv Version Number : 2. doi : 10.48550/ARXIV.1409.8641.

[171] K. Hadeler. « Free boundary problems in biological models ». In : *Free boundary problems : Theory and applications* 2 (1983).

[172] H. Engler. « Relations between travelling wave solutions of quasilinear parabolic equations ». In : *Proceedings of the American Mathematical Society* 93.2 (1985). doi : 10.1090/S0002-9939-1985-0770540-6.

[173] J. An, C. Henderson et L. Ryzhik. « Pushed, pulled and pushmi-pullyu fronts of the Burgers-FKPP equation ». In : *Journal of the European Mathematical Society* (2023). DOI : 10.4171/jems/1407.

[174] J. Billingham et D. Needham. « The development of travelling waves in quadratic and cubic autocatalysis with unequal diffusion rates. I. Permanent form travelling waves ». In : *Philosophical Transactions of the Royal Society of London. Series A : Physical and Engineering Sciences* 334.1633 (1991). DOI : 10.1098/rsta.1991.0001.

[175] M. A. Lewis, B. Li et H. F. Weinberger. « Spreading speed and linear determinacy for two-species competition models ». In : *Journal of Mathematical Biology* 45.3 (2002). DOI : 10.1007/s002850200144.

[176] M. Arias et al. « Fast and heteroclinic solutions for a second order ODE related to Fisher-Kolmogorov ?s equation ». In : *Calculus of Variations* 21.3 (2004). DOI : 10.1007/s00526-004-0264-y.

[177] C. Marcelli et F. Papalini. « A new estimate on the minimal wave speed for travelling fronts in reaction–diffusion–convection equations ». In : *Electronic Journal of Qualitative Theory of Differential Equations* 10 (2018). DOI : 10.14232/ejqtde.2018.1.10.

[178] R. D. Benguria et M. C. Depassier. « Variational characterization of the speed of propagation of fronts for the nonlinear diffusion equation ». In : *Communications in Mathematical Physics* 175.1 (1996). DOI : 10.1007/BF02101631.

[179] R. D. Benguria et M. C. Depassier. « Speed of Fronts of the Reaction-Diffusion Equation ». In : *Physical Review Letters* 77.6 (1996). DOI : 10.1103/PhysRevLett.77.1171.

[180] E. C. Elliott et S. J. Cornell. « Dispersal Polymorphism and the Speed of Biological Invasions ». In : *PLoS ONE* 7.7 (2012). Sous la dir. de M. Heil. DOI : 10.1371/journal.pone.0040496.

[181] V. Volpert. *Elliptic Partial Differential Equations : Volume 2 : Reaction-Diffusion Equations*. T. 104. Monographs in Mathematics. Basel : Springer Basel, 2014. DOI : 10.1007/978-3-0348-0813-2.

[182] A. I. Volpert, V. A. Volpert et V. A. Volpert. *Traveling wave solutions of parabolic systems*. T. 140. OCLC : 57479340. Providence, R.I. : American Mathematical Society, 1994.

[183] M. Banerjee, V. Vougalter et V. Volpert. « Doubly nonlocal reaction–diffusion equations and the emergence of species ». In : *Applied Mathematical Modelling* 42 (2017). DOI : 10.1016/j.apm.2016.10.041.

[184] M. Adimy, A. Chekroun et B. Kazmierczak. « Traveling waves in a coupled reaction–diffusion and difference model of hematopoiesis ». In : *Journal of Differential Equations* 262.7 (2017). DOI : 10.1016/j.jde.2016.12.009.

[185] M. Adimy, A. Chekroun et B. Kazmierczak. « Traveling waves for reaction-diffusion PDE coupled to difference equation with nonlocal dispersal term and time delay ». In : *Mathematical Modelling of Natural Phenomena* 17 (2022). DOI : 10.1051/mmnp/2022021.

[186] A. Kolmogorov. « Étude de l'équation de la diffusion avec croissance de la quantité de matière et son application à un problème biologique ». In : *Moscow Univ. Bull. Math.* 1 (1937).

[187] A. Okubo. « Diffusion and ecological problems : mathematical models ». In : *Biomath* 10 (1980). Publisher : Springer-Verlag.

[188] H. G. Othmer et S. Levin, éd. *Nonlinear Oscillations in Biology and Chemistry*. T. 66. Lecture Notes in Biomathematics. Berlin, Heidelberg : Springer Berlin Heidelberg, 1986. doi : 10.1007/978-3-642-93318-9.

[189] E. E. Holmes. « Are Diffusion Models too Simple ? A Comparison with Telegraph Models of Invasion ». In : *The American Naturalist* 142.5 (1993). doi : 10.1086/285572.

[190] T. Hillen. « Hyperbolic models for chemosensitive movement ». In : *Mathematical Models and Methods in Applied Sciences* 12.07 (2002). doi : 10.1142/S0218202502002008.

[191] J. A. Carrillo et al. « Double milling in self-propelled swarms from kinetic theory ». In : *Kinetic & Related Models* 2.2 (2009). doi : 10.3934/krm.2009.2.363.

[192] J. A. Carrillo, R. Eftimie et F. K. O. Hoffmann. *Non-local kinetic and macroscopic models for self-organised animal aggregations*. Version Number : 1. 2014. doi : 10.48550/ARXIV.1407.2099.

[193] T. Hillen et A. Stevens. « Hyperbolic models for chemotaxis in 1-D ». In : *Nonlinear Analysis : Real World Applications* 1.3 (2000). doi : 10.1016/S0362-546X(99)00284-9.

[194] J. Saragosti et al. « Directional persistence of chemotactic bacteria in a traveling concentration wave ». In : *Proceedings of the National Academy of Sciences* 108.39 (2011). doi : 10.1073/pnas.1101996108.

[195] M. Kac. « A stochastic model related to the telegrapher's equation ». In : *The Rocky Mountain Journal of Mathematics* 4.3 (1974). Publisher : JSTOR.

[196] K. P. Hadeler. « Hyperbolic travelling fronts ». In : *Proceedings of the Edinburgh Mathematical Society* 31.1 (1988). doi : 10.1017/S001309150000660X.

[197] V. Méndez et J. Camacho. « Dynamics and thermodynamics of delayed population growth ». In : *Physical Review E* 55.6 (1997). doi : 10.1103/PhysRevE.55.6476.

[198] S. Fedotov. *Traveling waves in reaction-diffusion system*. arXiv :cond-mat/9807352. 1998.

[199] K. P. Hadeler. « Reaction transport systems in biological modelling ». In : *Mathematics Inspired by Biology*. Sous la dir. de V. Capasso. T. 1714. Series Title : Lecture Notes in Mathematics. Berlin, Heidelberg : Springer Berlin Heidelberg, 1999. doi : 10.1007/BFb0092376.

[200] V. Méndez, J. Fort et J. Farjas. « Speed of wave-front solutions to hyperbolic reaction-diffusion equations ». In : *Physical Review E* 60.5 (1999). doi : 10.1103/PhysRevE.60.5231.

[201] B. Gilding et R. Kersner. « Wavefront solutions of a nonlinear telegraph equation ». In : *Journal of Differential Equations* 254.2 (2013). doi : 10.1016/j.jde.2012.09.007.

[202] E. Bouin, V. Calvez et G. Nadin. « Hyperbolic traveling waves driven by growth ». In : *Mathematical Models and Methods in Applied Sciences* 24.06 (2014). arXiv :1110.3242 [math]. doi : 10.1142/S0218202513500802.

[203] V. Méndez, D. Campos et W. Horsthemke. « Growth and dispersal with inertia : Hyperbolic reaction-transport systems ». In : *Physical Review E* 90.4 (2014). doi : 10.1103/PhysRevE.90.042114.

[204] E. Barbera, C. Currò et G. Valenti. « On discontinuous travelling wave solutions for a class of hyperbolic reaction–diffusion models ». In : *Physica D : Nonlinear Phenomena* 308 (2015). doi : 10.1016/j.physd.2015.06.011.

[205] E. Barbera et G. Valenti. « Wave features of a hyperbolic reaction–diffusion model for Chemotaxis ». In : *Wave Motion* 78 (2018). doi : 10.1016/j.wavemoti.2018.02.004.

[206] F. Filbet et S. Jin. « A class of asymptotic preserving schemes for kinetic equations and related problems with stiff sources ». In : *Journal of Computational Physics* 229.20 (2010). arXiv :0905.1378 [math]. doi : 10.1016/j.jcp.2010.06.017.

[207] B. Després et F. Lagoutière. « Un schéma non linéaire anti-dissipatif pour l'équation d'advection linéaire ». In : *Comptes Rendus de l'Académie des Sciences - Series I - Mathematics* 328.10 (1999). doi : 10.1016/S0764-4442(99)80301-2.

[208] R. Leveque et H. Yee. « A study of numerical methods for hyperbolic conservation laws with stiff source terms ». In : *Journal of Computational Physics* 86.1 (1990). doi : 10.1016/0021-9991(90)90097-K.

[209] C. Lattanzio et al. *Analysis and numerics of the propagation speed for hyperbolic reaction-diffusion models*. arXiv :2206.09714 [cs, math]. 2022.

[210] A. M. Spormann. « Gliding Motility in Bacteria : Insights from Studies of *Myxococcus xanthus* ». In : *Microbiology and Molecular Biology Reviews* 63.3 (1999). doi : 10.1128/MMBR.63.3.621-641.1999.

[211] J. S. Mattick. « Type IV Pili and Twitching Motility ». In : *Annual Review of Microbiology* 56.1 (2002). doi : 10.1146/annurev.micro.56.012302.160938.

[212] D. Kaiser et C. Crosby. « Cell movement and its coordination in swarms of myxococcus xanthus ». In : *Cell Motility* 3.3 (1983). doi : 10.1002/cm.970030304.

[213] S. Müller et al. « Bacillaene and Sporulation Protect Bacillus subtilis from Predation by Myxococcus xanthus ». In : *Applied and Environmental Microbiology* 80.18 (2014). Sous la dir. d'A. M. Spormann. doi : 10.1128/AEM.01621-14.

[214] S. Müller et al. « Predation by Myxococcus xanthus Induces Bacillus subtilis To Form Spore-Filled Megastructures ». In : *Applied and Environmental Microbiology* 81.1 (2015). Sous la dir. de M. A. Elliot. doi : 10.1128/AEM.02448-14.

[215] W. H. DePas et al. « Biofilm Formation Protects Escherichia coli against Killing by Caenorhabditis elegans and Myxococcus xanthus ». In : *Applied and Environmental Microbiology* 80.22 (2014). Sous la dir. de H. Nojiri. doi : 10.1128/AEM.02464-14.

[216] M. Vasse et al. « Killer prey : Ecology reverses bacterial predation ». In : *PLOS Biology* 22.1 (2024). Sous la dir. de L. Søgaard-Andersen. doi : 10.1371/journal.pbio.3002454.

[217] L. J. Shimkets et D. Kaiser. « Induction of coordinated movement of Myxococcus xanthus cells ». In : *Journal of Bacteriology* 152.1 (1982). doi : 10.1128/jb.152.1.451-461.1982.

[218] K. A. O'Connor et D. R. Zusman. « Development in Myxococcus xanthus involves differentiation into two cell types, peripheral rods and spores ». In : *Journal of Bacteriology* 173.11 (1991). doi : 10.1128/jb.173.11.3318-3333.1991.

[219] R. Eftimie, G. De Vries et M. A. Lewis. « Complex spatial group patterns result from different animal communication mechanisms ». In : *Proceedings of the National Academy of Sciences* 104.17 (2007). doi : 10.1073/pnas.0611483104.

[220] O. Sozinova et al. « A three-dimensional model of myxobacterial fruiting-body formation ». In : *Proceedings of the National Academy of Sciences* 103.46 (2006). doi : 10.1073/pnas.0605555103.

[221] O. Sliusarenko, D. R. Zusman et G. Oster. « Aggregation during Fruiting Body Formation in *Myxococcus xanthus* Is Driven by Reducing Cell Movement ». In : *Journal of Bacteriology* 189.2 (2007). doi : 10.1128/JB.01206-06.

[222] A. Scheel et A. Stevens. « Wavenumber selection in coupled transport equations ». In : *Journal of Mathematical Biology* 75.5 (2017). doi : 10.1007/s00285-017-1107-8.

[223] R. Eftimie. « Hyperbolic and kinetic models for self-organized biological aggregations and movement : a brief review ». In : *Journal of Mathematical Biology* 65.1 (2012). doi : 10.1007/s00285-011-0452-2.

[224] V. Méndez, S. A. Fedotov et W. Horsthemke. *Reaction-transport systems : mesoscopic foundations, fronts, and spatial instabilities*. Springer series in synergetics. Berlin Heidelberg : Springer, 2010.

[225] E. P. Zemskov et W. Horsthemke. « Diffusive instabilities in hyperbolic reaction-diffusion equations ». In : *Physical Review E* 93.3 (2016). doi : 10.1103/PhysRevE.93.032211.

[226] G. Consolo, C. Currò et G. Valenti. « Pattern formation and modulation in a hyperbolic vegetation model for semiarid environments ». In : *Applied Mathematical Modelling* 43 (2017). doi : 10.1016/j.apm.2016.11.031.

[227] G. Consolo et al. « Oscillatory periodic pattern dynamics in hyperbolic reaction-advection-diffusion models ». In : *Physical Review E* 105.3 (2022). doi : 10.1103/PhysRevE.105.034206.

[228] C. Currò et G. Valenti. « Pattern formation in hyperbolic models with cross-diffusion : Theory and applications ». In : *Physica D : Nonlinear Phenomena* 418 (2021). doi : 10.1016/j.physd.2021.132846.

[229] J. S. Ritchie, A. L. Krause et R. A. Van Gorder. « Turing and wave instabilities in hyperbolic reaction–diffusion systems : The role of second-order time derivatives and cross-diffusion terms on pattern formation ». In : *Annals of Physics* 444 (2022). doi : 10.1016/j.aop.2022.169033.

[230] M. Avery et al. « Instability in large bounded domains—branched versus unbranched resonances ». In : *Nonlinearity* 34.11 (2021). doi : 10.1088/1361-6544/ac2a15.

[231] L. E. Sidney et al. « Concise Review : Evidence for CD34 as a Common Marker for Diverse Progenitors ». In : *Stem Cells* 32.6 (2014). doi : 10.1002/stem.1661.

[232] H. H. Chang et al. « Transcriptome-wide noise controls lineage choice in mammalian progenitor cells ». In : *Nature* 453.7194 (2008). doi : 10.1038/nature06965.

[233] D. R. Sisan et al. « Predicting rates of cell state change caused by stochastic fluctuations using a data-driven landscape model ». In : *Proceedings of the National Academy of Sciences* 109.47 (2012). doi : 10.1073/pnas.1207544109.

[234] U. Herbach et al. « Inferring gene regulatory networks from single-cell data : a mechanistic approach ». In : *BMC Systems Biology* 11.1 (2017). doi : 10.1186/s12918-017-0487-0.

[235] P. C. Bressloff. *Stochastic Processes in Cell Biology : Volume I*. T. 41. Interdisciplinary Applied Mathematics. Cham : Springer International Publishing, 2021. doi : 10.1007/978-3-030-72515-0.

[236] M. Estavoyer et al. *Modeling relaxation experiments with a mechanistic model of gene expression*. 2024. doi : 10.1101/2024.04.04.588028.

[237] D. J. Nicholson. « Is the cell really a machine ? » In : *Journal of Theoretical Biology* 477 (2019). doi : 10.1016/j.jtbi.2019.06.002.

[238] J.-J. Kupiec. « A probabilistic theory for cell differentiation, embryonic mortality and DNA c-value paradox ». In : *Organisms. Journal of Biological Sciences* Vol 4 (2020). Artwork Size : 80-85 Pages Publisher : Organisms. Journal of Biological Sciences. doi : 10.13133/2532-5876/16964.

[239] D. Noble. « Genes and causation ». In : *Philosophical Transactions of the Royal Society A : Mathematical, Physical and Engineering Sciences* 366.1878 (2008). doi : 10.1098/rsta.2008.0086.

[240] E. Schrödinger. « What is life ? The physical aspect of the living cell. » In : (1944).

[241] T. Kalmar et al. « Regulated Fluctuations in Nanog Expression Mediate Cell Fate Decisions in Embryonic Stem Cells ». In : *PLoS Biology* 7.7 (2009). Sous la dir. de M. A. Goodell. doi : 10.1371/journal.pbio.1000149.

[242] D. T. Gillespie. « A general method for numerically simulating the stochastic time evolution of coupled chemical reactions ». In : *Journal of Computational Physics* 22.4 (1976). doi : 10.1016/0021-9991(76)90041-3.

[243] M. S. Ko. « A stochastic model for gene induction ». In : *Journal of Theoretical Biology* 153.2 (1991). doi : 10.1016/S0022-5193(05)80421-7.

[244] J. Peccoud et B. Ycart. « Markovian Modeling of Gene-Product Synthesis ». In : *Theoretical Population Biology* 48.2 (1995). doi : 10.1006/tpbi.1995.1027.

[245] A. Raj et al. « Stochastic mRNA Synthesis in Mammalian Cells ». In : *PLoS Biology* 4.10 (2006). Sous la dir. d'U. Schibler. DOI : 10.1371/journal.pbio.0040309.

[246] C. Albayrak et al. « Digital Quantification of Proteins and mRNA in Single Mammalian Cells ». In : *Molecular Cell* 61.6 (2016). DOI : 10.1016/j.molcel.2016.02.030.

[247] A. Sarkar et M. Stephens. *Separating measurement and expression models clarifies confusion in single-cell RNA sequencing analysis*. 2020. DOI : 10.1101/2020.04.07.030007.

[248] U. Herbach. « Stochastic Gene Expression with a Multistate Promoter : Breaking Down Exact Distributions ». In : *SIAM Journal on Applied Mathematics* 79.3 (2019). DOI : 10.1137/18M1181006.

[249] R. Karmakar et I. Bose. « Graded and binary responses in stochastic gene expression ». In : *Physical Biology* 1.4 (2004). DOI : 10.1088/1478-3967/1/4/001.

[250] E. Laurenti et B. Göttgens. « From haematopoietic stem cells to complex differentiation landscapes ». In : *Nature* 553.7689 (2018). DOI : 10.1038/nature25022.

[251] C. Fourneaux et al. « Differentiation is accompanied by a progressive loss in transcriptional memory ». In : *BMC Biology* 22.1 (2024). DOI : 10.1186/s12915-024-01846-9.

[252] N. E. Phillips et al. « Memory and relatedness of transcriptional activity in mammalian cell lineages ». In : *Nature Communications* 10.1 (2019). DOI : 10.1038/s41467-019-09189-8.

[253] B. Perthame. *Transport Equations in Biology*. Frontiers in Mathematics. Basel : Birkhäuser Basel, 2007. DOI : 10.1007/978-3-7643-7842-4.

[254] B. Chereda et J. V. Melo. « Natural course and biology of CML ». In : *Annals of Hematology* 94.S2 (2015). DOI : 10.1007/s00277-015-2325-z.

[255] B. Laperrousaz et al. « Primitive CML cell expansion relies on abnormal levels of BMPs provided by the niche and on BMPRIb overexpression ». In : *Blood* 122.23 (2013). DOI : 10.1182/blood-2013-05-501460.

[256] A. M. Vershik. « Long History of the Monge-Kantorovich Transportation Problem : (Marking the centennial of L.V. Kantorovich's birth !) » In : *The Mathematical Intelligencer* 35.4 (2013). DOI : 10.1007/s00283-013-9380-x.

[257] S. M. Castillo-Hair et al. « FlowCal : A User-Friendly, Open Source Software Tool for Automatically Converting Flow Cytometry Data from Arbitrary to Calibrated Units ». In : *ACS Synthetic Biology* 5.7 (2016). DOI : 10.1021/acssynbio.5b00284.

[258] R. A. Horn et C. R. Johnson. *Matrix Analysis*. 1re éd. Cambridge University Press, 1985. DOI : 10.1017/CBO9780511810817.

[259] B. Schwanhäusser et al. « Global quantification of mammalian gene expression control ». In : *Nature* 473.7347 (2011). DOI : 10.1038/nature10098.

[260] D. Nicolas, N. E. Phillips et F. Naef. « What shapes eukaryotic transcriptional bursting ? » In : *Molecular BioSystems* 13.7 (2017). DOI : 10.1039/C7MB00154A.

[261] D. J. Venzon et S. H. Moolgavkar. « A Method for Computing Profile-Likelihood-Based Confidence Intervals ». In : *Applied Statistics* 37.1 (1988). DOI : 10.2307/2347496.

[262] A. Raue et al. « Structural and practical identifiability analysis of partially observed dynamical models by exploiting the profile likelihood ». In : *Bioinformatics* 25.15 (2009). DOI : 10.1093/bioinformatics/btp358.

[263] D. Zipori. « The nature of stem cells : state rather than entity ». In : *Nature Reviews Genetics* 5.11 (2004). DOI : 10.1038/nrg1475.

[264] E. Ventre et al. « One model fits all : Combining inference and simulation of gene regulatory networks ». In : *PLOS Computational Biology* 19.3 (2023). Sous la dir. de C. Herrmann. DOI : 10.1371/journal.pcbi.1010962.

[265] C. Haass et D. J. Selkoe. « Soluble protein oligomers in neurodegeneration : lessons from the Alzheimer's amyloid β-peptide ». In : *Nature Reviews Molecular Cell Biology* 8.2 (2007). DOI : 10.1038/nrm2101.

[266] M. Sakono et T. Zako. « Amyloid oligomers : formation and toxicity of Aβ oligomers ». In : *The FEBS Journal* 277.6 (2010). DOI : 10.1111/j.1742-4658.2010.07568.x.

[267] U. Sengupta, A. N. Nilson et R. Kayed. « The Role of Amyloid-β Oligomers in Toxicity, Propagation, and Immunotherapy ». In : *EBioMedicine* 6 (2016). DOI : 10.1016/j.ebiom.2016.03.035.

[268] C. Soto. « Unfolding the role of protein misfolding in neurodegenerative diseases ». In : *Nature Reviews Neuroscience* 4.1 (2003). DOI : 10.1038/nrn1007.

[269] S. I. A. Cohen et al. « Proliferation of amyloid-β42 aggregates occurs through a secondary nucleation mechanism ». In : *Proceedings of the National Academy of Sciences* 110.24 (2013). DOI : 10.1073/pnas.1218402110.

[270] R. M. Murphy et M. M. Pallitto. « Probing the Kinetics of β-Amyloid Self-Association ». In : *Journal of Structural Biology* 130.2-3 (2000). DOI : 10.1006/jsbi.2000.4253.

[271] S. Nag et al. « Nature of the Amyloid-β Monomer and the Monomer-Oligomer Equilibrium ». In : *Journal of Biological Chemistry* 286.16 (2011). DOI : 10.1074/jbc.M110.199885.

[272] G. Forloni et C. Balducci. « Alzheimer's Disease, Oligomers, and Inflammation ». In : *Journal of Alzheimer's Disease* 62.3 (2018). Sous la dir. de G. Perry et al. DOI : 10.3233/JAD-170819.

[273] J. W. Kinney et al. « Inflammation as a central mechanism in Alzheimer's disease ». In : *Alzheimer's & Dementia : Translational Research & Clinical Interventions* 4.1 (2018). DOI : 10.1016/j.trci.2018.06.014.

[274] I. Ciuperca et al. « A qualitative analysis of an Aβ -monomer model with inflammation processes for Alzheimer's disease ». In : *Royal Society Open Science* 11.5 (2024). DOI : 10.1098/rsos.231536.

[275] N. F. Al-Ghraiybah et al. « Glial Cell-Mediated Neuroinflammation in Alzheimer's Disease ». In : *International Journal of Molecular Sciences* 23.18 (2022). doi : 10.3390/ijms231810572.

[276] I. Lopategui Cabezas, A. Herrera Batista et G. Pentón Rol. « The role of glial cells in Alzheimer disease : potential therapeutic implications ». In : *Neurología (English Edition)* 29.5 (2014). doi : 10.1016/j.nrleng.2012.10.009.

[277] G. W. Kreutzberg. « Microglia : a sensor for pathological events in the CNS ». In : *Trends in Neurosciences* 19.8 (1996). doi : 10.1016/0166-2236(96)10049-7.

[278] H. Akiyama. « Inflammation and Alzheimer's disease ». In : *Neurobiology of Aging* 21.3 (2000). doi : 10.1016/S0197-4580(00)00124-X.

[279] H. Kettenmann et al. « Physiology of Microglia ». In : *Physiological Reviews* 91.2 (2011). doi : 10.1152/physrev.00011.2010.

[280] M. Andrade-Restrepo et al. « Modeling the spatial propagation of Aβ oligomers in Alzheimer's Disease ». In : *ESAIM : Proceedings and Surveys* 67 (2020). Sous la dir. de V. Calvez et al. doi : 10.1051/proc/202067003.

[281] I. Ciuperca et al. « Alzheimer's disease and prion : An *in vitro* mathematical model ». In : *Discrete & Continuous Dynamical Systems - B* 22.11 (2017). doi : 10.3934/dcdsb.2019057.

[282] W. Hao et A. Friedman. « Mathematical model on Alzheimer's disease ». In : *BMC Systems Biology* 10.1 (2016). doi : 10.1186/s12918-016-0348-2.

[283] F. Matthäus. « Diffusion versus network models as descriptions for the spread of prion diseases in the brain ». In : *Journal of Theoretical Biology* 240.1 (2006). doi : 10.1016/j.jtbi.2005.08.030.

[284] F. Matthäus. « The spread of prion diseases in the brain — models of reaction and transport on networks ». In : *Journal of Biological Systems* 17.04 (2009). doi : 10.1142/S0218339009003010.

[285] M. Bertsch et al. « Alzheimer's disease : a mathematical model for onset and progression ». In : *Mathematical Medicine and Biology : A Journal of the IMA* (2016). doi : 10.1093/imammb/dqw003.

[286] J. E. Pearson. « Complex Patterns in a Simple System ». In : *Science* 261.5118 (1993). doi : 10.1126/science.261.5118.189.

[287] W. Mazin et al. « Pattern formation in the bistable Gray-Scott model ». In : *Mathematics and Computers in Simulation* 40.3-4 (1996). doi : 10.1016/0378-4754(95)00044-5.

[288] V. K. Vanag et I. R. Epstein. « Out-of-phase oscillatory Turing patterns in a bistable reaction-diffusion system ». In : *Physical Review E* 71.6 (2005). doi : 10.1103/PhysRevE.71.066212.

[289] V. Weide Rodrigues, D. Cristina Mistro et L. A. Díaz Rodrigues. « Pattern Formation and Bistability in a Generalist Predator-Prey Model ». In : *Mathematics* 8.1 (2019). doi : 10.3390/math8010020.

[290] T. A. S. Al-Karkhi et al. « Bloom Formation and Turing Patterns in an Infochemical Mediated Multitrophic Plankton Model ». In : *International Journal of Bifurcation and Chaos* 30.10 (2020). DOI : 10.1142/S0218127420300281.

[291] D. Gilbarg et N. S. Trudinger. *Elliptic Partial Differential Equations of Second Order*. T. 224. Classics in Mathematics. Berlin, Heidelberg : Springer Berlin Heidelberg, 2001. DOI : 10.1007/978-3-642-61798-0.

[292] J. L. Aragón et al. « Nonlinear effects on Turing patterns : Time oscillations and chaos ». In : *Physical Review E* 86.2 (2012). DOI : 10.1103/PhysRevE.86.026201.

[293] R. Liu, S. Liaw et P. Maini. « Oscillatory Turing patterns in a simple reaction-diffusion system ». In : (2007).

[294] K. Manna et M. Banerjee. « Spatiotemporal pattern formation in a prey–predator model with generalist predator ». In : *Mathematical Modelling of Natural Phenomena* 17 (2022). DOI : 10.1051/mmnp/2022007.

[295] G. Gambino, M. C. Lombardo et M. Sammartino. « Cross-diffusion-induced subharmonic spatial resonances in a predator-prey system ». In : *Physical Review E* 97.1 (2018). DOI : 10.1103/PhysRevE.97.012220.

[296] H. Uecker et D. Wetzel. « Snaking branches of planar BCC fronts in the 3D Brusselator ». In : *Physica D : Nonlinear Phenomena* 406 (2020). DOI : 10.1016/j.physd.2020.132383.

[297] J. Rivers-Auty et al. « Anti-inflammatories in Alzheimer's disease—potential therapy or spurious correlate ? » In : *Brain Communications* 2.2 (2020). DOI : 10.1093/braincomms/fcaa109.

[298] ADAPT Research Group. « Naproxen and celecoxib do not prevent AD in early results from a randomized controlled trial ». In : *Neurology* 68.21 (2007). DOI : 10.1212/01.wnl.0000260269.93245.d2.

[299] A. R. Group. « Cognitive Function Over Time in the Alzheimer's Disease Anti-inflammatory Prevention Trial (ADAPT) : Results of a Randomized, Controlled Trial of Naproxen and Celecoxib ». In : *Archives of Neurology* 65.7 (2008). DOI : 10.1001/archneur.2008.65.7.nct70006.

[300] T. Ozben et S. Ozben. « Neuro-inflammation and anti-inflammatory treatment options for Alzheimer's disease ». In : *Clinical Biochemistry* 72 (2019). DOI : 10.1016/j.clinbiochem.2019.04.001.

[301] Imbimbo. « Are NSAIDs useful to treat Alzheimer's disease or mild cognitive impairment ? » In : *Frontiers in Aging Neuroscience* (2010). DOI : 10.3389/fnagi.2010.00019.

[302] M. M. Ali et al. « Recommendations for Anti-inflammatory Treatments in Alzheimer's Disease : A Comprehensive Review of the Literature ». In : *Cureus* (2019). DOI : 10.7759/cureus.4620.

[303] B. J. Walker et al. « VisualPDE : Rapid Interactive Simulations of Partial Differential Equations ». In : *Bulletin of Mathematical Biology* 85.11 (2023). DOI : 10.1007/s11538-023-01218-4.

Propagation and pattern formation in biology

Abstract : This thesis explores the modeling of propagation phenomena and the emergence of periodic patterns in space :

• This thesis also focuses on the emergence of bird feathers during ovogenesis. During this process, feather follicles generally emerge row by row, following a medio-lateral wave, through a two-step development process : first, a condensation of the dermis making it competent, followed by the emergence of cell aggregates leading to the formation of future feathers. Using a reaction-diffusion-taxis model, we propose, through linear and weakly nonlinear analysis, explicit formulas for the speeds associated with these two steps. Through a numerical study of the interaction between these two steps, we propose a formula for the emergence speed of feathers during avian morphogenesis.

• Another project developed during this thesis involves the invasion of the predatory bacterium *Myxococcus xanthus*. These bacteria can form clusters with properties distinct from those of isolated cells. Notably, they possess two different motility systems : adventurous (A) motility for isolated bacteria and social (S) motility for bacteria in clusters. This difference leads to significant variations in individual speed and movement type. To model the collective invasion of this bacterium, we propose and study several models, such as a prey-predator model, a reaction-diffusion model, and a nonlinear kinetic model with size structure. The numerical and theoretical study of traveling wave solutions allows us to identify the factors influencing the predation speed. Notably, our latest model suggests that the interaction between A and S motilities is synergistic.

• A significant part of my thesis focuses on the modeling of cell relaxation experiments. These experiments involve selecting a sub-fraction of a cell population and observing the speed at which this sub-population returns to its equilibrium state. To model this phenomenon, we propose a two-state mechanistic model that takes proliferation into account. To compare our model with experimental data, we conducted a relaxation experiment of the CD34 antigen on the surface of TF1-BA cells. Whether isolating populations with the highest or lowest levels of CD34 expression, we observe in both cases that after approximately 25 days, the CD34 distribution in the population returns to its initial steady state. Numerical simulations of our model, based on parameter values estimated from our experimental data, showed that the model solutions closely align with our experimental results.

• Finally, we study the spatial patterns of a reaction-diffusion system modeling the formation of amyloid plaques in the brain related to Alzheimer's disease. Linear analysis and numerous numerical simulations reveal several types of spatially heterogeneous solutions. An in-depth analysis of the stability and bifurcations of stable patterns allows us to formulate conjectures on the influence of inflammation and microglial cells in the formation of amyloid plaques.

Keywords : Turing patterns ; Traveling waves ; Modeling.

Propagation et émergence de motifs en biologie

Résumé : Cette thèse explore la modélisation de phénomènes de propagation et d'émergence de motifs dans l'espace :

• Une partie importante de ma thèse se concentre sur l'émergence des plumes d'oiseaux lors de l'ovogenèse. Au cours de celle-ci, les follicules plumeux émergent généralement rangée par rangée, suivant une vague médio-latérale, à travers un processus de développement en deux étapes : d'abord, une densification du derme le rendant compétent, suivie de l'émergence d'agrégats de cellules menant à la formation des futures plumes. En utilisant un modèle de réaction-diffusion-taxis nous proposons, à l'aide d'une analyse linéaire et faiblement non linéaire, des formules explicites des vitesses associées à ces deux étapes. Grâce à une étude numérique de l'interaction entre ces deux étapes, nous proposons une formule de la vitesse d'émergence des plumes lors de la morphogenèse aviaire.

• Cette thèse se focalise également sur l'invasion de la bactérie prédatrice *Myxococcus xanthus*. Les bactéries *M. xanthus* sont capables de former des agrégats ayant des propriétés différentes des bactéries isolées. Notamment, elles possèdent deux systèmes de motilité complètement différents : la motilité aventureuse (A) pour les bactéries isolées et la motilité sociale (S) pour les bactéries dans les agrégats. Cette différence entraîne des variations significatives dans la vitesse individuelle et le type de mouvement effectué. Pour modéliser l'invasion collective de cette bactérie, nous proposons et étudions plusieurs modèles : par exemple un modèle proie-prédateur, un modèle de réaction-diffusion et un modèle cinétique non linéaire avec une structure en taille. L'étude numérique et théorique des solutions d'onde progressive permet de déterminer les facteurs influençant la vitesse de prédation. Notamment, notre dernier modèle suggère que l'interaction entre les motilités A et S est synergique.

• Un autre projet développé lors de cette thèse porte sur la modélisation des expériences de relaxation cellulaire. Ces expériences consistent à sélectionner une sous-fraction d'une population cellulaire et à observer la vitesse à laquelle cette sous-population revient à son état de repos ou d'équilibre. Pour modéliser ce phénomène, nous proposons un modèle mécaniste à deux états prenant en compte la prolifération. Afin de confronter notre modèle aux données expérimentales, nous avons mené une expérience de relaxation de l'antigène CD34 à la surface des cellules TF1-BA. Que ce soit en isolant les populations avec les niveaux d'expression de CD34 les plus élevés ou les plus bas, nous observons dans les deux cas qu'après environ 25 jours, la distribution de CD34 dans la population revient à son état stationnaire initial. Des simulations numériques de notre modèle, basées sur des valeurs de paramètres estimées à partir de nos données expérimentales, ont montré que les solutions du modèle s'alignent étroitement aux résultats de nos expériences.

• Enfin, nous étudions les motifs spatiaux d'un système de réaction-diffusion modélisant la formation des plaques amyloïdes dans le cerveau en lien avec la maladie d'Alzheimer. Une analyse linéaire et de nombreuses simulations numériques révèlent plusieurs types de solutions spatialement hétérogènes. L'analyse approfondie de la stabilité et des bifurcations des motifs stables nous permet de formuler des conjectures sur l'influence de l'inflammation et des cellules microgliales dans la formation des plaques amyloïdes.

Mots clés : Motifs de Turing, Ondes progressives, Modélisation.

Image en couverture : Image générée à l'aide du logiciel `VisualPDE` [303].

UNIVERSITÉ DE LYON